Advances in Nanostructured Materials via Templated Sol-Gel Structure Control and Self-Assembly

A DISSERTATION
SUBMITTED TO THE FACULTY OF
UNIVERSITY OF MINNESOTA
BY

Stephen G. Rudisill

IN PARTIAL FULFILLMENT OF THE REQUIREMENTS
FOR THE DEGREE OF
DOCTOR OF PHILOSOPHY

Advisor: Andreas Stein

April 2015

Acknowledgements

This dissertation is the result of well over a decade of preparation, study, and research, and could not have been accomplished without the help and inspiration of so many people. I'd like to thank at least some of them here.

Thanks to Greg Wilson and George Lisensky, who inspired my love of chemistry and nanoscience with their engaging and dedicated approaches to science education.

Many heartfelt thanks to Stein Group members, past and present, for their wisdom, advice, and mutual support. To the researchers who made material contributions to this dissertation—Nicholas Petkovich, Luke Venstrom, Daniel Boman, Nick Hein, Denis Terzic, Sammy Shaker, Tingting Quan, Réginald Le Maire, Mike DiVito, and Camille Malonzo—thank you all for your work, support, and insight. *Ad astra per aspera.*

I am incredibly grateful to Alex Rudd and David Josephson: you kept me balanced and gave me perspective—frequently over burritos—when I needed it most.

I would also like to thank the professors I've worked with during my graduate school career; Jane Davidson for her efforts and feedback on thermochemical cycling, Lee Penn for her untiring willingness to be on my committees, Allison Hubel for her advice and patience while I re-learned biochemistry. Finally, thanks to my advisor, Andreas Stein, for his ingenuity, guidance, and support throughout my graduate school career.

To my parents, thank you for laying the groundwork for who I would become.

And lastly, the greatest possible thanks to my wonderful wife and children. You are my life, and without your love and support, I surely would have shattered long before I ever made it here.

Dedication

To Rhiannon, Ethan, and Evelyn—we made it!

Abstract

This dissertation describes a body of work focused on understanding and improving morphology control of nanoporous structures via their aqueous chemistry. Synthesis of materials was carried out primarily using the Pechini process with metal nitrates and colloidal crystal templates. CeO_2 and CeO_2-derived compounds were used for a substantial portion of the dissertation as they are useful for thermochemical cycling experiments. Templated CeO_2 shows a tenfold improvement over an untemplated material as well as a nanoparticle powder under lab-scale thermochemical cycling experiments.

The Pechini process itself was then investigated as a means to obtain greater structural control over colloidal crystal templated materials. The process was demonstrated to involve phase separation, which allowed for the production of microspheres and bicontinuous networks of templated CeO_2-based solids. Microspheres produced were between 1–3 μm in size, with polydispersity less than 15%. Further experimentation demonstrated that this phase separation methodology was generalizable to Fe_2O_3 and Mn_3O_4, though higher polydispersities were obtained for these materials.

The final research project accomplished in this dissertation involves a method to produce ordered collagen fibrils through the incorporation of nanocrystalline cellulose during fibrillogenesis. Results were verified via scanning electron microscopy and a mechanism was proposed based on infrared spectroscopy results indicating a decrease in collagen-collagen hydrogen bonding.

Table of Contents

List of Tables ix

List of Figures x

Chapter 1: Introduction to Nanoporous Solids 1

1.1 Aqueous Synthesis and/or Self-Assembly of Solid-State Materials 1

1.1.1 The Chemistry and Materials Science of Porous Structures 2

1.1.2 Generation of Nanoporous Architectures 3

1.1.3 Structural Elements of 3DOM Materials 5

1.1.4 Porous Materials and High Temperature Applications 7

1.1.5 3DOM Materials Under Thermal Stress 9

1.2 Solar Thermochemical Energy Generation 10

1.2.1 Thermochemical Cycling of Metal Oxides 12

1.2.2 Thermochemical Cycles and Catalysis 14

1.2.3 Water Splitting vs. CO_2 Splitting 15

1.2.4 Concentrating Solar Power (CSP) Systems 16

1.3 Sol-Gel Chemistry and Untemplated Porosity 17

1.3.1 Metal-Oxide Gelation & Mediators 20

1.3.2 Phase Separation in Sol-Gel Synthesis 22

1.3.3 Discussion of Step-Growth Polymerization 28

1.4 Biologically-Occurring Self-Assembly 33

1.4.1 Corneal Prosthetics and Collagen Self-Assembly 34

1.5 Summary 37

Chapter 2: Thermochemical Cycling of Nanoporous Ceramics 39
2.1 Introduction 39
2.1.2 Solar Thermochemical Cycling with Porous CeO_2 39
2.2 Morphological Considerations of CeO_2 Thermochemical Cycling 41
2.3 Experimental Methods 45
2.3.1 Synthesis of colloidal crystal templates and CeO_2 samples 45
2.3.2 Reactivity and productivity testing 46
2.4 Results and Discussion 49
2.4.1 Morphological Study 49
2.4.2 Thermal behavior 55
2.4.3 Thermochemical Cycling 56
2.4.4 Final sample morphology 74
2.5 Summary of Morphological Studies 77
2.6 Acknowledgements 78
Chapter 3: Tuning the Thermal Resistance of Nanoscale Ceramics 79
3.1 Introduction 79
3.1.1 Doped CeO_2 Materials 79
3.2 Experimental Methods 81
3.2.1 Synthesis of Colloidal Crystals and 3DOM Metal Oxides 81
3.2.2 Thermal Testing of 3DOM Metal Oxides 82
3.2.3 Characterization of Materials 82
3.3 Results and Discussion 83

3.3.1 Binary and Ternary CeO_2 Mixed-Oxides 83
3.3.2 In-Depth Study of Ce-Zr Mixed-Oxides 86
3.3.3 Limiting Morphology Changes in 3DOM CeO_2 90
3.3.4 Literature-Guided Synthesis of Quaternary Oxides 93
3.4 Conclusions 97
3.5 Acknowledgements & Copyright 97
Chapter 4: Microstructural Evolution in Templated Pechini Precursors 98
4.1 Introduction 98
4.2 Experimental Section 104
4.2.1 Materials & Reagents 104
4.2.2 Template Synthesis 104
4.2.3 Porous Microsphere Synthesis 105
4.2.4 Materials Characterization 106
4.3. Results and Discussion 106
4.3.1 Microstructural Variation in 3DOM Ce-based Oxides 106
4.3.2 Effects of Alkaline Earth Metals in Solid Solutions with CeO_2 111
4.3.3 Effects of Gel Components on $Ce_{0.5}Mg_{0.5}O_{1.5}$ 113
4.3.4. Confinement and Charge Effects 120
4.3.5. Single-Cation CeO_2 Materials 122
4.4 Conclusions 124
4.5 Acknowledgements 125
Chapter 5: Generalizing Pechini-Based Polymerization-Induced Phase Separation 126

5.1 Introduction 126
5.2 Experimental 129
5.2.1 Materials & Reagents 129
5.2.2 Template Synthesis 130
5.2.3 Synthesis of Porous Microspheres and Bicontinuous Networks 130
5.2.4 Characterization 131
5.3 Results and Discussion 131
5.3.1 Overview of Structures and Morphologies Observed 131
5.3.2 Molecular Weight, Stoichiometric Balance, and Morphology 135
5.3.3 Obstacles to Generalization 144
5.3.4 Morphological Variation in Fe_2O_3 and Mn_3O_4 Pechini Gels 147
5.3.5 Tuning Templating Behavior via Precursor Composition 150
5.3.6 Construction of Partial Phase Diagrams 154
5.4 Conclusions 161
5.5 Acknowledgements 162
Chapter 6: Controlling Self-Assembly of Collagen Fibrils Ex Vivo 163
6.1 Introduction 163
6.2 Materials and Methods 166
6.2.1 Materials 166
6.2.2 Concentrating the Collagen Solutions 167
6.2.3 Preparation of Collagen Composites 167
6.2.4 Biocompatibility Studies 168

6.2.5 Characterization 169
6.2.6 Statistics 170
6.3 Results 171
6.3.1 Collagen Gel Network Morphology 171
6.3.2 Biocompatibility 177
6.3.3 Chemical Interactions 178
6.4 Discussion 181
6.4.1 Formation of Collagen Gel Networks 181
6.4.2 Mechanism of Collagen Alignment 183
6.5 Conclusions 186
6.6 Acknowledgements 187
Chapter 7: Future Directions for Porous Materials Design 188
7.1 Chemical Energy Storage via Thermochemical Cycling 188
7.2 Sol-Gel Materials via Phase Separation 192
7.3 Formation of Ordered Collagen Fibrils 194
7.4 A Self-Assembled Conclusion 195
Bibliography 197

List of Tables

Table 2.1. Morphological characteristics of the CeO_2 materials before and after thermochemical cycling, measured from images in Figure 2.3 54

Table 3.1. Precursor compositions for CeO_2 and CeO_2 solid solution materials prepared via MeOH infiltration. Crystallite sizes of the products are provided where data is available 85

Table 3.2. Grain sizes of the Ce-Zr mixed oxides measured via the Scherrer equation and wall thicknesses measured from SEM analysis 89

Table 5.1. List of materials synthesized by composition, with a description of product morphologies.....135

Table 5.2. K_f Data and binding modes for Ce^{3+}, Mn^{2+}, Fe^{3+} 152

List of Figures

Figure 1.1. (left) Schematic diagram of the colloidal crystal templating process for producing 3DOM materials and SEM images illustrating the different morphologies obtained by surface templating (a) vs. volume templating (b) of 3DOM W materials. The blue and red circles indicate tetrahedral and octahedral nodes, respectively. Figure reprinted from ref. 19 with permission. 6

Figure 1.2. SEM images of macroporous α-Al2O3 calcined at 1150 °C for 6 h (left) and further calcined at 1300 °C for 4 h (right). The larger cube-like nodes result from the octahedral holes in the PMMA template, whereas the smaller tetrahedral nodes arise from the tetrahedral holes. Sintering causes the nodes to grow at the expense of the struts, which become even thinner. Image reproduced from ref. 30, reprinted with permission. 10

Figure 1.3 Reaction scheme for solar thermochemical cycling of CeO_2 13

Figure 1.4. The four most common setups for CSP systems. (a) Trough, (b) tower, (c) dish, and (d) double concentration. 17

Figure 1.5. Sol-gel synthesis at-a-glance. Shows the microstructures developed during the process, as well as the products which can be obtained by "halting" the structural evolution. Image adapted from ref. 79, reprinted with permission.....20

Figure 1.6. 2-D slices of computed structures of a two-phase system resulting from spinodal decomposition with differing levels of granularity. The structure results from randomly oriented sine waves, defined by the concentration of one phase in the other. These structures were computed using (a) 20, (b) 50, and (c) 100 sine waves. Note that while the phases do not appear interconnected in their 2-D representation, they are indeed interconnected in the third dimension. Image from ref. 98, reprinted with permission. ...24

Figure 1.7. TEM images of a Fe-Mn-Al-C alloy which has undergone spinodal decomposition. Samples were held at 650 °C for (a) 180 min, (b) 6,000 min, and (c) 48,800 min, and then quenched in an ice brine bath. Image from ref. 103, reprinted with permission. 25

Figure 1.8. A qualitative tertiary phase diagram showing the structures available by the sol-gel method with phase separation in silica. Increasing organic additive concentration (in this case PEO) leads to a decrease in observed pore size, while increasing solvent concentration increases pore volume. Structure types include bicontinuous networks and microspheres. Image from ref. 42, reprinted with permission. 27

Figure 1.9. Carothers' diagram showing molecular weight distributions for condensation polymers by reaction extent. Note that as p approaches 1 (from 0.9 to 0.999), greater fractions of higher molecular weight molecules are obtained. Figure from ref. 117, reprinted with permission.. 31

Figure 1.10. Image of star "polymers" (branched structures) assembled from gold nanorods. X_L, X_M, and X_s denote long, medium, and short chains on the "polymer" chain. Scale bars are 200 nm. Image from ref. 119, reprinted with permission.. 32

Figure 1.11. D-banding in collagen, resulting from consistent spacing between the C and N termini of adjacent collagen molecules. Figure from ref. 145, reprinted with permission. 37

Figure 2.1. Schematic diagram of the reactor system employed in this work. 48

Figure 2.2. The controlled temperature in the IR furnace for four representative cycles. Data for two separate runs are shown to demonstrate reproducibility.....48

Figure 2.3. Representative SEM images of CeO_2 materials with the four morphologies used in this study. In commercial CeO_2 before (a) and after cycling (b), little change is observed. For 3DOM CeO_2 before (c) and after cycling (d), although the walls have undergone significant sintering and, in some areas, the order has been lost, the pore structure remains interconnected. For NOM CeO_2 before (e) and after cycling (f), the most prominent change after cycling is an increase in skeletal wall thickness; otherwise, the overall morphology of the structure remains unchanged. Finally, for D-3DOM CeO_2 before (g) and after cycling (h), it is clear that the sample has undergone extensive sintering.....52

Figure 2.4. XRD patterns of the materials investigated in this work (before and after cycling) are shown above. The left column contains patterns of the as-made samples. Peak broadening is observed in the templated materials, since they are nanocrystalline. For the commercial material with micrometer-sized grains there is no observed line broadening. The right column contains the patterns of the sample after thermochemical cycling. No line broadening is observed, indicating that the crystallite size is substantially greater than before cycling. All peaks in the patterns match those of the literature pattern for cubic fluorite CeO_2.....53

Figure 2.5. The rate of O_2 and CO production over 3DOM CeO_2 in cycles 34–36 (representative of stable cycling) and the corresponding temperature recorded by the temperature probe embedded in the sample.....57

Figure 2.6. O_2 production rate from 3DOM CeO_2 versus heating rate. Rapid heating is correlated with rapid O_2 release because the reduction of ceria in the present study is heat-transfer-limited.....58

Figure 2.7. (a) The total O_2 (triangles) and CO (circles) gas produced in each thermochemical cycle over 3DOM, NOM, D-3DOM, and commercial CeO_2. (b) The maximum temperature recorded by the temperature probe embedded in the sample during reduction in each cycle.....60

Figure 2.8. (a) The maximum temperature attained by the thermocouple probe at the interior of the samples during reduction (T_{max}) and the minimum temperature attained by the thermocouple probe during oxidation (T_{min}) during all thermochemical cycles. (b) The difference between the maximum and minimum temperatures shown in (a).....61

Figure 2.9. Feature size increases in 3DOM CeO_2 by cycle, as measured via SEM. For cycles 1 and 6, where the ordered structure was retained, the walls were measured. As the average size increases, the distribution of feature sizes increases as well. Feature size triples by cycle 15, and gradually increases past that point. 64

Figure 2.10. Images of 3DOM CeO_2 from approximately the same region in the bed for cycles 1, 6, 10, 15, 25, and 35, panels a–f respectively. 65

Figure 2.11. Estimation of sample temperatures from sample morphologies. These SEM images show representative areas of thermochemically cycled 3DOM CeO_2 (left) and 3DOM CeO_2 treated for 1 h at a specific temperature in a conventional furnace (right). (a) A moderately sintered area of thermochemically cycled 3DOM CeO_2, indicative of ~60 % of the sample has a similar morphology as (b) 3DOM CeO_2 sintered at 1150 °C for 1 h. (c) A heavily sintered area of thermochemically cycled 3DOM CeO_2, indicative of ~10–20 % of the sample has a similar morphology as (d) 3DOM CeO_2 sintered at 1250 °C for 1 h.....67

Figure 2.12. SEM images show the presence of a thermal gradient in the 3DOM CeO_2 sample thermochemically cycled. (a) A piece of 3DOM CeO_2 that was located next to the sample thermocouple. (b) An enlarged view of a region closer to the wall of the process tube than (c) the region which was adjacent to the thermocouple. The typical morphology observed in (b), a disordered, interconnected pore network results from sintering. In contrast, the originally templated 3DOM morphology, though lightly sintered, is readily apparent in (c). 68

Figure 2.13. (a) Rates of gas production for the different CeO_2 morphologies taken from representative cycles. (b) The temperature measured by the sensor at the interior of the samples for the same cycles. 70

Figure 2.14. Rate of CO (green) and O_2 (blue) production for 3DOM CeO_2 is shown for the entire course of thermochemical cycling. The temperature measured by the thermocouple embedded in the sample is also shown (red). 71

Figure 2.15. Rate of CO (green) and O_2 (blue) production for NOM CeO_2 is shown for the entire course of thermochemical cycling. The temperature measured by the thermocouple embedded in the sample is also shown (red). 71

Figure 2.16. Rate of CO (green) and O_2 (blue) production for D-3DOM CeO_2 is shown for the entire course of thermochemical cycling. The temperature measured by the thermocouple embedded in the sample is also shown (red). 72

Figure 2.17. Rate of CO (green) and O_2 (blue) production for the commercial CeO_2 is shown for the entire course of thermochemical cycling. The temperature measured by the thermocouple embedded in the sample is also shown (red). 72

Figure 2.18. Characteristic CO production from nonporous CeO_2 over long timescales. The inset shows the abrupt drop in CO production at the end of an oxidation step during rapid cycling, showing that oxidation was incomplete when the CO_2 flow was shut off..73

Figure 3.1. Examples of 3DOM structure observed in CeO_2 and several binary solid solutions. (a) 3DOM CeO_2. (b) 3DOM $Ce_{0.8}Zr_{0.2}O_2$. (c) 3DOM $Ce_{0.66}Gd_{0.33}O_{1.83}$. (d) 3DOM $Ce_{0.8}Sm_{0.2}O_{1.9}$. The structure is very similar in each case, addition of dopant does not affect the template morphology in any way....84

Figure 3.2. Experimental XRD patterns for materials synthesized. All show a good match with the literature pattern for CeO_2. Small peaks observed at 52.4° 2θ arise from the aluminum sample holder. 85

Figure 3.3. TEM images of 3DOM Ce-Zr solid solutions cycled isothermally at 825 °C with H_2. (a) CeO_2, (b) $Ce_{0.9}Zr_{0.1}O_2$, (c) $Ce_{0.8}Zr_{0.2}O_2$, (d) $Ce_{0.7}Zr_{0.3}O_2$, (e) $Ce_{0.6}Zr_{0.4}O_2$, (f) $Ce_{0.5}Zr_{0.5}O_2$. 89

Figure 3.4. SEM images of binary and ternary oxides as synthesized (left column), after sintering at 1300 °C for 2 h (middle column), and after sintering at 1400 °C for 2 h (right column). (a–c) 3DOM CeO_2, as-synthesized, 1300 °C, and 1400 °C. (d–f) 3DOM $Ce_{0.8}Sm_{0.2}O_{1.9}$, with the same temperatures listed above. (g–i) 3DOM $Ce_{0.8}Sm_{0.1}La_{0.1}$, same temperatures. (j–l) 3DOM $Ce_{0.8}Zr_{0.1}La_{0.1}$, same temperatures. 92

Figure 3.5. XRD patterns of representative CZYC samples showing the lack of impurity phases. As with the binary and ternary mixed-oxides, metal additives fully incorporate into the fluorite lattice. 94

Figure 3.6. SEM images of CZYC samples showing morphological characteristics. (a) CZYC7, a representative sample of the morphology of the as-prepared materials. (b) CZYC3 treated at 1400 °C for 2 h. (c) CZYC5 treated at 1400 °C for 2 h. (d) CZYC6 treated at 1400 °C for 2 h. (e) CZYC4 treated at 1400 °C for 2 h. (f) CZYC4 treated at 1400 °C for 22 h. (g) As-prepared wood-templated CZYC4. (h) CZYC7 treated at 1400 °C for 2 h. 96

Figure 3.7. SEM images of variations on the CZYC4 composition after treatment at 1400 °C for 2 h. (a) CZYM1 and (b) CZSC1. 97

Figure 4.1. The Pechini process in confinement. Top: complexation of cations by citric acid followed by cross-linking of citric acid by ethylene glycol. Bottom: Depending on synthesis parameters, either macroporous microspheres or extended structures with hierarchical macroporosity are formed. 102

Figure 4.2. SEM images of structures observed in colloidal-crystal-templated Pechini syntheses. (a) 3DOM CeO_2, synthesized from a precursor with a EG:CA:TMI ratio of 12:3:4. (b) Hierarchically structured network of 1:3:1 3DOM $Ce_{0.5}Mg_{0.5}O_{1.5}$. (c) Microspheres comprised of 1:1:1 3DOM $Ce_{0.5}Mg_{0.5}O_{1.5}$. (d) A fracture plane from a KPS-initiated CCT infiltrated with a 2:1:1 $Ce_{0.5}Mg_{0.5}O_{1.5}$ precursor and treated at 90 °C for 23 h. Microspheres developing inside the template can be observed. 108

Figure 4.3. TEM image of a single "211" $Ce_{0.5}Mg_{0.5}O_{1.5}$ microsphere. Inset: A selected-area electron diffraction pattern showing rings, as opposed to a single array of dots, indicates that the sphere is polycrystalline.....110

Figure 4.4. SEM image of "211" $Ce_{0.5}Mg_{0.5}O_{1.5}$ microspheres after resuspension in water and vortex stirring for 15 minutes. The suspension was dispersed on a stub, dried, coated with 5 nm of Pt, and then imaged. The smooth, cracked background is the carbon adhesive on the SEM stub.....111

Figure 4.5. SEM images and XRD patterns for ceramic powders derived from Pechini gels at the 3:1:1 (EG:CA:TMI) composition. (a) The $Ce_{0.5}Sr_{0.5}O_{1.5}$ sample consisted of microspheres approximately 1–2 μm in diameter, and contained a substantial amount of $SrCO_3$. (b) The $Ce_{0.5}Ca_{0.5}O_{1.5}$ product showed little evidence for microspheres but formed a solid solution. (c) The $Ce_{0.5}Mg_{0.5}O_{1.5}$ product consisted of slightly smaller microspheres than the $Ce_{0.5}Sr_{0.5}O_{1.5}$ sample, but also formed a solid solution. The sharp peak at 52.3 ˚2θ (*) is from the Al sample holder.....112

Figure 4.6. (a–c) SEM images demonstrating size control in 3DOM microspheres of $Ce_{0.5}Mg_{0.5}O_{1.5}$ templated with a KPS-initiated PMMA CCT (negative surface charge). (a) 3:1:1 CeMg, average sphere diameter 1.00 ± 0.16 μm. (b) 2:1:1 CeMg, average sphere diameter 1.55 ± 0.27 μm. (c) 1:1:1 CeMg, average sphere diameter 2.91 ± 0.43 μm, average macropore spacing 353 ± 4 nm. (d–f) SEM images of $Ce_{0.5}Mg_{0.5}O_{1.5}$ templated with an AMPA-initiated PMMA CCT (positive surface charge). (d) 3:1:1 $Ce_{0.5}Mg_{0.5}O_{1.5}$ shows no evidence of spheres. (e) 2:1:1 $Ce_{0.5}Mg_{0.5}O_{1.5}$ consists of a bicontinuous network with embedded spheroids. (f) 1:1:1 $Ce_{0.5}Mg_{0.5}O_{1.5}$ shows microspheres similar to what was observed with the KPS-initiated PMMA template, but with less regularity in the spheres and extensive polydispersity, average macropore spacing 268 ± 5 nm. (g–i) SEM images of 2:1:1 Ce-Mg oxides with decreasing Mg content. (j–l) SEM images of a phase-pure CeO_2 system. (j) 2:1:1 CeO_2, no microspheres are observed, but a network with hierarchical porosity is present. (k) 1:3:2 CeO_2, average sphere diameter 1.68 ± 0.30 μm. (l) 3:3:2 CeO_2, average sphere diameter 1.06 ± 0.21 μm. Insets on (k) and (l) show these spheres at higher magnification. Samples shown in (g–l) were prepared with a KPS-initiated PMMA CCT. 115

Figure 4.7. Histograms of microsphere sizes of the following samples: (a) “311”, “211”, and “111” $Ce_{0.5}Mg_{0.5}O_{1.5}$, (b) “132” and “332” CeO_2. 116

Figure 4.8. (a) SEM images of Pechini-derived Ce-Mg oxides with varying EG and CA content and differing microstructure. Images are denoted by the molar ratios of components within the precursor in the form EG:CA:TMI. Gel compositions with a 1:1 ratio of CA:TMI (x11) form spheres at different levels of growth based on the ethylene glycol content. Gel compositions with higher ratios of CA:TMI (X21, X31) result in bicontinuous networks (3DOM material interspersed with void space) in varying extents of spinodal decomposition. Scheme at center adapted from Ref. 207. (b) Graph of precursor compositions for $Ce_{0.5}Mg_{0.5}O_2$ materials depicted in (a) by EG and CA content, normalized to TMI. 118

Figure 4.9. SEM image of "111" $Ce_{0.5}Mg_{0.5}O_{1.5}$ synthesized with a loosely capped vial to permit slow escape of water. The "filling" of 3DOM material is much higher, so that fewer non-templated regions are present than in syntheses where water is retained in the vial.....120

Figure 4.10. SEM images of templated (KPS-PMMA) (a–c) and untemplated (d–f) Pechini gel-derived Ce-Mg oxides after calcination. (a) and (d) "121" $Ce_{0.5}Mg_{0.5}O_{1.5}$. (b) and (e) "221" $Ce_{0.5}Mg_{0.5}O_{1.5}$. (c) and (f) "111" $Ce_{0.5}Mg_{0.5}O_{1.5}$. None of the untemplated materials display similar microstructure to the templated ones, despite having the same gel composition and identical processing. 121

Figure 4.11. PXRD pattern of CeO_2 microspheres synthesized with no magnesium. Aside from peak broadening due to the nanocrystalline nature of the product, an exact match for the CeO_2 literature pattern is observed. 124

Figure 5.1. SEM micrographs of CeO_2 132 treated at (a) 90 °C for 24 h, (b) 80 °C for 16 h, and (c) 40 °C for 24 h. These samples were prepared using 489 nm PMMA spheres in the CCT and a nitrate precursor. 137

Figure 5.2. Molecular structures of the polyester linkers and chelating agents used in this study. Stoichiometric balance for the polymerization is affected by the degree of multifunctionality in these molecules. 138

Figure 5.3. SEM micrographs of $Ce_{0.5}Mg_{0.5}O_{1.5}$ 211 sample preparations with (a) no reagent substitutions, (b) substitution of glycerin for EG, (c) substitution of malic acid for CA, and (d) substitution of both glycerin and malic acid for EG and CA respectively. All the above samples were prepared using 489 nm PMMA spheres in the CCT. (e) $Ce_{0.5}Mg_{0.5}O_{1.5}$ 211 prepared with 395 nm PMMA spheres, no reagent substitutions. (f) $Ce_{0.5}Mg_{0.5}O_{1.5}$ 211 prepared with 362 nm PMMA spheres, no reagent substitutions. All samples were prepared from nitrate metal salts and were gelled at 90 ˚C for 24 h. 140

Figure 5.4. SEM images of PMMA spheres in the CCT (a) as synthesized, (b) exposed to EG, or (c) exposed to glycerin. 141

Figure 5.5. Qualitative plot of the observed structures versus the extent of polyesterification. “3DOM” refers to an extended macroporous structure that is defined only by the CCT with no discernable microstructure aside from the ordered network of pores left after template removal. 143

Figure 5.6. SEM images and photographs depicting the influence of counterions in metal precursors on microstructure. (a) SEM image of $Ce_{0.5}Mg_{0.5}O_{1.5}$ 211 prepared with $Ce(NO_3)_3 \cdot 6H_2O$, reproduced from Figure 5.2a for comparison. (b) SEM image of $Ce_{0.5}Mg_{0.5}O_{1.5}$ 211 prepared with $CeCl_3 \cdot 7H_2O$. (c) SEM image of $Ce_{0.5}Mg_{0.5}O_{1.5}$ 211 with doubled NO_3^- concentration. (d) Photographs of CeO_2 132 precursor solutions before (top) and after gelation at 90 °C for 18 h (bottom). The gelation time was 24 h for the samples depicted in (a)–(c). All samples were prepared using 489 nm spheres in the CCT. 146

Figure 5.7. SEM images of Mn_3O_4 compositions and Fe_2O_3 compositions. (a) Mn_3O_4 132. (b) Mn_3O_4 331. (c) Mn_3O_4 341. (d) Fe_2O_3 111. (e) Fe_2O_3 615. (f) Fe_2O_3 113. All samples were prepared using 489 nm spheres in the CCT and were gelled at 90 ˚C for 24 h. 148

Figure 5.8. Graphical depiction of metal-oxide particle morphology obtained in the CCT in the two types of templating processes: (a) volume templating, where complete filling of the void spaces between spheres occurs, and (b) surface templating, where metal ions or metal-containing precursor preferentially fills interstices at the sphere surfaces, leaving solvent or combustible material in the center of the voids. Volume templating combined with particle disassembly of a 3DOM structure results in solid particles produced from the original tetrahedral and octahedral template voids.[172, 255] Surface templating produces hollow particles in a similar manner. 151

Figure 5.9. SEM and TEM images of Mn_3O_4 411 using a CCT template with 362 nm PMMA spheres. (a) SEM image highlighting the bimodal distribution of spheres. Red circles indicate large spheres, yellow circles indicate small ones. (b) TEM image showing the hollow nature of the spheres. (c) TEM image showing a section of the sample with surface replication of the octahedral hole morphology without substantial densification. Samples were gelled at 90 ˚C for 24 h. 152

Figure 5.10. SEM images showing morphologies observable in $Ce_{0.5}Mg_{0.5}O_{1.5}$ via modification of EG:CA:TMI ratios. The three numbers listed in each image refer to the integral molar ratios of EG:CA:TMI. For example: 331 refers to 3 mol EG: 3 mol CA: 1 mol TMI. The same notation is used in the other figures. 155

Figure 5.11. SEM images showing morphologies observable in CeO_2 via modification of EG:CA:TMI ratios. 156

Figure 5.12. SEM images showing morphologies observable in Mn_3O_4 via modification of EG:CA:TMI ratios. 157

Figure 5.13. SEM images showing morphologies observable in Fe_2O_3 via modification of EG:CA:TMI ratios. 158

Figure 5.14. Additional SEM images showing morphologies observable in Fe_2O_3 via modification of EG:CA:TMI ratios. 159

Figure 5.15. Phase diagrams generated from multiple precursor compostions and observations of morphology in those samples for several metal-oxides: $Ce_{0.5}Mg_{0.5}O_{1.5}$, CeO_2, Mn_3O_4, and Fe_2O_3. 160

Figure 6.1. Schematic of the structures formed during collagen assembly and fibrillogenesis. Addition of NCC to a solution of soluble type I collagen at pH 3 and raising the pH to 11 yields a uniform alignment of fibrils. When NCC is excluded, fibrils form with random orientation. 166

Figure 6.2. SEM images of collagen gelled and prepared via the method detailed above. (a) 150 mg/mL collagen (NC0). Note the large dispersity in fibril diameter and the lack of coherent direction. (b) Cross-sectional image of NC0. (c) 150 mg/mL collagen with 2 wt% NCC added before gelation (NC2). Fibrils are well-aligned and fall in a narrower distribution. (d) Cross-sectional image of NC2. Arrows in the inset point at NCC particles in the interior of the sectioned film. (e) 150 mg/mL collagen with 16 wt% NCC (NC16), similar alignment effects are observed as for NC2. NCC particles can be observed as the bright specks on the surface of the film. (f) NCC particles observed by TEM. The dark spots are the NCC particles on a Formvar film, most observed are smaller than 100 nm in diameter. Inset: a single NCC particle. Scale bar: 20 nm. 172

Figure 6.3. SEM images of (a) NC2 and (b) NC16 showing the alignment effect over extended areas. The images also show more large aggregates of NCC in NC16 compared to NC2, which is typical for most of these samples.....173

Figure 6.4. SEM images at higher magnification for (a) NC2 and (b) NC16.....174

Figure 6.5. Histograms derived from measuring fibrils in SEM images. (a) Diameters of the fibrils. Addition of NCC is demonstrated to substantially narrow the distribution of fibril sizes. (b) Fibril angles relative to the absolute frame of the image. Addition of NCC produces orientation of fibrils along a narrow spread of angles. 175

Figure 6.6. UV-vis spectra of collagen composites prepared with 0, 2, and 16 wt% NCC, and comparable thickness (~200 μm). Scattering behavior is wavelength-dependent, thus the decreased transmittance observed at lower wavelengths. Inset: the difference in transparency between NC2 and NC16 can be seen by eye. 177

Figure 6.7. Fluorescent images of HFFs cultured on the surface of the NC2 composite gel obtained after (a) 1 h, (b) 24 h, and (c) 72 h of incubation. The calcein AM stain shows good cell viability and growth over 3 days (green = viable, red/circled = dead). The length of the scale bars is 10 μm. 178

Figure 6.8. FT-IR spectra for NCC, collagen (NC0), and composite (NC16) samples. (a) Spectral region from 4000 to 800 cm-1. (b) Expanded region from 4000 to 3000 cm^{-1}, including a difference spectrum generated by subtracting the NC0 spectrum from the NC16 spectrum to show the peak shift induced by the addition of NCC. (c) Expanded region from 1750 to 1550 cm^{-1}, showing that the addition of NCC caused no change in the amide I region. Spectra have been offset for clarity. 179

Figure 6.9. SEM images of gelled collagen networks with (a) 2 wt% methylcellulose and (b) 16 wt% methylcellulose. 181

Figure 6.10. Proposed mechanism of fibril alignment. Free collagen molecules (blue) in solution preferentially adhere to NCC particles (green) due to hydrogen bonding between the collagen side chains and the NCC surface. The surface-stabilized collagen molecules form oriented fibrils, generating a preferred alignment in the final structure. Possible hydrogen bonding interactions between two collagen polypeptides and NCC are shown in the red box.....184

Figure 7.1. CeO_2 nonstoichiometry (represented here as "y") charted vs. partial pressure of oxygen (pO_2) charted at temperatures from 600 °C to 1400 °C. The lines are calculated values, while the circles are experimental data points. The dashed lines indicate appropriate conditions, a nonstoichiometry of 0.1 mol O/formula unit and 10^{-5} pO_2. Note that to achieve this nonstoichiometry at this pO_2, temperatures greater than 1400 °C are necessary. Image adapted from ref. 287 with permission from Elsevier.....190

Chapter 1: Introduction to Nanoporous Solids

Sections of this chapter are reproduced in part from "Maintaining the Structure of Templated Porous Materials for Reactive and High-Temperature Applications" by Rudisill, S. G.; Wang, Z.; and Stein, A. in *Langmuir*, **2012**, *28*, pp 7310-7324.

1.1 Aqueous Synthesis and/or Self-Assembly of Solid-State Materials

This thesis work explores a number of chemical approaches to the production of solid materials with small (i.e., μm- and/or nm-scale), ordered features, with the aim of providing facile routes to these structures for applications, ranging from energy conversion to biomaterials. Multiple strategies are considered, all involving aqueous solutions or suspensions of precursors: templating materials with nanoscale "molds," exploitation of phase instability within a precursor solution, and/or self-assembly of structures. In the investigation, tuning, and optimization of these strategies, a number of physical and chemical properties must be considered; predominantly size, shape, charge, and polarity of the precursor molecules, particles, and/or template, along with the mechanisms of polymerization and gelation within these aqueous precursors.

Two major applications of these structures are considered, first, a thermochemical process to convert combustion byproducts (CO_2 and H_2O) to fuel-producing feedstocks (CO and H_2). This process requires solid, manipulable, and highly porous catalyst powders which can withstand temperatures exceeding 1200 °C while still retaining enough surface area to yield sufficient reactivity. The second application is the construction of an artificial cornea, which demands an aqueous, biocompatible gel

material with sufficient rigidity, elasticity, and optical transparency to fulfill or exceed the anatomical role of the natural tissue. To shed some light on the complexity produced by the often-interdependent synthesis factors mentioned above, as well as the design constraints resulting from practical application of the desired materials, an overview of these topics follows, starting with porous materials themselves.

1.1.1 The Chemistry and Materials Science of Porous Structures

Solid-state materials synthesis has a long history, including some of the earliest chemistry performed by man. Metal smithing, a practice dating back thousands of years, is the art of modifying material structure and properties by manipulating fundamentally atomic behaviors—doping, crystalline phases, crystallite size and shape—by controlling and tuning synthesis conditions to produce materials with desirable strength, hardness, and density for a variety of applications. In the past two centuries, our knowledge and understanding of these structure-property relationships has progressed from a purely empirical set of repeatable observations, to an atomistic understanding of crystal structures, stability, and phase transformations.

The aim of metallurgists and ceramicists, historically, has been to produce dense structures, those which contain few holes, or pores. Increasing porosity of a material tends to severely decrease its strength and increase its brittleness; however, there are many applications for which "holey" materials are of critical importance; these include heterogeneous catalysis,[1, 2] chemical separation,[3, 4] electrochemical devices,[5, 6] and many others.

1.1.2 Generation of Nanoporous Architectures

Humans have been using porous materials such as foams, sponges, and soil for centuries. But *designing* nanoscale porosity, with features and pores hundreds of times smaller than a human hair, requires a much more involved approach, typically necessitating the growth of a shaped material ("bottom-up"), as opposed to the fashioning or machining of a preformed structure into the desired shape ("top-down"). Given the conceptual complexities of creating a bottom-up synthesis process, it stands to reason that among the first known nanoporous architectures were natural materials, a class of aluminosilicates known as zeolites, discovered in the 18th century.[7] These microporous materials found use as sorbents, petroleum cracking catalysts, and cleansing agents. Given their widespread usefulness, they were a synthetic target of many inorganic chemists and engineers. In the 20th century, a number of synthetic methods were developed to produce both natural and artificial zeolites.[8] With these silica-based syntheses, the design and engineering of nanoscale porosity became not just a possibility, but a field unto itself.

Today, porous materials can be synthesized on every length scale, with pore dimensions from angstroms to millimeters, in a variety of compositions: silicates, metal-oxides, metals, carbon, organics and polymers. The area of interest in this thesis is predominantly the macroporous regime (pores >50 nm in diameter). Pores of this size are typically obtained through the use of templating or "nanocasting," i.e., producing a micro- or nanoscale mold, filling that mold with the desired material, and then removing the mold. Other pore regimes are defined based on their size, such as mesopores (2–50

nm in diameter), which can be templated or, as is in the case in this work, exist as "textural" mesopores; the result of crystallites failing to space-fill perfectly and leaving void spaces between themselves. The last size regime includes the micropores (<2 nm in diameter), which are more commonly observed in silicates and carbon materials such as zeolites or activated charcoal rather than metal oxides.

Three-dimensionally ordered macroporous (3DOM) materials, or "inverse opals" are a class of materials used as a platform for investigating reactivity, heat stability, and structure development of solids synthesized during this thesis work. They are produced by depositing a precursor or active material into the interstices of a colloidal crystal. This colloidal crystal template is then removed, either thermally or through chemical etching, leaving the inverse replica of the colloidal crystal. The colloidal crystal templates are produced through synthesis of monodisperse spheres, 20–600 nm in diameter. The spheres are typically composed of silica, polystyrene, or poly(methyl methacrylate), [9-12] though other, more exotic polymers can be used to adjust the polarity or morphology of the spheres. A variety of techniques can be employed to synthesize the spheres, such as the Stöber method or emulsion polymerization,[13]. These sphere dispersions are then gravitationally sedimented and dried, resulting in ordered face-centered cubic (fcc) arrays of the spheres. These arrays are very similar to the structure of natural opals.

The ordered arrays can then be infiltrated with metal salt solutions or sol-gel precursors and calcined or pyrolyzed. If polymer spheres are used, they will be combusted or depolymerized under this thermal treatment step. Silica spheres must be removed by chemical etching with hydrofluoric acid or potassium hydroxide. A wide

range of compositions can be produced by this method, including metals,[14] oxide and non-oxide ceramics,[12, 15] carbon,[16] inorganic salts,[15] and polymers.[17]

1.1.3 Structural Elements of 3DOM Materials

The inverse opal structure is, theoretically, 74% void space. Actual space filling of the network is typically lower, considering gel condensation and material shrinkage during calcination or pyrolysis. The structure itself consists of a series of "nodes," in two shapes—octapodal and tetrapodal—which are connected by curved struts which taper to their thinnest dimension at the midpoint. These nodes result from the octahedral and tetrahedral holes in the parent fcc lattice. For template spheres in the 300–500 nm range, the resulting octapodal and tetrapodal nodes have dimensions on the order of 100 nm. The connecting struts are 10s of nm thick. The pores of the material are on the same order of magnitude as the original template, though there is some shrinkage of the pores, reducing the pore volume by 10–30% of the templating spheres.[18]

The morphology of the walls varies depending on the synthesis method. Depending on the electrostatic interactions between the surfaces of the template and the infiltrating precursor, the material will "surface template" or "volume template," leading to two distinct morphologies (Figure 1.1). Surface-templated 3DOM structures result from net attractive forces between the infiltrated material and the template. The walls of the material trace the contours of the spheres very closely, leading to small windows between pores and more space-filling of the structure, giving a continuous appearance. Volume-templated 3DOM structures are much more open, with larger windows (100s of nm in diameter) between pores. The walls are thinner, being much more strut-like.

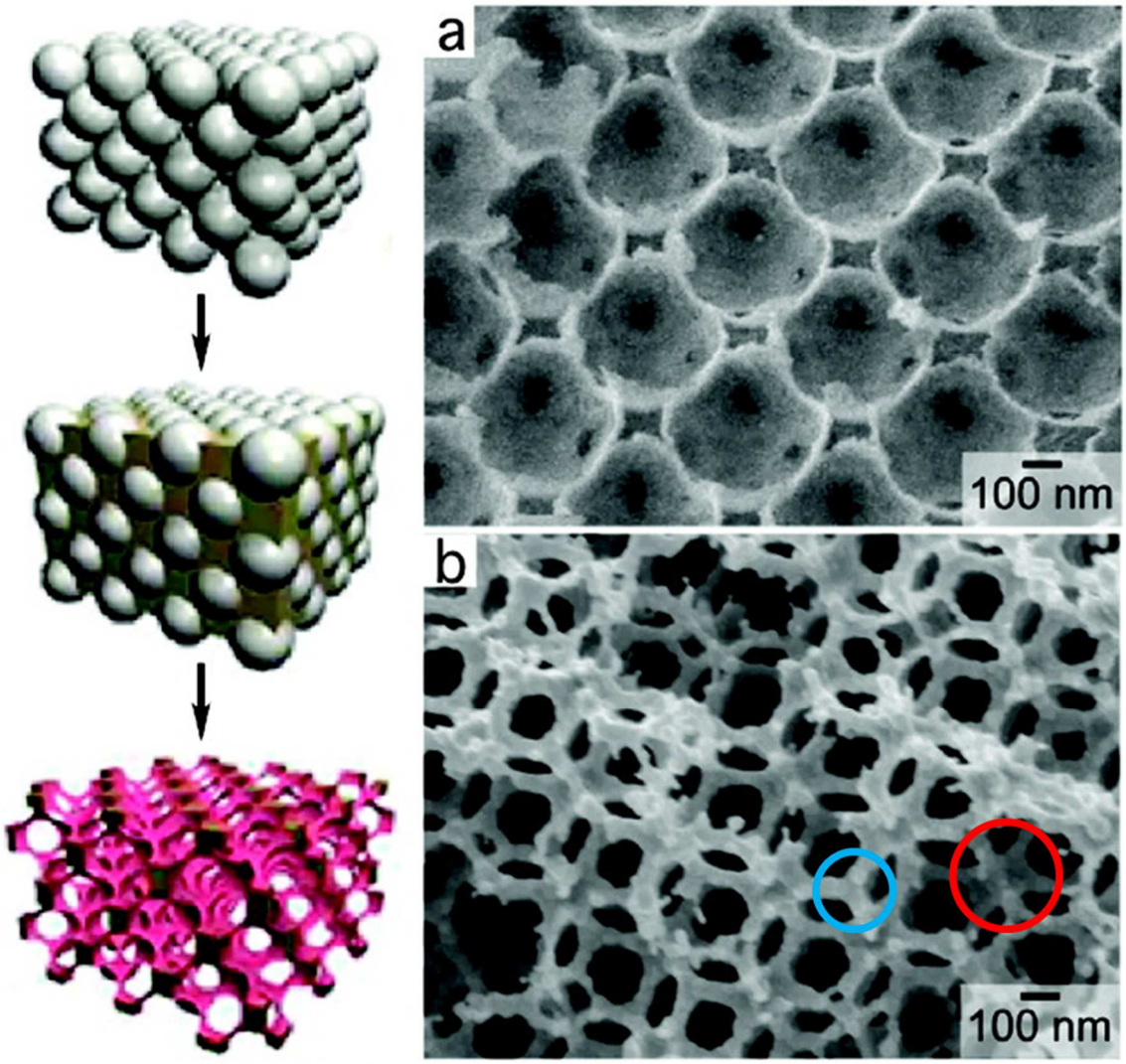

Figure 1.1. (left) Schematic diagram of the colloidal crystal templating process for producing 3DOM materials and SEM images illustrating the different morphologies obtained by surface templating (a) vs. volume templating (b) of 3DOM W materials. The blue and red circles indicate tetrahedral and octahedral nodes, respectively. Figure adapted from ref. 19, reprinted with permission. †

† Adapted with permission from Denny, N. R.; Han, S. E.; Norris, D. J.; Stein, A., Effects of Thermal Processes on the Structure of Monolithic Tungsten and Tungsten Alloy Photonic Crystals. *Chem. Mater.* **2007,** 19, 4563-4569. Copyright 2007 American Chemical Society.

1.1.4 Porous Materials and High Temperature Applications

In the last three decades, much progress has been made in synthesizing functional materials with structural features on multiple length scales ranging from the macroscopic to the nanometer domain. Structural hierarchy is a distinguishing feature in many of these materials. For instance, in the realm of porous materials, it is now possible to synthesize materials that contain well-defined micropores which can accommodate individual molecules, coexisting with mesopores and macropores to facilitate rapid mass transport.[20] Structures with bicontinuous or even tricontinuous phases can be fabricated that allow, for example, electron transport through one phase and ion transport through another phase.[21-23] Such nanoporous architectures have been demonstrated to provide benefits for a variety of technological applications, including the thermochemical conversion process mentioned above. From filtration to catalysis, electrochemistry to insulation, and energy storage to conversion, materials with nanoscale porosity are becoming increasingly desirable for making industrial and consumer processes and products cleaner and more efficient.

As fabrication techniques continue to improve and control over material architectures reaches smaller dimensions, new challenges arise. In many of the applications mentioned, the materials are exposed to reactive environments or high temperatures that, in some cases, approach or exceed 1000 °C. These conditions can create problems for generating and maintaining structural features and thus the enhanced activity derived from these

features. As the length scales of solid components in these porous materials are decreased, in pursuit of higher surface areas or more specific activity, it becomes more challenging to maintain the structure under extreme conditions.

Micro- and nano-architectures undergo a large degree of morphological change when exposed to reactive or otherwise extreme environments, known as "sintering."[24] Much of this change is predictable and well-studied in ceramic processing literature,[25] however, the focus of ceramicists is largely to enhance and exploit these processes to yield materials of near-theoretical density, in order to maximize mechanical strength and thermal resistance, or to eliminate permeability.[26, 27] But, for nanostructured materials, which depend on maintaining nanoscale features in order to retain efficacy, the focus is on limiting the extent of sintering.

Sintering is a general term comprising a number of different processes that occur when materials are at high temperatures. Virtually all of these processes are driven by the heightened atom diffusion brought about by exposure to high temperatures, high pressures, and reactive environments. For the purposes of this thesis, grain growth is the most important of these processes. Grain growth is governed by the migration of grain boundaries – the interfaces between individual crystallites in a polycrystalline material – allowing for crystallites to grow into and eventually consume their neighboring crystallites.[24, 28] As the dimensions of these crystallites approach and/or exceed the dimensions of the nano/microstructure containing them, the structure itself will become disrupted.

1.1.5 3DOM Materials Under Thermal Stress

The 3DOM architecture is a good model system to begin examining these processes. The structure can be considered as an array of cubic and tetrahedral "nodes," originating from the octahedral and tetrahedral holes of the parent fcc sphere lattice (Figure 1.1). These nodes are connected by curved walls, or struts, which taper to a thin section at the midpoint between two nodes. During sintering, areas with high concentrations of grain boundaries tend to grow faster, and larger grains tend to grow at the expense of smaller ones.[24, 28, 29] This results in the nodes and walls behaving differently at high temperature, as the larger, polyhedral nodes, with more grain boundaries, tend to grow at the expense of the smaller, columnar walls. So, there is a gradual shift in morphology as the material sinters.

These effects were studied in detail for the sintering of monolithic 3DOM α-alumina at temperatures of 1000–1350 °C.[30] The structure first becomes considerably more open, as the width of the walls decreases, leading to an increase in the size of the windows linking pores together. This is similar to what occurs in other, less ordered porous materials.[31] However, as the temperature is increased, these more strut-like walls begin to shrink longitudinally, as more material is consumed by the nodes, until the nodes are entirely in contact with one another. Order is still retained at this point, but the windows and pores have shrunk considerably. After this point, order is gradually lost as nodes grow into one another, leaving a disordered porous network, and eventually, a non-porous solid.

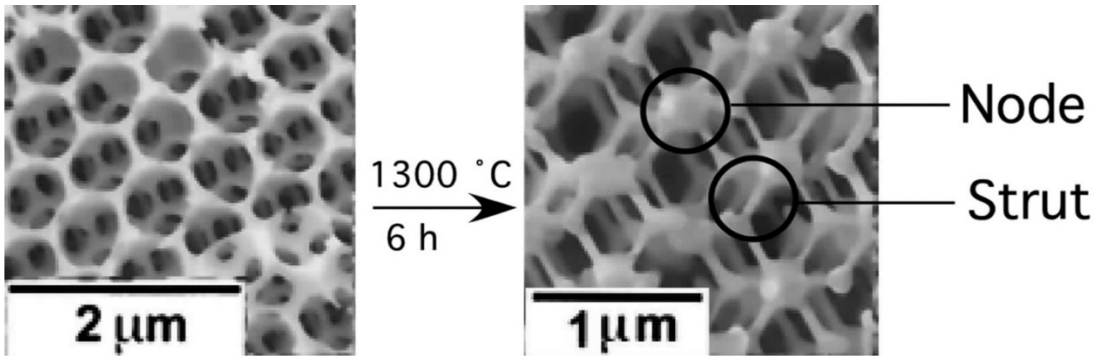

Figure 1.2. SEM images of macroporous α-Al2O3 calcined at 1150 °C for 6 h (left) and further calcined at 1300 °C for 4 h (right). The larger cube-like nodes result from the octahedral holes in the PMMA template, whereas the smaller tetrahedral nodes arise from the tetrahedral holes. Sintering causes the nodes to grow at the expense of the struts, which become even thinner. Image reprinted from ref. 30 with permission.[†]

1.2 Solar Thermochemical Energy Generation

Fossil fuels currently dominate both electricity generation and power for transportation, as they are inexpensive, widely available, and possess high energy density. Technologies for conversion of chemical energy in these fuels into useful work (such as steam turbines and internal combustion engines) have been in use for centuries, but these convenient sources of energy are not limitless, nor without cost. As natural supplies of oil, coal, and natural gas are depleted, extraction becomes increasingly difficult, leading to higher prices.[32] Combustion of carbon-based fuels produces high concentrations of CO_2 in the atmosphere, which have been correlated with significant increases in global temperatures and disruption of the natural environment.[33] Anthropogenic CO_2 emissions and their related climate effects have been linked to

[†] Reprinted with permission from Sokolov, S.; Bell, D.; Stein, A., Preparation and Characterization of Macroporous α-Alumina. *J. Am. Ceram. Soc.* **2003,** 86, 1481-1486. Copyright 2003 John Wiley & Sons.

disappearing arctic ice and melting of permafrost, which may have severe impacts on human life.[34, 35] It is clear that renewable alternatives to fossil fuels, such as solar or wind energy, are of vital importance to keeping the environmental and energy costs of human technological progress to a minimum.

Solar radiation is an attractive source of power due to the sheer amount of energy that is delivered to the planet. Estimates of total solar flux incident on the landmass of Earth are on the order of 10^{17} watts, by comparison, the total energy consumption of human life is on the order of 10^{14} watts.[36, 37] However, converting and storing this energy—even 0.1% of it—with high efficiency remains a significant challenge.[38] One potential solution to this problem lies in concentration of sunlight, used to drive thermochemical cycling of cerium oxide (CeO_2) to split H_2O or CO_2, producing usable chemical fuels in the form of H_2 or CO.[39-42] This redox cycling of CeO_2 in the solid state is a surface-limited process, making use of the well-documented reversible oxygen storage capabilities of CeO_2.[43-46] Hydrogen produced by this process could be directly combusted, or combined with CO to produce liquid hydrocarbons via the Fischer-Tropsch process.[47, 48] Water-splitting using the bulk material has been demonstrated by many groups.[39, 40, 49]

In order to achieve efficient, reliable, long-term conversion, the active CeO_2 material must have high surface area, favorable mass transport properties, and significant resistance to densification.[49] Thus, nanostructured CeO_2 has great potential for significant increases in productivity of these systems. Chapter 2 of this thesis addresses and evaluates three-dimensionally ordered macroporous (3DOM) CeO_2 as a material for this purpose. 3DOM CeO_2 possesses a number of advantageous properties for this

application, including high surface area, complete interconnectivity of pores, and low tortuosity.[50] Despite these advantages, there are still a variety of challenges to overcome in producing a useful, functional 3DOM CeO_2 material for this system.

1.2.1 Thermochemical Cycling of Metal Oxides

The history of solar thermal water-splitting can be traced back to a 1950–1960s era military project loosely referred to as the "Energy Depot."[51, 52] This project sought to produce small-scale, mobile nuclear reactors which could be employed to supply electrical and heat energy, but also act as an on-site source of chemical fuels. This was proposed to be accomplished by direct thermolysis of water.[53] However, this approach proved infeasible, as the temperatures required for significant hydrogen production from thermal water splitting are prohibitively high ($\Delta G = 0$ at 4700 K).[54] Additionally, at these temperatures, separation of H_2 and O_2 is virtually impossible with even modern separation technologies, due to the strong driving force for the products to recombine.[55] In addition, fission reactors could only provide usable temperatures to a "jacketed" catalyst system up to roughly 1000 °C.[56] Thus, the focus shifted to concentrating solar power (CSP) systems, which can generate higher temperatures, and thermochemical cycling was introduced to lower the required temperatures for water-splitting.

The thermochemical cycles considered here take advantage of the redox activity of metal oxides in order to thermally drive highly endothermic processes at lower temperatures than would be required for the direct reaction. These cycles are typically two-step processes which follow the general scheme:

$$M_xO_y \rightleftharpoons M_xO_{y-1} + 0.5\ O_2 \quad (1)$$

$$M_xO_{y-1} + XO \rightleftharpoons M_xO_y + X \quad (2)$$

where M is a metal, and X is the compound of interest (for the purposes of this paper, H_2 or CO). The first step (1) is a high-temperature endothermic reduction of the metal oxide that thermally dissociates a portion of the metal-oxygen bonds and reduces the metal to a lower oxidation state. The second step (2) is a lower-temperature exothermic oxidation by water vapor or CO_2, returning the metal to its initial oxidation state and regenerating the original material. (Figure 1.3)

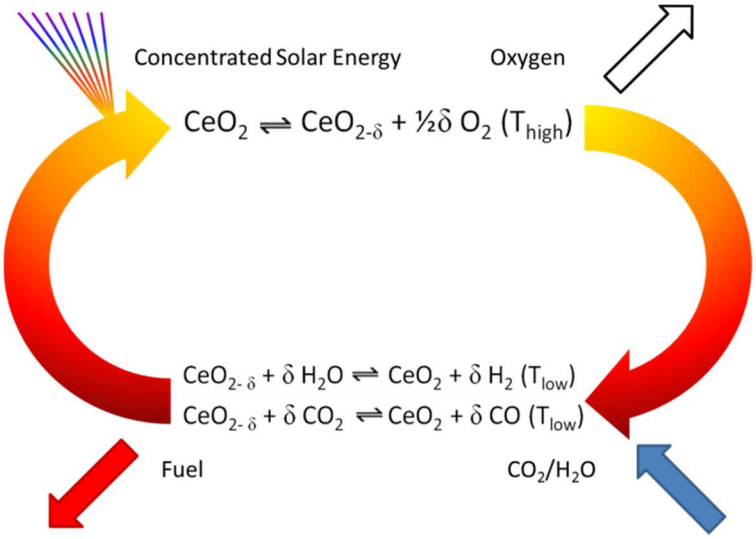

Figure 1.3 Reaction scheme for solar thermochemical cycling of CeO_2.

More than 280 cycles are known, ranging over a wide variety of compounds. Abanades *et al.*[54] have narrowed this wide field down to the most promising cycles based on minimizing the complexity of the operating conditions required and maximizing the productivity of the material. For instance, materials having a reduction step in excess of 2500 °C (W-WO_3) or requiring extra separation steps (SbO_2-SbO_3, HI intermediate) were

eliminated. Cycles which are most feasible from technological and thermodynamic standpoints tend to have a high ΔT between the two steps, intrinsic separation of reactive components (*e.g.* H_2 is produced in a separate step from O_2), and high theoretical production limits.

At these high temperatures, depending on the particular metal used, phase changes can occur. For instance, the oxidation step of the Zn-ZnO water-splitting cycle is a homogeneous reaction between H_2O and Zn vapors, resulting in the production of solid ZnO.[57] Likewise, the reduction step produces gaseous Zn from solid ZnO. Having the active material convert to the liquid or gas phases can result in significant losses during cycling, as active material is gradually removed from the system by carrier gases.[58] Thus, it is advantageous to have a material that remains in the solid phase throughout the cycle.

In some cycles, including those employing CeO_2, retention of the solid phase must be accomplished through incomplete reduction via the production of oxygen vacancies in the metal oxide lattice.[59] This is described by introducing another stoichiometric term, the extent of reduction (δ). Incorporating this term into (1) and (2) yields the following reactions:

$$M_xO_y \rightleftharpoons M_xO_{y-\delta} + 0.5\delta\ O_2 \quad (3)$$

$$M_xO_{y-\delta} + \delta\ XO \rightleftharpoons M_xO_y + \delta \quad (4)$$

which demonstrate δ's direct relation to the productivity of the system.

1.2.2 Thermochemical Cycles and Catalysis

The metal oxides used in these cycles can be loosely considered heterogeneous catalysts. The material lowers the overall energy barrier to water or CO_2 splitting, and the

reaction is itself heterogeneous, occurring only at the interface between the solid and gas phases. Thus, maximizing surface area is critical for optimal activity of the catalyst. However, unlike most heterogeneous catalysts (which simply provide surfaces for a reaction to take place), the metal oxide is chemically altered by the exchange of oxygen during the cycle.

Oxygen diffusion in ceramic oxides is a surface-limited process.[43, 60] Fortunately, this means that a high surface area material should have enhanced kinetics of reduction.[49, 61] In addition, both experimental and computational studies suggest that oxygen vacancies have higher stability at the surface than the bulk.[62-64] This suggests that materials with high surface area can be reduced to higher levels of δ.

1.2.3 Water Splitting vs. CO_2 Splitting

The most prevalent application of thermochemical cycles in the literature is water-splitting.[39, 65-67] However, CO_2 splitting with thermochemical cycles has also been demonstrated.[68-71] The two reactions are similarly endothermic ($XO \rightleftharpoons X + O_2$ at STP where X = CO_2, 282.98 kJ/mol; where X = H_2O, 285.83 kJ/mol), but temperatures required for the two processes are vastly different. While H_2O was previously mentioned to undergo significant conversion to H_2 at 4500 °C in the absence of a catalyst, CO_2 can be converted to CO at temperatures below 2500 °C.[72] Thus, direct CO_2 splitting is possible and has been addressed in the literature, but a "one-step" conversion still has significant challenges in the form of very high temperatures and difficult product separation. Both of these issues can be resolved by two-step thermochemical cycling. Additionally, in a research lab setting, CO_2 is the more facile of the two reactants to

study. This is for two reasons: first, CO_2 does not require heated tubing to remain in the gas phase, as H_2O does, and second, its concentration can be readily controlled and maintained throughout an experiment by preparing a tank. Gas-phase H_2O must be generated or prepared *in situ* using a heater or steam generator.

1.2.4 Concentrating Solar Power (CSP) Systems

The high temperatures necessary for most of these cycles to take place are most easily accessible through concentration of solar radiation.[55] CSP systems are a well-established technology for harnessing solar thermal energy. These systems use arrays of mirrors to focus solar radiation incident on a wide area into a much smaller one.[73] There are four types of CSP systems in use: trough, tower, dish, and double-concentration configurations (Fig. 1.4).[55] The concentration ratio of these systems is measured in "suns," where one sun is the solar flux incident on a square meter of land.

The trough system (Figure 1.4a, 30–100 suns) is a half-cylindrical, parabolic mirror that can rotate about its center of curvature to track the sun in one dimension, focusing sunlight onto a rod located at the focal point of the mirror. The tower system (Figure 1.4b, 300–1500 suns) involves a large array of heliostats, mirrors that adjust to reflect sunlight on a single point regardless of the sun's position. These heliostats focus sunlight onto a tower-mounted reactor. Dish systems (Figure 1.4c, 1000–5000 suns) use a paraboloid mirror and track in three dimensions. The double-concentration system (Figure 1.4d, 5000–10000 suns) is the tower configuration, except the heliostats concentrate sunlight onto a hyperboloid mirror, which then concentrates the sunlight at a reactor on the ground.[55, 74]

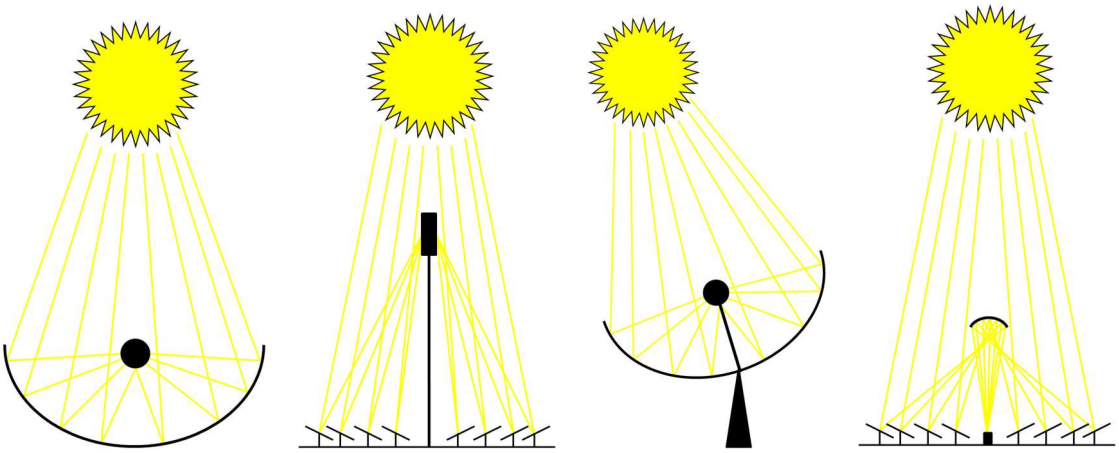

Figure 1.4. The four most common setups for CSP systems. (a) Trough, (b) tower, (c) dish, and (d) double concentration.

These systems, when employed, are typically used to drive electricity-generating steam turbines in power plants.[75] However, depending on the level of concentration, the temperatures generated can be well in excess of 1500 °C.[73] This intense, localized heating can be used to drive the endothermic reactions required to perform water and/or CO_2 splitting. However, the heat is supplied through radiative transfer of visible light. Thus, the optical properties of the substance are also important to the heating (and thus, cycling) of the material.

1.3 Sol-Gel Chemistry and Untemplated Porosity

Given the high temperatures of many heterogeneous catalysis processes and the tendency of these materials to lose their porosity and surface area at those temperatures, materials with different pore sizes and feature sizes are necessary to optimize reactivity under these differing regimes. Micron-scale features may be of importance for high temperature methods, such as thermochemical cycling of CeO_2. This thesis details a large

body of work aimed at the production of micron-scale and hierarchical porosity through attentive precursor design and tuning of the interactions between precursor and template.

As noted in section 1.1.1, solids can be produced directly from the solution phase and made to conform to the shape of molds or templates within that structure. For silicates, this process is relatively straightforward: a source of silicate anion—typically a silicon alkoxide such as tetraethoxysilane (TEOS)—is provided and then hydrolyzed under acidic conditions, producing ethanol and protonated silicic acid, $Si(OH)_4$. These protonated silicic acid molecules are incredibly short-lived in solution, as they will immediately self-condense with any available silicon hydroxyl. With mild heating, this self-condensation process gradually produces longer polysiloxanes which themselves further self-condense into an extended network of porous silica gel. The discovery of this behavior occurred over 150 years ago, as Ebelmen synthesized the first silicon ester (likely TEOS) in 1846,[76] and later observed its gradual transition from a solution to a glassy solid under acidic conditions. Many metal-oxide solids can be produced through this alkoxide route as well, most commonly ZrO_2 and TiO_2, though several others have been synthesized as well.[77]

This gelation behavior also occurs in metal salts, though with considerably less kinetic control than is afforded by the alkoxide method.[78] The process is somewhat similar, but due to the strongly electropositive nature of the metal ions, the kinetics of the condensation may be so rapid as to be uncontrollable. In this method, metal salt is dissolved in an aqueous system, where it separates into a cation and some number of counterions. These counterions are substituted by oxo-, hydroxo-, and/or aquo- groups

from the aqueous solvent depending on its pH. Self-condensation will then occur, with the rate depending strongly on the pH of the aqueous solution, as in the alkoxide method, resulting in small oxide clusters, which are rapidly converted to larger metal-oxide crystallites. These crystallites gradually aggregate to form an extended network of solid material with randomly distributed pores. The pores arise from the inability of the polycrystalline particulates to space-fill perfectly, and are endemic to the sol-gel synthesis of any metal-oxide. It is important to note that the solvent in which the sol-gel reaction occurs will be trapped within these pores unless some effort is taken to remove it.

Figure 1.5 shows the wide variety of structure types available through these condensation reactions. A series of classifications are given depending on the preparation and the properties which result from those preparations.[79] Figure 1.5. specifically denotes *xerogels* and *aerogels*, both of which result from removal of the solvent after gelation. Xerogels are the most commonly encountered and most easily synthesized variety of solid gel materials. These are structures that, after formation of the gel state, have been substantially densified via evaporation of a solvent with high surface tension, such as water. This densification results in a gel material with randomly oriented pores predominantly on the macroporous/mesoporous length scales. Aerogels, on the other hand, inherit the highly microporous, open, and extremely low-density structure of the gel prior to solvent removal. This is accomplished by exchanging the solvent with a low or near-zero surface tension solvent, such as supercritical CO_2. In addition to these two types of gels, there are several other classifications that are similarly named for their

preparation. *Hydrogels* or *solvogels* are gels in which the pores remain filled with water or another solvent. *Cryogels* are the result of solvent removal via freeze-drying.

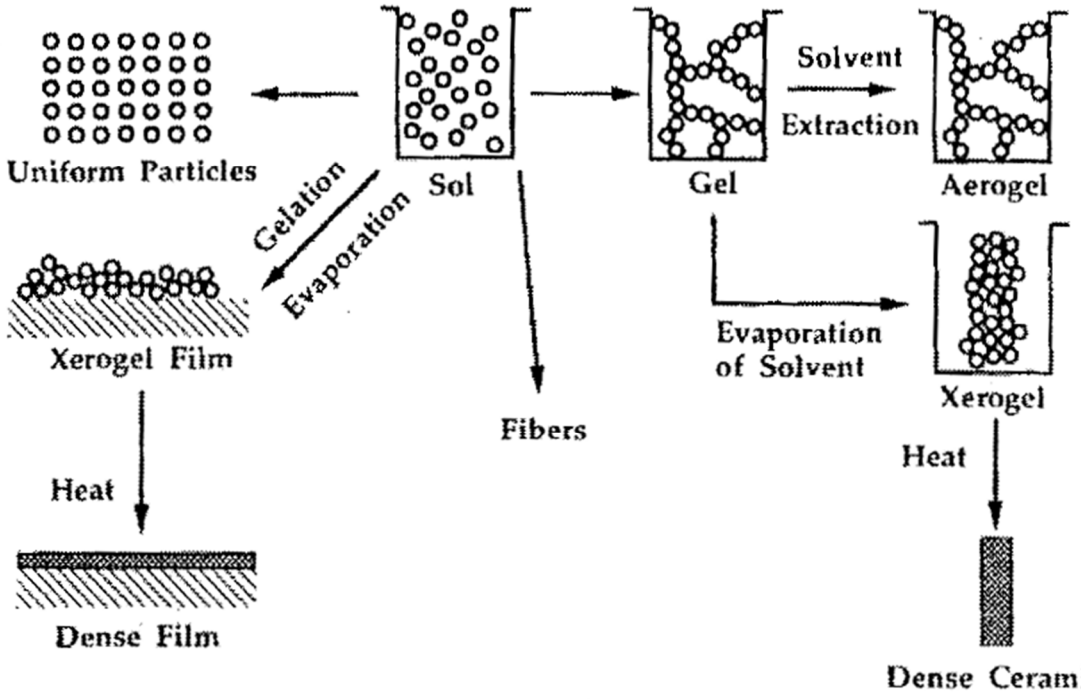

Figure 1.5. Sol-gel synthesis at-a-glance. Shows the microstructures developed during the process, as well as the products which can be obtained by "halting" the structural evolution. Image adapted from ref. 79, reprinted with permission.[†]

1.3.1 Metal-Oxide Gelation & Mediators

As shown above, the conditions under which the gelation process takes place substantially affect the final structure, both its morphology and porosity. Additionally, the

[†] Reprinted with permission from Brinker, C. J.; Scherer, G. W., *Sol-gel science: the physics and chemistry of sol-gel processing*. Gulf Professional Publishing: 1990. Copyright 1990 Elsevier.

chemistry and kinetics of the gelation process itself can affect the structure. Studying structural evolution during the sol-gel process constitutes a substantial portion of this thesis; therefore, some discussion of the parameters that can be adjusted in these syntheses is merited. The sol-gel process occurs in simple solutions of metal salts when those solutions are perturbed by the addition of acid or base. While a wide variety of oxides can be accessed via this basic metal-salt approach, it lacks control in the gelation process; only the pH and metal salt concentrations can be adjusted. Several molecules can be added to enhance control over gel formation, usually carboxylic acids (such as citric acid or EDTA) which chelate metal cations, slowing the formation of oxo linkages between metals and allowing for greater control over grain size.[80-83] Citric acid in particular is used in combustion syntheses of metal-oxide nanopowders, as metal citrates can react with nitric acid to form a viscous, but highly flammable gel. When the gel is ignited, the main-group components gasify, leaving a nanocrystalline metal-oxide powder.[84-86]

Ethylene glycol and citric acid can act as monomers for the formation of a branched polyester. Combined with the ability of citric acid to chelate most water-stable metal cations,[87] this process, patented by Maggio Pechini in 1967,[88] allows for the random distribution and spatial isolation of individual cations within a precursor prior to calcination or pyrolysis. The primary advantage of this technique is realized in the production of solid solutions or doped oxides. A frequent problem encountered in these syntheses is the segregation of the two oxides during calcination.[89, 90] Doped structures and solid solutions tend to have higher formation energies due to oxygen vacancies or

molecular/crystalline strain caused by the differing size and charge of heteroatoms within a host oxide. So, given the extensive formation of oxo-bridged metal-oxide particles in the sol phase, it is relatively common to observe binary oxide impurities in the doped structure. The Pechini process constrains diffusion of the individual atoms by locking them into a polymeric material, preventing the formation of these single-metal oxides. The organic polymer backbone is then removed during calcination, leaving only the phase-pure mixed oxide.

1.3.2 Phase Separation in Sol-Gel Synthesis

Synthesizing oxide ceramics from alkoxide precursors can allow for several interesting—and controllable—morphological behaviors which arise directly from the chemistry of the precursor. Nakanishi observed that sol-gel precursors such as TEOS and TMOS could produce SiO_2 in the form of micron- to nanoscale spheres or open networks with micron-scale porosity, if hydrolyzed and gelled in the presence of polar polymer additives.[91] By adjusting the polarity of the medium through the addition of alcohol or polymers like poly(ethylene oxide) (PEO)[92, 93] and poly(acrylic acid) (PAA),[94, 95] silica-rich and silica-lean phases develop within the sol. As the silica precursor condenses, generating larger, and thus less soluble, silica oligomers, these phases will separate and de-mix via the spinodal decomposition mechanism.[96]

Spinodal decomposition is a result of solution instability, and it occurs when a mixture crosses the spinodal curve on its phase diagram. This curve is defined by the condition where the second derivative of the Gibbs energy of mixing is equal to zero. In a more relatable sense, once a two-component mixture crosses the spinodal, $\Delta G < 0$ for the

generation of a new pure phase of one component or the other across the mixture.[97] This yields an infinitesimal activation energy for new phases, meaning that small fluctuations in concentration (i.e., a slope toward slightly solute-rich or solute-lean areas) lead to the formation of near solute-pure and solvent-pure phases in close proximity. These phases gradually (or rapidly, depending on diffusion rates) expand to encompass the entire mixture, thus resulting in the "decomposition" of the mixture into two discrete phases.

The structural behavior of spinodal decomposition from isotropic systems was first mathematically described by Cahn[97, 98] using previous work with Hilliard,[99] and is a general process that can occur in any homogeneous two-component mixture. In essence, it is the transformation of a metastable isotropic mixture into a heterogeneous two-phase system as governed by the free energies of the two phases in their mixed and demixed states, the rate of diffusion within the mixture, and the surface energy between the two phases. Typical structures are shown in Figure 1.6. As the process continues, the two phases will eventually "coarsen" to the point where they are fully separated, like a mixture of oil and water that is allowed to stand until two layers are observed.

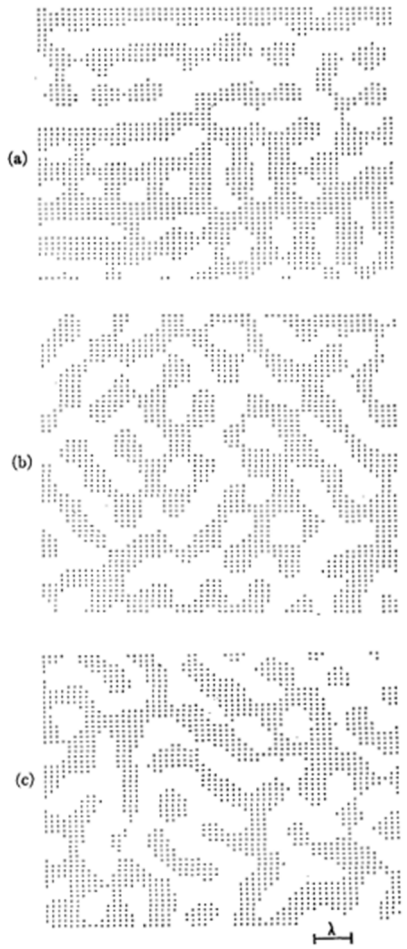

Figure 1.6. 2-D slices of computed structures of a two-phase system resulting from spinodal decomposition with differing levels of granularity. The structure results from randomly oriented sine waves, defined by the concentration of one phase in the other. These structures were computed using (a) 20, (b) 50, and (c) 100 sine waves. Note that while the phases do not appear interconnected in their 2-D representation, they are indeed interconnected in the third dimension. Image from ref. 98, reprinted with permission.†

Structures produced by demixing, coarsening, and separation can be difficult to isolate, as changes in temperature, phase, and/or concentration may push the mixture out of the spinodal region, resulting in nucleation and growth of single-phase materials, or

† Reprinted with permission from Cahn, J. W., Phase Separation by Spinodal Decomposition in Isotropic Systems. *J. Chem. Phys.* **1965,** 42, 93-99. Copyright 2004 AIP Publishing LLC.

the reformation of an isotropic solution. Thus, early observations of the phenomenon and its associated morphology were in metastable metal alloys.[100-102] The high thermal conductivity of metals allows for uniform heating of a sample to a temperature at which spinodal decomposition began, and then uniform quenching of the sample yielding "snapshots," so to speak, of the spinodal decomposition process and its associated microstructure. The microstructure of these samples can be imaged via transmission electron microscopy (Figure 1.7), yielding contrast between the two phases based on crystalline strain introduced by fluctuations in solute concentration[103] or diffraction contrast.[104]

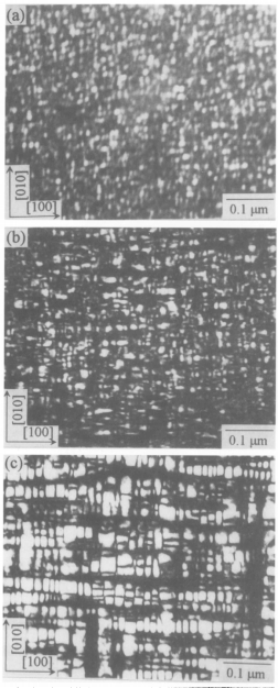

Figure 1.7. TEM images of a Fe-Mn-Al-C alloy which has undergone spinodal decomposition. Samples were held at 650 °C for (a) 180 min, (b) 6,000 min, and (c) 48,800 min, and then quenched in an ice brine bath. Image from ref. 103, reprinted with permission from Elsevier.†

† Reprinted with permission from Choo, W. K.; Kim, J. H.; Yoon, J. C., Microstructural change in austenitic Fe-30.0wt%Mn-7.8wt%Al-1.3wt%C initiated by spinodal decomposition and its influence on mechanical properties. *Acta Mater.* **1997,** 45, 4877-4885. Copyright 1997 Elsevier.

In sol-gel systems where spinodal decomposition mechanisms are energetically preferred, this decomposition process occurs simultaneously with the conversion of the silica-rich phase to a solid.[42] Thus, under appropriate conditions, the partially-decomposed structure can be "locked" into place by the gelation process itself, without the need for a quench. After solidification of the silica and removal of the solvent, a bicontinuous network of consisting of interconnected silica and void spaces. A number of different structures are accessible depending on the rate of gelation, as determined by the concentrations of solvent and polymeric additive (Figure 1.8).

Hierarchical structures can also be produced in these sol-gel phase separation materials, though it requires careful tuning of reagents. Block co-polymers can be used as polarity-modifying additives, as mentioned above; however, if sufficient concentrations of these polymers are used (i.e., at the critical micelle concentration), they can act as templates within the silica-rich phase. Hwang et al. accomplished this effect in both SiO_2 and TiO_2, producing a bicontinuous network of mesoporous material. The TiO_2 version of the material represented a significant improvement over other mesoporous TiO_2 when tested as a Li-ion battery anode.[105]

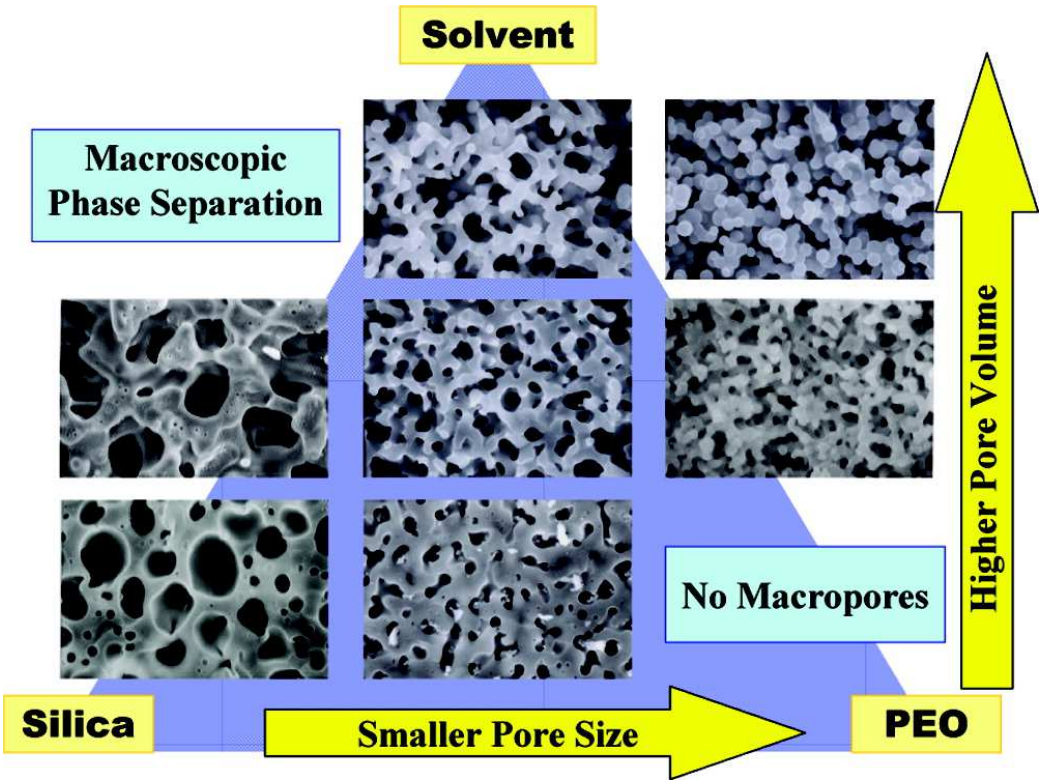

Figure 1.8. A qualitative tertiary phase diagram showing the structures available by the sol-gel method with phase separation in silica. Increasing organic additive concentration (in this case PEO) leads to a decrease in observed pore size, while increasing solvent concentration increases pore volume. Structure types include bicontinuous networks and microspheres. Image from ref. 42, reprinted with permission.[†]

These structures have been produced in crystalline materials as well, such as ZrO_2[106] and TiO_2,[107] essentially demonstrating that the methodology is general to tetrafunctional alkoxide species. The spinodal decomposition process is a function of increasing incompatibility between the metal-rich and metal-lean phases within the precursor. The degree of this incompatibility is itself a function of alkoxide hydrolysis and M-O-M bond formation, so, differences in reaction rate for these two processes will result in

[†] Reprinted with permission from Nakanishi, K.; Tanaka, N., Sol–Gel with Phase Separation. Hierarchically Porous Materials Optimized for High-Performance Liquid Chromatography Separations. *Acc. Chem. Res.* **2007,** 40, 863-873. Copyright 2007 American Chemical Society.

differences in the morphology obtained for a given precursor composition. The primary synthetic difference when moving from silicon to a transition metal alkoxide is one of reactivity. Silicon alkoxides will often take days to gel after hydrolysis, unless treated at an elevated temperature. This is not the case for many Ti alkoxides, such as titanium isopropoxide, which hydrolyzes and forms a gel immediately after its addition to water. In this case, careful selection of reagents and solvents is necessary to produce the desired structures. Konishi et al., for instance, used titanium *n*-butoxide as a titanium source and conducted the condensation in formamide to avoid rapid condensation.[107]

1.3.3 Discussion of Step-Growth Polymerization

The processes detailed above are, at their core, polymerization reactions. In particular, the products are condensation polymers whose polymerization reactions are governed by step-growth kinetics. Because the Nakanishi results show a strong correlation between the rate and/or extent of condensation and the morphology of the resulting solid, the behavior and limitations of these reactions is of critical importance to understanding the interplay between chain length and morphology.

The first synthetic polymer, Bakelite,[108] was a step-growth polymer. Many others since then have been industrially and commercially important—nylon, polyurethanes, polyesters—and are still in use today.[109] The initial hurdle for producing useful versions of these materials was achieving high molecular weights, that is, high enough that the resulting product would be solid and mechanically robust, and not a viscous hydrogel.[110] Much of the work on understanding molecular weight and its relation to reaction

conditions in step-growth polymers was performed by Wallace Carothers and his research group at DuPont in the 1920s and 30s. [110-113]

Step-growth polymers can be further divided into addition polymers and condensation polymers, the difference being that during polymerization, a condensation polymer forms bonds by eliminating a low-molecular weight side product, such as water, whereas an addition polymer will not.[111, 114] The Pechini process discussed above involves the formation of a condensation polymer, as the gel is formed via the dehydration reaction between carboxylic acid and alcohol moieties. While the mechanism does not differ between the two types, condensation polymers tend to be self-limiting during their polymerization, as the production of water during the synthesis drives the equilibrium of the polymerization reaction towards the reactants, limiting the extent of polymer formation. Unless solvent is removed during the process, molecular weights obtained will be lower than for a comparable addition polymer synthesis.

The primary feature defining step-growth polymers is that their growth itself is fundamentally controlled by stoichiometry and equilibrium of the reactants and products. Unlike chain-growth polymers, the polymerization reaction is not "initiated" or "terminated" by adding or removing a reactive site from a monomer or polymer chain.[115] Rather, all the monomers, oligomers, and/or polymers in a polymerizing mixture possess at least two reactive sites which will link together when the activation barrier for their reaction is overcome (typically in the form of elevated temperature).[116] A "step" consists of a single linkage between two monomers, a polymer and a monomer, or two polymers,

and each step is considered mechanistically equivalent, as the reactivity of the endgroups is the determining factor in the energetic likelihood of a step occurring.[116]

Consequently, one might assume there is no upper bound on the length of a step-growth polymer. Because polymer-to-polymer linkages have equal reactivity with any other linkages, there is no thermodynamic or energetic barrier to a given reaction mixture forming a single, incredibly massive chain, as long as any side products can be removed to drive the reaction. However, the statistical probability of finding a free end-group to react with decreases with increasing extent of reaction (denoted *p*, and defined as the fraction of reacted end-groups at a given stage in the polymerization), simply due to steric hindrance resulting from longer and longer chains.[117] Diffusion limitations, such as the increasing viscosity and insolubility of larger molecules, also come into play.[109, 118] These factors make monomer-monomer and monomer-polymer reactions strongly kinetically preferred, and also cause the overall reaction rate to decrease as the reaction progresses. Because polymer-polymer linkages are those which are most efficient at increasing molecular weight of a chain, these kinetic limitations prevent substantial fractions of long-chain molecules from being obtained until *p* approaches 1 (Figure 1.9), i.e. when enough monomer has been consumed such that polymer-polymer linkages become more favorable.[117]

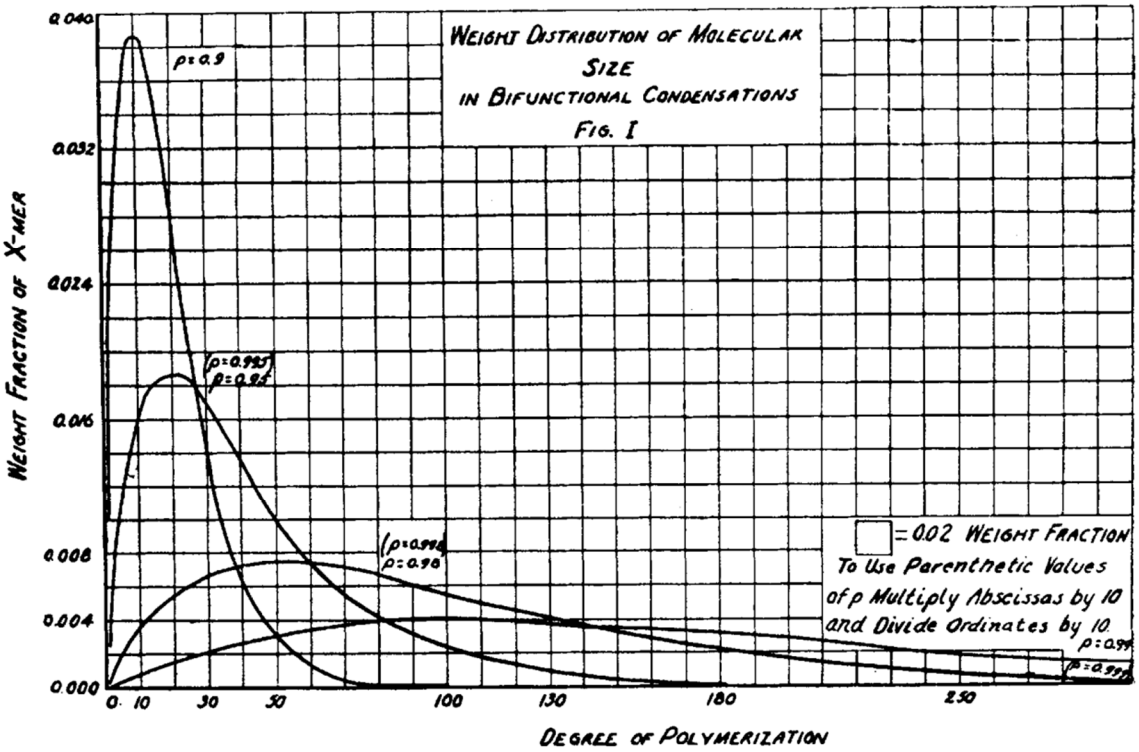

Figure 1.9. Carothers' diagram showing molecular weight distributions for condensation polymers by reaction extent. Note that as p approaches 1 (from 0.9 to 0.999), greater fractions of higher molecular weight molecules are obtained. Figure from ref. 117, reprinted with permission.[†]

Finally, the importance of stoichiometric balance to the average chain length of polymer obtained cannot be overstated. The above discussion of kinetic limitations assumes a 1:1 ratio between the two different reactive groups in the system. If this ratio is modified, an additional limitation occurs which only becomes more pronounced as *p* approaches 1. Consider two monomers with endgroups "A" and "B" respectively. If A:B is 2:1, the oligomers produced in the early stages of the reaction will all be "capped" by A groups. As the reaction becomes increasingly diffusion-limited at higher *p*, the likelihood of finding a B-capped polymer *and* bringing an A endgroup into close enough

[†] Reprinted with permission from Carothers, W. H., Polymers and polyfunctionality. *Trans. Faraday Soc.* **1936,** 32, 39-49. Copyright 1969 Royal Society of Chemistry.

proximity for a reaction to occur becomes vanishingly small. A more detailed description of the mathematics governing this process can be found in Chapter 5.

Despite the study of step-growth polymers being nearly a century old, there are still plenty of new discoveries to be made, particularly in the inorganic/sol-gel chemistry fields. The vast majority of study and experimentation on polymers has involved organic compounds. However, inorganic compounds, which can function under the same regimes, can be described with the same kinetics. For example, much of the behavior already observed in organic polymers can be replicated in the assembly of one-dimensional nanoparticle arrays[119] (Figure 1.10).

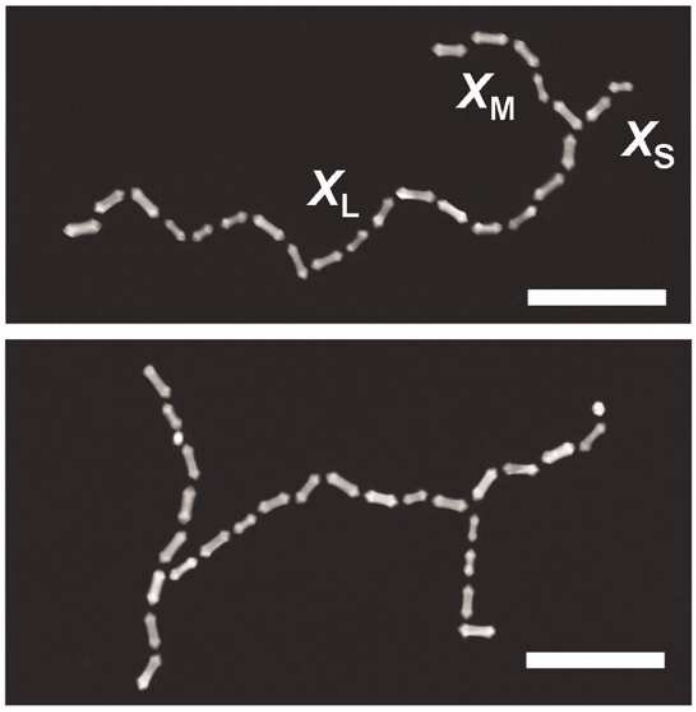

Figure 1.10. Image of star "polymers" (branched structures) assembled from gold nanorods. X_L, X_M, and X_s denote long, medium, and short chains on the "polymer" chain. Scale bars are 200 nm. Image from ref. 119, reprinted with permission.[†]

[†] Reprinted with permission from Liu, K.; Nie, Z.; Zhao, N.; Li, W.; Rubinstein, M.; Kumacheva, E., Step-Growth Polymerization of Inorganic Nanoparticles. *Science* **2010,** 329, 197-200. Copyright 2010 The American Association for the Advancement of Science.

1.4 Biologically-Occurring Self-Assembly

The previous sections have discussed formation of porous, ordered, and/or disordered structures in ceramics and metal-oxides. In order to address nanoarchitectures for medical applications, we must turn to biochemical and biological materials, and the production of porosity and periodicity in those systems. Many ordered morphologies are produced in biological systems via self- or directed assembly. For example, animals which form chitinous, lime, or silicate shells and exoskeletons often have patterned structures,[120, 121] such as *Morpho* butterflies,[122, 123] plankton such as diatoms,[124, 125] and vertebrate bones,[126, 127] This has led to the genesis of a field within solid state chemistry and nanoscience devoted to study, templating, and replication of these structures, known as bio-inspired or biomimetic synthesis. The same properties which make these materials valuable to their host organisms (e.g. color, mechanical robustness, permeability) make them useful in microscale technology and devices.

In the biochemical and medical fields, there is great interest in mimicking the shape, composition, and function of biological structures, such that a material synthesized *ex vivo* will be compatible with its *in vivo* counterpart. Implantation of prosthetics or donor tissue depends strongly on biocompatibility as a result of host organisms' immune responses. Several attempts at reproducing anatomical structures such as bones and teeth are present in the literature. While many of them depend on biological assembly mechanisms (e.g., growing materials from cell cultures)[128] to produce the original structure, several have focused on *ex vivo* syntheses of biological tissue.[129-132] The use of nanoparticulate hydroxyapatite as an artificial bone material has been successful enough

that it sees consistent use in the medical and dental fields.[133] The final section of this thesis describes new techniques to modulate the assembly of anatomical structures, specifically corneas, without the need for biological "structure directing agents," such as proteins, host organism cell cultures, or pre-existing tissue.

1.4.1 Corneal Prosthetics and Collagen Self-Assembly

The human body is replete with composite materials that contain self-assembled, ordered structures which provide important functionality, such as mechanical strength, elasticity, structural support, substrates for cell growth, etc. One of the clearest examples of structural order enabling biological function in humans is the cornea, the transparent, protective coating for the eye's lens and iris. The cornea additionally functions as a lens itself, contributing substantial refraction as a part of the eye.[134] It is composed of collagen, the most common protein in animals, including humans.[135] It is primarily a mechanical support structure, providing elasticity and tensile strength to a number of anatomical features, including skin, bone, tendons, ligaments, etc.[135]

Corneas are an appealing target for prosthetics and/or artificial tissue synthesis for a number of reasons. First, corneal disease and injury are unfortunately common, estimates indicate that as many as 10 million people could benefit from a corneal transplant, with up to 2.5 million being added each year.[136] Supplies of donor corneas are limited—only 40,000 transplants are performed annually in the United States—and current prosthetics require substantial follow-up and replacement after 5-15 years.[137] Second, the design of a prosthetic is not limited by tissue rejection, as many organs are. Because the cornea *in vivo* has limited vasculature and no blood supply, it is known as an "immune privileged"

tissue, in that transplant procedures involving prosthetics or donor corneas do not provoke an immune or inflammatory response.[138] Thus, the only requirement for biocompatibility is that epithelial (on the outer surface of the cornea) and endothelial (inner surface) cells may attach and grow on the surface of the material. Many prosthetic corneas have been produced and several are currently in use. The most common materials are PMMA, such as in the Boston keratoprosthesis,[139] but newer prosthetics are formed from copolymers with more hydrophilic properties, enabling the formation of hydrogels with enhanced permeability and diffusion.[140] These properties are important for homeostasis of the cells in the epithelial and endothelial layers which maintain optical clarity through water balance.[141]

Of course, the ultimate goal for corneal prosthetic materials would be an *ex vivo* synthesis of an artificial, but "true" corneal layer, consisting of the same nanostructured collagen that a biologically-produced cornea does. There are several hurdles to overcome to achieve this goal, not the least of which is a limited understanding of the corneal collagen self-assembly process.[142] Collagen self-assembly occurs in both "directed" and "undirected" forms. If an aqueous solution of collagen is partially dehydrated, the concentration and viscosity increases associated with this loss of water will result in the formation of fibrils, or *fibrillogenesis*. Essentially, as individual collagen strands are forced into proximity, they minimize their energy by hydrogen bonding with other nearby strands.[143] Fibrils, having a higher degree of bonding interactions than solvated collagen, are naturally lower energy structures. Fibrillogenesis can be induced in low-concentration solutions via changing pH, as many of the side groups in the collagen molecule contain

weakly acidic protons.[142] Collagen molecules tend to be stable at low pHs (~3–5), whereas fibrils are the preferred structure at higher pH (7–10), when hydrogen bond acceptor sites are ubiquitous.

Collagen in tissues is typically present in the form of fibers, high-aspect ratio structures with diameters between 1 and 20 μm, depending on the tissue.[144] These fibers result from bundling of fibrils, high-aspect ratio nanostructures with similar length but diameters of 10s of nanometers. Fibrils themselves result from collagen molecules being twisted together, like laid rope. Also like laid rope, the fibrils have a consistent repeat distance, arising from the helical twisting of collagen molecules around each other. This repeat distance is approximately 67 nm, and can be observed by techniques capable of probing that periodicity, such as small-angle x-ray diffraction (SAXS) and TEM (Figure 1.11).[145] Corneal collagen, unlike the collagen in most tissues, has had its self-assembly process halted before fiber formation can occur, meaning the structure consists of fibrils.

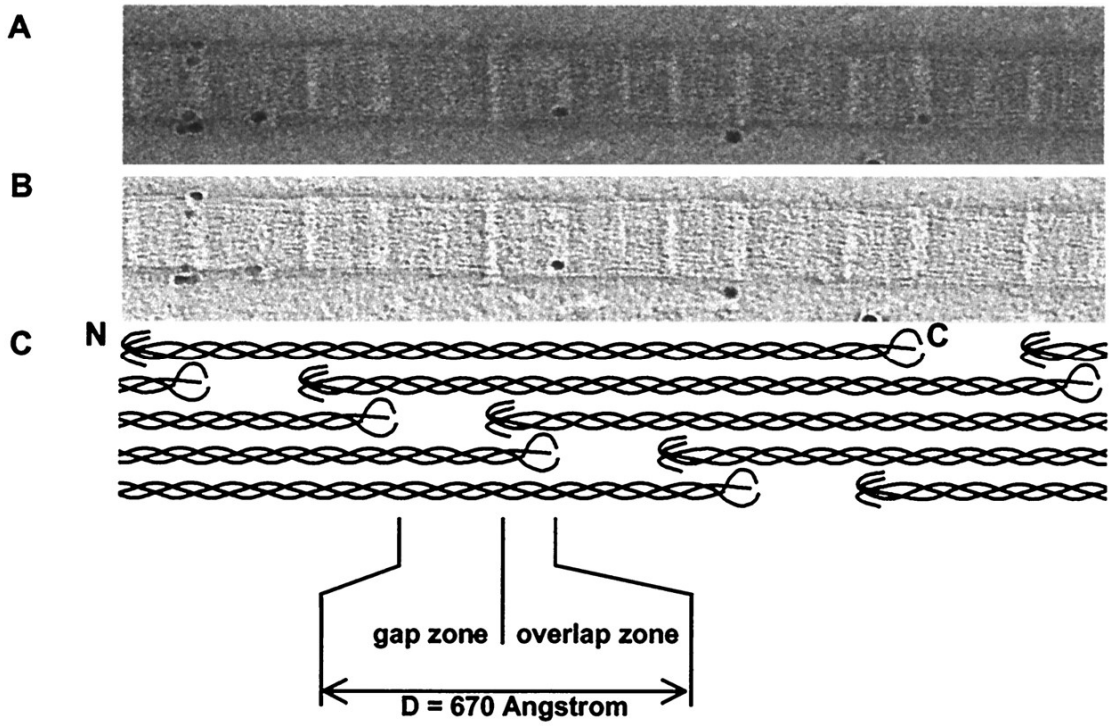

Figure 1.11. D-banding in collagen, resulting from consistent spacing between the C and N termini of adjacent collagen molecules. Figure from ref. 145, reprinted with permission.[†]

1.5 Summary

Templated and self-assembled porous materials on a variety of length scales have wide applications in industrial and medical technology. Several strategies for the formation of these materials have been described above. A clear, conceptual understanding of the molecular behavior and interactions between components in mixed systems is critical to the advancement of micro- and nanoporous materials synthesis. Porous materials design is a burgeoning field that is expanding in several areas, this

[†] Reprinted with permission from Holmes, D. F.; Gilpin, C. J.; Baldock, C.; Ziese, U.; Koster, A. J.; Kadler, K. E., Corneal collagen fibril structure in three dimensions: Structural insights into fibril assembly, mechanical properties, and tissue organization. *P. Natl. Acad. Sci. USA* **2001,** 98, 7307-7312. Copyright (2001) National Academy of Sciences, U.S.A.

thesis aims to aid in that expansion, and where possible, extend known science to new systems.

From here, this thesis proceeds with a detailed discussion of morphology effects on thermochemical cycling of CeO_2 (Chapter 2) along with some exploration of composition control aimed at reducing the detrimental effects of sintering on the surface area of the catalysts (Chapter 3). Chapters 4 and 5 present a method which adapts Nakanishi sol-gel phase separation to metal-salt precursors, as well as an attempt to demonstrate that method as general to most metals on the periodic table. Chapter 6 discusses a means of producing collagen fibril organization *ex vivo* through the interaction of the collagen with nanocrystalline cellulose. The final chapter will summarize the results of this thesis in context of the current state of the art in each of these fields and indicate avenues for continued discovery.

Chapter 2: Thermochemical Cycling of Nanoporous Ceramics

2.1 Introduction

2.1.2 Solar Thermochemical Cycling with Porous CeO_2

CeO_2 is a material currently under study for its ability to split H_2O and CO_2 at high temperatures. This is accomplished by thermally disassociating oxygen from the CeO_2 lattice at a high temperature (>1000 °C), producing a non-stoichiometric oxide, $CeO_{2-\delta}$. CeO_2 is then regenerated from this non-stoichiometric oxide by flowing H_2O or CO_2 over the surface at a lower temperature (<1000 °C), producing H_2 or CO.[40] The thermal dissociation step is sufficiently rapid for bulk ceria,[49] however, the kinetics of the fuel-production step benefit greatly from enhanced surface area.[146]

Venstrom *et al.* demonstrated that, compared to a non-templated material of similar crystallite size, 3DOM materials have improved thermal resistance, leading to retention of surface area.[49] Two CeO_2 materials were synthesized using the same precursor, one infiltrated into a colloidal crystal template and then calcined, the other poured into a combustion boat and then calcined. Each was thermochemically cycled at 800 °C, using H_2 as a reducing agent. N_2 sorption experiments and TEM imaging showed that the nanocrystalline non-templated material, while possessing a BET surface area >100 m^2/g, lost nearly all surface area after thermal treatment at 800 °C, down to 1 m^2/g. Meanwhile,

the 3DOM material, synthesized with the same method, started with a surface area at 30 m^2/g, and retained a surface area on the order of 10 m^2/g.

Sintering of the material is a significant challenge for retaining sufficient surface area during thermal treatment. Excessive grain growth of nano-/micro-crystalline CeO_2 at high temperatures (≥800 °C) has been observed by many groups.[41, 49] However, the sintering of the material can be limited through the addition of dopants to the structure. This exploits a phenomenon known as "solute drag," where the solute ions in a solid solution intrinsically resist grain boundary migration.[147] This is due to the crystallite surfaces at grain boundaries offering lower-energy sites to solute atoms, which will invariably have differing size and/or charge from the solvent crystal.[148] As a grain boundary moves, these solute atoms are forced into higher coordination, and thus higher energy states; this creates a thermodynamic barrier to grain boundary migration.

Zr ions are commonly-used additives in CeO_2 systems due to their ability to increase the reducibility of CeO_2.[41, 43] Petkovich *et al.* have demonstrated the effects of various levels of Zr incorporation on structure retention in 3DOM CeO_2.[89] As Zr is incorporated into the material in increasing fractions, the thermal stability of the nanostructure at 800 °C increases significantly. Grain sizes, as measured by Scherrer analysis of XRD patterns, increase by a factor of more than 10 in the pure material, but at a 1:1 Ce:Zr mixture, grain growth is limited to a factor of 2. Structurally, virtually no change is observed in this 1:1 solid solution after thermal treatment, however, the overall productivity of the material decreases. In this case, the 30 mol% Zr solid solution gave

identical productivity to the CeO_2 sample, while retaining its nanostructure under the thermal treatment conditions, despite mild sintering.

2.2 Morphological Considerations of CeO_2 Thermochemical Cycling

Of the various methods for sustainable generation of fuel, pathways that directly harness solar energy have the potential to play a prominent role in shaping the transition away from fossil fuels. A vast amount of solar energy strikes the surface of the Earth every day, many times the projected yearly energy needs for the entire planet through 2050.[149] Converting this abundant resource into transportable, chemical forms can be achieved in diverse ways, including biological photosynthesis,[150, 151] linked solar cell/electrolyzer systems,[152] semiconductor photocatalysis,[153] and others.[154-157] Many methods rely on the visible portion of the solar spectrum, failing to take advantage of the 52% of solar energy contained in the UV and IR regions. In contrast, thermochemical conversion of solar energy to fuels utilizes the entire solar spectrum. In thermochemical fuel production, concentrated solar energy provides the high-temperature process heat to drive endothermic reaction cycles.[55, 158-160] One such cycle is based on the two-step reduction and oxidation of cerium dioxide (CeO_2). CeO_2 is reduced at high temperature (Eq. 2.1) with solar energy, and oxidized at a lower temperature by H_2O (Eq. 2.2), CO_2 (Eq. 2.3), or H_2O/CO_2 mixtures to produce H_2, CO, or syngas and regenerate CeO_2. Syngas is a precursor to liquid hydrocarbon fuels that are compatible with the existing gasoline, diesel, and jet fuel infrastructure.[69, 161]

$$CeO_2(s) \rightarrow CeO_{2-\delta}(s) + \delta/2\ O_2(g) \qquad (1100–1600\ °C) \qquad \text{Eq. 2.1}$$

$$CeO_{2-\delta}(s) + \delta\ H_2O(g) \rightarrow CeO_2(s) + \delta\ H_2(g) \qquad (500–1000\ °C) \qquad \text{Eq. 2.2}$$

$$CeO_{2-\delta}(s) + \delta\ CO_2(g) \rightarrow CeO_2(s) + \delta\ CO(g) \qquad (500–1000\ °C) \qquad \text{Eq. 2.3}$$

The unique properties of CeO_2 make it a promising candidate for solar thermochemical fuel production.[40, 41, 49, 68, 89, 146, 158, 161-164] CeO_2 can be reduced to a significant degree of non-stoichiometry without any phase changes, retaining a cubic fluorite crystal structure.[165] An advantage of retaining a single crystalline phase during two-step thermochemical cycling is that product gases are separated intrinsically. Complications that arise from solid-to-liquid and solid-to-gas transitions in thermochemical cycling, such as extensive sintering[66, 166] and recombination of the reduced oxide with product gases,[67, 167] are avoided.

However, substantial engineering challenges remain that must be overcome before thermochemical fuel production with CeO_2 can be employed on an industrial scale. The efficiency of a recently-reported proof-of-concept reactor utilizing CeO_2 is below one percent. This is primarily because of a lack of heat recuperation between the high and low temperature steps of the cycle, but also because the rate of ceria reduction was slow.[158, 168] One important challenge is to increase the rate of reduction and oxidation, allowing for increased fuel production over a given span of time.

The addition of an interconnected porous network to CeO_2 may allow for more rapid fuel production when compared to nonporous materials.[169] Recent research has shown that the chemical steps at the gas-solid interface strongly influence the overall kinetics of H_2 and CO production.[49] Other research suggests that the solid-state ionic transport of O_2

may also impact the rate of oxidation.[170] To these ends, synthesizing CeO_2 with a high accessible surface area and small feature sizes should increase the rate of fuel production.[146]

We previously synthesized three-dimensionally ordered macroporous (3DOM) CeO_2 via the use of colloidal crystal templating and different liquid precursors.[89, 146] 3DOM CeO_2 features an interconnected, face-centered cubic (fcc) pore structure and a moderately high surface area.[146] The material was chemically reduced in hydrogen and reoxidized by exposure to H_2O or CO_2. At 827 °C and in a 3–4% H_2O and CO_2 gas flow, 3DOM CeO_2 produced H_2 and CO 2–3 times faster than untemplated, nanocrystalline CeO_2 and commercially-available CeO_2 granules.[146] The kinetic advantage of the 3DOM architecture was also apparent in cerium-zirconium mixed oxides.[89] The prior work considered the impact of morphology on the low temperature, fuel production step,[89, 146] omitting the high temperature, O_2-producing step. The release of O_2 from CeO_2 is favored, however, at temperatures above 1100 °C for the reducing atmospheres envisioned for solar thermochemical cycling,[171] and structural changes in porous CeO_2 induced by thermal treatment are much more prevalent at these temperatures. Thermally-activated sintering and associated grain growth can greatly reduce the available surface area of 3DOM CeO_2 or other porous ceramic oxide materials, and, in extreme cases, eliminate interconnected porosity through crystallite growth and extensive densification of the material.[30, 146, 172]

To make solar thermochemical cycling of CeO_2 relevant for fuel production, the process must balance the rate of cycling (a kinetic parameter) and the fuel produced per

cycle (which depends on both kinetics and thermodynamics) to increase the overall rate of fuel production. Prior work has focused on the latter, producing more fuel per cycle in a thermodynamic approach by reducing CeO_2 at high reduction temperatures of 1500–1600 °C where CeO_2 releases more O_2 at chemical equilibrium.[40, 49, 164] High reduction temperatures, however, also have the effect of increasing reradiation losses, which places challenging constraints on the solar concentration system. In the present study, we evaluate an alternative approach to increasing the overall rate of fuel production by utilizing CeO_2 with advanced morphologies, including 3DOM CeO_2, that permit rapid rates of oxidation. This behavior, in turn, allows for more rapid thermochemical cycling rates that increase fuel production at reduction temperatures below 1500 °C.[169]

In this study we examine the influence of pore structure on the productivity and overall reaction kinetics of CO_2 splitting by full thermochemical cycling with CeO_2, i.e., thermal rather than chemical reduction and subsequent fuel production. Four materials with different morphologies are analyzed: 3DOM CeO_2, non-ordered macroporous (NOM) CeO_2, aggregates of anisotropic nanoparticles obtained from the mechanical disassembly of 3DOM CeO_2 (D-3DOM CeO_2) into its structural building blocks,[173] and a commercially-obtained, nonporous CeO_2 control sample. Each material is thermochemically cycled in an identical fashion to compare the rate of fuel production. The initial and post-cycling structural characteristics of these materials are studied via electron microscopy, X-ray diffraction, and nitrogen sorption measurements. We find that, despite some morphological changes induced by sintering, macroporous materials produce fuel via thermochemical cycling with significantly faster kinetics compared to a

nonporous control sample, maintaining stable cycle-to-cycle fuel production. This demonstrates the substantial benefit that engineering porosity into CeO_2 can provide for improving fuel productivity.

2.3 Experimental Methods

Cerium(III) chloride heptahydrate (99.9%), citric acid (99.5+%, ACS grade), and methyl methacrylate (99%) were all obtained from Sigma-Aldrich. Potassium persulfate (99.9%) was obtained from Fisher Scientific. Ethylene glycol (99+%) was obtained from Mallinckrodt Chemicals. Nonporous cerium oxide (99.9%, Figure 2.3a) was obtained from Alfa Aesar. Nitrogen gas (10.5 ± 0.1 ppm O_2, balance N_2), CO_2 (99.99%), CO (99.9%), Ar (99.999%), O_2 (99%), were supplied by Airgas. All reagents were used as received. De-ionized water (18.2 MΩ·cm) was used in all syntheses.

2.3.1 Synthesis of colloidal crystal templates and CeO_2 samples

A dispersion of 515 ± 12 nm-diameter colloidal spheres of poly(methyl methacrylate) (PMMA) was synthesized by emulsifier-free emulsion polymerization of methyl methacrylate (MMA), following a published method for the preparation of colloidal crystal templates.[174] Potassium persulfate was used as the initiator in the mixture consisting of 20% v/v of MMA in water. The polymerization was carried out at 70 °C with a stirring rate of 300 RPM.

3DOM CeO_2 was prepared by colloidal crystal templating. Templates were produced through gravity sedimentation of the aforementioned sphere dispersions. A Pechini sol-gel precursor was prepared by combining citric acid, ethylene glycol, cerium chloride heptahydrate and water in a 3:1:1:37 molar ratio. This solution was then infiltrated into

the PMMA colloidal crystal templates in a sealed container for 12 h at 25 °C. The mass ratio of precursor solution to template was 3:4. The infiltrated templates were gelled at 90 °C for 24 h. The thermally-treated materials were calcined in a tube furnace (using a 2 °C/min ramp rate) at 310 °C for 2 h and 450 °C for 2 h under static air to remove the template and crystallize the gel. A light yellow, opalescent powder was obtained.

Some of the 3DOM CeO_2 was further processed to produce a mixture of anisotropic nanoparticles and sub-3 μm particles of 3DOM CeO_2. This material (D-3DOM CeO_2) was produced by placing an aqueous slurry of 3DOM CeO_2 in a sonicating bath until it formed a stable suspension (*ca.* 8 h), then allowing the suspension to dry. This procedure resulted in a packed cake, which was manually crushed into a powder.

Finally, non-ordered macroporous material (NOM CeO_2) was synthesized using similar methods. NOM CeO_2 was produced through a modification in the template: rather than allowing the colloidal dispersion of PMMA spheres to sediment slowly, ~200 mL of the dispersion was heated to 70 °C on a hot plate while stirring. After 24 h, the water had evaporated, resulting in a white powder. This powder was then infiltrated with the precursor solution, thermally cured and calcined following the same procedure as for the 3DOM CeO_2 material.

2.3.2 Reactivity and productivity testing

The four CeO_2 powder samples were thermochemically cycled in a fixed bed reactor (Figure 2.1) in order to elucidate the rate and stability of fuel production. Each of the CeO_2 powders, synthesized and commercial, were sieved to between 180 μm and 840 μm and loaded into an alumina process tube (9.5 mm i.d.) to form a packed bed. An infrared

image furnace (Ulvac-Riko VHT-E44) irradiated the process tube to rapidly heat the sample inside. The furnace was controlled using a Pt-Pt/Rh thermocouple protected in an alumina sheath located 6 mm downstream of the sample. Using a thermocouple isolated from the sample to control the furnace replicates, as closely as possible within the constraints of an IR source, the conditions in a solar reactor where the radiation supplied to heat the ceria is not controlled by the temperature of the material. Rather, the ceria temperature is a consequence of the radiative heat flux. Thus, to fairly compare ceria of different morphologies, it is imperative that the power level of the IR furnace be controlled independently of the sample. Repeatable levels of IR radiation were achieved with a PID control algorithm, set such that the control thermocouple followed a user-specified profile, as shown in Figure 2.2. An alumina disk with gas flow channels held the samples in a fixed axial position. A second Pt-Pt/Rh thermocouple probe was placed in contact with the sample on its upstream face. The time response of the sheathed thermocouple was on the order of 30 s, slower than the extremely fast temperature ramping rate. The samples were reduced in a 100 ± 2 mL min^{-1} (298 K, 1bar) flow of N_2 containing 10.5 ± 0.1 ppm O_2 by rapidly increasing the sample temperature (~800 °C/min) over 18 seconds, and then holding the furnace at an elevated power level for an additional minute. The samples were then rapidly cooled by reducing the intensity of the infrared radiation, and were oxidized in a 100 mL min^{-1} flow of CO_2 (25 mol%, balance N_2, impurities < 0.0001%). The oxidation flow was terminated after 2 minutes and the 10.5 ppm O_2 flow reestablished for subsequent reduction. Gas flows were controlled identically between samples.

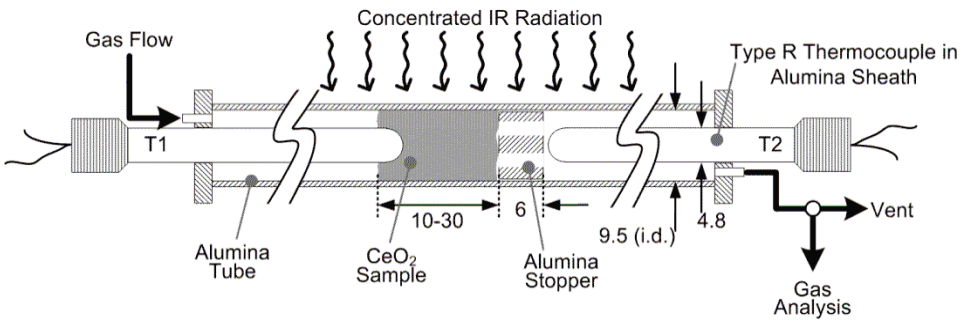

Figure 2.1. Schematic diagram of the reactor system employed in this work.

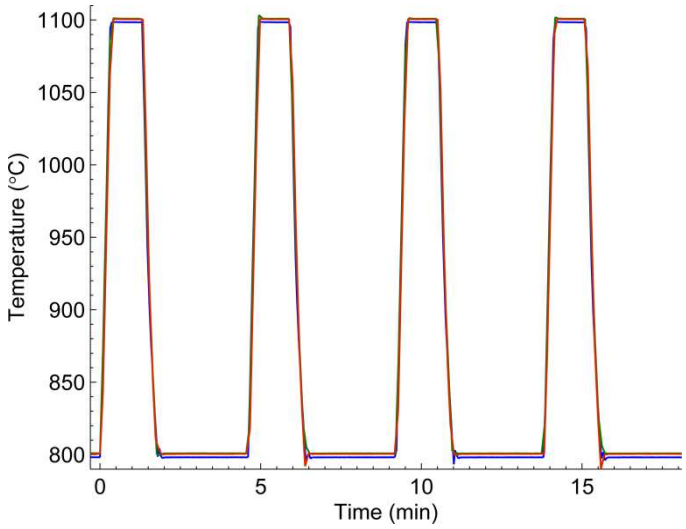

Figure 2.2. The controlled temperature in the IR furnace for four representative cycles. Data for two separate runs are shown to demonstrate reproducibility.

The O_2 and CO evolved from the CeO_2 samples were measured with a Raman Laser Gas Analyzer (RLGA, Atmosphere Recovery Inc. model 129a). The RLGA was calibrated prior to each experiment using gas mixtures of known O_2 and CO

concentration to an accuracy of 0.02 mol%. Measurements were obtained every second. Uncertainty in the productivity data was calculated using sequential perturbation.

2.3.3 Characterization of Materials

The morphology of the materials before and after cycling was studied by scanning electron microscopy (SEM). Unless otherwise specified, materials were imaged from the random dispersion of powders recovered from the bed. Samples were mounted on stubs with carbon tape and coated with 75 Å of Pt, then imaged on a JEOL 6500 electron microscope. To estimate the relative fractions of ordered porous, disordered porous, and heavily sintered regions in the cycled materials, numerous fragments of the sample bed were imaged and analyzed. Powder X-ray diffraction (XRD) patterns of the samples were obtained using an X'Pert Pro Diffractometer outfitted with an X'Celerator detector. Radiation was supplied by a Co anode (Kα, λ = 1.789 Å) operated at 45 kV and 40 μA. Nitrogen sorption isotherms were gathered using a Quantachrome Autosorb iQ_2. Samples were outgassed for 12 h at 200 °C at 1 milliTorr. Brunauer-Emmett-Teller (BET) surface areas were calculated from the pressure range $0.05 < P/P_0 < 0.3$ of the adsorption branch, and total pore volumes were calculated from the point $P/P_0 = 0.995$ on the adsorption branch.

2.4 Results and Discussion

2.4.1 Morphological Study

Four materials, each with differing initial morphologies, were prepared for thermochemical cycling in our reactor system. Morphological considerations will be exceedingly important in the subsequent discussion, so the initial morphologies (Figure

2.3a, c, e, g) will be considered here. Templated CeO_2 materials were prepared using polymer spheres as hard templates and a Pechini gel precursor. Consequently, all these materials contain nanocrystallites of approximately the same average size (10 nm, as determined by the Scherrer equation from XRD patterns, Figure 2.4) as synthesized. With regard to the pore architecture, 3DOM CeO_2 (Figure 2.3c) possesses an interconnected, periodic network of macropores with fcc symmetry, templated from the parent fcc lattice of the PMMA colloidal crystal. Alternatively, this network can be described as a series of 92 ± 10 nm and 189 ± 16 nm "nodes" arising from tetrahedral and octahedral interstitial sites in the fcc template, which are connected to each other by "struts" with average dimensions of 48 ± 6 nm at their narrowest points. NOM CeO_2 (Figure 2.3e) was prepared to evaluate the importance of order *vs.* disorder in the macropore array. Like 3DOM CeO_2, it possesses an interconnected pore network, but in NOM CeO_2, the macropores are disordered. The width of the walls of the solid network varies considerably (mean width 172 ± 118 nm), this variance resulting from the disordered colloidal template used for the synthesis. D-3DOM CeO_2 was prepared to examine the effect of bulk density on reactivity while keeping initial feature dimensions of the wall skeleton and thermal history comparable to those in 3DOM CeO_2. D-3DOM CeO_2 (Figure 2.3g) is comprised of ultrasonically disassembled particles from 3DOM CeO_2. It was expected that these pack more closely than the original 3DOM CeO_2, thereby affecting gas transport and heat transfer in the packed bed of the material. Approximately 90% of the D-3DOM CeO_2 exists as anisotropic nanoparticles—the tetrapodal and octapodal nodes of the parent 3DOM CeO_2, which have broken apart at the

comparatively thinner walls[173]—with the remainder being small particles of intact 3DOM CeO_2 with a maximum particle size of ~3 μm. Many of the intact 3DOM CeO_2 particles in the D-3DOM CeO_2 sample are coated with smaller disassembled fragments. Relevant feature sizes are identical to the 3DOM material. Nitrogen sorption measurements showed that the BET surface area of D-3DOM CeO_2 was *ca.* twice as high as that of its parent material, a consequence of exposing new surfaces after fracturing the 3DOM sample. However, the pore volume was smaller due to the denser packing of the disassembled particles. Morphological characteristics of the porous samples are summarized in Table 2.1. As a control, nonporous, sintered CeO_2 (Figure 2.3a), was obtained from Alfa Aesar. This material contains fused μm-scale crystallites (size range: ca. 5–10 μm), and some residual textural pores that are likely a result of incomplete densification.

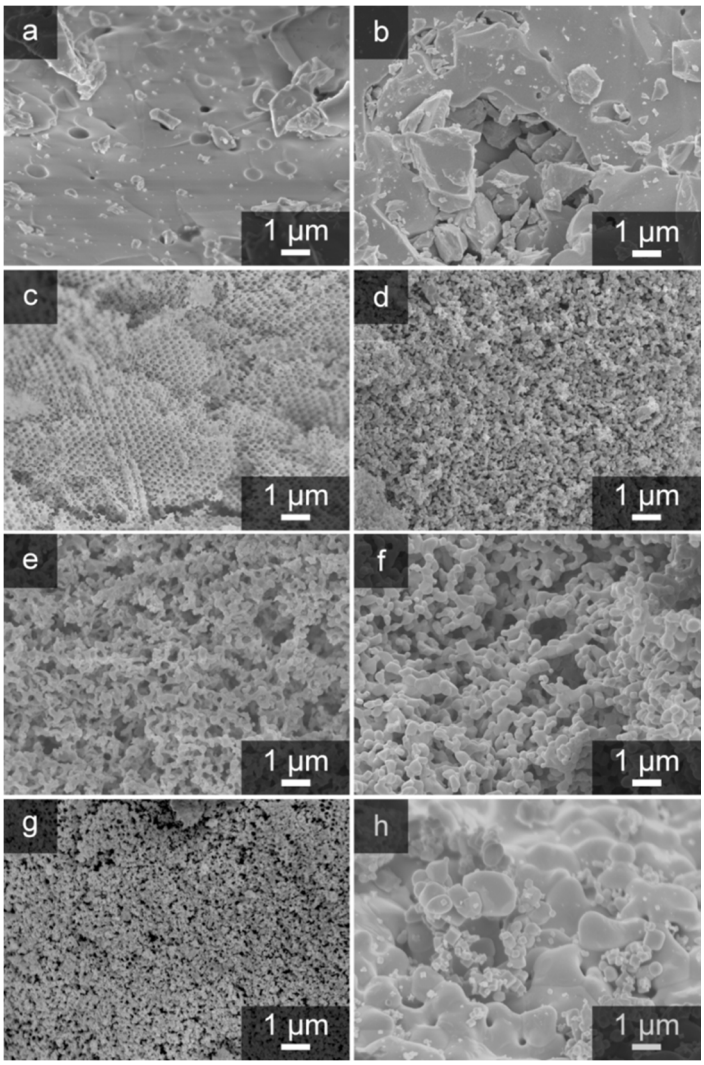

Figure 2.3. Representative SEM images of CeO_2 materials with the four morphologies used in this study. In commercial CeO_2 before (a) and after cycling (b), little change is observed. For 3DOM CeO_2 before (c) and after cycling (d), although the walls have undergone significant sintering and, in some areas, the order has been lost, the pore structure remains interconnected. For NOM CeO_2 before (e) and after cycling (f), the most prominent change after cycling is an increase in skeletal wall thickness; otherwise, the overall morphology of the structure remains unchanged. Finally, for D-3DOM CeO_2 before (g) and after cycling (h), it is clear that the sample has undergone extensive sintering.

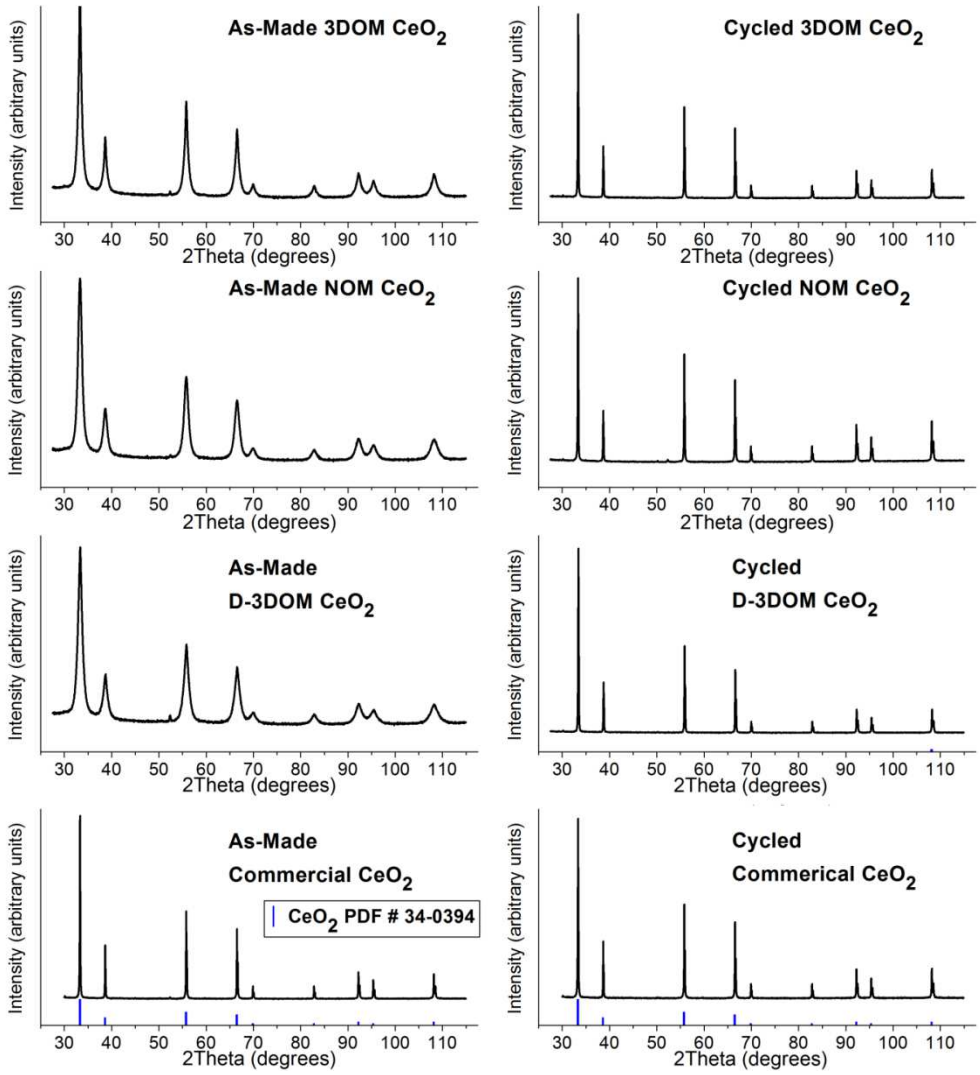

Figure 2.4. XRD patterns of the materials investigated in this work (before and after cycling) are shown above. The left column contains patterns of the as-made samples. Peak broadening is observed in the templated materials, since they are nanocrystalline. For the commercial material with micrometer-sized grains there is no observed line broadening. The right column contains the patterns of the sample after thermochemical cycling. No line broadening is observed, indicating that the crystallite size is substantially greater than before cycling. All peaks in the patterns match those of the literature pattern for cubic fluorite CeO_2.

Table 2.1. Morphological characteristics of the CeO_2 materials before and after thermochemical cycling, measured from images in Figure 2.3.

Material	BET surface area (m^2 g^{-1})		Total pore volume (cm^3 g^{-1})		Feature sizes[a] (nm)	
	as-made	cycled	as-made	cycled	as-made	cycled
3DOM CeO_2	47.6	3.95	0.412	0.012	48 ± 6[b] 92 ± 10[c] 189 ± 16[d]	148 ± 70
NOM CeO_2	47.3	4.1	0.111	0.011	172 ± 118	341 ± 158
D-3DOM CeO_2	95.7	4.3	0.318	0.010	92 ± 10[c] 189 ± 16[d]	230 ± 114[f] most > 1000
Commercial CeO_2	<1	<1	0.002	0.002	N/A[e]	N/A[e]

[a] Measured from SEM images in Figure 2.3.

[b] Average wall thickness at the thinnest points, based on 150 measurements for each reported value.

[c] Tetrapodal node size.

[d] Octapodal node size.

[e] Not applicable; due to the lack of porosity and massive (200–800 μm) feature sizes, a statistically significant data set could not be collected.

[f] This value refers to the average of the smaller particles observed in SEM images. Most of the sample consists of micrometer-sized grains.

2.4.2 Thermal behavior

The thermal properties of the synthesized materials were also determined. The conduction of energy through the fixed beds is governed by the volume-averaged Fourier's law. The effective thermal conductivity of porous materials depends on the coupled conduction of energy through the solid and fluid volumes, and must be estimated in the absence of experimental data. Using the commonly employed geometric mean model, the thermal conductivity of porous ceria is given by

$$k_{\text{eff}} = k_{\text{f}}^{\phi} k_{\text{s}}^{1-\phi} \qquad \text{Eq. 2.4}$$

where ϕ is the porosity, k_{f} is the thermal conductivity of the fluid phase, and k_{s} is the thermal conductivity of the bulk ceria.[175] Assuming that the fluid volume is filled with N_2, the effective thermal conductivity of the 3DOM CeO_2 and commercially-available dense CeO_2 were estimated. The overall porosity of the packed bed of 3DOM CeO_2 was 90%, including voids due to interparticle spaces and voids within the individual porous particles. The porosity of the commercially-available dense CeO_2 was due only to interparticle spacing and was on the order of 20%. The packed bed of dense ceria conducts energy more rapidly with an effective thermal conductivity of 0.6 W m^{-1} K^{-1}, six times that of 3DOM ceria at 0.1 W m^{-1} K^{-1}, the main difference between the two beds being the porosity of the particles. The effective thermal conductivity of the NOM and D-3DOM CeO_2 falls between the limiting cases of 3DOM CeO_2 and commercial CeO_2. Convection for flow through or around the bed is not anticipated to be a dominant mode of heat transfer. The Reynolds and Nusselt numbers (using the correlation by Whitaker[176]) are on the order of 3.0 and 1.1, respectively, for flow through the fixed beds.

Note, however, that while convection may not be a dominant mode of energy transport through the samples, the temperature of the gas in the tube is expected to be in thermal equilibrium with the tube walls and ceria due to the low thermal capacitance of the gas. Radiation also contributes to the transport of energy through the packed beds. Measurements of the radiative properties of porous and dense ceria suggest that dense ceria has a slightly higher absorbance of IR radiation, as porous ceria strongly back-scatters radiation in the 1000–1700 nm spectrum.[38] Due to the similar sizes of the dense and porous particles and the IR spectrum anticipated for temperatures ~1500 K, the packed beds of dense and porous ceria are anticipated to transport energy by radiation similarly. Thus, the primary difference in heat transfer between the samples is due to conduction.

2.4.3 Thermochemical Cycling

The materials were subjected to 50+ thermochemical cycles. A single thermochemical cycle involved, as a first step, the partial reduction of CeO_2 under a N_2/10.5 ppm O_2 blend for a total of 78 seconds at a high temperature, with a typical temperature profile shown in Figure 2.5 for the case of 3DOM CeO_2. When heated at rates up to 800 °C/min (as might be expected when directly irradiated by concentrated solar energy), 3DOM CeO_2 rapidly released oxygen. Oxygen evolution was complete before the end of this step. Similar to other porous materials,[49] the rate of oxygen release from the 3DOM CeO_2 correlates with the rate of temperature rise measured by the thermocouple embedded in the sample, indicating that the O_2 release rate is limited primarily by heat transfer, and not kinetics. The heat-transfer-limited nature of the rate of

reduction was confirmed by comparing the rate of O_2 release in 3DOM CeO_2 heated at different rates (Figure 2.6). In the second step of the cycle, the material was quickly cooled to a target temperature of ca. 850 °C while CO_2 was injected in the reactor. During this process, CO was rapidly produced, and the 3DOM CeO_2 was reoxidized in less than 90 seconds. These fast rates of O_2 and CO production over 3DOM CeO_2 were stable for 55 cycles with negligible loss of productivity. The thermochemical cycling rates in the present work are, to my knowledge, the fastest to have been demonstrated for temperatures between 850 and 1250 °C. Rapid cycling rates are an important pathway for increasing the throughput of fuel over a given period of time.

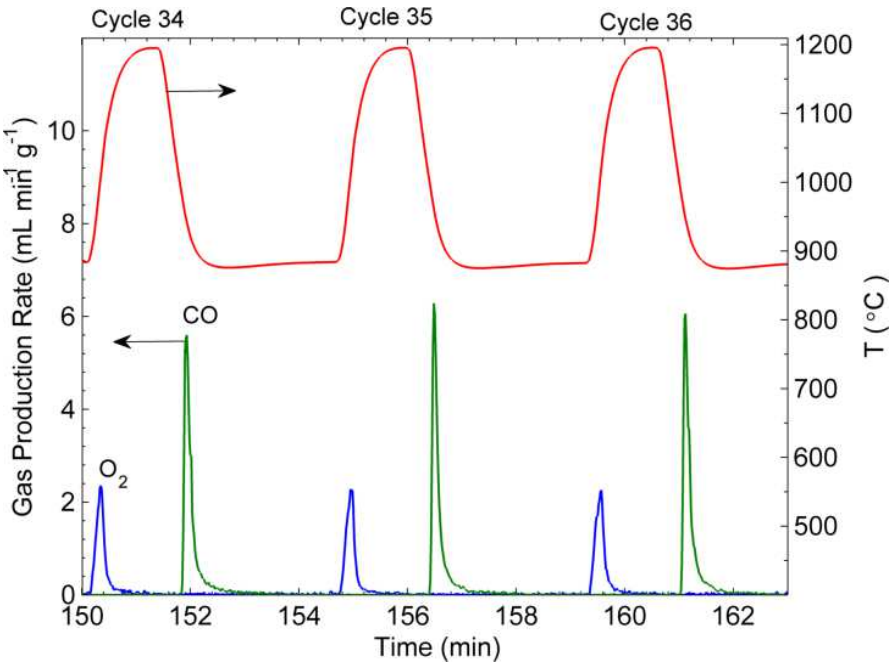

Figure 2.5. The rate of O_2 and CO production over 3DOM CeO_2 in cycles 34–36 (representative of stable cycling) and the corresponding temperature recorded by the temperature probe embedded in the sample.

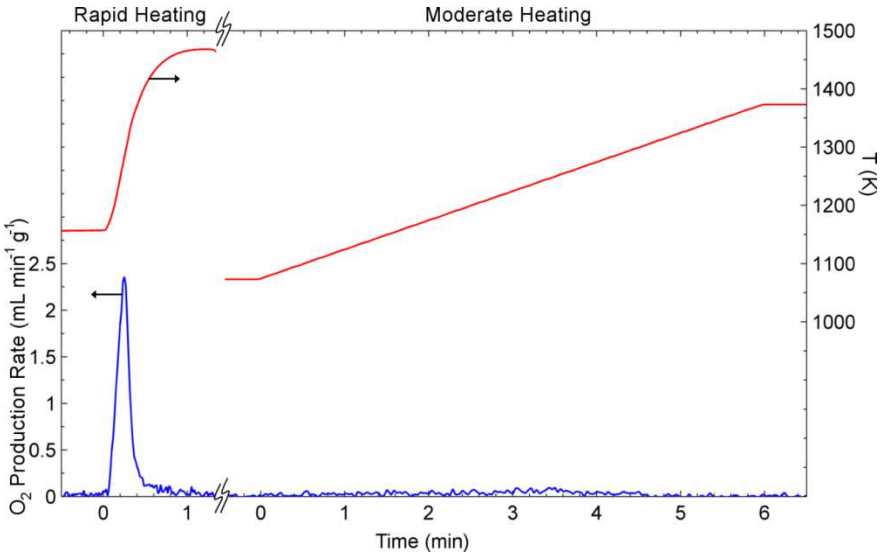

Figure 2.6. O_2 production rate from 3DOM CeO_2 versus heating rate. Rapid heating is correlated with rapid O_2 release because the reduction of ceria in the present study is heat-transfer-limited.

Important differences are observed in the overall CO productivity of CeO_2 materials with various morphologies. Figure 2.7 shows the productivity of the 3DOM, NOM, D-3DOM, and commercial CeO_2 over multiple thermochemical cycles. Because, to a first approximation, the 3DOM and NOM samples behave similarly to each other, I will discuss them together and refer to them as the macroporous CeO_2 samples. While all materials exhibited stable cycle-to-cycle fuel production, the macroporous CeO_2 reacted faster than the D-3DOM and commercial CeO_2, as evidenced by the tenfold difference in the fuel produced between the macroporous samples and the D-3DOM/commercial samples within the fixed 3.5 min cycle period. Quantitatively, the representative specific CO productivity for the materials in a given cycle once productivities stabilize is 0.9 ± 0.1 mL g^{-1} for 3DOM CeO_2 and 1.0 ± 0.2 mL g^{-1} for NOM CeO_2, reported for conditions of standard temperature and pressure (STP). The commercially-available, sintered CeO_2

and the D-3DOM CeO_2 produced an order of magnitude less CO, with specific CO productivity values in a given cycle of 0.06 ± 0.03 mL g^{-1} for commercial CeO_2 and 0.08 ± 0.06 mL g^{-1} for D-3DOM CeO_2. The contrast between the productivities of the commercial CeO_2, the D-3DOM CeO_2, and the macroporous CeO_2 is attributed to the morphologies of the samples. In fact, as will be shown in the subsequent discussion, the D-3DOM and commercial samples exhibit such comparably slow kinetics that the materials fail to reach the chemical equilibrium limit for fuel production during fast cycling, unlike the macroporous samples.

The average rate of fuel production is a good metric for summarizing the kinetic behavior of a particular material. This rate is calculated by dividing the overall gas production by the total time required to reach a 95% reaction extent for reduction and oxidation. In our study, the rate of CO production observed for 3DOM CeO_2 was 50 mL $g^{-1}h^{-1}$; for NOM CeO_2, 30 mL $g^{-1}h^{-1}$; for D-3DOM, 2 mL $g^{-1}h^{-1}$; and for the commercial CeO_2, 2 mL $g^{-1}h^{-1}$. These results were for a reduction temperature of 1200 °C or less. In other work, a porous monolith reduced at 1500 °C produced 50 mL $g^{-1}h^{-1}$ of H_2, and a similar material produced 130 mL $g^{-1}h^{-1}$ of CO.[11, 20]

The rise in cycle-to-cycle CO production from the 3DOM and NOM CeO_2 samples over the first 20 cycles tracks the maximum temperature attained by the temperature probe embedded in the sample (Figure 2.7b). For an atmosphere with a fixed oxygen partial pressure (p_{O2} = 1.01×10^{-5} atm), thermodynamics show that CeO_2 is reduced to a greater extent at higher temperatures.[177] Therefore, the rise in the 3DOM and NOM CeO_2 productivities over the first 20 cycles shows that the system is behaving as expected

thermodynamically. Based on the maximum temperature attained by the probe embedded in the samples, the thermodynamically predicted limit for fuel production from CeO_2 is 0.6 mL g^{-1} of CO and 0.3 mL g^{-1} of O_2 (corresponding to 1200 °C and 1.01×10^{-5} atm O_2 partial pressure). The 3DOM and NOM CeO_2 produced more CO and O_2 than this limit. For the equilibrium thermodynamics relevant to our system, 3DOM and NOM CeO_2 would need to have an average temperature of 1250 °C to produce the measured amount of CO/O_2.[177] Therefore, the sample was, on average, 50 °C hotter than the thermocouple reading. Given the time response of the probe, the low effective thermal conductivity of porous CeO_2, and the high heat fluxes involved for rapid heating and cooling, an under-reporting of this magnitude is reasonable.

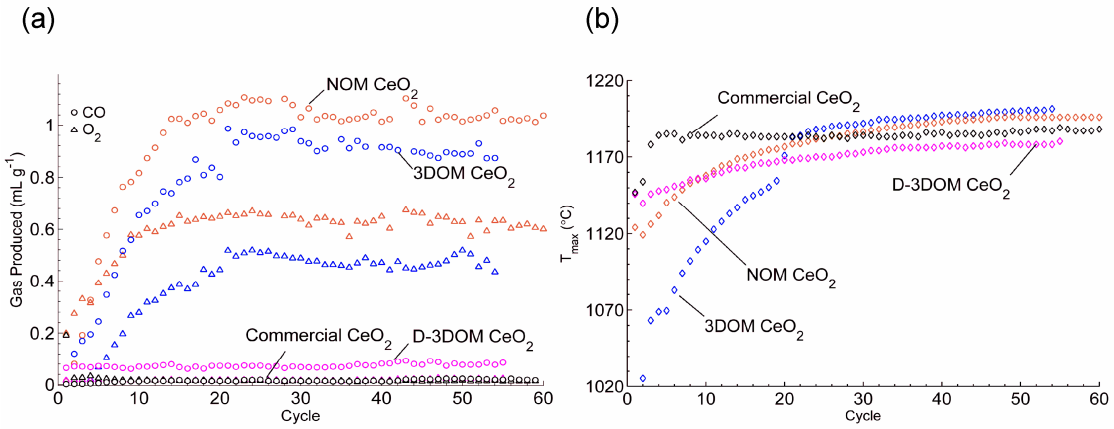

Figure 2.7. (a) The total O_2 (triangles) and CO (circles) gas produced in each thermochemical cycle over 3DOM, NOM, D-3DOM, and commercial CeO_2. (b) The maximum temperature recorded by the temperature probe embedded in the sample during reduction in each cycle.

The present study reveals that sample morphology not only influences chemical reaction rates, but also influences heat transfer, which can substantially impact the

thermochemical cycling behavior of ceria undergoing rapid heating and cooling since ceria non-stoichiometry is a strong function of temperature.[177] Comparison of the maximum temperatures measured during reduction (Figure 2.7b) and minimum temperatures measured during oxidation (Figure 2.8) elucidates the differences in heat transfer among the four samples. For brevity, we restrict our attention to the maximum temperature data here and discuss the minimum temperature data in the supporting information. There are two key features of the data in Figure 2.7b: the spread in the maximum temperature in early cycles and the increase of the maximum temperature from cycle-to-cycle in the three synthesized samples.

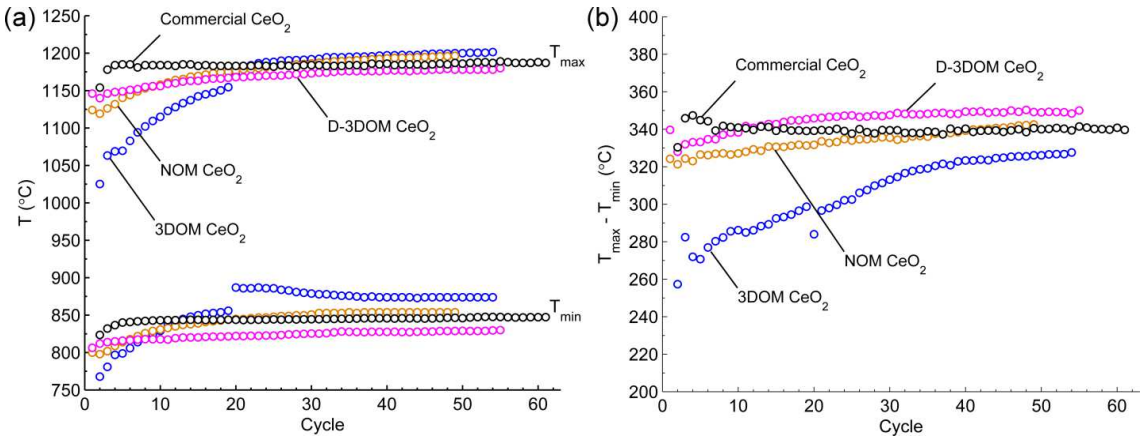

Figure 2.8. (a) The maximum temperature attained by the thermocouple probe at the interior of the samples during reduction (T_{max}) and the minimum temperature attained by the thermocouple probe during oxidation (T_{min}) during all thermochemical cycles. (b) The difference between the maximum and minimum temperatures shown in (a).

The cycle-to-cycle change in the minimum temperature further corroborates the differences in heat transfer among the four samples. The macroporous samples have a

lower effective thermal conductivity than the denser and less porous D-3DOM and commercial samples. Consequently, the macroporous samples heat up slower than the D-3DOM and commercial samples in the first 20 cycles (prior to significant physical changes), as shown in Figure 2.8b. The corollary is that the macroporous samples also cool down slower, which results in a smaller temperature swing between the maximum temperature of reduction and the minimum temperature of oxidation in the first 20 cycles. Figure 2.8b shows the difference between these two temperatures, confirming the expected trend in the temperature swing for the macroporous samples. As the macroporous samples sinter and their effective conductivity increases, the window between the maximum temperature of reduction and the minimum temperature of oxidation increases with the cycle number. In contrast, the temperature swing is unchanged for the commercial sample during cycling as this material experiences little physical change. Figure 2.8a also shows that, like the maximum temperature of reduction, the minimum temperature of oxidation increases during cycling for the macroporous samples as they are, overall, heated to a higher temperature when exposed to the intense infrared radiative output of the furnace.

The difference in the maximum temperature measured at the interior of the fixed beds in the early cycles is an artifact of the conductive heat transfer properties of the samples. The packed bed of the commercially-available dense CeO_2 features a higher effective conductivity and a slightly higher absorbance of IR radiation. Consequently, for the dense commercial sample, energy is more rapidly transported towards the interior of the fixed bed, and the temperature there rises more rapidly. In the case of the porous samples, the

lower effective conductivity prevents the rapid transfer of thermal energy, and the temperature at the interior of the bed rises more slowly. Thus, in the early cycles, the maximum temperature attained at the interior of the commercial CeO_2 bed is higher than the maximum temperature at the interior of the porous samples.

The increasing trend from cycle-to-cycle of the maximum temperature in the 3DOM, NOM, and D-3DOM CeO_2 is due to structural changes, including a volume reduction. As the initially porous materials undergo thermally induced physical changes, their conductive and radiative transport properties also change, becoming more like those of dense ceria. Furthermore, and perhaps more significant, the beds of the porous ceria shrink during cycling, leading to a reduction in the bed diameter. As a result, the length scale for heat transfer decreases, and the overall conductance of the beds increase. In combination, the transport of energy through the beds of the porous samples becomes rapid enough that the maximum temperature attained at the bed interior is similar to that of the dense, commercial ceria. The ~10 ˚C separation of the asymptotic values of the maximum temperature is attributed to the different final diameters of the beds of the macroporous samples and the unchanged diameter of the bed of the commercial sample. Changes in the morphology throughout the cycling experiment were confirmed in a separate experiment in which very small samples of 3DOM CeO_2 were removed for imaging at specific cycles: 1, 6, 10, 15, 25, and 35 (Figure 2.9). The images measured can be found in the supporting information (Figure 2.10). An effort was made to ensure that all the samples removed had experienced the same thermal treatment within the bed, and thus would be morphologically comparable to one another. The curve produced from

feature size measurements on the resulting images correlates with the rise in temperatures observed for the porous materials, corroborating our hypothesis that sintering of the porous materials made them more thermally conductive. Both the temperature of 3DOM CeO_2 (Figure 2.7b) and its feature sizes (Figure 2.9) approach asymptotic values, suggesting that the performance beyond cycle 35 (where gas production per cycle is stable) should remain stable for longer-term cycling.

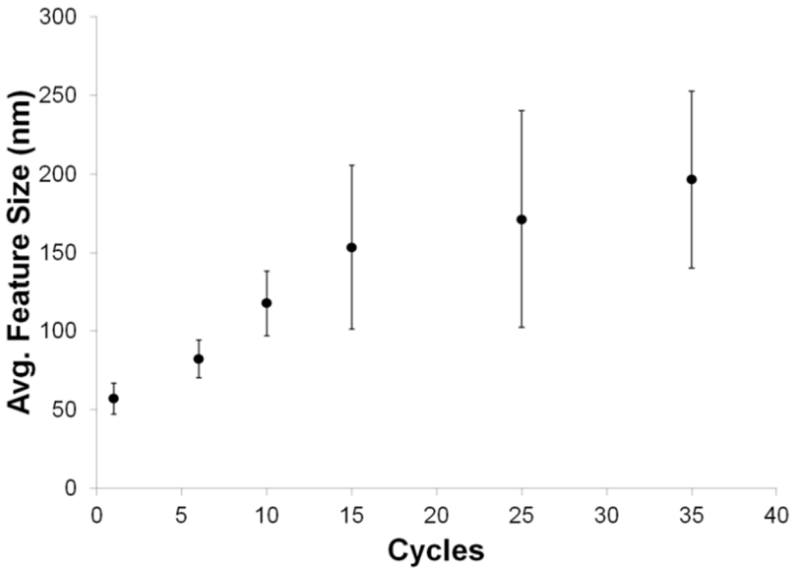

Figure 2.9. Feature size increases in 3DOM CeO_2 by cycle, as measured via SEM. For cycles 1 and 6, where the ordered structure was retained, the walls were measured. As the average size increases, the distribution of feature sizes increases as well. Feature size triples by cycle 15, and gradually increases past that point.

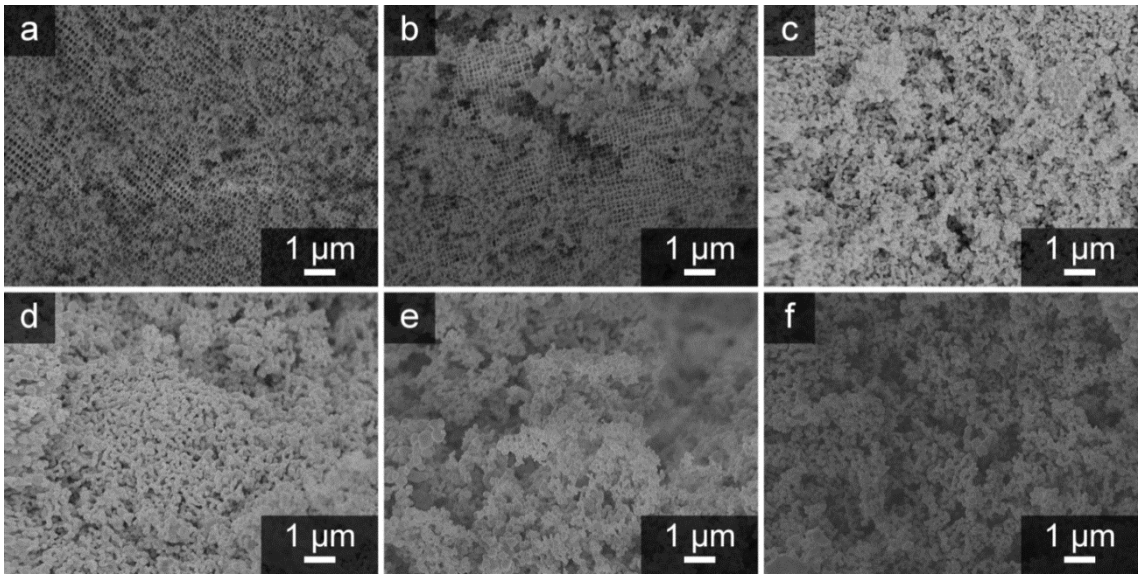

Figure 2.10. Images of 3DOM CeO_2 from approximately the same region in the bed for cycles 1, 6, 10, 15, 25, and 35, panels a–f respectively.

An additional consequence of the low effective conductivity of the samples and the high heat fluxes required for rapid heating and cooling is that temperature gradients exist in the beds. These gradients were indirectly observed in 3DOM CeO_2 via SEM imaging of structural variations. The morphology of 3DOM and NOM CeO_2 was spatially non-uniform after cycling, indicative of differential densification due to the presence of a temperature gradient. In 10–20 % of the cycled 3DOM and NOM CeO_2 materials, the original morphology was largely maintained, indicating that these regions were cooler than the spatially-averaged sample temperature. Most (>60%) of the cycled 3DOM and NOM CeO_2 contained the more characteristic disordered, interconnected pore morphology described previously (Figure 2.3d, f). Other areas (~10–20%) in both the cycled 3DOM and NOM CeO_2 were highly sintered, containing few pores and crystallites on the order of several µm. Based on a comparison of the morphologies of material in

these regions to samples that were heated more slowly in a conventional furnace, it appears that the external surfaces of the rapidly heated samples reached temperatures between 1150 and 1250 °C (Figure 2.11). To confirm the presence of a temperature gradient in the packed beds, a small cross-section of the 3DOM CeO_2 bed (~800 μm) near the central thermocouple was removed and imaged along the radial direction. Significant structural differences can be observed between the outer and inner edges of this piece (Figure 2.12). Figure 2.12c shows the internal structure of this fragment, in which the ordered macroporosity (along with its sub-100 nm feature sizes) is retained. In the region closer to the exterior of the bed (Figure 2.12b), this macroporous structure can no longer be observed, and the average feature sizes are >200 nm.

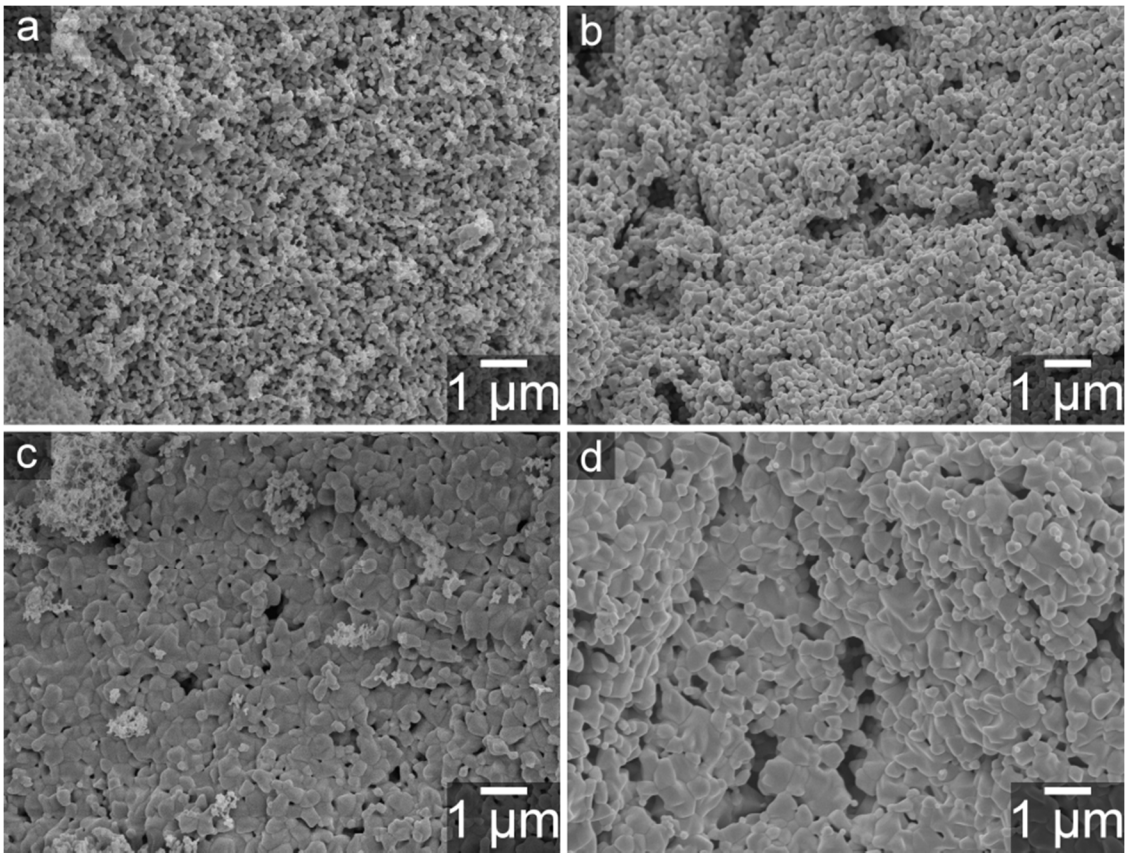

Figure 2.11. Estimation of sample temperatures from sample morphologies. These SEM images show representative areas of thermochemically cycled 3DOM CeO_2 (left) and 3DOM CeO_2 treated for 1 h at a specific temperature in a conventional furnace (right). (a) A moderately sintered area of thermochemically cycled 3DOM CeO_2, indicative of ~60 % of the sample has a similar morphology as (b) 3DOM CeO_2 sintered at 1150 °C for 1 h. (c) A heavily sintered area of thermochemically cycled 3DOM CeO_2, indicative of ~10–20 % of the sample has a similar morphology as (d) 3DOM CeO_2 sintered at 1250 °C for 1 h.

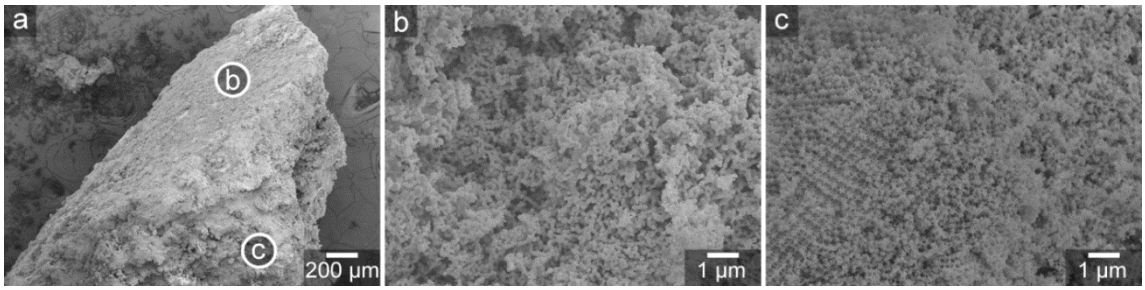

Figure 2.12. SEM images show the presence of a thermal gradient in the 3DOM CeO_2 sample thermochemically cycled. (a) A piece of 3DOM CeO_2 that was located next to the sample thermocouple. (b) An enlarged view of a region closer to the wall of the process tube than (c) the region which was adjacent to the thermocouple. The typical morphology observed in (b), a disordered, interconnected pore network results from sintering. In contrast, the originally templated 3DOM morphology, though lightly sintered, is readily apparent in (c).

This behavior is similar to that of many nanocrystalline materials studied in the ceramics literature.[178] Substantial morphological variance was observed over hundreds of micrometers in Y-doped ZrO_2 ceramics sintered at 1300 °C (dwell time 2 h) with a ramp rate of only 20 °C/min.[179] In our experiment, the ramp rates achieved by our reactor system are an order of magnitude higher, and the estimated thermal conductivity of the initial materials are similar (0.10 W/m·K for CeO_2, 0.06 W/m·K for Y-doped ZrO_2). Given the demonstrated advantages of rapid heating rates for gas evolution from these materials, we suggest that structural and thermal gradients will likely exist in reactor systems using porous CeO_2. These are important factors which must be considered in reactor design.

While thermal transport in the dense and macroporous samples ultimately led to the two materials attaining similar maximum temperatures during reduction (after ~25

cycles), differences in their fuel production behavior remained substantial, as shown in Figure 2.7a. Although the macroporous structure conducts thermal energy more slowly than the dense structures, it permits rapid fuel production and consequently high fuel productivity (Figure 2.7a).

Figure 2.13 is an expanded graph of O_2 and CO production rates, showing two representative cycles for each of the four CeO_2 morphologies. The peak O_2 production rates follow the order of intensities NOM > 3DOM >> D-3DOM ≈ nonporous CeO_2, with a large gap between the macroporous samples and the two denser materials. O_2 evolution from the 3DOM and NOM CeO_2 terminates at nearly the same time. For the CO production peaks, however, interesting differences in the rate of CO production can be observed by focusing on the trailing end of each peak. Whereas the rate drops quickly for 3DOM CeO_2, a longer decay tail is observed for the sample with disordered porosity, NOM CeO_2. This may be a consequence of less pore interconnectivity in the NOM material (*e.g.,* dead-end channels), so that the internal surface cannot be accessed by CO_2 as rapidly as for the 3DOM material, and release of CO is also inhibited. The difference could also be due to the ~40 °C lower oxidation temperature of the NOM CeO_2 relative to the 3DOM CeO_2. The commercial and D-3DOM CeO_2 samples produced CO far more slowly than the other CeO_2 samples (illustrated in Figure 2.6, full data sets available in figures 2.14–2.17), which impacted CO productivity. The rate of oxidation of these two denser samples was so slow that the 2 minutes allotted for oxidation were insufficient to fully utilize the non-stoichiometry developed during reduction. For the commercial CeO_2, over the first few cycles, the amount of O_2 produced exceeded the amount of CO

produced and exhibited a downward cycle-to-cycle trend, indicating that vacancies were being formed during reduction and left unfilled during oxidation. Eventually the cyclic O_2 production stabilized, and the $CeO_{2-\delta}$ was cycled between two partially reduced states.

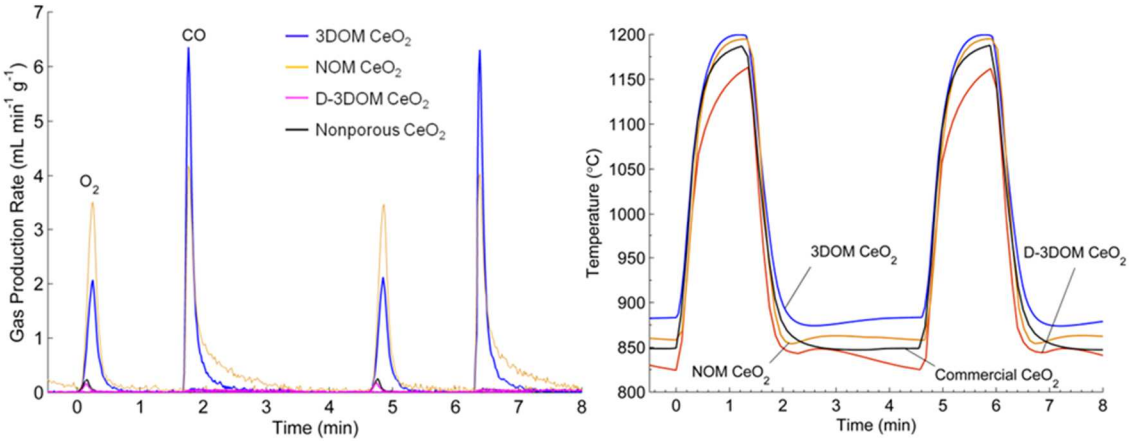

Figure 2.13. (a) Rates of gas production for the different CeO_2 morphologies taken from representative cycles. (b) The temperature measured by the sensor at the interior of the samples for the same cycles.

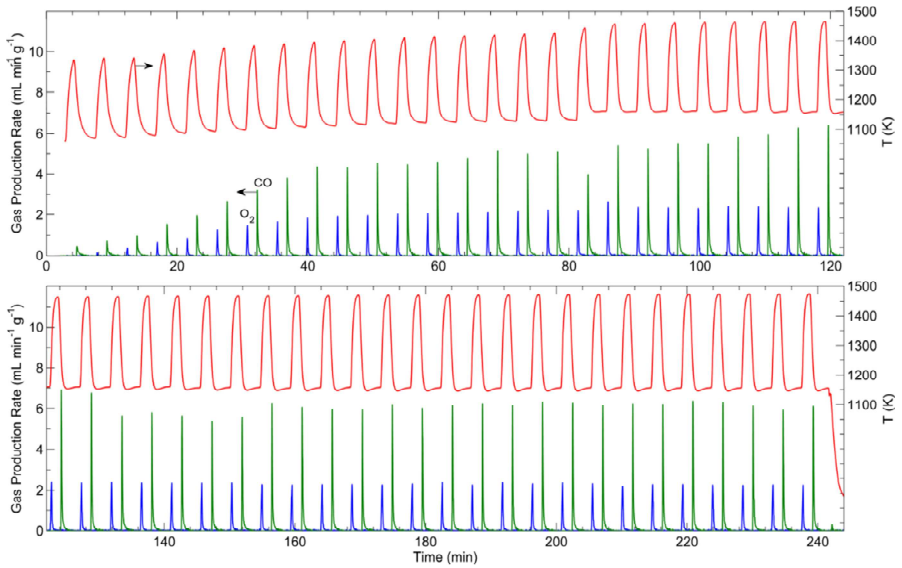

Figure 2.14. Rate of CO (green) and O_2 (blue) production for 3DOM CeO_2 is shown for the entire course of thermochemical cycling. The temperature measured by the thermocouple embedded in the sample is also shown (red).

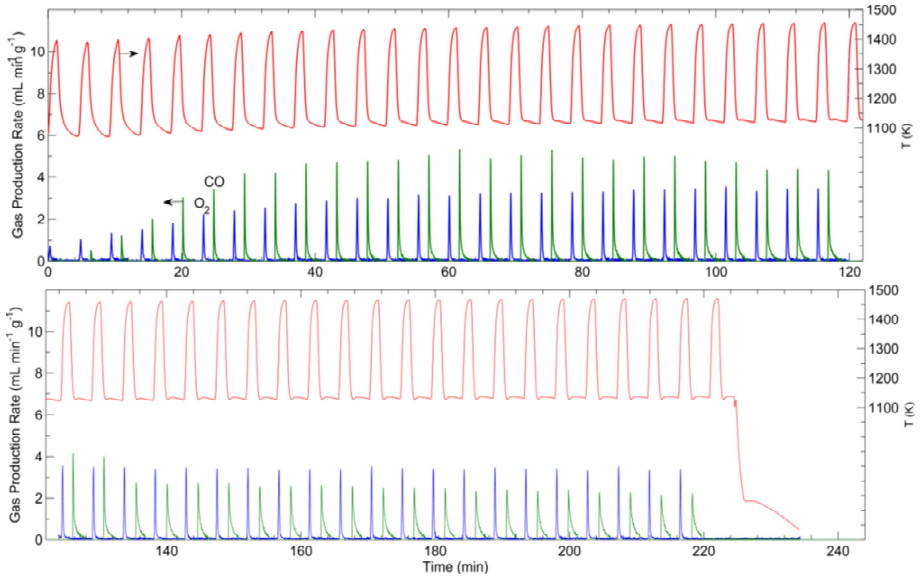

Figure 2.15. Rate of CO (green) and O_2 (blue) production for NOM CeO_2 is shown for the entire course of thermochemical cycling. The temperature measured by the thermocouple embedded in the sample is also shown (red).

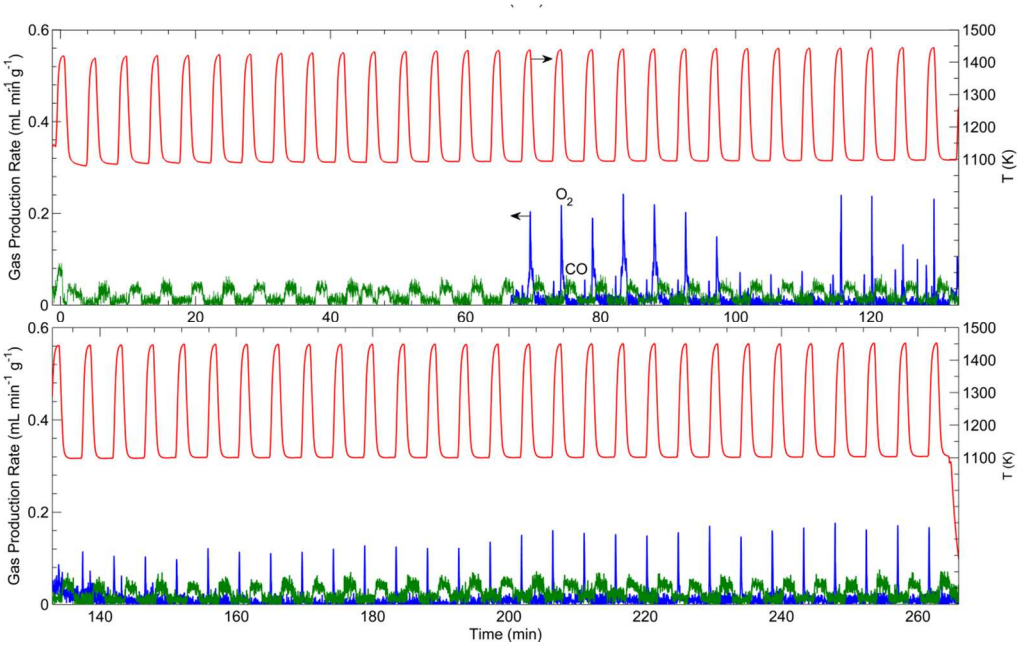

Figure 2.16. Rate of CO (green) and O_2 (blue) production for D-3DOM CeO_2 is shown for the entire course of thermochemical cycling. The temperature measured by the thermocouple embedded in the sample is also shown (red).

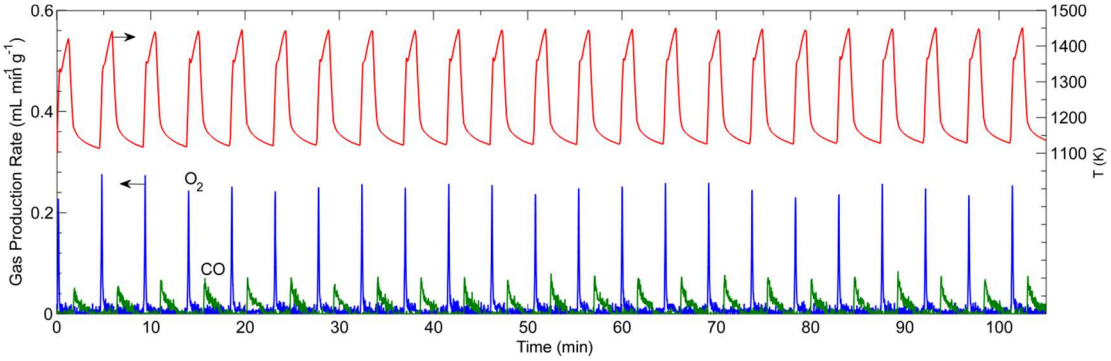

Figure 2.17. Rate of CO (green) and O_2 (blue) production for the commercial CeO_2 is shown for the entire course of thermochemical cycling. The temperature measured by the thermocouple embedded in the sample is also shown (red).

Evidence for incomplete utilization of the non-stoichiometry can be seen in the rate of CO production in time. At the end of the 2-minute oxidation when the CO_2 flow was turned off, the CO production curve dropped abruptly (Figure 2.18, inset). When the same material was left to oxidize over a longer period of time, the CO peak decreased gradually over the course of 15 minutes (Figure 2.18), before dropping below the detection level of the gas analyzer. We suggest that, given enough time, stoichiometric re-oxidation would have occurred.

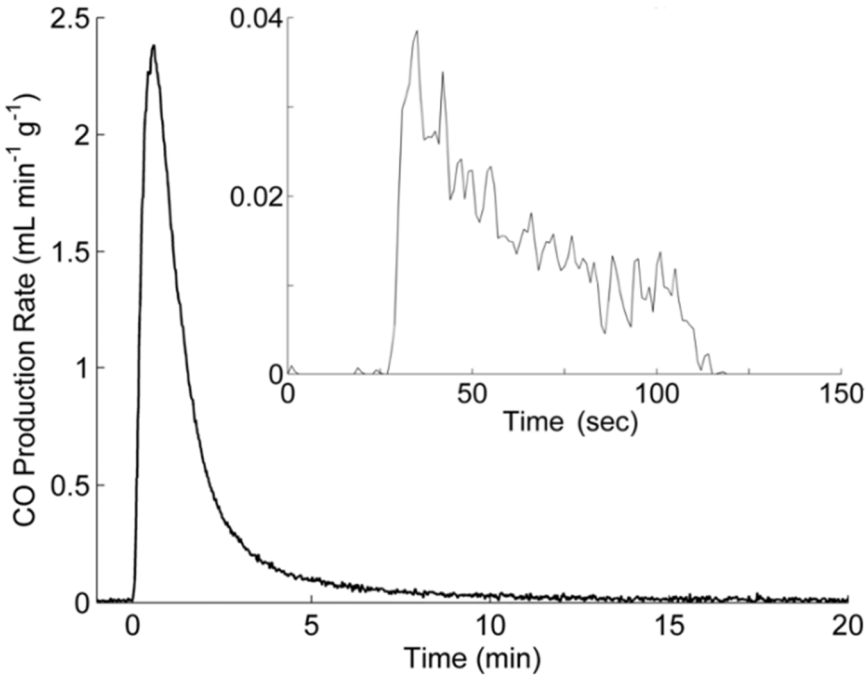

Figure 2.18. Characteristic CO production from nonporous CeO_2 over long timescales. The inset shows the abrupt drop in CO production at the end of an oxidation step during rapid cycling, showing that oxidation was incomplete when the CO_2 flow was shut off.

Incomplete utilization of the non-stoichiometry is a kinetic effect; thermodynamics indicates that the CeO_2 should be completely reoxidized under these conditions. This

slow rate of oxidation of commercial CeO_2 is to be expected when we consider its morphology. The commercial CeO_2 is comprised of nonporous, polycrystalline granules of sintered CeO_2 that remain unchanged during thermochemical cycling (Figure 2.3b). Without any appreciable porosity, surface sites available for oxidation are restricted to the very limited external surface area of the commercial CeO_2 particles. The macroporosity of the 3DOM and NOM CeO_2 provides additional surface area in these materials that substantially increases the rates of CO production relative to the commercial CeO_2 particles. Furthermore, the thin solid walls of 3DOM and NOM CeO_2 lead to shorter length scales for oxygen ion diffusion in the solid than in the commercial particles. However, due to the rapid rate of this diffusion in CeO_2 at temperatures above 800 °C, it is not likely that the transport of oxygen ions in the solid limited the oxidation of ceria in any of the samples tested in the present study. We estimate, using an approach similar to that presented in ref. 2, that the characteristic diffusion time is on the order of seconds for the commercial CeO_2 particles with the longest diffusion length scales, i.e., shorter than the measured oxidation times.

2.4.4 Final sample morphology

To aid in the interpretation of the different reactive properties of the various CeO_2 materials, all samples were characterized after thermochemical cycling. Exposure to the thermochemical cycling temperatures caused all three of the templated CeO_2 samples to sinter and experience considerable crystallite growth, as evidenced by the sharpening of reflections in the XRD patterns (Figure 2.4). SEM images show that the ordered structure of the 3DOM CeO_2 was lost after cycling (Figure 2.3d), but the majority of both the

3DOM and NOM CeO_2 samples (Figure 2.3f) retained a disordered, interconnected network of pores (>60% of the cycled samples). After cycling, the average wall thickness in the 3DOM sample was 148 ± 70 nm and had a wider size distribution than before cycling, due to the loss of order. The NOM sample did not undergo a drastic morphological change; its random, interconnected network remained, although the wall thickness had increased by a factor of 2. The average wall thickness was 341 ± 158 nm, considerably larger than for the 3DOM material due to more extensive interparticle contact, which would promote sintering. After cycling, the D-3DOM sample was extensively sintered, showing only few small particles with feature sizes below several hundred nanometers (Figure 2.3h). Most of the material consisted of sintered micrometer-sized grains, leaving little porosity. Under the equilibrium conditions during N_2 sorption analysis, a surface area comparable to that of the macroporous samples was measured for D-3DOM CeO_2 after cycling. We attribute this to a combination of factors: first, there is a small amount of unsintered material in each of the porous samples resulting from the thermal gradients observed during cycling (Figure 2.12). In addition, the specific surface area of uncycled D-3DOM CeO_2 is twice that of the 3DOM and NOM CeO_2 samples; this enhanced surface area allows for less mass of unsintered material to produce the same amount of surface area. Second, the extensive sintering of the majority of the sample (Figure 2.3h), producing μm-scale grains with limited porosity, likely blocks gas access to these regions. The sintered morphologies of the 3DOM and NOM materials both have a clear network of interconnected porosity, which is not observed in the D-

3DOM CeO_2 It is plausible that reactants cannot reach the unsintered material, resulting in the slow kinetics observed in the cycling experiments.

The initial and final morphologies of the porous materials, paired with the observed performance above, yield substantial insight into the behavior of these materials under thermal cycling conditions. Our results suggest that accessible surface areas, interconnected pore space and feature sizes of solid materials are important parameters in controlling productivity and reaction kinetics. The interconnected porosity in the 3DOM and NOM CeO_2 materials provides ready access for reagents to the relatively large surface area throughout the volume of the reacting CeO_2 particles. It also facilitates evolution of the product gases. A greater accessible surface area enhances the rate of oxidation in NOM and 3DOM CeO_2, leading to the stark differences in the rate of CO production between the porous and nonporous CeO_2 seen in Figure 2.6. Maximum rates for CO production are an order of magnitude greater for the porous samples compared to the nonporous commercial sample. However, once a reasonable amount of surface area (ca. 2–10 $m^2\ g^{-1}$) is available, oxygen evolution is not particularly sensitive to it (Figure 2.7). Instead, the fuel-production step is most sensitive to morphology, presumably due to a rate-limiting mechanistic step involving gas adsorption to, conversion at, or desorption from the CeO_2 surface. Thus, the enhanced reactivity of the 3DOM and NOM CeO_2 samples is a consequence of their engineered porosity.

An additional consideration relates to the small feature sizes (Table 2.1) of the wall skeleton in 3DOM and NOM CeO_2, facilitating rapid distribution of the oxygen ions throughout the bulk CeO_2 solid. The characteristic time scale for solid-state oxygen

transfer in CeO_2 has been estimated to be between 0.1 and 2 ms in the temperature range from 500–800 °C for 5 μm-diameter grains.[49] Given that, in the templated macroporous materials, wall dimensions were almost two orders of magnitude smaller, even shorter times for oxygen diffusion are expected in these samples. The rate of CO production over the 3DOM and NOM CeO_2 is thus primarily controlled by the rate of the surface step in the heterogeneous CO_2-splitting chemistry, while the rate of CO production from the commercial CeO_2 is slowed by both the surface step and oxygen ion diffusion through several hundred micrometers of solid material. In the case of D-3DOM CeO_2, even though initial feature sizes resemble those of the parent 3DOM CeO_2 material, the reduced open space and more extensive sintering behavior is responsible for the lower productivity.

2.5 Summary of Morphological Studies

Four CeO_2 samples with differing morphologies were evaluated for CO_2 splitting under thermochemical cycling conditions. A reduction temperature of ~1200 °C allowed for appreciable fuel production over 3DOM and NOM CeO_2 while retaining an open, porous morphology necessary to realize kinetic advantages. These advantages have great potential for practical thermochemical reactor systems, as they allow for fuel production at lower temperatures by enabling faster cycling. At a reduction temperature of 1200 °C, productivities and rates of CO production for samples with macroporous morphologies and solid feature sizes between ca. 50 and 350 nm were found to be an order of magnitude larger than for nonporous CeO_2 and D-3DOM CeO_2. The differences in

reactivity between the materials are related to differences in surface accessibility. A comparison of the two best performing samples, 3DOM and NOM CeO_2, showed that the extent of pore periodicity did not influence productivity, but the more periodic 3DOM structure ensured interconnected porosity, which improved the kinetics of the oxidation step. In addition, the 3DOM structure showed greater resistance to sintering than the other morphologies, because the macropores reduced the overall contact between grains. The use of porous materials also enabled an investigation of temperature gradients resulting from rapid heating/cooling in thermochemical systems. These results demonstrate the importance of engineered architecture of active materials in thermochemical cycles that involve solid-gas interfaces.

2.6 Acknowledgements

The description of thermal conductivities and reaction kinetics detailed in section 2.4.2, and the description of the reactor process in section 2.4.3 were supplied by Luke Venstrom. Luke, Daniel Boman, and Tingting Quan operated the reactor, colleted, and aided in the interpretation of data presented in figures 2.2, 2.5-2.8, and 2.13-2.18. Nick Petkovich supplied figure 2.12 and the discussion of the thermal gradients present in the material after cycling, as well as some of the XRD data presented in figure 2.4. Syntheses of large batches of material required for the cycling experiments were provided by Nicholas Hein.

Chapter 3: Tuning the Thermal Resistance of Nanoscale Ceramics

3.1 Introduction

This chapter follows up on the results of Chapter 2, but rather than focusing on morphology changes, here, I make compositional adjustments to the CeO_2 material and assess whether these changes can allow for retention of nanostructure at temperatures in the 1300-1400 °C range. The 3DOM structure is employed as a model system for observing grain growth and structure loss, as it has well-defined features of uniform size. Thus when these features are altered or destroyed under thermal stress, the changes are immediately obvious under qualitative analysis techniques such as SEM.

3.1.1 Doped CeO_2 Materials

As observed in the previous chapter, maintaining structures of materials with high surface area and/or small feature sizes becomes increasingly difficult as temperature increases. Structural considerations, such as feature size and spatial localization, are limited in their effectiveness to prevent sintering. The upper limit on process temperature before structure is lost depends on the composition of the material. Thus, further

improvements in generating thermally resistant nanostructured materials must involve modifying the chemical composition of the solid.

There is substantial correlation between the melting point of an oxide and its sintering behavior. Sintering is driven by ion diffusion in the solid state; the melting point of an oxide is an indicator of the amount of energy required to put all the molecules of a particular compound into a state of constant diffusion. The melting point of a material is an indicator of the lattice energy; the higher the melting point, the more energy is required to break bonds and allow solid-state diffusion.[180] Thus, lower melting solids require less energy to undergo solid-state diffusion. CeO_2 has a strikingly high melting point of 2400 °C; as such, there are few options for oxides that have higher melting points than it: ZrO_2, HfO_2, CaO, MgO, and Y_2O_3 are commonly used in the ceramic literature.[31, 181-186]

It has been observed, in many systems, that impurities in a ceramic material often limit the extent of grain growth.[147, 187] This is due to an effect known as "solute drag." When a ceramic is heated, grain growth causes the boundaries to migrate. However, as the boundaries travel, they must "drag" with them the dopant atoms, which intrinsically resist diffusion through the lattice.[147] This effect can be significant; studies carried out on CeO_2 doped with 6% calcium showed average grain size limited to 30 nm when heated to 1625 K at 10 K/min, whereas the pure material under the same processing parameters had an average grain size of 400 nm.[187]

3.2 Experimental Methods

Cerium(III) chloride heptahydrate (99.9%), citric acid (99.5+%, ACS grade), and methyl methacrylate (99%) were all obtained from Sigma-Aldrich. Potassium persulfate (99.9%) was obtained from Fisher Scientific. Ethylene glycol (99+%) was obtained from Mallinckrodt Chemicals. All reagents were used as received. De-ionized water (18.2 MΩ·cm) was used in all syntheses.

3.2.1 Synthesis of Colloidal Crystals and 3DOM Metal Oxides

A dispersion of 515 ± 12 nm-diameter colloidal spheres of poly(methyl methacrylate) (PMMA) was synthesized by emulsifier-free emulsion polymerization of methyl methacrylate (MMA), following a published method for the preparation of colloidal crystal templates.[174] Potassium persulfate was used as the initiator in the mixture consisting of 20% v/v of MMA in water. The polymerization was carried out at 70 °C with a stirring rate of 300 RPM.

3DOM metal oxide refractories were prepared by colloidal crystal templating. A Pechini precursor was prepared by combining citric acid, ethylene glycol and water in a 3:1:37 molar ratio. Mixtures of two to four metal chloride salts, chosen from among $CeCl_3$:$7H_2O$, YCl_3:$6H_2O$, $LaCl_3$:XH_2O, $GdCl_3$:$6H_2O$, $NdCl_3$:$6H_2O$, $PrCl_3$:$7H_2O$, $ZrOCl_2$:$8H_2O$, $CaCl_2$:$4H_2O$, $SmCl_3$:$6H_2O$, and $MgCl_2$:$4H_2O$, were added such that the total molar ratio of cations to ethylene glycol was 1:1. Optimal additive concentrations were selected using guidance from the literature;[41, 187, 188] ternary and quaternary oxide samples were extrapolated from existing binary oxides. This solution was then infiltrated into the PMMA colloidal crystal templates in a sealed container for 12 h at 25 °C. The

mass ratio of precursor solution to template was 3:4. The infiltrated templates were gelled at 90 °C for 24 h. The thermally-treated materials were calcined in a tube furnace (using a 2 °C/min ramp rate) at 310 °C for 2 h and 450 °C for 2 h under static air to remove the template and crystallize the gel. In all cases, a light yellow, opalescent powder was obtained.

3.2.2 Thermal Testing of 3DOM Metal Oxides

The quaternary oxide powders produced were tested for sintering behavior by calcination in static air at 1400 and 1500 °C for 4 h unless otherwise specified. Samples were loaded into a high-alumina content combustion boat (99.8%, CoorsTek; Golden, CO, USA) and placed in a Carbolite (Hope, UK) STF 16/180 tube furnace. Samples were heated at 8 °C/min to the calcination temperature, and then cooled to room temperature at the same rate.

3.2.3 Characterization of Materials

The morphology of the materials before and after cycling was studied by scanning electron microscopy (SEM). Samples were mounted on stubs with carbon tape and coated with 75 Å of Pt, then imaged on a JEOL 6700 electron microscope. Image data was produced by measuring feature sizes in ImageJ. For any reported size, 150 measurements were taken. Powder X-ray diffraction (XRD) patterns of samples of interest were obtained using an X'Pert Pro diffractometer outfitted with an X'Celerator detector. Radiation was supplied by a Co anode (Kα, λ = 1.789 Å) operated at 45 kV and 40 μA.

3.3 Results and Discussion

3.3.1 Binary and Ternary CeO_2 Mixed-Oxides

A wide variety of CeO_2-based mixed-oxides were investigated to determine the best structures for thermal resistance (Table 3.1). Initial studies focused primarily on binary oxides, that is, the mixture of CeO_2 with one other "dopant" cation, such as ZrO_2 or other rare earths (e.g., La, Sm, Gd). Many of these materials were synthesized and characterized by SEM (Figure 3.1) and XRD (Figure 3.2). All samples showed the 3DOM structure (see Chapter 1, section 1.1.2) upon initial calcination at 310 °C and 450 °C for two hours. Additionally, all samples were solid solutions in CeO_2, that is, they showed only diffraction peaks resulting from the CeO_2 fluorite lattice. This indicates that all or nearly all dopant cations were incorporated into the CeO_2 structure, and were resting at the Ce sites. Furthermore, there is a slight upward shift in the patterns which contain Zr^{4+}, as its ionic radius is 86 pm, compared to the 101 pm of Ce^{4+}. The other lanthanides (in the 3+ oxidation state) tend to be close to Ce^{4+} in size, particularly the ions later in the series, such as Sm and Gd, as a result of the so-called "lanthanide contraction." The d-spacings of the (111) reflection for these materials are listed in Table 3.1, and the observed shifts are consistent with the expected behavior as a result of ionic radius.

Table 3.1. Precursor compositions for CeO_2 and CeO_2 solid solution materials prepared via MeOH infiltration. Crystallite sizes of the products are provided where data is available.

Material	MeOH (g)	$CeCl_3$ (g)	Precursor 2 (g)	Precursor 3 (g)	Grain Size (nm)	d_{111} (Å)
CeO_2	3.0	3.00	--	--	14.3	3.14
$Ce_{0.8}Zr_{0.2}O_2$	3.0	2.50	$ZrOCl_2$, 0.43	--	7.4	3.11
$Ce_{0.8}Sm_{0.2}O_{1.9}$	3.0	2.50	$SmCl_3$, 0.50	--	13.9	3.12
$Ce_{0.67}Gd_{0.33}O_{1.833}$	8.0	4.28	$GdCl_3$, 2.16	--	12.4	3.13
$Ce_{0.8}La_{0.2}O_{1.9}$	3.0	2.50	$LaCl_3$, 0.47	--	14.5	3.15
$Ce_{0.8}Sm_{0.1}Zr_{0.1}O_{1.95}$	3.0	2.50	$SmCl_3$, 0.28	$ZrOCl_2$, 0.22	9.0	3.12
$Ce_{0.8}Sm_{0.1}La_{0.1}O_{1.9}$	3.0	2.50	$SmCl_3$, 0.28	$LaCl_3$, 0.24	7.8	3.16
$Ce_{0.8}La_{0.1}Zr_{0.1}O_{1.95}$	3.0	2.50	$LaCl_3$, 0.25	$ZrOCl_2$, 0.22	9.7	3.13
$Ce_{0.8}Pr_{0.1}Zr_{0.1}O_2$	3.0	2.50	$PrCl_3$, 0.26	$ZrOCl_2$, 0.22	6.8	3.13
$Ce_{0.8}Pr_{0.1}Nd_{0.1}O_{1.95}$	3.0	2.50	$PrCl_3$, 0.26	$NdCl_3$, 0.27	6.5	3.16

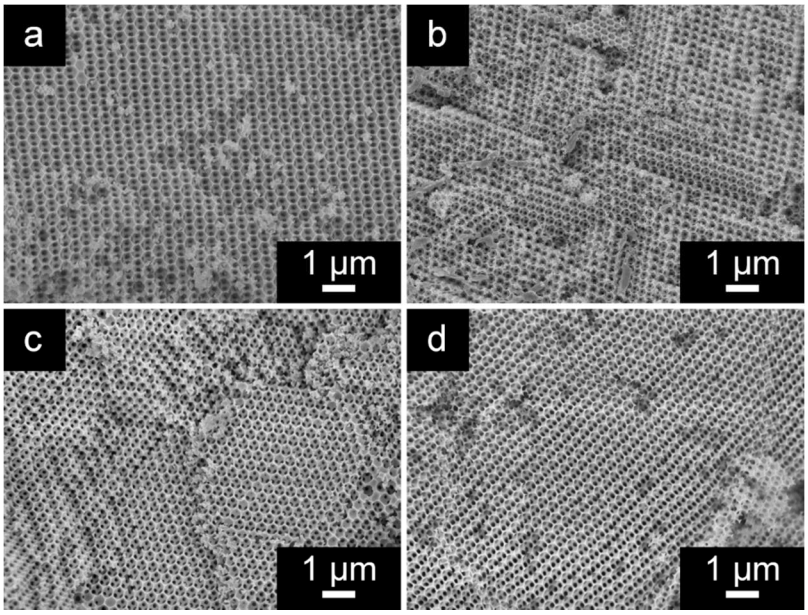

Figure 3.1. Examples of 3DOM structure observed in CeO_2 and several binary solid solutions. (a) 3DOM CeO_2. (b) 3DOM $Ce_{0.8}Zr_{0.2}O_2$. (c) 3DOM $Ce_{0.66}Gd_{0.33}O_{1.83}$. (d) 3DOM $Ce_{0.8}Sm_{0.2}O_{1.9}$. The structure is very similar in each case, addition of dopant does not affect the template morphology in any way.

Some of these samples were tested in the reactor apparatus described in Chapter 2. With the exception of the Zr samples, the doped materials tended to generate less H_2 or CO in comparison to the neat CeO_2 sample. This is likely because, while they change the lattice parameters of CeO_2 like Zr, the dopants are 3+ cations, which introduce "unfillable" oxygen vacancies into the material. Each Ce^{4+} cation that is replaced by a 3+ lanthanide cation results in a site in the lattice that is oxygen-deficient at ambient conditions, and (in order to maintain the lattice's charge balance) irreversibly so. Because these oxygen vacancies are unfillable, they do not participate in the oxidation step and thus lower the observed fuel production.

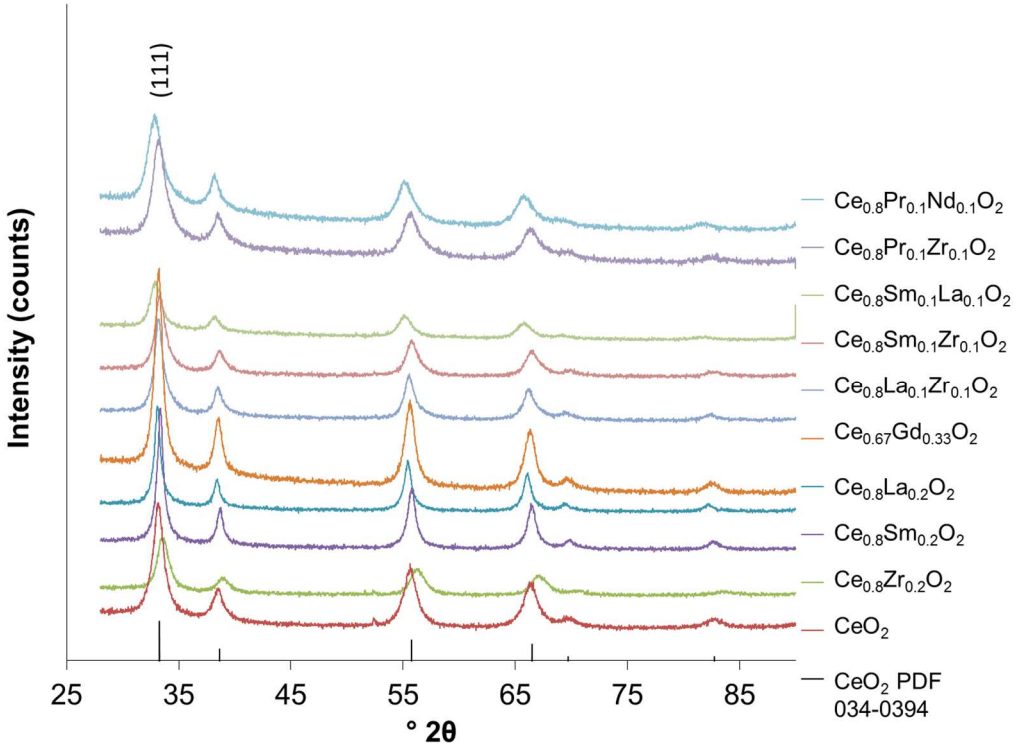

Figure 3.2. Experimental XRD patterns for materials synthesized. All show a good match with the literature pattern for CeO_2. Small peaks observed at 52.4° 2θ arise from the aluminum sample holder.

3.3.2 In-Depth Study of Ce-Zr Mixed-Oxides

Ce-Zr mixed oxides are well known in the automotive industry for having enhanced oxygen storage and release behavior, compared to CeO_2 alone. Thus, investigating their behavior under thermochemical cycling conditions was a natural choice.. In the course of this work, a detailed study of the morphology changes at different Zr inclusion levels was undertaken.

The 3DOM $Ce_{1-x}Zr_xO_2$ samples underwent structural changes which were particularly noticeable in the CeO_2, $Ce_{0.9}Zr_{0.1}O_2$, and $Ce_{0.8}Zr_{0.2}O_2$ samples, and observed via TEM. A thinning of the walls and wider windows between pores are observed, producing a more "open" structure. Despite these changes, the overall 3DOM structure is retained after cycling for all Zr concentrations.

The effect of increasing Zr content with respect to postcycling morphology in 3DOM $Ce_{1-x}Zr_xO_2$ is evident from the TEM images. For the cycled 3DOM CeO_2 sample (Figure 3.4a), the structure of the walls has been drastically altered. Single crystallites comprise the walls between nodes in the 3DOM structure, and the nodes themselves are composed of large, fused grains. However, as was noted in the SEM images, the macroporosity and ordering of the structure is still intact. In the samples that contain Zr, changes to wall thickness and window size are mitigated with increasing Zr content (Figure 3.3b–f). This trend continues to the 3DOM $Ce_{0.5}Zr_{0.5}O_2$ sample, the structure of which undergoes very little morphological change after cycling. The changes in the wall structure are from sintering processes, which result in material being transported to the nodes (as observed

in the SEM analysis) of the 3DOM skeleton at the expense of the walls. This Ostwald ripening-like effect has been observed in other 3DOM systems.[19, 30] It is clear that incorporation of high levels of Zr is beneficial from a structural standpoint. For the reactions conducted at 825 °C, near-perfect retention of the 3DOM structure can be obtained through addition of Zr.

Increasing the Zr content (Figure 3.3b–f) causes the extent of grain growth to decrease significantly. The grain sizes observed in the TEM fit reasonably well with the trends established by Scherrer equation data obtained from XRD. (Table 3.2) For the CeO_2 sample, the average grain size has already exceeded the intially observed wall thickness. In the $Ce_{0.9}Zr_{0.1}O_2$, and $Ce_{0.8}Zr_{0.2}O_2$ samples (Figure 3.3a–c), the grains have grown to approximately half the dimensions of the walls, which can be readily observed in the TEM. For $Ce_{0.7}Zr_{0.3}O_2$ and $Ce_{0.6}Zr_{0.4}O_2$ samples (Figure 3.3d and e), the grains do increase in size, but are still substantially smaller than the walls. Finally, for $Ce_{0.5}Zr_{0.5}O_2$ (Figure 3.3f), there is minimal change in the grain size, such that it does not affect the observed 3DOM structure.

Table 3.2. Grain sizes of the Ce-Zr mixed oxides measured via the Scherrer equation and wall thicknesses measured from SEM analysis.

Material	Crystallite Size (as-made, nm)	Crystallite Size (cycled, nm)	Wall thickness (cycled, nm)
CeO_2	7.4	73.8	37 ± 6
$Ce_{0.9}Zr_{0.1}O_2$	5.1	18.2	33 ± 5
$Ce_{0.8}Zr_{0.2}O_2$	4.1	14.8	39 ± 6
$Ce_{0.7}Zr_{0.3}O_2$	5.5	11.6	57 ± 6
$Ce_{0.6}Zr_{0.4}O_2$	4.4	10.6	48 ± 7
$Ce_{0.5}Zr_{0.5}O_2$	5.9	9.7	47 ± 7

These materials were thermochemically and isothermally cycled at 825 °C. The thermal reduction step (discussed in Chapter 2) was simulated with an H_2 reduction at the aforementioned temperature. For this set of mixed oxides, the highest H_2 productivity was observed for $Ce_{0.8}Zr_{0.2}O_2$. Past the 20% Zr level, replacing more and more redox-active Ce^{4+} ions with inactive Zr^{4+} ions was detrimental to the material's cycling performance.[89] So, while including high levels of Zr is highly beneficial for structure retention, it has a negative effect on reactivity.

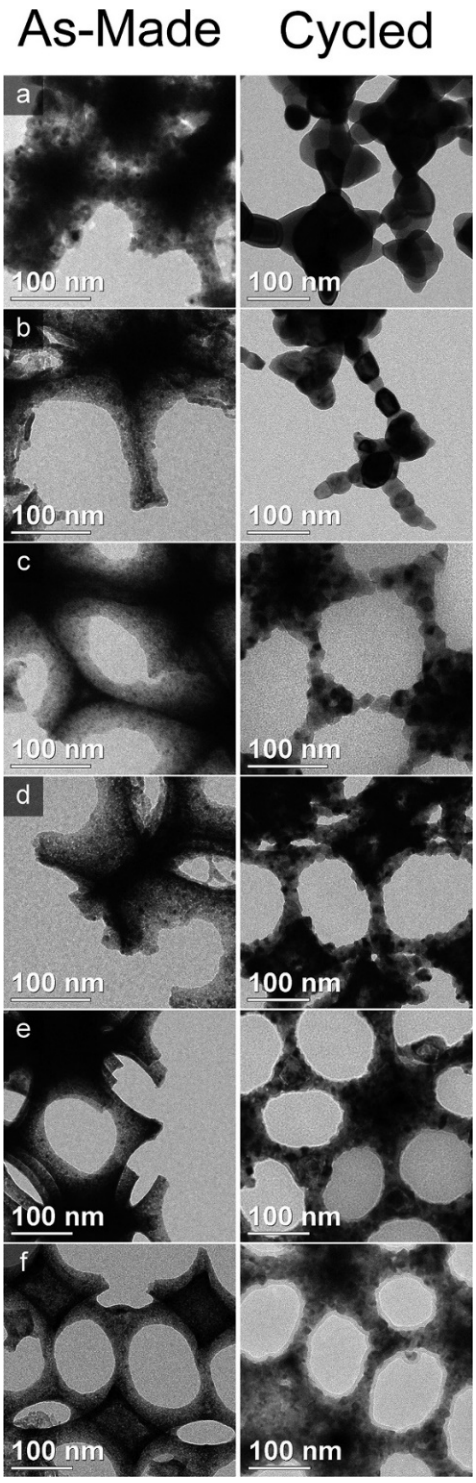

Figure 3.3. TEM images of 3DOM Ce-Zr solid solutions cycled isothermally at 825 °C with H_2. (a) CeO_2, (b) $Ce_{0.9}Zr_{0.1}O_2$, (c) $Ce_{0.8}Zr_{0.2}O_2$, (d) $Ce_{0.7}Zr_{0.3}O_2$, (e) $Ce_{0.6}Zr_{0.4}O_2$, (f) $Ce_{0.5}Zr_{0.5}O_2$.

Substantial variations were observed in thermal stability of the oxides. Work both in our lab and elsewhere has conclusively demonstrated that lower grain sizes are obtained in $Ce_xZr_yO_2$ solid solutions than in unadulaterated CeO_2.[41] These lower grain sizes arise from reduced sintering which I attribute to solute drag, as described in section 3.1. In particular, the La- and Sm-doped samples showed comparable sintering behavior to Ce-Zr solid solutions, and so several ternary oxides (Ce-X-Y-O) were produced to investigate both the degree of grain growth resistance conferred by these dopants, as well as any synergistic effects between dopants.

3.3.3 Limiting Morphology Changes in 3DOM CeO_2

Nanostructured CeO_2 (Figure 3.4a) undergoes remarkable structural change when exposed to temperatures in excess of 1000 °C, as demonstrated in Chapter 2. The "kinetic barrier" to sintering that the 3DOM structure imparts to CeO_2 is overcome when heating a sample to higher temperatures than the 1250 °C used in that study, as a result of densification processes bringing the walls into closer contact. At 1300 and 1400 °C, (Figure 3.4b, c) the nanoscale feature sizes retained in that work are gone, replaced with μm-scale grains, even within two hours. To retain small feature sizes at these temperatures, we can exploit solute drag. Figure 3.4 shows the mixed-oxides with the least degree of grain growth.

$Ce_{0.8}Sm_{0.2}O_{1.9}$ (Figure 3.4d–f) shows a significant improvement in lowering the grain sizes observed at high process temperatures. Still, at 1400 °C, very minimal porosity remains, despite the sub-μm grain size. Once La^{3+} ions are incorporated alongside Sm^{3+} (still at a total concentration of 80 mol% CeO_2) we observe a more drastic reduction in

grain size while maintaining an open structure in the final product (Figure 3.4g–i). At 1300 °C, (Figure 3.4h) cube-like particles can be observed, indicating the retention of the octahedral node morphology from the original 3DOM lattice. Finally, $Ce_{0.8}Zr_{0.1}La_{0.1}O_{1.9}$ (Figure 3.4j–l) results in even finer structure at the 1300 °C treatment level (Figure 3.4k), but heating the sample to 1400 °C results in a structure with substantially thicker walls than the $Ce_{0.8}Sm_{0.1}La_{0.1}O_{1.9}$ material. However, compared to the Sm-doped binary oxide, the remaining pores are significantly larger.

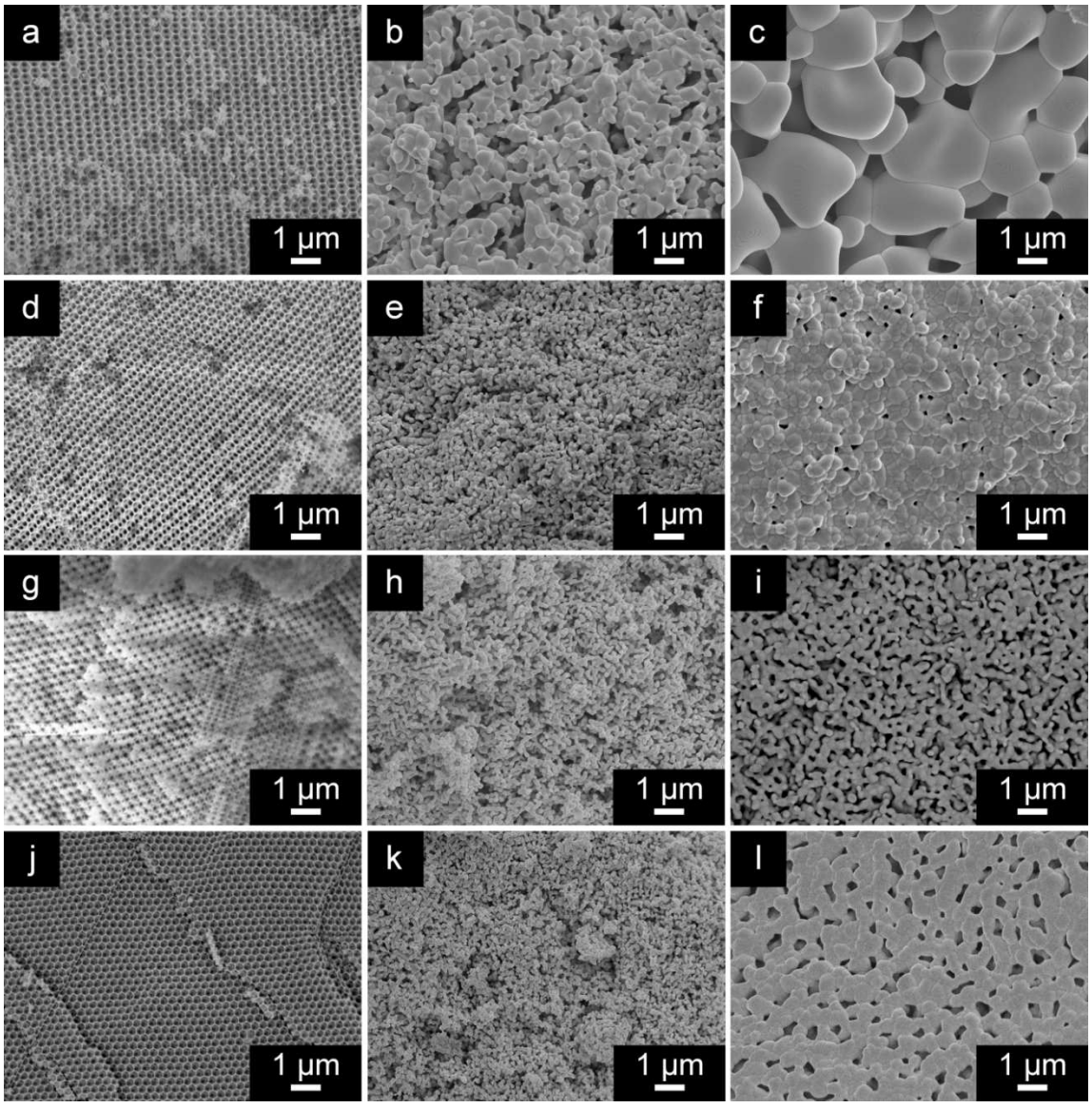

Figure 3.4. SEM images of binary and ternary oxides as synthesized (left column), after sintering at 1300 °C for 2 h (middle column), and after sintering at 1400 °C for 2 h (right column). (a–c) 3DOM CeO_2, as-synthesized, 1300 °C, and 1400 °C. (d–f) 3DOM $Ce_{0.8}Sm_{0.2}O_{1.9}$, with the same temperatures listed above. (g–i) 3DOM $Ce_{0.8}Sm_{0.1}La_{0.1}$, same temperatures. (j–l) 3DOM $Ce_{0.8}Zr_{0.1}La_{0.1}$, same temperatures.

3.3.4 Literature-Guided Synthesis of Quaternary Oxides

After observing the success of the ternary oxides in increasing the resistance of CeO_2-based materials towards grain growth and sintering at 1300–1400 °C, I began using a fourth additive to attempt to retain the 3DOM structure at these temperatures. Calcium additives have been shown to substantially decrease the grain growth of CeO_2 ceramics under strongly sintering conditions. Incorporating 6 wt% of Ca into CeO_2 allowed the material to retain a grain size of 30 nm after treatment at 1500 °C for 6 h.[187] Y is another common additive for increasing thermal resistance in CeO_2, often used in solid-oxide fuel cells which operate at or above 1000 °C.[189, 190] The final additive is Zr, considering the well-known reactivity enhancement it confers upon CeO_2[45, 191] (as well as the grain growth results discussed in the previous section).

Table 3.3 summarizes the compositions of the samples synthesized, along with their abbreviated designations which will be used in the following discussion. Previous results and literature searches indicated preferred ranges for Zr (10–20 mol%) and Ca (5–10 mol%), and for the most part, these ranges were adhered to rigidly. Optimal ranges for Y incorporation are not as clear in the literature, so the mol% of Y across the samples synthesized had the greatest degree of variation. Additionally, two samples with additive substitutions (Y for Sm, and Ca for Mg respectively) were prepared, using the molar ratios from the CZYC4 sample. XRD results (Figure 3.5) indicate that, like the previous preparations, dopants fully incorporate into the fluorite lattice.

Table 3.3. Quaternary oxide sample names and compositions.

Sample Designation	Ce (mol%)	Zr (mol%)	Y (mol%)	Ca (mol%)
CZYC1	80	10	5	5
CZYC2	70	10	10	10
CZYC3	45	20	20	15
CZYC4	60	20	15	5
CZYC5	70	20	5	5
CZYC6	50	20	25	5
CZYC7	55	10	30	5
CZSC1	60	20	15	5
CZYM1	60	20	15	5

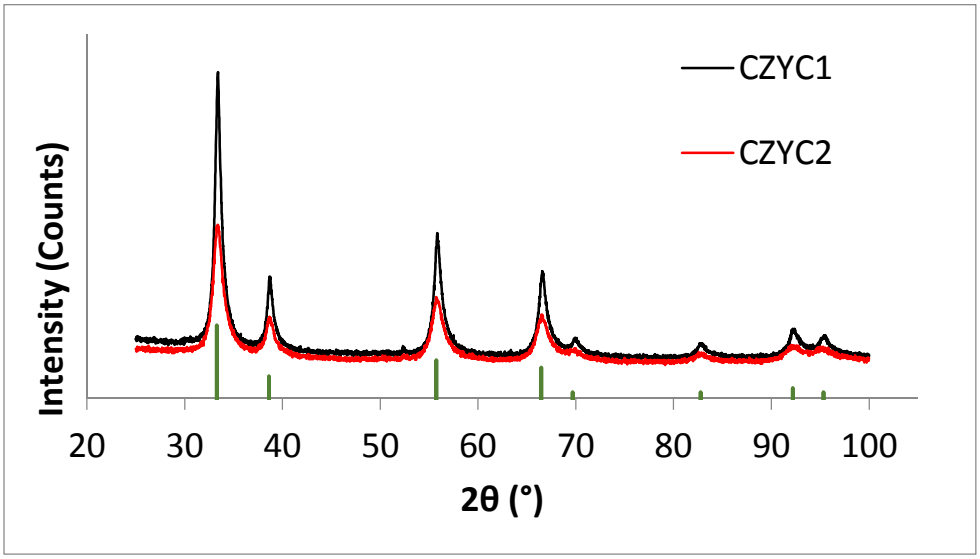

Figure 3.5. XRD patterns of representative CZYC samples showing the lack of impurity phases. As with the binary and ternary mixed-oxides, metal additives fully incorporate into the fluorite lattice.

SEM images showing a representative sample of the morphologies obtained for these compositions are shown in Figure 3.5. The material with the best sintering resistance was CZYC4, which, while still losing the 3DOM structure after calcination at …, generated a highly open, wormlike network of smooth grains with sub-μm features (Figure 3.5e). After further heat treatment of the material (22 h at 1400 °C), this open network is retained, though the observed feature sizes have increased to the 1–3 μm scale (Figure 3.6f). Within this quaternary compositional framework, the full range of structures observed in the previous investigations can be seen; CZYC7 (Figure 3.6h) sinters nearly as much as CeO_2 itself, while CZYC3, CZYC5, and CZYC6 (Figure 3.6b-d) have similar behavior to the ternary oxides studied in section 3.3.3. A wood-templated version of the material[192] with the highest thermal resistance was prepared (Figure 3.6g), primarily as a proof-of-concept for future research directions which will be discussed in Chapter 7.

Given the CZYC4's superior resistance to sintering, I created an additional 3DOM material using the same mol% of dopants in CZYC4, but swapping out Y^{3+} for Sm^{3+}. Sm^{3+} conferred substantial sintering resistance on its own and in concert with La^{3+} in the binary and ternary systems. A second sample was produced by substituting the Ca^{2+} ion with Mg^{2+}, considering the strongly refractory properties of MgO. Images of these samples after treatment at 1400 °C for 2 h (Figure 3.7) show that the materials have poorer sintering resistance than the CZYC4 material.

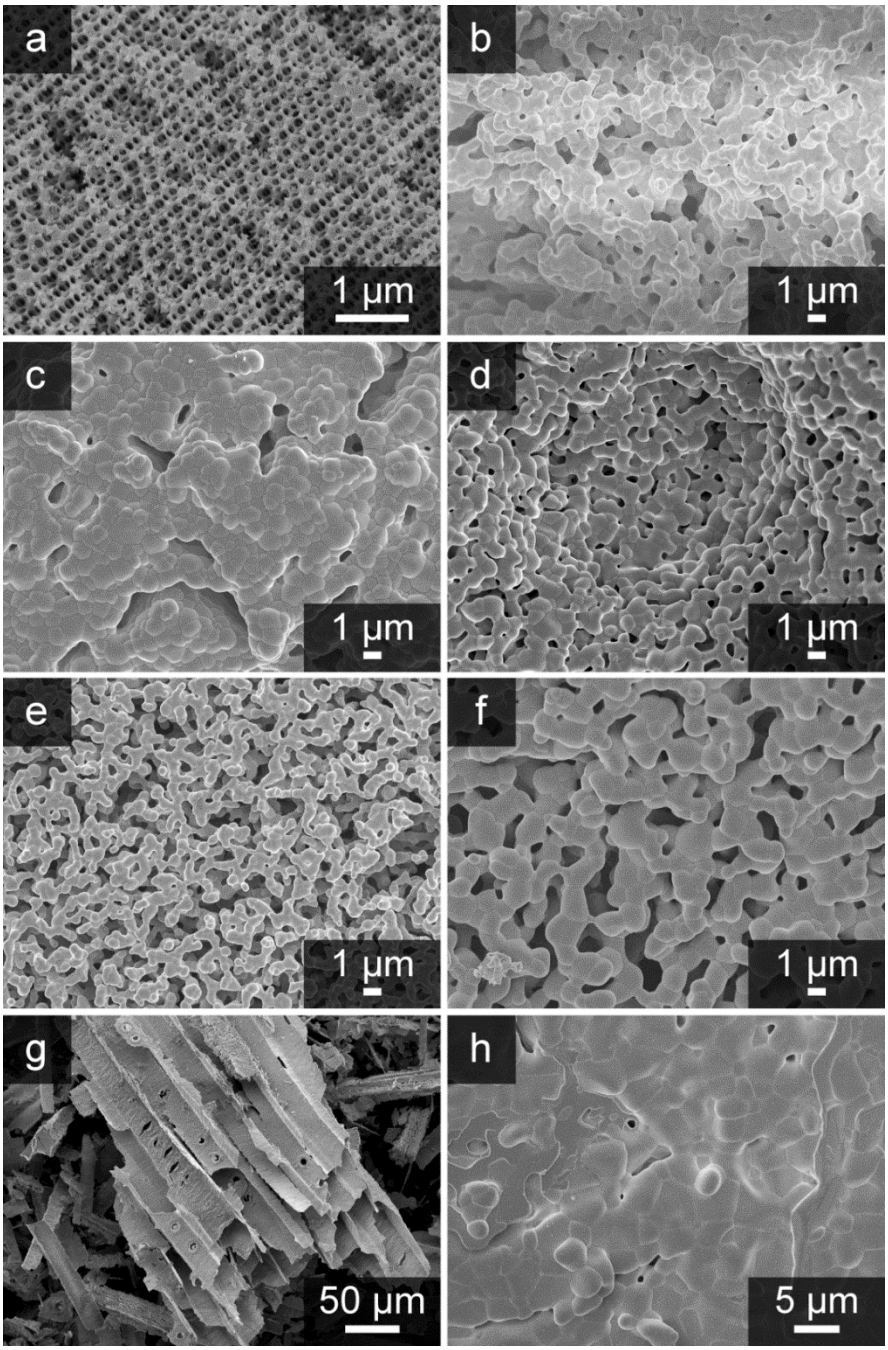

Figure 3.6. SEM images of CZYC samples showing morphological characteristics. (a) CZYC7, a representative sample of the morphology of the as-prepared materials. (b) CZYC3 treated at 1400 °C for 2 h. (c) CZYC5 treated at 1400 °C for 2 h. (d) CZYC6 treated at 1400 °C for 2 h. (e) CZYC4 treated at 1400 °C for 2 h. (f) CZYC4 treated at 1400 °C for 22 h. (g) As-prepared wood-templated CZYC4. (h) CZYC7 treated at 1400 °C for 2 h.

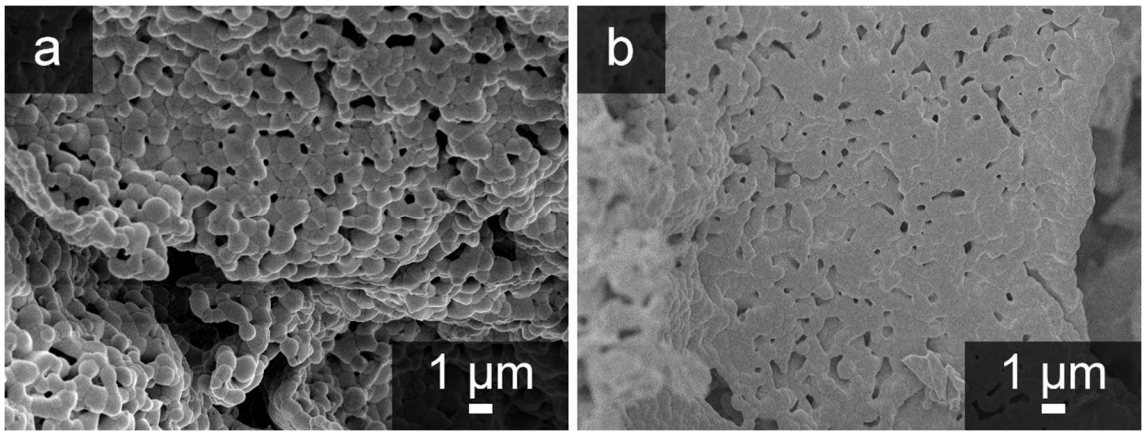

Figure 3.7. SEM images of variations on the CZYC4 composition after treatment at 1400 °C for 2 h. (a) CZYM1 and (b) CZSC1.

3.4 Conclusions

Sintering behavior of binary, ternary, and quaternary mixed oxides of 3DOM CeO_2 was investigated in an attempt to discover a composition which could retain the 3DOM structure at temperatures exceeding 1300 °C. Ce-Zr mixed oxides were investigated in detail via TEM at 800 °C, showing a clear trend in greater retention of small grain sizes with higher inclusion of Zr. While some compositions produced did retain some order at 1300 °C (e.g. $Ce_{0.8}Sm_{0.1}La_{0.1}O_{1.9}$), nanostructure was always lost at 1400 °C. Of the yttria-zirconia based quaternary oxides synthesized, CZYC4 (or $Ce_{0.6}Zr_{0.2}Y_{0.15}Ca_{0.05}O_{1.9}$), retained the smallest (sub-µm) feature sizes, despite losing the 3DOM structure.

3.5 Acknowledgements & Copyright

Several SEM images of the binary and ternary oxides were obtained by Dr. Nicholas Petkovich. Synthesis and thermal treatment of the CZYC series of materials was partially accomplished by Nicholas Hein.

Chapter 4: Microstructural Evolution in Templated Pechini Precursors

4.1 Introduction

Micro- and nanostructured ceramics are required in a variety of applications, including heterogeneous catalysis,[193, 194] photonic pigments,[195] and sensors,[196, 197] among many others. In accordance, a great deal of scientific attention has been focused on methods to directly generate these materials with a wide range of morphologies and pore size distributions. Of particular interest are hierarchically porous materials,[198-203] that is, materials which contain pores of at least two differing length scales, as they allow for the advantages of each individual type of pores (e.g., high surface area from very small pores and improved mass transport from larger pores) to be combined within the same material.

As material designs become more complex, understanding the mechanisms of morphological evolution within ceramic synthesis is of critical importance to both the improvement of existing materials and development of new ones. Sol-gel techniques, in particular, allow for convenient incorporation of a variety of structural features during synthesis. Most commonly, these features are introduced and controlled through the use of templates, i.e., sacrificial materials which are removed during or after the synthesis,

leaving voids in the ceramic. These templates fall into two categories, “hard” and “soft”. Hard templates, including colloidal particles and porous solids, act as molds with fixed structure, whereas soft templates, such as surfactant assemblies, form more dynamic templating structures in the form of micellar arrays.

Hard templates are used in the generation of three-dimensionally ordered macroporous (3DOM) materials or inverse opals, and have often been employed as a platform for producing hierarchically porous materials.[199, 204-206] The synthesis of 3DOM materials involves infiltration of a colloidal crystal template (CCT) with a sol-gel precursor, followed by calcination or pyrolysis to condense and, in many cases, crystallize the precursor and remove the template. Additional “soft” templating agents may be added to the precursor, producing secondary porosity in the walls of the material. However, morphological control is also desirable at larger length scales, and this can be established within the sol-gel precursor and gelation processes themselves.

In metal alkoxide-based systems the mechanisms of structural variations within liquid precursors have been studied extensively.[207-209] In the case of alkoxysilanes, for instance, after hydrolysis of the starting material, silica chains begin to grow via condensation of Si-OH groups. The consumption of these polar Si-OH bonds gradually decreases the polarity of the growing chains, leading to phase separation within the mixture.[210] This phase separation involves either nucleation and growth within the solution or spinodal decomposition to a bicontinuous network. The mechanism by which the phase separation progresses is highly dependent on reactant concentration, particularly of the mineral acid used to catalyze the reaction.[210] Removal of solvent and further condensation yields

macroporous structures consisting of interconnected microspheres in the case of nucleation and growth, and continuous, randomized porous silica networks for spinodal decomposition. Structures obtained can be further tuned by the addition of polar, hydrogen-bonding additives such as poly(acrylic acid) or other polymers.[211, 212]

To obtain metal-oxide microspheres with controllable sizes, a variety of synthetic routes have been demonstrated in the literature. Spray pyrolysis has been widely employed for the generation of microspheres and micrometer-scale powders.[213, 214] This technique involves spraying a metal-containing precursor (typically an aqueous solution of metal salts) through a nozzle, producing droplets which are then passed through a hot zone or onto a hot substrate, removing solvent, and crystallizing the desired products. The sizes and morphologies of spheres can be adjusted by modification of the precursor and process parameters (spray pressure, droplet velocity, temperature etc.).[214] Even without the physical formation of droplets, sol-gel systems can form these structures. Hydrolysis of metal alkoxides can yield microspheres if the conditions are controlled, for example, hydrolysis of zirconium tetrapropoxide in alcoholic solution produces microspheres with low-polydispersity if long-chain carboxylic acids (C6-C18) are added to the mixture.[73] The formation of spheres has been attributed to the development of micelle-like structures around hydrolyzing zirconium alkoxides, as well as the varying solubility of the carboxylic acids in the alcoholic solvent. In hydrothermal syntheses, polycrystalline ceramic spheres are often observed. Frequently, target morphologies are hollow; these can be formed with templates, which are then removed via calcination.[215] In the absence

of a template, hollow spheres typically form via Ostwald ripening and/or processes involving Kirkendall effects.[46, 216-218]

When complex phases are targeted, it is difficult to form true solid solutions of mixed metal oxides with many of these methods due to phase segregation processes. For example, sol-gel syntheses of YBCO superconductors are often complicated by phase segregation issues due to the tendency of barium salts to precipitate out of solution, requiring precise pH control.[219] The Pechini sol-gel method skirts this issue by sequestering the individual cations within a polymer. The method involves chelating metal cations in aqueous solution with citric acid (Scheme 1) and then linking those individual chelates together via a thermally-activated polyesterification with ethylene glycol.[88] Calcination of the resulting gel at moderate temperatures (typically, 300–600 °C) yields polycrystalline ceramics with nanoscale grains, and frequently yields solid solutions with high phase purity. The Pechini method has been applied to a variety of ceramics across the periodic table. CeO_2 is one of these ceramics, with wide-ranging applications in heterogeneous catalysis at varying temperatures,[89, 220, 221] which can benefit from enhanced surface area and nano- or microstructural engineering.[50] Additionally, CeO_2 is used as an electrolyte for solid oxide fuel cells.[190, 222]

Here, I demonstrate that the Pechini process, when carried out within the confinement of a CCT, is influenced significantly by the template. In particular, when applied to mixed ceria-alkaline earth metal oxide systems, the combined effects of Pechini precursor composition and templating environment influence the macroscopic morphology of the product beyond the scale of individual templating spheres. Hence, product morphology is

controllable, making it possible to synthesize macroporous spheres of relatively uniform and controllable sizes, as well as extended solids with hierarchical porosity.

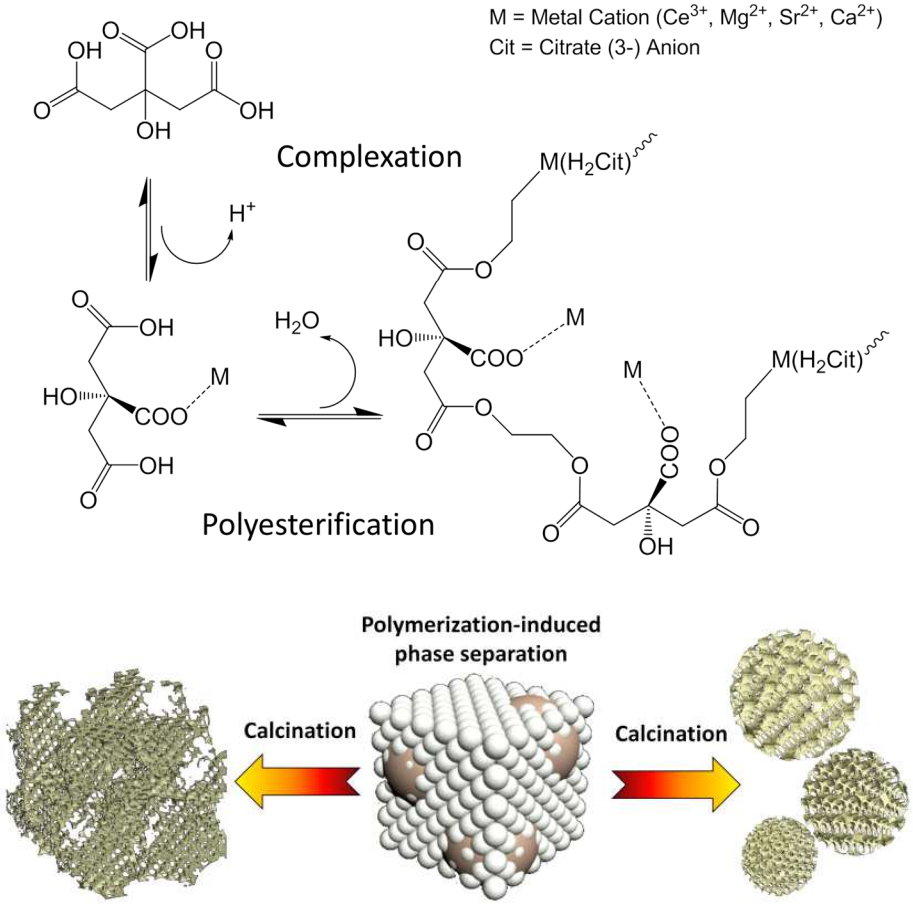

Figure 4.1. The Pechini process in confinement. Top: complexation of cations by citric acid followed by cross-linking of citric acid by ethylene glycol. Bottom: Depending on synthesis parameters, either macroporous microspheres or extended structures with hierarchical macroporosity are formed.

Other methods have been used to generate shaped particles within CCTs. Electrodeposition of ZnO within a CCT allows for the growth of interconnected, micron-scale sheets of 3DOM ZnO.[223] Controlled growth of single crystals within a CCT can yield 3DOM materials with micrometer dimensions and shapes dictated by the single

crystals themselves.[224] Spheres, cubes, and octahedra could be generated by precipitating $CaCO_3$ via introduction of $(NH_4)_2CO_3$ to an infiltrated solution of $CaCl_2$.[225] 3DOM Co_3O_4 microspheres have also been produced by infiltrating a silica CCT with a $Co(NO_3)_2 \cdot 6H_2O$ melt, however, control over the product morphology and diameter appears to be limited.[226] To my knowledge, there is only one report of ceramic microspheres resulting directly from a Pechini-type synthesis, without additional processing. Wang *et al*. produced non-templated MoO_2 microspheres with high polydispersity from $MoCl_2$, citric acid, ethylene glycol, and sulfuric acid combined in a hydrothermal bomb and treated at 180 °C.[227] However, no internal porosity was present in these microspheres, and the mechanism of formation for these spheres is poorly understood.

To that end, here I present a thorough investigation of microstructural evolution in templated Pechini gels. The result is a simple, highly tunable method to generate hierarchical micro/nanostructure in CeO_2-based Pechini-type sol-gel systems, including discrete porous microspheres with low polydispersity. The mechanisms of microstructure formation are found to be analogous to alkoxysilane-based syntheses, deriving from phase segregation in the forming gel, but influenced by the presence and identity of the hard CCT. The two pathways discussed above (nucleation and growth vs. spinodal decomposition) can be accessed through adjustment of the molar ratios of gel components, and a variety of structures can be generated. Additionally, I provide evidence that structural evolution in these systems is heavily influenced by electrostatic

forces at the template–precursor interface as well as by the degree of polymerization in the sol-gel.

4.2 Experimental Section

4.2.1 Materials & Reagents

2,2'-Azobis(2-methylpropionamidine) dihydrochloride (AMPA, 97%), cerium(III) nitrate heptahydrate (99%), citric acid monohydrate (CA, 99.5+%, ACS grade), and methyl methacrylate (99%) were all obtained from Sigma-Aldrich, potassium persulfate (KPS, 99.9%) and calcium nitrate tetrahydrate (99.5+%, ACS grade) from Fisher Scientific, magnesium nitrate hexahydrate (99%) and strontium nitrate tetrahydrate (99%) from General Chemical Corporation, and ethylene glycol (EG, 99+%) from Mallinckrodt Chemicals. All reagents were used as received. De-ionized water (>18 MΩ·cm), filtered on-site, was used in all syntheses.

4.2.2 Template Synthesis

CCTs were synthesized through emulsifier-free emulsion polymerization (EFEP) of methyl methacrylate to produce colloidal poly(methyl methacrylate) (PMMA) spheres, followed by gravity sedimentation of those spheres into fcc arrays.[174] Two different initiators, KPS[174] and AMPA,[228] were used to provide spheres with negative surface charge (average sphere diameter: 500 ± 8 nm) or positive surface charge (diameter: 400 ± 8 nm), respectively. The polymerization produced aqueous colloidal dispersions containing ca. 20 wt% PMMA, which were then poured into crystallization dishes, covered with aluminum foil, and sedimented to form the CCTs.

4.2.3 Porous Microsphere Synthesis

Aqueous precursor solutions were prepared by dissolving $Ce(NO_3)_3 \cdot 6H_2O$, an alkaline earth metal nitrate (M^{2+}), citric acid, and ethylene glycol in water. The alkaline earth metal nitrates used were $Sr(NO_3)_2 \cdot 4H_2O$, $Mg(NO_3)_2 \cdot 6H_2O$, or $Ca(NO_3)_2 \cdot 4H_2O$. The Ce^{3+}:M^{2+} molar ratio was kept constant at 1:1 unless otherwise specified, and the water:total metal ion (TMI) molar ratio was kept constant at 36:1. Phase-pure CeO_2 was also synthesized. The molar ratios of EG:CA:TMI in the precursor were varied to produce different samples, which are designated by these ratios in the form X:Y:Z. For example, a 3:1:1 $Ce_{0.5}Mg_{0.5}O_2$ precursor consisted of 2.17 g of $Ce(NO_3)_3 \cdot 6H_2O$, 1.28 g of $Mg(NO_3)_2 \cdot 6H_2O$, and 2.10 g of citric acid, dissolved in 1.86 g of ethylene glycol and 6.48 g of water.

The precursor solutions were infiltrated into CCTs and heat-treated at 90 °C for 24 h in tightly sealed glass vials, causing the precursor to form a hard gel within the template. These gelled composites were calcined in a tube furnace under static air at 310 °C and 450 °C (2 °C/min ramp, 2 h dwell time at each temperature). This produced yellow mm-scale powders, which could be mixed with water, then dispersed and suspended by vortex stirring for 10 minutes. Suspensions were stable for 3–4 days before settling, and could then be redispersed by mechanical agitation. Additionally, control samples prepared from the precursor mixtures themselves (without a template) were treated using the above procedure, i.e., sealed in vials, gelled, and calcined.

4.2.4 Materials Characterization

The morphology of the materials was examined using scanning electron microscopy (SEM). Materials, as produced, were mounted on stubs with carbon tape and subsequently coated with 75 Å of Pt, then imaged with a JEOL 6700 electron microscope. Size measurements were performed using ImageJ software (NIH). Each reported sphere size was averaged from 300 individual measurements, and particle size distributions were plotted from the same data set. Powder X-ray diffraction (XRD) patterns of materials were obtained using an X'Pert Pro diffractometer outfitted with an X'Celerator detector. Radiation was supplied by a Co anode (Kα, λ = 1.789 Å) operated at 45 kV and 40 μA. Transmission electron microscope (TEM) imaging and electron diffraction were performed using an FEI Tecnai T12 microscope (LaB_6 filament) operated at 120 kV. TEM samples were prepared by dispersing the material on a carbon-coated Cu grid from the aqueous suspensions mentioned above.

4.3. Results and Discussion

4.3.1 Microstructural Variation in 3DOM Ce-based Oxides

CeO_2, with its fluorite structure, is highly accommodating in the formation of single-phase solid solutions through the incorporation of dopants.[164, 229] However, for high concentrations of dopant atoms or at higher temperatures, phase separation can occasionally be observed in the material, as dopant-rich and dopant-lean areas develop.[89] The Pechini method allows for these dopant atoms to remain dispersed throughout the lattice even at higher concentrations. Additionally, this method employs aqueous precursors that can be easily infiltrated into a template.

Typical syntheses of 3DOM materials by the Pechini method yield powders with up to mm-scale granules, where each of these granules consists of solid, nanocrystalline material with a face-centered cubic array of interconnected macropores (Figure 4.1a).[89, 230] A few defects and cracks are observed in the periodic structure; frequently, these are attributed to localized incomplete infiltration of the template and lack of control during drying, respectively. Nonetheless, the powders tend to be opalescent, a result of the regular spacing of pores; this leads to Bragg diffraction of visible light.

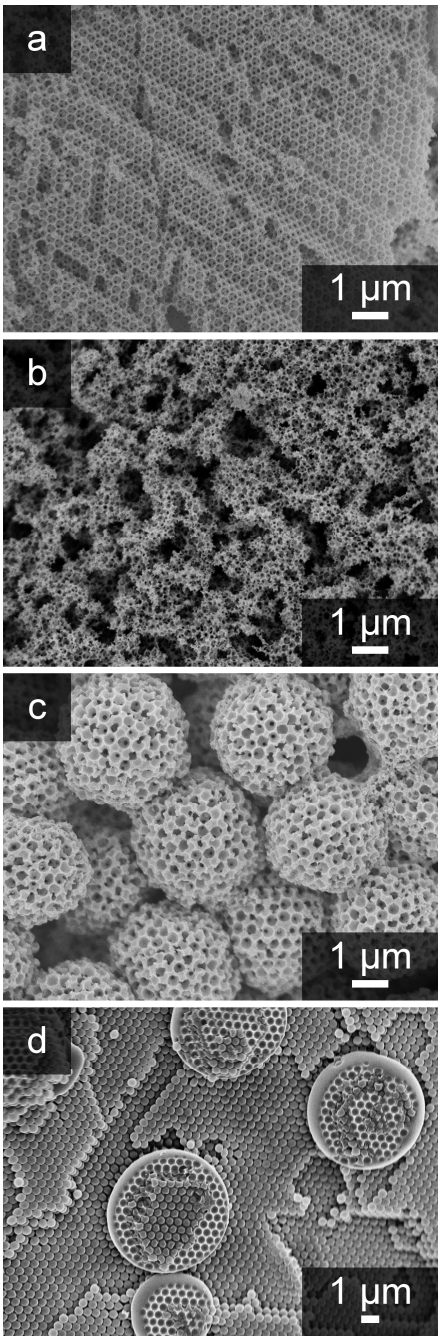

Figure 4.2. SEM images of structures observed in colloidal-crystal-templated Pechini syntheses. (a) 3DOM CeO_2, synthesized from a precursor with a EG:CA:TMI ratio of 12:3:4. (b) Hierarchically structured network of 1:3:1 3DOM $Ce_{0.5}Mg_{0.5}O_{1.5}$. (c) Microspheres comprised of 1:1:1 3DOM $Ce_{0.5}Mg_{0.5}O_{1.5}$. (d) A fracture plane from a KPS-initiated CCT infiltrated with a 2:1:1 $Ce_{0.5}Mg_{0.5}O_{1.5}$ precursor and treated at 90 °C for 23 h. Microspheres developing inside the template can be observed.

However, with certain precursor compositions—that is, EG:CA:TMI (total metal ion) ratios—the density of non-templated void spaces in the material becomes more pronounced throughout the produced powders (Figure 4.2b). Although the ordered pore structure is maintained in the solid features, μm-scale wormlike voids run throughout the system. Other compositions yield 3DOM microspheres between 1–3 μm in size (Figure 4.2c). The spheres produced have reasonably consistent shapes and sizes within a given synthesis (polydispersity <15%), and appear to maintain the array of pores left by the CCT, with average macropore spacings of 353 ± 4 nm. Spherical domains of heat-treated precursor material are also observed within the CCT before calcination (Figure 4.2d). While previously reported syntheses of microspherical 3DOM materials have relied on carefully-controlled growth of single crystals,[225] it is notable that the shapes of microspheres in this system are not related to the crystallinity of the product, as each microsphere is polycrystalline (Figure 4.3).

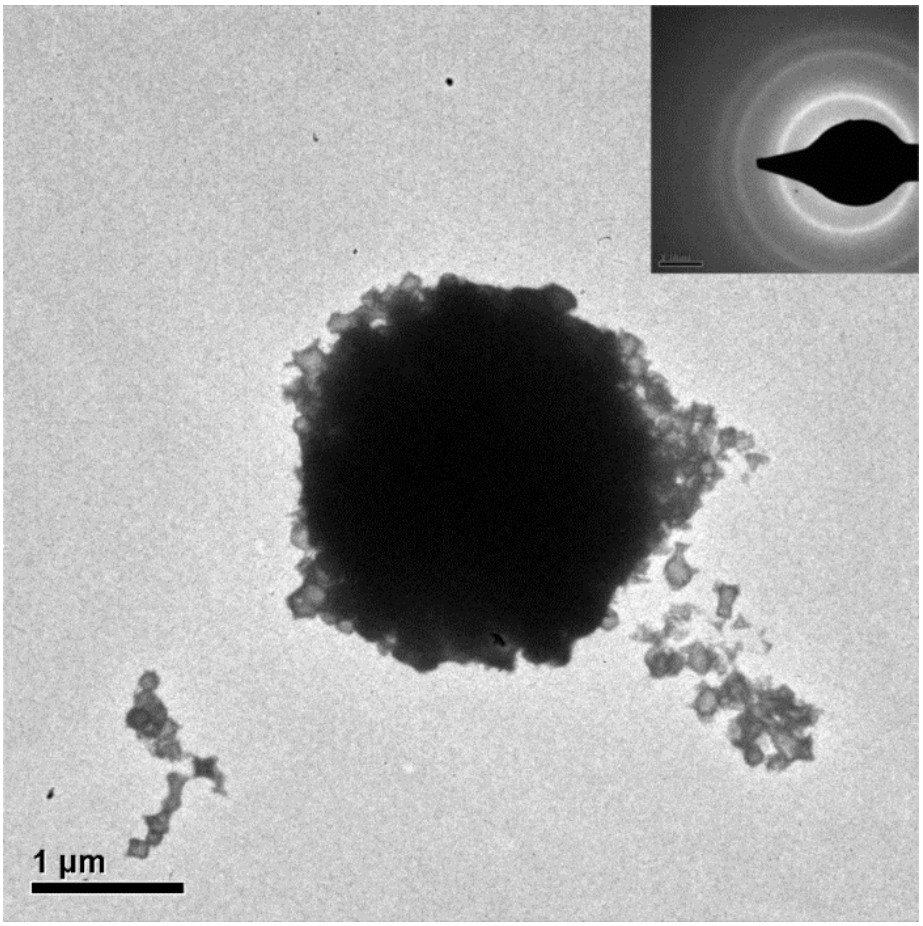

Figure 4.3. TEM image of a single "211" $Ce_{0.5}Mg_{0.5}O_{1.5}$ microsphere. Inset: A selected-area electron diffraction pattern showing rings, as opposed to a single array of dots, indicates that the sphere is polycrystalline.

Rather, the morphological variations are dictated by phase separation of polymeric precursors, as will be shown below. Additionally, the spheres are separable and dispersible in aqueous suspension, simply by adding water to the calcined powders and vortex mixing the suspension for 10–15 minutes (Figure 4.4).

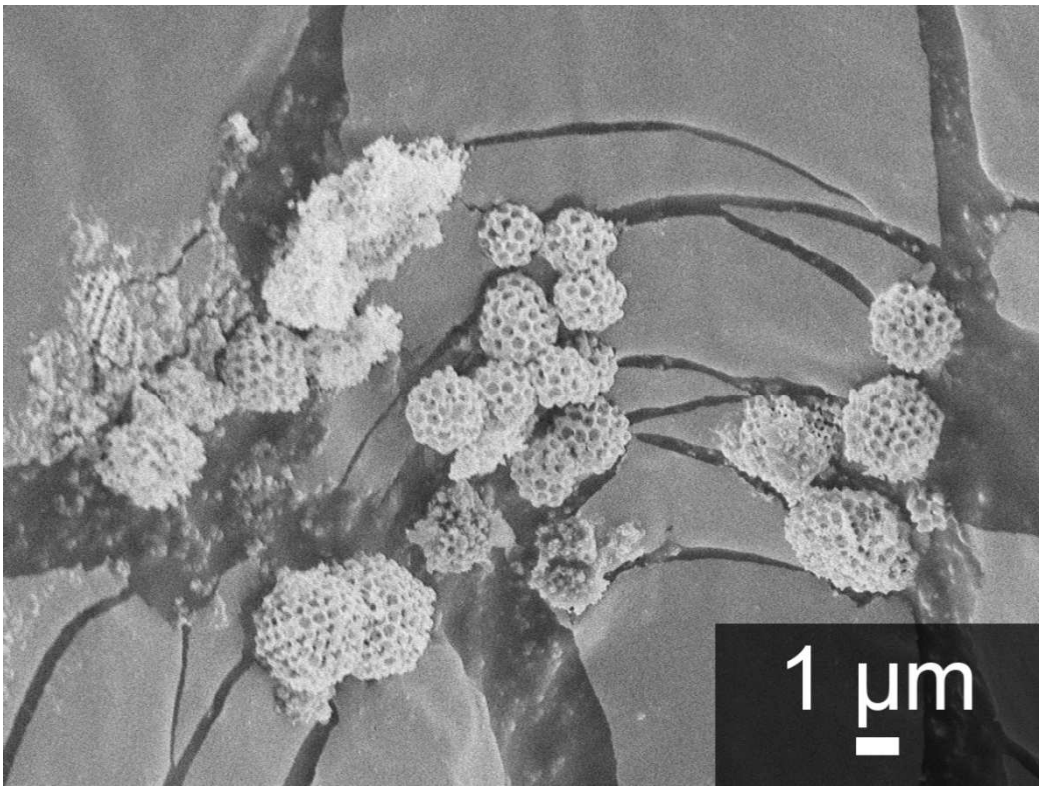

Figure 4.4. SEM image of "211" $Ce_{0.5}Mg_{0.5}O_{1.5}$ microspheres after resuspension in water and vortex stirring for 15 minutes. The suspension was dispersed on a stub, dried, coated with 5 nm of Pt, and then imaged. The smooth, cracked background is the carbon adhesive on the SEM stub.

4.3.2 Effects of Alkaline Earth Metals in Solid Solutions with CeO_2

The spherical structures were initially observed in systems containing solid solutions with alkaline earth metals. We investigated the effect of changing the cation used, specifically by adding Sr, Ca, or Mg, with otherwise identical EG:CA:TMI ratios. Results are shown in Figure 4.5. Microspheres were observed in 3:1:1 $Ce_{0.5}Sr_{0.5}O_{1.5}$, which also contained a substantial amount of $SrCO_3$ as a second phase (Figure 4.5a). This phase resulted from the presence of carbon from the organic components and a calcination

temperature that was lower than the decomposition temperature of $SrCO_3$. Similarly, the 3:1:1 $Ce_{0.5}Ca_{0.5}O_{1.5}$ sample contained $CaCO_3$ (calcite) as a second phase, but few discernible microspheres were present; rather, this material consisted of a hierarchically-structured network with irregular voids surrounding patches of 3DOM material (Figure 4.5b). While perhaps less aesthetically pleasing, the observation of this structure is critically important in later discussion of the mechanisms of formation for these structures. $Ce_{0.5}Mg_{0.5}O_{1.5}$, on the other hand, formed similar microstructures to the Ce–Sr solid solutions while remaining nearly phase pure (Figure 4.5c), due to the fact that magnesium carbonate decomposes below the calcination temperature of 450 ˚C. As such, this material ($Ce_{0.5}Mg_{0.5}O_{1.5}$) was used as the platform for further exploration of the synthesis parameters and their relation to microstructural evolution in the materials.

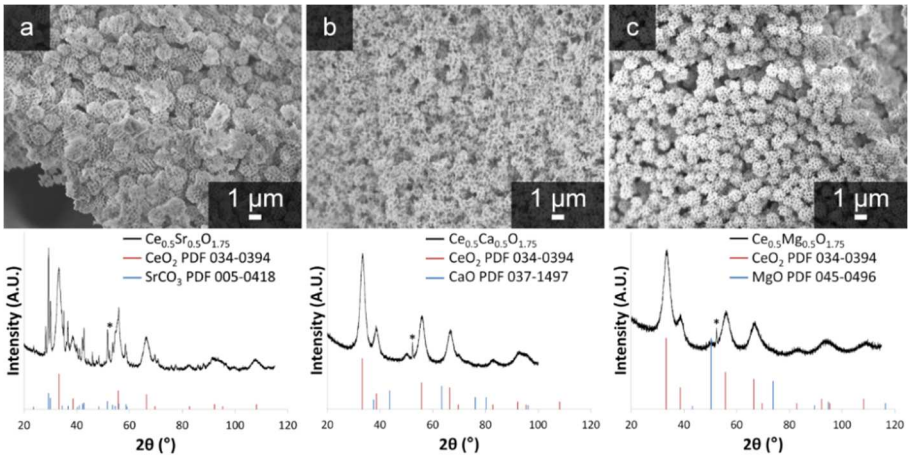

Figure 4.5. SEM images and XRD patterns for ceramic powders derived from Pechini gels at the 3:1:1 (EG:CA:TMI) composition. (a) The $Ce_{0.5}Sr_{0.5}O_{1.5}$ sample consisted of microspheres approximately 1–2 µm in diameter, and contained a substantial amount of $SrCO_3$. (b) The $Ce_{0.5}Ca_{0.5}O_{1.5}$ product showed little evidence for microspheres but formed a solid solution. (c) The $Ce_{0.5}Mg_{0.5}O_{1.5}$ product consisted of slightly smaller microspheres than the $Ce_{0.5}Sr_{0.5}O_{1.5}$ sample, but also formed a solid solution. The sharp peak at 52.3 ˚2θ (*) is from the Al sample holder.

4.3.3 Effects of Gel Components on $Ce_{0.5}Mg_{0.5}O_{1.5}$

The Pechini process (Figure 4.1) involves chelation of metal cations by CA to form complexes. These complexes are then linked together by an esterification reaction with EG, gradually forming a gel within aqueous or alcoholic solutions. The concentration of each of these components has an impact on the resulting polyesterification. The extent of polymerization is controlled by the amount of EG relative to CA. CA controls the extent of chelation, which directly influences the degree of metal incorporation in the gel. With a low fraction of CA:TMI (less than 1:1), free metal ions remain, which will not be contained by the gel network, limiting the extent of polymerization and potentially leading to reprecipitation of the salt after drying. At high concentrations of CA, multiple CA molecules can chelate single cations,[231] which may alter the charge of complexes and degree of branching during polymerization, i.e., with greater coordination, complexes are less positively charged or potentially negative, and can be branched more easily, as there are more available carboxylic acid sites per cation.

Related to this discussion, it is interesting to note that $Ce_{0.5}Ca_{0.5}O_{1.5}$ did not form microspheres under the conditions examined. The only functional difference between the Ca and Mg cations is ionic radius, which affects the acid stability constant for citrate complexes of each ion. The stability constant is considerably higher for Ca (log K = 3.5) than Mg (log K = 3.2) and Sr (log K = 2.8).[87] Considering that the precursor solutions are at low pH (1–2), this may suggest that it is in fact slightly-deficient chelation which may be a requirement for the generation of microspheres (see also later discussion).

Upon adjusting the EG concentration within the $Ce_{0.5}Mg_{0.5}O_{1.5}$ synthesis, the size of the spheres changes substantially (Figure 4.6a–c). Particle size distributions (as measured from the SEM images) can observed in Figure 4.7.

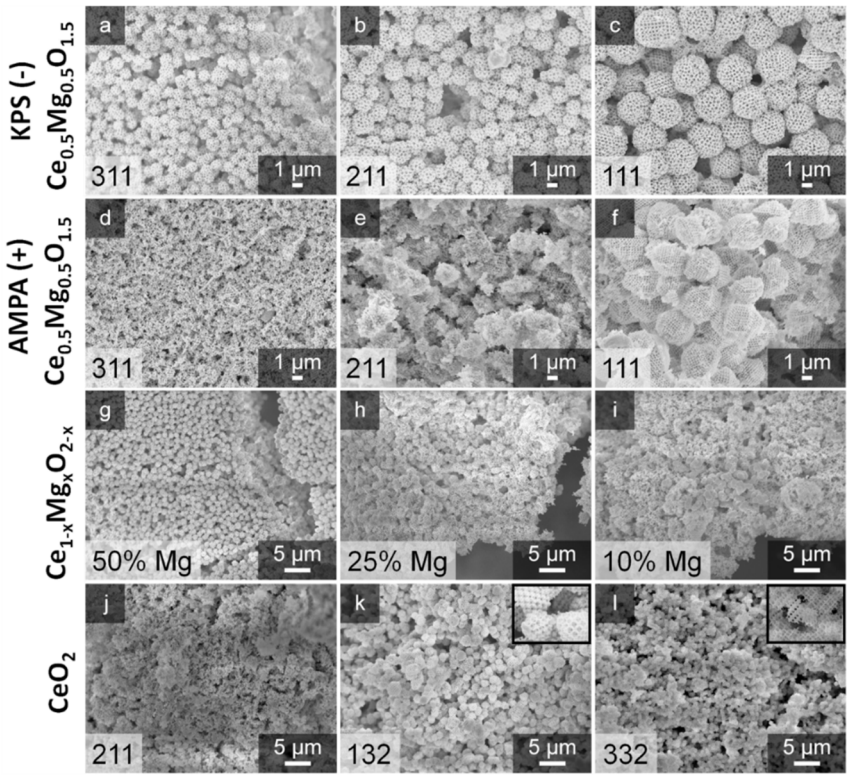

Figure 4.6. (a–c) SEM images demonstrating size control in 3DOM microspheres of $Ce_{0.5}Mg_{0.5}O_{1.5}$ templated with a KPS-initiated PMMA CCT (negative surface charge). (a) 3:1:1 CeMg, average sphere diameter 1.00 ± 0.16 µm. (b) 2:1:1 CeMg, average sphere diameter 1.55 ± 0.27 µm. (c) 1:1:1 CeMg, average sphere diameter 2.91 ± 0.43 µm, average macropore spacing 353 ± 4 nm. (d–f) SEM images of $Ce_{0.5}Mg_{0.5}O_{1.5}$ templated with an AMPA-initiated PMMA CCT (positive surface charge). (d) 3:1:1 $Ce_{0.5}Mg_{0.5}O_{1.5}$ shows no evidence of spheres. (e) 2:1:1 $Ce_{0.5}Mg_{0.5}O_{1.5}$ consists of a bicontinuous network with embedded spheroids. (f) 1:1:1 $Ce_{0.5}Mg_{0.5}O_{1.5}$ shows microspheres similar to what was observed with the KPS-initiated PMMA template, but with less regularity in the spheres and extensive polydispersity, average macropore spacing 268 ± 5 nm. (g–i) SEM images of 2:1:1 Ce-Mg oxides with decreasing Mg content. (j–l) SEM images of a phase-pure CeO_2 system. (j) 2:1:1 CeO_2, no microspheres are observed, but a network with hierarchical porosity is present. (k) 1:3:2 CeO_2, average sphere diameter 1.68 ± 0.30 µm. (l) 3:3:2 CeO_2, average sphere diameter 1.06 ± 0.21 µm. Insets on (k) and (l) show these spheres at higher magnification. Samples shown in (g–l) were prepared with a KPS-initiated PMMA CCT.

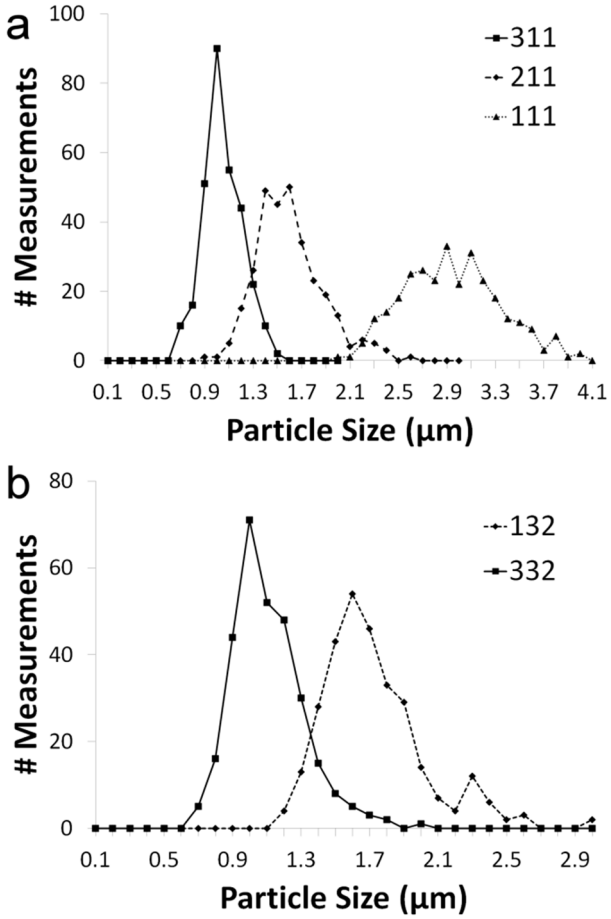

Figure 4.7. Histograms of microsphere sizes of the following samples: (a) "311", "211", and "111" $Ce_{0.5}Mg_{0.5}O_{1.5}$, (b) "132" and "332" CeO_2.

As the EG concentration increases, the sphere size decreases. It is interesting to note that the decrease occurs in direct proportion to the EG:TMI ratio (i.e., doubling the EG content halves the size of the spheres, increasing the EG content by 3/2 yields spheres 2/3 the size). In order to properly interpret these results, we have to take a closer look at the mechanisms of microstructural evolution in sol-gel systems.

Generation of microstructure in sol-gel materials occurs predominantly along two distinct pathways (Figure 4.8a).[207] In the first case, small spherical particles consisting of

larger oligomers nucleate within the precursor solution, and then gradually grow as they draw more reagents from the solution. Eventually, these growing spheres begin to recombine and fuse, forming a dense gel network. In the second case, a bicontinuous system arises uniformly throughout the structure via spinodal decomposition, due to growing differences in properties (polarity, viscosity, charge) between the two phases during gelation. This bicontinuous system can further decompose to form individual spheroids or oblong particles with high polydispersity and less regularity in shape than nucleated particles. The particular pathway followed is determined by the position on the phase diagram of the precursor sol (Figure 4.8b).[207]

With different Pechini gel compositions (i.e., different concentrations of EG, CA and metal ions), a variety of microstructures were obtained, which yield insight into the mechanism behind the formation of these microspheres. The two structure types mentioned above can be observed under two distinct regimes in the synthesis of $Ce_{0.5}Mg_{0.5}O_{1.5}$ (Figure 4.5b). When the ratio of CA to metal ions exceeds 1:1, microstructure evolution appears to progress by the spinodal decomposition route, with varying degrees of progression, dependent on EG and CA concentrations. When the ratio is 1:1, however, microspheres are observed, with morphology indicative of the nucleation/growth pathway. The degree of chelation within the material clearly has a substantial effect on the mechanism of growth.

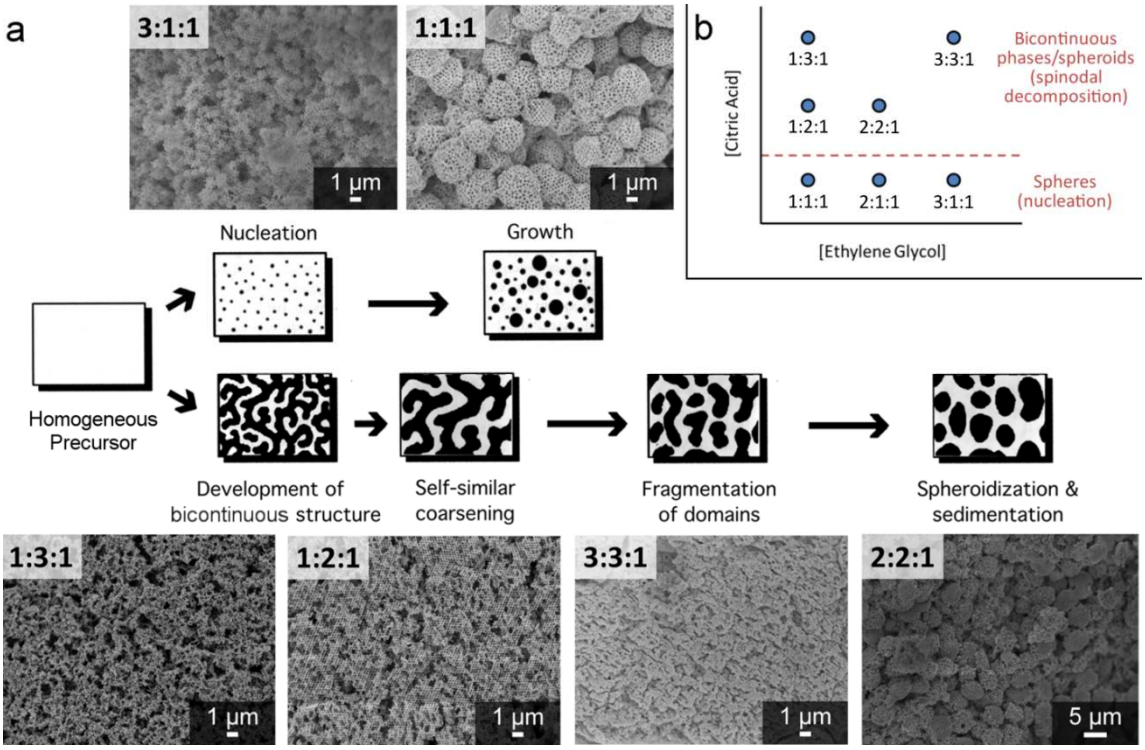

Figure 4.8. (a) SEM images of Pechini-derived Ce-Mg oxides with varying EG and CA content and differing microstructure. Images are denoted by the molar ratios of components within the precursor in the form EG:CA:TMI. Gel compositions with a 1:1 ratio of CA:TMI (x11) form spheres at different levels of growth based on the ethylene glycol content. Gel compositions with higher ratios of CA:TMI (X21, X31) result in bicontinuous networks (3DOM material interspersed with void space) in varying extents of spinodal decomposition. Scheme at center adapted from Ref. [207]. (b) Graph of precursor compositions for $Ce_{0.5}Mg_{0.5}O_2$ materials depicted in (a) by EG and CA content, normalized to TMI.

Considering Figure 4.6 in this light, with high EG:CA ratios (Figure 4.6a), sphere growth appears to be limited, whereas more growth is observed at ratios approaching 1:1 (Figure 4.6c). The logical source of this morphological change is not a "limitation" of sphere growth *per se*, as the extent of reaction remains unaffected by excess reactant, but rather an increase in nucleation sites under high ethylene glycol concentrations. For

condensation, or "step-growth" polymerizations like polyesterification, stoichiometric monomer imbalance has a strong effect on molecular weight of the resultant polymers. The greater the imbalance, the lower the molecular weight for the same extent of reaction.[116] To illustrate: in our system, when EG is in excess, it becomes statistically more likely that any free citrate complexes will react with an EG monomer rather than an EG-terminated oligomer. Thus, more short-chain oligomers are formed than in a system with balanced reactants, yielding a greater number of shorter chains overall when the reaction reaches equilibrium. With an equal number of functional groups present, growing chains have equal access to the EG and CA functionalities, resulting in longer chains. As long as the average chain length becomes high enough to cause the polymer to precipitate out of solution (i.e., yielding formation of a microsphere), we propose that the average size of the microspheres should reflect the extent of polymerization.

It should also be noted that as the reaction progresses, oligomer-oligomer condensation reactions become more likely. However, the extent of reaction is also controlled by the water present in the system, as water is a product of the esterification reaction. When vials are left loosely capped, extended 3DOM structures are obtained rather than microspheres or hierachical bicontinuous networks (Figure 4.9). The loss of water shifts the equilibrium of the system further to the product side (Figure 4.1), causing chains (spheres) to link together and combine, forming a largely continuous structure.

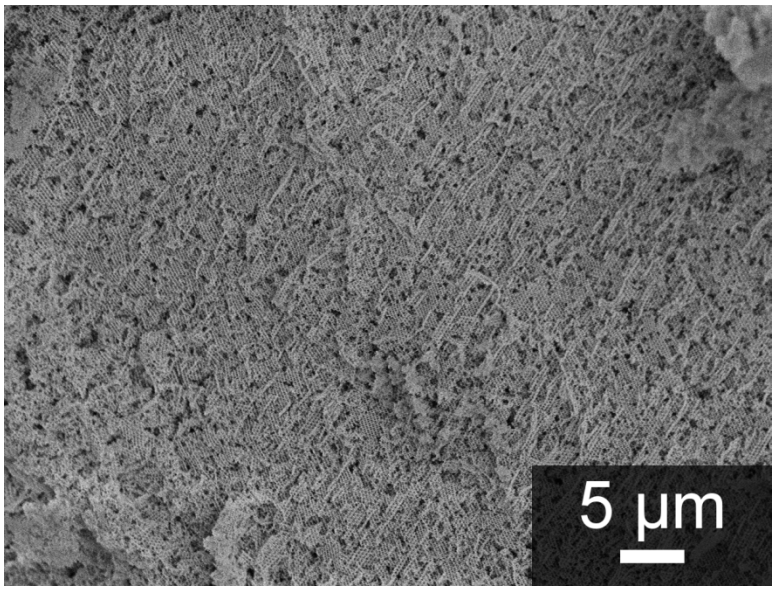

Figure 4.9. SEM image of "111" $Ce_{0.5}Mg_{0.5}O_{1.5}$ synthesized with a loosely capped vial to permit slow escape of water. The "filling" of 3DOM material is much higher, so that fewer non-templated regions are present than in syntheses where water is retained in the vial.

4.3.4. Confinement and Charge Effects

The effects of confining the polymerization process within the CCT and those of the surface charge of the CCT on the resulting microstructure were also investigated. When the materials are prepared in the absence of a template, completely dissimilar, largely disordered morphologies and no microspheres are observed (Figure 4.10). It is clear that the template plays a significant role in the formation of these microstructures, at least under the precursor conditions tested. Considering the physical nature of the CCTs, two likely factors emerge: first is the simple physical effect of confining the precursor within the colloidal crystal, and the capillary forces acting on the liquid as a result. The

second factor is the surface charge present on the PMMA spheres themselves, which arises from charged initiator molecules embedded in and on the spheres.

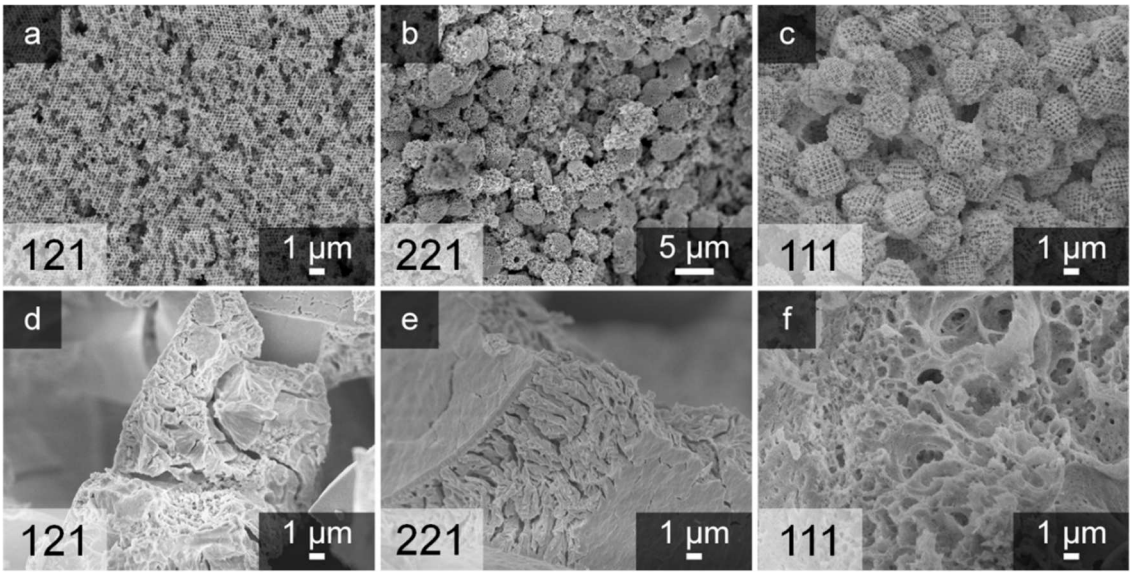

Figure 4.10. SEM images of templated (KPS-PMMA) (a–c) and untemplated (d–f) Pechini gel-derived Ce-Mg oxides after calcination. (a) and (d) "121" $Ce_{0.5}Mg_{0.5}O_{1.5}$. (b) and (e) "221" $Ce_{0.5}Mg_{0.5}O_{1.5}$. (c) and (f) "111" $Ce_{0.5}Mg_{0.5}O_{1.5}$. None of the untemplated materials display similar microstructure to the templated ones, despite having the same gel composition and identical processing.

The emulsifier-free emulsion polymerization employed to produce these CCTs depends on the use of water-soluble initiators. These initiators produce charged functional groups on the surface of the PMMA spheres. All of the materials discussed thus far were generated with KPS-initiated spheres, with negative surface charge. Figure 4.6d–f shows the 3:1:1/2:1:1/1:1:1 series generated using AMPA-initiated spheres with a positive surface charge. This series is analogous to that shown in Figure 4.6a–c for KPS-initiated templating spheres. Switching the charge on the spheres substantially changes the behavior of the precursor during gelation, as evidenced by the lack of spheres in the

3:1:1 and 2:1:1 samples. The 1:1:1 material developed spheres, but had extremely high polydispersity, as different areas within the sample revealed spheres of greatly differing diameters. These observations lead to the conclusion that electrostatic interactions between the gel phase and the template influence the product morphology over extended length scales.

Above, we investigated the relationship of the CA:TMI ratio on the microstructure. Given the considerable effect of template charge on the system (the charge of which would be predominantly controlled by the degree of chelation), it was necessary to further clarify this relationship. By changing the relative proportions of cation types within the precursor solution, we were able to modify the average cation charge without affecting the CA:TMI ratio. For $Ce_{0.5}Mg_{0.5}O_{1.5}$, the average charge of metal ions in the precursor solution is +2.5. When the precursor contains progressively lower Mg^{2+}/Ce^{3+} ratios (increasing average cation charge, approaching +3) while holding the other synthesis parameters constant, the spheres initially observed at the 50 mol% ratio gradually disappear (Figure 4.6g–i), and a bicontinuous network is generated instead.

4.3.5. Single-Cation CeO_2 Materials

The question remains, then, how do we generate microspheres of the pure CeO_2 material? What we have observed here is that the alkaline earth metal additives alter the electrostatic environment of the precursor, making it more conducive to the production of microspheres. We can draw an analogy to the field of block copolymer emulsions, in which mesostructure is highly dependent on equilibria determined by initial reagent concentrations. Different structures can be obtained by changing the concentration of

polymer, water, and oil phases within an emulsion. Here we have a similar phase diagram, but with concentrations of EG, CA, and ion charge being the determining factors. If one is changed, the others can be adjusted to compensate.

Following this logic, we found that microspheres can be generated in the pure CeO_2 material by shifting the citric acid concentration to higher values, but approximately in the same proportion to the average cation charge. In the $Ce_{0.5}Mg_{0.5}O_{1.5}$ system, the molar ratio of CA to charge was 2:5. Based on the results shown in Figure 4.8, a "sweet spot" exists for sphere generation around this ratio. When pure CeO_2 (Figure 4.11) was prepared using identical gel compositions to $Ce_{0.5}Mg_{0.5}O_{1.5}$ syntheses that produced spheres (Figure 4.6j), no microspheres were observed.

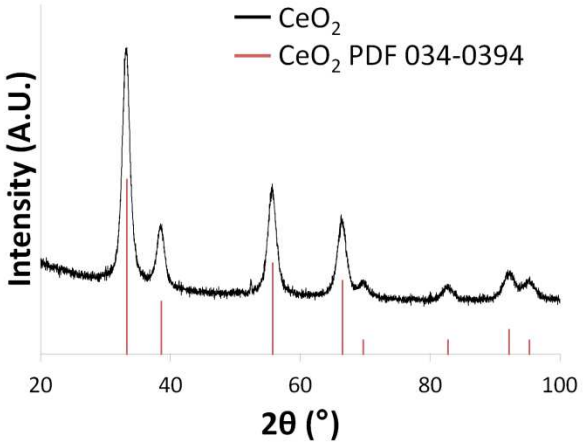

Figure 4.11. PXRD pattern of CeO_2 microspheres synthesized with no magnesium. Aside from peak broadening due to the nanocrystalline nature of the product, an exact match for the CeO_2 literature pattern is observed.

Here the ratio of CA:average cation charge is low, around 1:3 (1 mol CA : 1 mol Ce^{3+}). When this was increased to 1:2 (3 mol CA : 2 mol Ce^{3+}), microspheres consisting

of pure CeO_2 were formed (Figure 4.6k). The system functions identically to the $Ce_{0.5}Mg_{0.5}O_{1.5}$ preparations; modifying ethylene glycol concentration allows for control of microsphere size in the same fashion (Figure 4.6l). Sphere sizes for the 1:3:2 and 3:3:2 syntheses were 1.68 ± 0.30 μm and 1.06 ± 0.21 μm respectively; polydispersities of these spheres were slightly higher than for $Ce_{0.5}Mg_{0.5}O_{1.5}$ spheres of similar size, at 17% for the 1:3:2 and 20% for the 3:3:2 (Figure 4.7).

4.4 Conclusions

3DOM microspheres and bicontinuous networks with hierarchical porosity were produced both as alkaline earth metal–CeO_2 solid solutions, as well as pure CeO_2, through careful tuning of the Pechini precursor components. Reasonably low polydispersities, in the range of 10–15%, were found for $Ce_{0.5}Mg_{0.5}O_{1.5}$ microspheres. The average diameter of the microspheres was related to the extent of polymerization in the gel, and thus could be directly changed by altering the stoichiometric balance of monomers in the mixture. Meanwhile, the overall morphology of the structure (bicontinuous network or microspheres) was determined by the amount of chelating agent present in the precursor, and structures observed were analogous to those obtained via phase separation in alkoxysilane syntheses. The mechanism of structure formation (nucleation and growth vs. spinodal decomposition) could be adjusted; a nucleation–growth mechanism was predominantly observed when the molar ratio of CA to overall cation charge was between 2:5 and 1:2; spinodal decomposition was observed outside this range. The presence of the CCT was also a determining factor in the formation of microstructure; without it, the above-mentioned effects were not observed. We expect

that these structures can be generated with other metal ions that are chelated by citric acid, allowing for other ceramics to be accommodated through careful, rational adjustment of Pechini gel constituents. The compositional space accessible by this method will be probed in ongoing research. Future experiments will also focus on time-resolved characterization of the chelation and gelation behavior *in situ*, which could yield even more powerful control over ceramic morphology, from a technique that is both inexpensive and scalable.

4.5 Acknowledgements

Portions of this work were carried out in the University of Minnesota Characterization Facility which receives partial support from the NSF through the MRSEC, ERC, MRI, and NNIN programs.

Synthesis of the materials presented in this chapter was strongly supported by two very talented undergraduate researchers, Nicholas Hein and Denis Terzic.

Chapter 5: Generalizing Pechini-Based Polymerization-Induced Phase Separation

5.1 Introduction

Porous metal-oxides are of great importance to a variety of chemical processes and technologies. In particular, hierarchical structures incorporating both μm-scale and nanoscale features allow for increased surface area while maintaining open access to that surface area via controlled microstructure.[202] This is an advantage in applications such as heterogeneous catalysis,[2, 232, 233] and fuel cells[172, 234-236] where mass transfer and chemically accessible surface area dominate efficiency.[237] Additionally, spatial isolation of ceramic structural features through the introduction of void space has been shown to reduce sintering behavior in high temperature reactions.[208] Chromatography column efficiency can be improved by incorporating microstructured matrices.[42] Considering the above examples, the discovery, exploration, and optimization of chemical routes to porous ceramic particles with defined internal and external shapes and sizes are of interest to many different technical fields.

The sol-gel method is often used to synthesize metal-oxide ceramics, owing to its versatility and relative ease of synthesis.[79, 238, 239] Within this general scheme of preparing a solution, condensing it into a gel, and calcining to obtain the final product, structure-

modifying techniques such as hard[203, 215] and soft templating[240-242] can be employed to create porosity on differing length scales. In addition to incorporating internal pore structure via hard templating, it is sometimes possible to control the external shape of the porous products at the micrometer scale. For example, shaped CuO particles possessing a network of ordered pores have been synthesized by electrodeposition inside a colloidal crystal template (CCT) by modifying deposition conditions and electrolyte choice.[243] Sheets and other microstructures have been introduced to electrodeposited macroporous ZnO by modifying colloidal crystal surface chemistry or adding surfactants.[244] Other three-dimensionally ordered macroporous (3DOM) particles have been generated by growing single crystals within a CCT,[245] with the resultant particle shapes determined by the crystal shape.[225]

A convenient method of generating micrometer-scale structures within sol-gel precursors is polymerization-induced phase separation (PIPS). Originally discovered in sol-gel syntheses of silica using silicon alkoxides,[246] PIPS occurs due to the growing dissimilarities (polarity, electrostatics, viscosity) between a polymerizing silica gel and its solvent. These dissimilarities cause a gradual phase separation of the silica oligomers, which produces micrometer-scale solvent-rich and silica-rich regions within the precursor. By tailoring the reaction rate and equilibrium state[247] of the silica formation process, microstructures present at different points during the gelation of the precursor can be "locked in" and realized in the final structure obtained after calcination. The target structures can be modified in shape and size by changing gelation temperatures and reaction times, as well as the choice of reagents and their molar ratios. Changing the

silicon alkoxide concentration, adding methanol or ethanol to the aqueous solvent to modify its polarity,[247] increasing the acidity of the solvent,[247] and adding hydrophilic polymers to the system[94, 248] all have substantial effects on the resulting microstructure.

Recently, we demonstrated that morphologies very similar to those observed in these silica systems could be obtained in Pechini-type syntheses of 3DOM $Ce_{0.5}Sr_{0.5}O_{1.5}$, $Ce_{0.5}Mg_{0.5}O_{1.5}$, and CeO_2.[209] The Pechini method[88] is a sol-gel technique for forming metal-oxide ceramics with small crystallite sizes and (in the case of solid solutions) homogeneity. It involves the formation of a metal-carboxylic acid complex, typically with citric acid (CA), and then a polymerization of those complexes with a polyol such as ethylene glycol (EG) to form a metal-laced polyester. The primary advantage of this method is that the metal cations, bound to the polymer, remain isolated from each other and do not aggregate or produce crystalline products prior to the burnout of the polyester. This leads to the smaller, atomically homogeneous crystallites mentioned above.

In Chapter 4, I demonstrated that these chelate-controlled sol-gel reactions carried out in the confinement of a colloidal crystal template yield materials whose morphologies are, in part, controlled by interactions with the template but on a length scale beyond that of individual colloids in the template.[209] In particular, using examples of solid solutions based on cerium oxide, Idemonstrated the formation of uniform macroporous microspheres or bicontinuous structures with hierarchical porosity. In the microspheres, the macropores were molded by the CCT, but the external spherical shape derived from confined nucleation and growth during step-growth polymerization of the precursor gel. The hierarchically structured materials, on the other hand, resulted from spinodal

decomposition of the gel phases within the CCT. However, several open questions remained relating to the effect of the extent of polymerization of the metal-laced polyester on microstructure, the role of the cations in the generation of microstructure, and the applicability of the technique to non-Ce-based metal-oxides.

Here I address these open questions and deepens our understanding of PIPS in templated Pechini gels. I employ a number of synthetic strategies and modifications for ceria-based systems to probe the effects of electrostatics, gel molecular weight, cation charge and oxidation state, and precursor-template interactions on PIPS-induced morphology. In addition, I demonstrate the wider applicability of morphology control by PIPS in colloidal crystal templates with two test cases: Fe_2O_3 and Mn_3O_4 systems.

5.2 Experimental

5.2.1 Materials & Reagents

Cerium(III) nitrate hexahydrate (99%), cerium(III) chloride heptahydrate (99%), citric acid monohydrate (99.5+%, ACS grade), manganese(II) nitrate tetrahydrate (97%), DL-malic acid (99%), and methyl methacrylate (99%) were obtained from Sigma-Aldrich; potassium persulfate (KPS, 99.9%), iron(III) nitrate nonahydrate (99.6%), and glycerin (99.7%) from Fisher Scientific; magnesium nitrate hexahydrate (99%) from General Chemical Corporation; and ethylene glycol (99+%) from Mallinckrodt Chemicals. All reagents were used as received. De-ionized water (>18 MΩ·cm), filtered on-site, was used in all syntheses.

5.2.2 Template Synthesis

CCTs were synthesized through emulsifier-free emulsion polymerization of methyl methacrylate to produce colloidal poly(methyl methacrylate) (PMMA) spheres, followed by gravity sedimentation of those spheres into face-centered cubic (fcc) arrays.[174] KPS was used as an initiator. Diameters of PMMA spheres were varied by adjusting the amount of KPS and the amount of water in the synthesis. Three sets of spheres were obtained, with the following diameters and standard deviations: 362 ± 3 nm, 395 ± 3 nm, and 489 ± 4 nm. The polymerization produced aqueous colloidal dispersions containing ca. 20 wt% PMMA, which were then poured into crystallization dishes, covered with aluminum foil, and sedimented to form the CCTs.

5.2.3 Synthesis of Porous Microspheres and Bicontinuous Networks

Precursors were prepared by dissolving a metal nitrate salt (M^{q+}), CA, and EG in water. The metal nitrates used were $Fe(NO_3)_3 \cdot 9H_2O$, $Mn(NO_3)_2 \cdot 4H_2O$, $Ce(NO_3)_3 \cdot 6H_2O$, and/or $Mg(NO_3)_2 \cdot 6H_2O$. For one experiment, $Ce(NO_3)_3 \cdot 6H_2O$ was replaced with $CeCl_3 \cdot 7H_2O$. The water:total metal ion (TMI) molar ratio was kept constant at 36:1. The molar ratios of EG:CA:TMI in the precursor were varied to produce different samples, which are designated by these ratios in the form M_xO_y XYZ. Some samples were produced by substituting malic acid for CA, and glycerin for EG.

The precursor solutions were infiltrated into CCTs and heat-treated at 90 °C for 24 h in tightly sealed glass vials, causing the precursor to form a hard gel within the template. Different gelation temperatures were used for some samples to investigate morphological

effects. Once gelled, the samples were calcined in a tube furnace under static air at 310 °C and 450 °C (2 °C/min ramp, 2 h dwell time at each temperature).

5.2.4 Characterization

The morphology of the materials was examined using scanning electron microscopy (SEM). The powders were mounted on stubs with carbon tape and subsequently coated with 50 Å of Pt, then imaged on a JEOL 6700 electron microscope. Size measurements were performed using ImageJ software (NIH). Sphere sizes (where applicable) were averaged from 100 individual measurements for each sample. Powder X-ray diffraction (XRD) patterns of materials were obtained using an X'Pert Pro diffractometer outfitted with an X'Celerator detector and a Co anode (Kα, λ = 1.789 Å) operated at 45 kV and 40 μA.

5.3 Results and Discussion

5.3.1 Overview of Structures and Morphologies Observed

SEM images of the materials synthesized by combining the Pechini method with colloidal crystal templating reveal a variety of microstructural features. These features can be grouped into a series of categories, including microspheres, spheroids, bicontinuous materials, dense networks, and lamellar structures (Table 5.1). Materials defined as "microspheres" contain spherical objects with macropores derived from the PMMA template. Depending on the precursor composition, spheres may have different sizes and may interconnect. In a few compositions, the distinct objects are not regularly spherical and are then denoted as "spheroids". The microsphere morphology is the primary target of this investigation for two reasons. First, the microspheres are

comparatively easier to characterize in shape and size, allowing for more quantitative comparisons between differing precursor and metal-oxide compositions. Second, the number of precursor compositions that produce microspheres is limited, indicating a degree of precision required to control sample morphology.

"Bicontinuous network" refers to structures in which two interpenetrating phases are present (i.e., 3DOM material with templated pores and void spaces not defined by the hard template), where the two phases appear to be fully interconnected. The bicontinuous networks come in two varieties, "wormlike" and "chunks" depending on the structure of the 3DOM material. The terms "open" and "dense" are used to qualitatively describe the ratio of porous solid to void space that is not templated by the CCT, "open" structures having more void space, and "dense" structures having more solid material. Bicontinuous networks are typically observed with precursor compositions that deviate slightly from those that produce microspheres. Bicontinuous networks are the secondary target of this investigation, as they represent a class of structures with hierarchical porosity. A large number of compositions produce structures of this type, but due to the non-uniform nature of the network morphology and the differing ratios of porous solid to untemplated void space, it is more difficult to measure the features of these structures and make meaningful quantitative comparisons between samples.

"Dense network" refers to structures that are mostly filled with porous solid and do not contain additional precursor-induced microstructural variation. These are the typical 3DOM structures or inverse opal structures that are normally targeted by colloidal crystal templating methods. However, some of these dense networks contain micrometer-scale

holes that are not continuous; these holes likely arise from precursor effects (PIPS) rather than incomplete infiltration of the CCT. In addition some unique structures are obtained in narrow regions of phase space, including a lamellar structure, but the categories of microspheres, bicontinuous networks, and dense networks serve to describe the vast majority of structures observed in this work.

Table 5.1. List of materials synthesized by composition, with a description of product morphologies.

Cation	Composition	Morphology
Ce+Mg	111	Microspheres, diameter ~2.9 μm
Ce+Mg	211	Microspheres, diameter ~1.9 μm
Ce+Mg	311	Microspheres, diameter ~1.0 μm
Ce+Mg	121	Bicontinuous network, dense wormlike
Ce+Mg	221	Small, interconnected microspheres
Ce+Mg	411	Small, interconnected microspheres
Ce+Mg	131	Bicontinuous network, open wormlike
Ce+Mg	133	Large microspheres (> 5 μm), untemplated exterior
Ce+Mg	331	Bicontinuous network, chunks
Ce	132	Microspheres, diameter ~1.7 μm
Ce	232	Microspheres, diameter ~1.5 μm
Ce	332	Microspheres, diameter ~1.1 μm
Ce	111	Bicontinuous network, holey monolith
Ce	211	Bicontinuous network, holey monolith
Ce	311	Bicontinuous network, interconnected spheroids
Ce	221	Bicontinuous network, dense wormlike
Ce	312	Bicontinuous network, chunks
Ce	314	Bicontinuous network, chunks
Ce	321	Microspheres, diameter ~ 1.3 μm
Ce	121	Large spheroids separated along CCT “facets”
Ce	114	Bicontinuous network, chunks
Mn	132	Bicontinuous network, dense wormlike
Mn	221	Bicontinuous network, dense wormlike
Mn	211	Bicontinuous network, open wormlike
Mn	341	Microspheres, diameter ~1.6 μm
Mn	441	Network of interconnected spheres
Mn	421	Dense network, holes
Mn	321	Bicontinuous network, dense wormlike
Mn	331	Bicontinuous network, dense wormlike
Mn	521	Bicontinuous network, open chunks
Mn	123	Bicontinuous network, chunks
Mn	361	Bicontinuous network, chunks
Mn	721	Large, interconnected spheroids (>3 μm)
Mn	411	Hollow spheres
Mn	611	Hollow spheres
Mn	711	Hollow spheres
Fe	111	Bicontinuous network, chunks
Fe	112	Microspheres, diameter ~0.7 μm
Fe	113	Microspheres, diameter 1.6 μm
Fe	213	Dense network, holes
Fe	223	Bicontinuous network, wormlike
Fe	1–0.5–3	Bicontinuous network, wormlike
Fe	313	Lamellar structure
Fe	216	Bicontinuous network, dense wormlike
Fe	1–1.5–3	Bicontinuous network, wormlike
Fe	214	Bicontinuous network, open wormlike
Fe	314	Bicontinuous network, open wormlike
Fe	126	Bicontinuous network, open chunks
Fe	415	Small interconnected microspheres (~0.5 μm)
Fe	615	Small interconnected microspheres (~0.5 μm)
Fe	114	Bicontinuous network, open wormlike
Fe	122	Bicontinuous network, dense wormlike
Fe	322	Bicontinuous network, open chunks
Fe	613	Dense network, holes

In Chapter 4, I observed morphological variations arising from Pechini method syntheses of CeO_2 and the mixed oxide $Ce_{0.5}Mg_{0.5}O_{1.5}$ using CA as a complexing agent and EG as a cross-linker.[209] These metal-oxide compositions have a relatively large region in phase space that yields microspheres and spheroids of different sizes. Given this broad "phase space" available for the generation of microspheres and bicontinuous networks with these compositions, we examined the effects of a variety of reagent substitutions on microstructures in greater detail.

5.3.2 Molecular Weight, Stoichiometric Balance, and Morphology

Pechini gels are step-growth polyesters formed by a condensation reaction between EG and CA. The relationship between the extent of reaction during gelation processes and the relative ratio of monomers has been described in detail in the literature on step polymerization.[249] Specifically, the degree of polymerization $\bar{X}_n$ (the number-average value of monomer units present in the products of a polymerization reaction) is given by Carothers equation $\bar{X}_n = \frac{2}{2-pf_{avg}}$ for stoichiometric amounts of reactants, where p is the extent of the reaction, $f_{avg} = \frac{\sum N_i f_i}{\sum N_i}$ and N_i is the number of molecules of monomer i with functionality f_i. For nonstoichiometric reaction mixtures, the relationship becomes more complex because the extent of polymerization is limited by the deficient reactant, and the excess reagent lowers the functionality of the system.

To demonstrate the relationship of the degree of polymerization, and thus, molecular weight, to the microstructure observed, a series of samples were produced using different conditions, but the same molar ratios in the precursor. These compositions, $Ce_{0.5}Mg_{0.5}O_{1.5}$ 211 and CeO_2 132, were selected because they are known to produce microspheres of

moderate size, allowing facile detection of structural changes both small (e.g., microsphere diameter) and large (e.g., formation of bicontinuous networks).

The condensation reaction to form the pre-ceramic metal-laced polyesters is activated by heat. A simple experiment to observe the dependence of structure on molecular weight is to see how the structure changes with different gelation temperatures (Figure 5.1). The degree of polymerization is proportional to the polymerization rate constant (itself a temperature dependent value),[116] and so a slight reduction in gel temperature from 90 °C to 80 °C and shortened gelation time results in a substantial reduction in sphere size, from 1.60 ± 0.11 μm to 0.58 ± 0.08 μm (Figure 5.1b). Meanwhile, greater reductions in temperature result in a loss of the sphere morphology, and the production of a more monolithic 3DOM structure with isolated void spaces (Figure 5.1c).

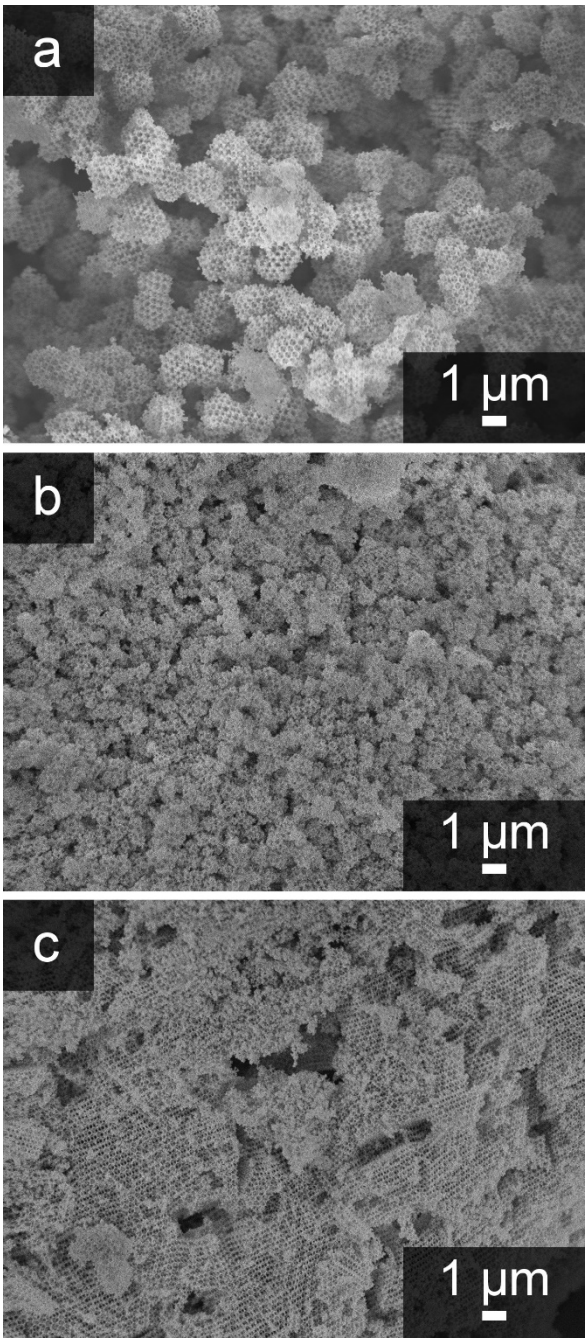

Figure 5.1. SEM micrographs of CeO_2 132 treated at (a) 90 °C for 24 h, (b) 80 °C for 16 h, and (c) 40 °C for 24 h. These samples were prepared using 489 nm PMMA spheres in the CCT and a nitrate precursor.

The final molecular weight distribution obtained depends on the balance of monomer "end groups," in this case, the balance of carboxylate to hydroxyl moieties. To modify the molecular weight of the gel without substantially changing the molar ratios of organic components to metal to water, CA and EG can be substituted with other polycarboxylic acids and polyols. In this study, we used the $Ce_{0.5}Mg_{0.5}O_{1.5}$ 211 precursor composition, but substituted CA for malic acid and EG for glycerin (Figure 5.2) in order to modify the number of reactive groups available for esterification without changing the organic, metal ion, and water molar ratios. This demonstrated drastic changes in morphology as they relate to functional group balance, indicating that the degree of polymerization controls not only microsphere size, but also the morphology of the material.

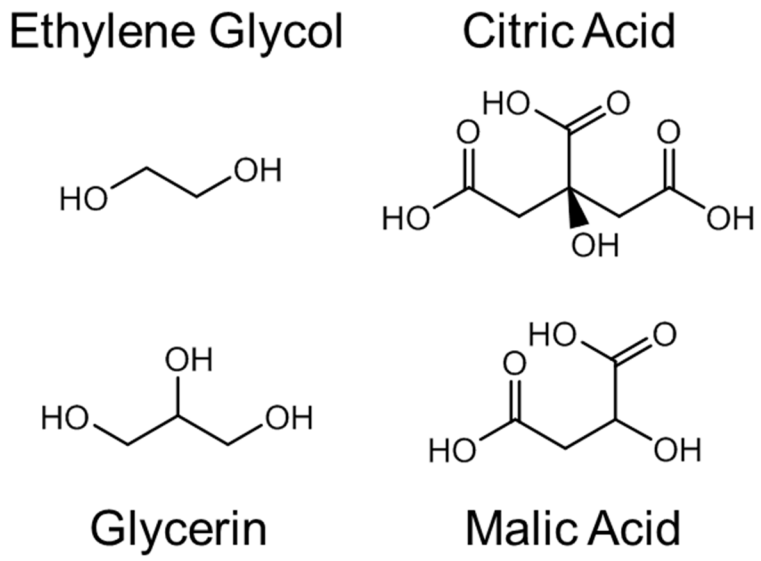

Figure 5.2. Molecular structures of the polyester linkers and chelating agents used in this study. Stoichiometric balance for the polymerization is affected by the degree of multifunctionality in these molecules.

Clear morphological variations result from substitutions of these reagents (Figure 5.3). With glycerin replacing EG, the spheres produced from the otherwise unmodified synthesis are smaller in diameter. Whereas the original spheres have a mean size of 1.32 ± 0.16 μm (Figure 5.3a), the glycerin-modified synthesis produces spheres with a mean size of 0.91 ± 0.17 μm (Figure 5.3b). Glycerin supplies one more –OH group per mole than EG, which affects the reactant balance. Considering that the EG component is already in excess of the CA monomer for the 211 composition, it is expected that a further increase in the number of –OH groups would limit the extent of polymerization. This confirms our previous conclusion, that reactant/functional group balance (i.e., gel molecular weight) is responsible for sphere size control. Additionally, the walls of the structure have been substantially coarsened, which is the result of excess glycerin partially swelling the PMMA template spheres and thus distorting the wall structure (Figure 5.4). The malic acid substituted synthesis does not generate spheres at all; rather, it produces a bicontinuous network that has not been observed for the $Ce_{0.5}Mg_{0.5}O_{1.5}$ 211 composition.

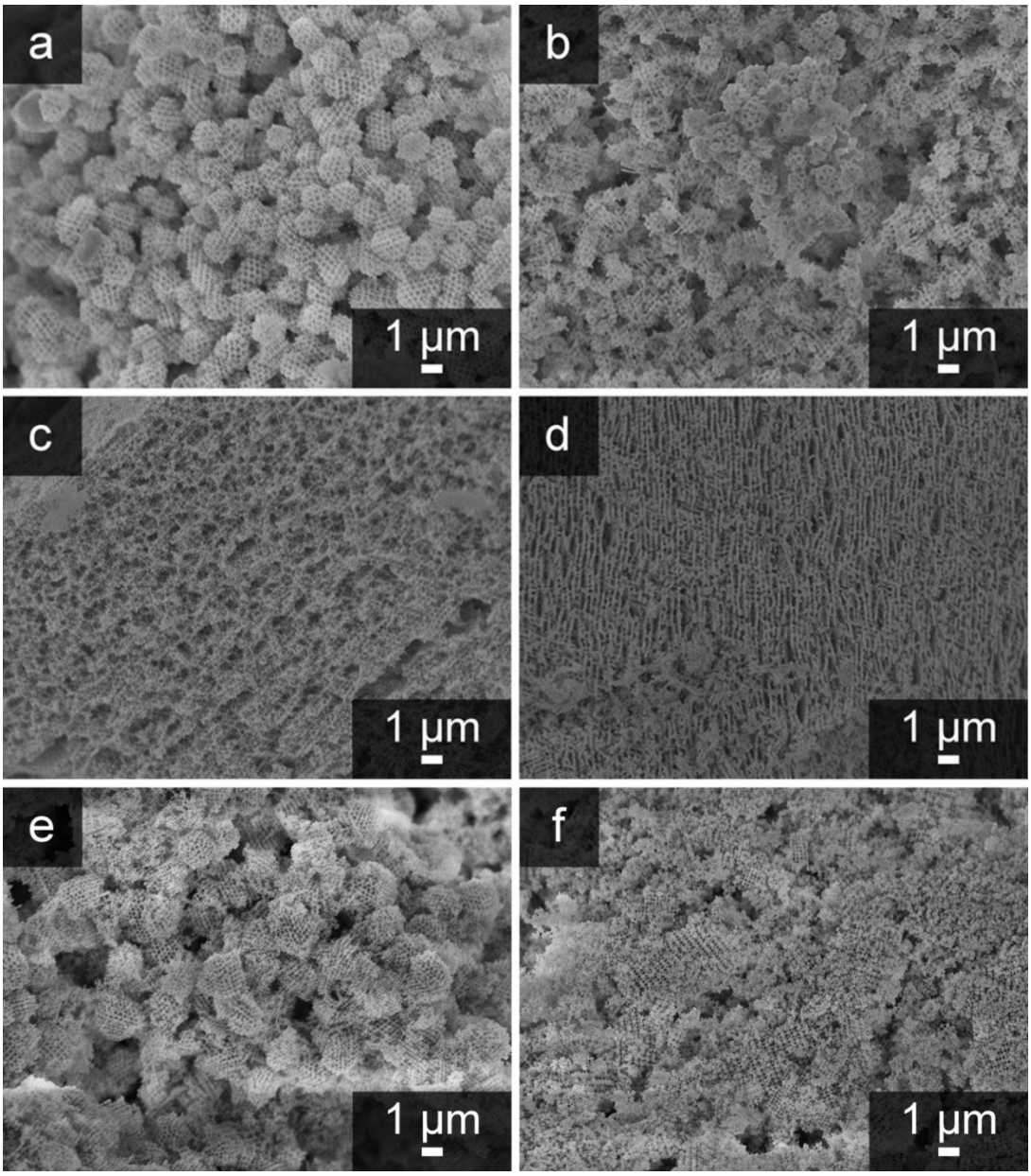

Figure 5.3. SEM micrographs of $Ce_{0.5}Mg_{0.5}O_{1.5}$ 211 sample preparations with (a) no reagent substitutions, (b) substitution of glycerin for EG, (c) substitution of malic acid for CA, and (d) substitution of both glycerin and malic acid for EG and CA respectively. All the above samples were prepared using 489 nm PMMA spheres in the CCT. (e) $Ce_{0.5}Mg_{0.5}O_{1.5}$ 211 prepared with 395 nm PMMA spheres, no reagent substitutions. (f) $Ce_{0.5}Mg_{0.5}O_{1.5}$ 211 prepared with 362 nm PMMA spheres, no reagent substitutions. All samples were prepared from nitrate metal salts and were gelled at 90 ˚C for 24 h.

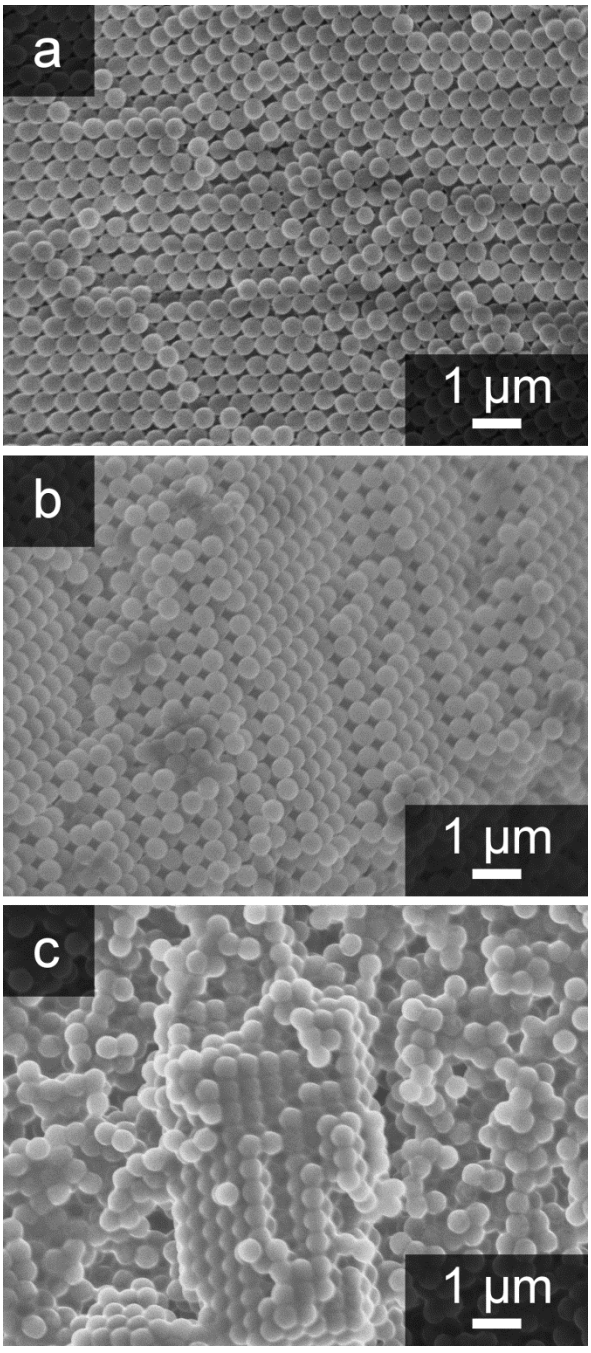

Figure 5.4. SEM images of PMMA spheres in the CCT (a) as synthesized, (b) exposed to EG, or (c) exposed to glycerin.

The above results link a series of factors that influence the average degree of polymerization (i.e., number-average chain length) to the microstructural morphology obtained. In the course of this work, numerous other samples with varied precursor composition were prepared (Table 5.1). On the basis of the morphologies observed for all of these samples, we propose that the microstructures follow a continuum determined by reaction extent/molecular weight of the Pechini polyester (Figure 5.5). When the extent of reaction is low (e.g., with a high reactant imbalance), the precursor is a solution consisting of relatively soluble oligomers that can pass freely throughout the interstitial space between spheres in the CCT. These oligomers fill that space evenly, and minimal microstructural effects from PIPS are observed. As the average molecular weight of the polyester increases, these oligomers combine to form longer chain polymers in the void space, creating polymer rich regions in the aqueous solution. As the molecular weight of the polymer increases further and the difference in polarity between the solvent-rich and polymer-rich regions with it, the polymer rich regions tend to minimize their interfacial area with the solvent, forming microspheres. For systems with less reactant imbalance, the polymerization process continues to progress and the spheres combine, forming a denser microstructure network in which void spaces are interconnected, but smaller. Finally, at the highest extents of reaction, the gel fully densifies into large "blocks" greater than 50 μm in diameter. The only μm-scale void spaces in the structure are cracks between these blocks that develop during drying and calcination of the infiltrated template.

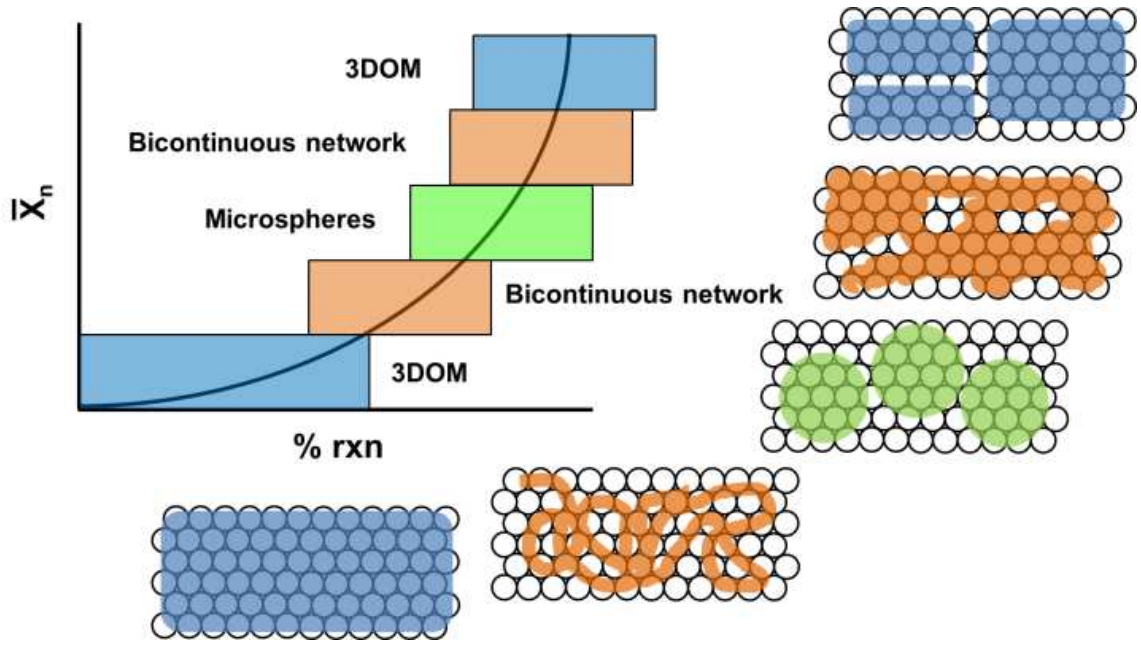

Figure 5.5. Qualitative plot of the observed structures versus the extent of polyesterification. "3DOM" refers to an extended macroporous structure that is defined only by the CCT with no discernable microstructure aside from the ordered network of pores left after template removal.

Further investigation of the involvement of the template, particularly with regards to confinement of the growing polyester gel within the PMMA CCT, has generated additional insights. By decreasing the diameter of the template spheres, two properties of the template-precursor interaction are affected: molecular motion/diffusion of the polymer precursor and template-precursor interfacial area. As the PMMA sphere diameter decreases, the size of the void space between templating spheres—specifically the octahedral and tetrahedral holes in the fcc array—concurrently decreases. This may lead to "pinning" of polymer molecules once they reach a given molecular weight, preventing expected phase separation behavior from occurring. Likewise, as the sphere

diameter decreases, the specific surface area of the template increases. The presence of intermolecular forces between the precursor and template (electrostatics, hydrogen bonding) were demonstrated to have an effect on morphology in previous work.[209]

The effect of sphere size on phase separation behavior was studied by synthesizing the 211 $Ce_{0.5}Mg_{0.5}O_{1.5}$ composition inside CCTs with sphere diameters of 362, 395, and 489 nm. With 489 nm spheres the 211 precursor composition produces uniform 3DOM microspheres (Figure 5.3a). SEM images reveal deviations from this microsphere morphology when smaller templating spheres are employed. With 395 nm templates, some microspheres are present, but the morphology is less consistent, and some areas of the sample (Figure 5.3e, left side of image) are more reminiscent of the bicontinuous networks. The spheres that are present are larger—1.95 ± 0.27 μm, compared with 1.32 ± 0.16 μm for the 489 nm template—and partially merged with one another. For 362 nm templates, the sphere morphology is absent, and domains have merged together more extensively (Figure 5.3f). Decreased diffusion capability of the polyesters in a matrix with narrower void spaces creates an additional constraint on the ability of the growing polymers to collide, resulting in a lower molecular weight, and thus a different morphology.

5.3.3 Obstacles to Generalization

Extending the PIPS methodology via the Pechini method to other metal-oxide systems seems trivial at first glance. Tuning reagent imbalance between CA and EG offers a powerful and direct route to manipulating molecular weight of Pechini polymers. However, examining the system from this perspective leads one to overlook the more

crucial "reagent" balance, i.e., the balance between EG and CA *complexes* of metal ions. Different metal ions have different formation constants (K_f) for citric acid complexes, leading to different stoichiometries in solution than the apparent EG:CA ratio. In fact, this behavior can be directly observed in the CeO_2 system, as the formation of CeO_2 from the reagents used in this study requires a change in oxidation state.

$Ce(NO_3)_3 \cdot 6H_2O$ is used as the Ce source for most of our experiments. However, replacing the NO_3^- counterions with Cl^- results in a complete change in morphology for an otherwise identical precursor composition (Figure 5.6a, b). This occurs because the NO_3^- ions participate in a redox reaction during the gelation step, namely the oxidation of Ce^{3+} to Ce^{4+}. When the oxidizing NO_3^- ions are replaced with the weakly reducing Cl^-, this oxidation does not occur during the gelation step, as evidenced by the lack of a color change (Figure 5.6d) upon removal from the oven. Ce^{3+} ions are colorless, whereas Ce^{4+} ions are yellow, thus the coloration of the resultant powders after calcination. This change in oxidation state would be accompanied by a change in K_f for the CA:Ce^{q+} complex, resulting in the altered morphology.

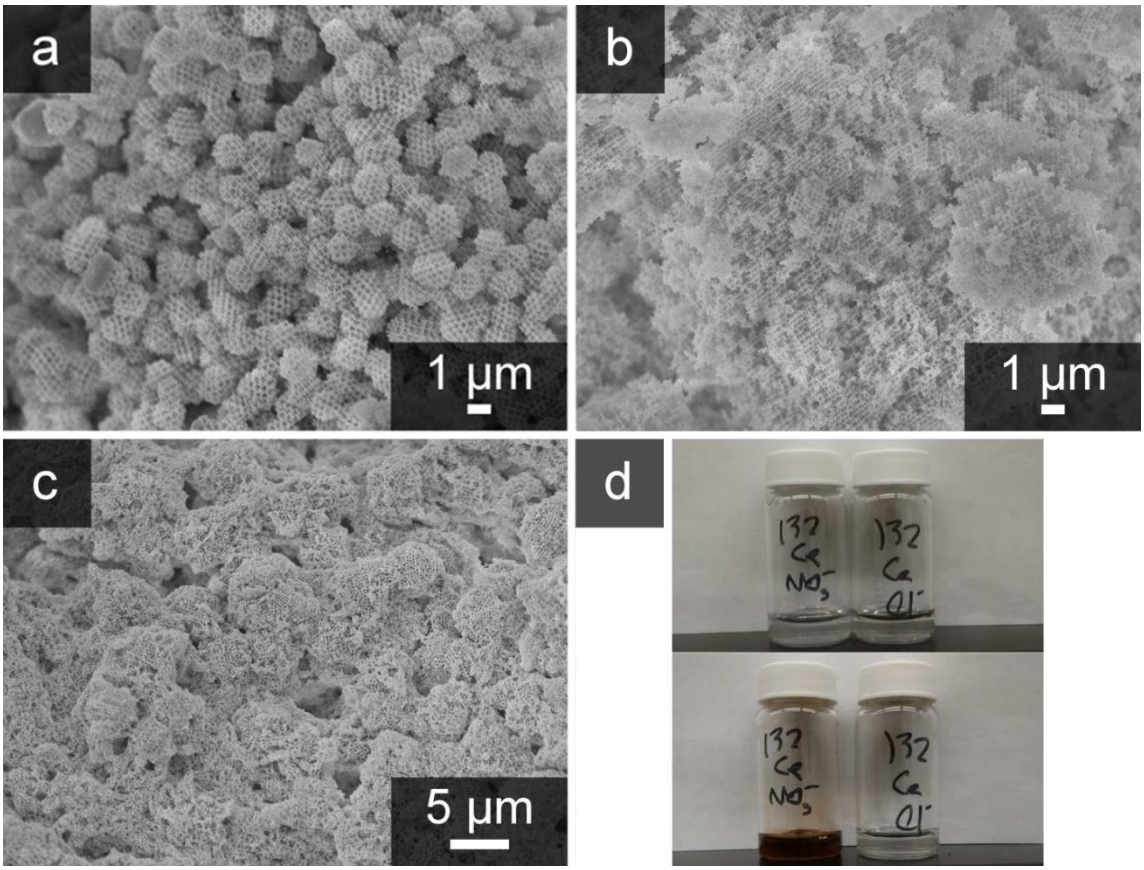

Figure 5.6. SEM images and photographs depicting the influence of counterions in metal precursors on microstructure. (a) SEM image of $Ce_{0.5}Mg_{0.5}O_{1.5}$ 211 prepared with $Ce(NO_3)_3 \cdot 6H_2O$, reproduced from Figure 5.2a for comparison. (b) SEM image of $Ce_{0.5}Mg_{0.5}O_{1.5}$ 211 prepared with $CeCl_3 \cdot 7H_2O$. (c) SEM image of $Ce_{0.5}Mg_{0.5}O_{1.5}$ 211 with doubled NO_3^- concentration. (d) Photographs of CeO_2 132 precursor solutions before (top) and after gelation at 90 °C for 18 h (bottom). The gelation time was 24 h for the samples depicted in (a)–(c). All samples were prepared using 489 nm spheres in the CCT.

When the concentration of NO_3^- in a $Ce_{0.5}Mg_{0.5}O_{1.5}$ precursor is doubled by adding HNO_3 to the solution, spheres are still formed, but they are larger and have in fact partially collided to form a bulbous, bicontinuous network structure (Figure 5.6c). An equal number of protons have been added, but, as the nitrate precursor solutions are at or

below pH 1 upon formation, the effect on pH is limited. We propose this behavior is a result of enhanced charge screening due to the increase in the concentration of NO_3^-, resulting in a lower Debye length for the growing polyesters.

Another aspect of the CA:Ce^{q+} interaction that must be kept in mind is that the binding strength and binding environment of the cation may be altered by the change in oxidation state. A stronger chelation of Ce^{4+} may result in reduced lability of the carboxylic acid groups of CA, which have a dual function as the binding agents for Ce cations as well as the end groups for the polyesterification reaction.[250] If carboxylic acid groups become unavailable for condensation, the reactant balance will be modified, resulting in unintended changes in molecular weight (and thus, morphology). This will be discussed further in the exploration of Fe_2O_3 and Mn_3O_4 systems as test cases for the general applicability of PIPS-based microstructural control in hard templates.

5.3.4 Morphological Variation in Fe_2O_3 and Mn_3O_4 Pechini Gels

Fe_2O_3 and Mn_3O_4 were selected as test systems based on their interactions with citric acid. We chose systems which had similar binding modes to those observed in the lanthanides, but presented substantial shifts in K_f and oxidation state of the final products. Mn^{2+} and Fe^{3+} serve these purposes appropriately for the available data.

As expected, varying precursor composition drastically affects the observed morphology in the sample (Figure 5.7). The Mn_3O_4 132 and Fe_2O_3 111 compositions (Figure 5.7a, d) correspond to EG:CA:M^{q+} ratios which produced microspheres for CeO_2 and $Ce_{0.5}Mg_{0.5}O_{1.5}$, respectively, clearly demonstrating that the change in cation identity and charge has changed the phase separation behavior of the precursor gel. Bicontinuous

networks are obtained for a variety of compositions in both systems, an example is shown in Figure 5.7b. Fe_2O_3 615 (Figure 5.7e) consists of microspheres where the diameter only encompasses 4~5 pores, making it difficult to discern edges and accurately measure the dispersion. More discernable microspheres are obtained for the compositions Mn_3O_4 341 and Fe_2O_3 113 (Figure 5.7c, f). Finally, a unique lamellar structure was observed for Fe_2O_3 313 (Figure 5.13g).

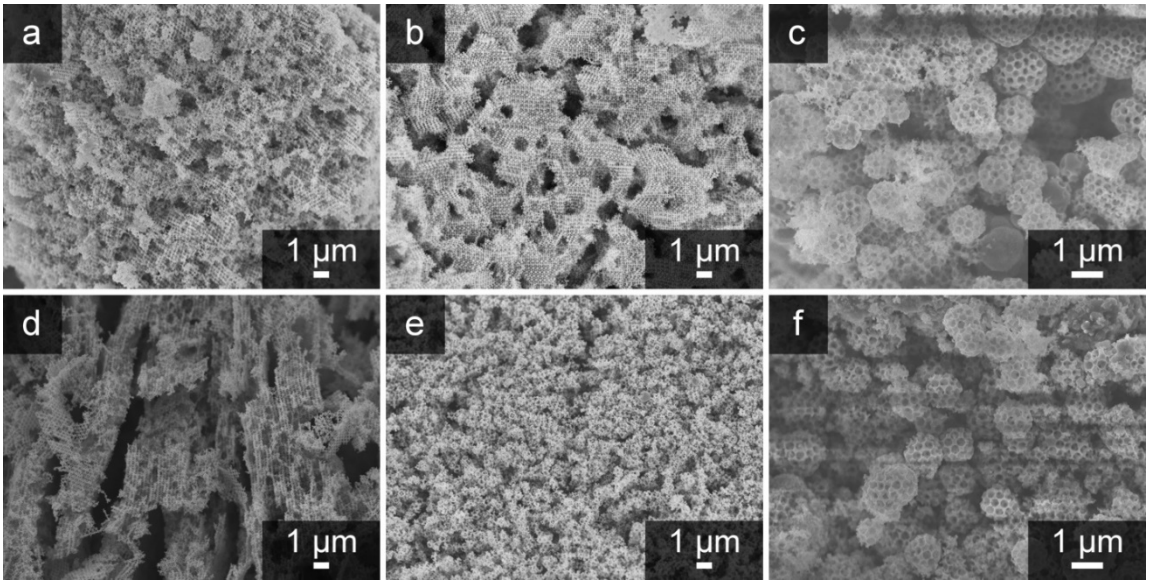

Figure 5.7. SEM images of Mn_3O_4 compositions and Fe_2O_3 compositions. (a) Mn_3O_4 132. (b) Mn_3O_4 331. (c) Mn_3O_4 341. (d) Fe_2O_3 111. (e) Fe_2O_3 615. (f) Fe_2O_3 113. All samples were prepared using 489 nm spheres in the CCT and were gelled at 90 ˚C for 24 h.

The Mn_3O_4 spheres are 1.30 ± 0.3 µm in diameter, and the Fe_2O_3 spheres are 1.32 ± 0.29 µm, a coefficient of variation (c_v, $\frac{\bar{x}}{\sigma}$) of 23% and 22% respectively. These spheres are less uniform than the $Ce_{0.5}Mg_{0.5}O_{1.5}$ microspheres obtained in previous work (c_v =

15%), but similar to those prepared in syntheses of phase-pure CeO_2 microspheres (c_v = 20%).[209]

These samples reveal a strong correlation between K_f for CA, the molar ratio of CA to metal cation, and the ultimate morphology of the sample. The selected cation has a pronounced effect on the reagant balance in the polyesterification due to differences in CA complex formation, underlining the critical importance of compensating for this behavior when applying the method of template-confined PIPS to different metal-oxides. The results further confirm that reagent balance (molecular weight) is the primary determinant of morphology obtained by this method, and thus provide a semi-empirical rule of thumb for generalization. Essentially, in order to "translate" a target microstructure—here, the microsphere morphology is considered the target because it is recognizable and easy to characterize—from one metal-oxide to another, one must compensate for the K_f of the metal by adjusting the CA concentration in the correct direction (Table 5.2) via Le Chatelier's principle. For lower K_f, this means driving the formation reaction with excess CA, whereas for higher K_f, this means limiting the formation of complex by reducing CA concentration. Mn^{2+} and Fe^{3+} are good "brackets" for this investigation, as most cations of interest have a CA K_f falling somewhere between 4 and 11.5.

Table 5.2. K_f Data and binding modes for Ce^{3+}, Mn^{2+}, Fe^{3+}.

Cation	Binding Mode[87]	K_f (CA)[87]	Microsphere CA:M^{q+}
Mn^{2+}	Mn(Cit)	4.15	4:1
Ce^{3+}	Ce(Cit)	7.95	1.5:1
Fe^{3+}	Fe(Cit)	11.5	1:3

5.3.5 Tuning Templating Behavior via Precursor Composition

Several studies of precursor-template interactions in 3DOM materials have focused on how the opal structure of the template is replicated in the templated product.[251-254] Common structures observed in CCT-templated materials are negative replicas of the CCT, or "volume templated" materials, in which the void space between spheres is completely filled by the ceramic material in the final product (Figure 5.8a). Other structures in which the majority of the solid material forms at the surface of the template spheres ("surface templated" materials) are formed in systems with strong precursor-template interactions and can produce hollow shapes in the interstitial region of the CCT and in some cases, discrete hollow spheres around the original template spheres (Figure 5.8b).

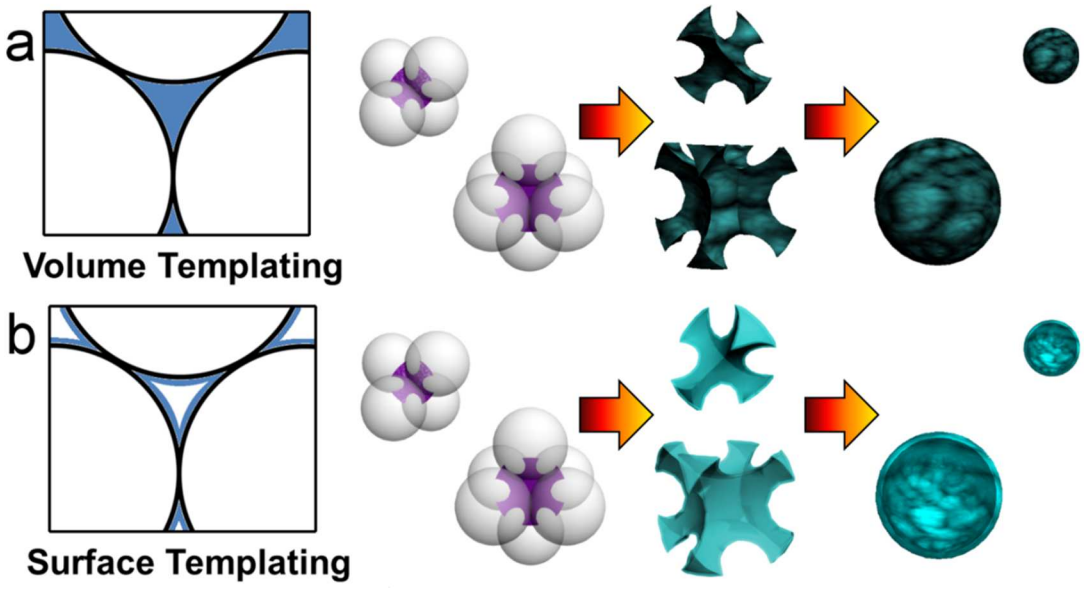

Figure 5.8. Graphical depiction of metal-oxide particle morphology obtained in the CCT in the two types of templating processes: (a) volume templating, where complete filling of the void spaces between spheres occurs, and (b) surface templating, where metal ions or metal-containing precursor preferentially fills interstices at the sphere surfaces, leaving solvent or combustible material in the center of the voids. Volume templating combined with particle disassembly of a 3DOM structure results in solid particles produced from the original tetrahedral and octahedral template voids.[173, 255] Surface templating produces hollow particles in a similar manner.

We have observed hollow structures in 3DOM Mn_3O_4, for which under EG-rich conditions (Mn_3O_4 411, 611, 711) and a small CCT sphere diameter (362 nm) a bimodal distribution of hollow spheres is obtained (Figure 5.9a). However, the spheres are too small (~100 nm and ~40 nm) to be simply replicas of the templating spheres. These sizes correlate reasonably well with the octahedral and tetrahedral holes of the template; for a 362 nm CCT these holes are approximately 145 nm and 79 nm, respectively.

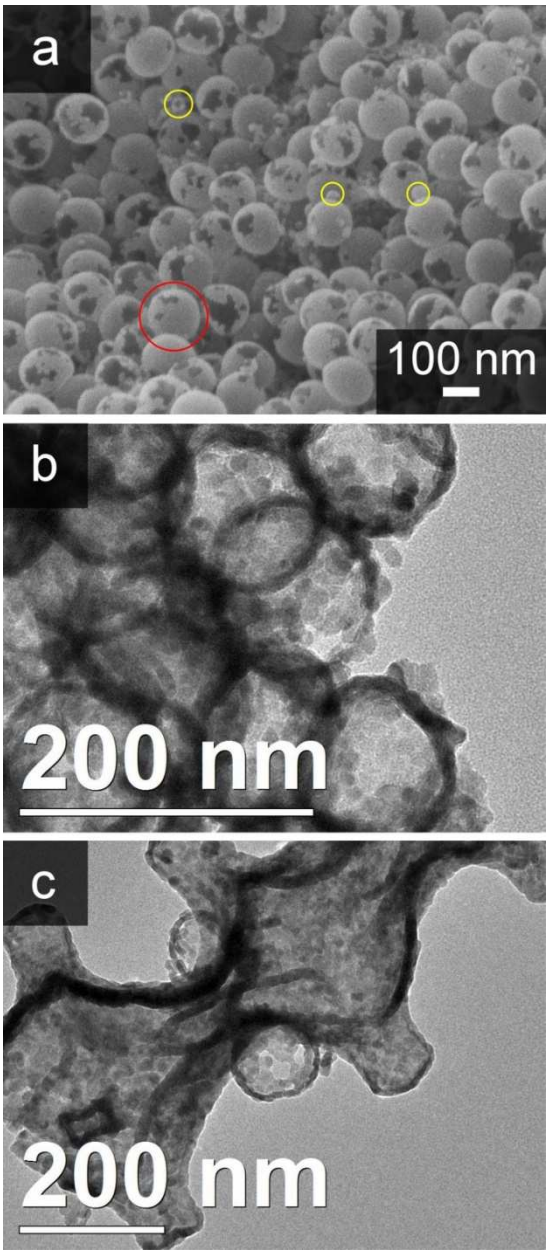

Figure 5.9. SEM and TEM images of Mn_3O_4 411 using a CCT template with 362 nm PMMA spheres. (a) SEM image highlighting the bimodal distribution of spheres. Red circles indicate large spheres, yellow circles indicate small ones. (b) TEM image showing the hollow nature of the spheres. (c) TEM image showing a section of the sample with surface replication of the octahedral hole morphology without substantial densification. Samples were gelled at 90 ˚C for 24 h.

We propose that these morphologies are also accessible through precursor design in Pechini PIPS systems and result from a combination of surface templating with disassembly of the 3DOM structure (Figure 5.8). 3DOM materials consist of a 3D array of tetrahedra and octahedra (2 tetrahedra for every octahedron) with concave faces. These polygonal particles are interconnected by "necks" at their vertices. Breaking or severing these necks via mechanical, chemical, or thermal means results in disassembly of the structure, yielding a bimodal distribution of nanoparticles with the original structure of the two types of nodes.[173, 255]

When the organic content of the precursor is increased to many times the concentration of the metal ion, the organic components crowd out existing cations within the void spaces between spheres. Additionally, many polyester molecules are being formed that are not complexed to cations; these polymer molecules are charge neutral. We propose that the metal-containing polyesters, being positively charged, have an affinity for the slightly negatively charged polymer spheres, and thus aggregate at the surface of the PMMA spheres. A high degree of reactant imbalance aids in this process, as the polymers may remain small enough to diffuse throughout the CCT. During calcination, the space-filling organic material is removed, leaving only a thin shell of metal-oxide. This process, leading to the formation of a hollow 3DOM structure, is known as surface templating.

Due to the very thin walls (< 20 nm) and moderate calcination temperature (450 °C), the hollow Mn_3O_4 tetrahedra and octahedra undergo densification processes which minimize the surface energy of the particles, first severing the necks, and then removing

the concave nature of the original particles, converting them to spherical shells. However, this process does not affect the low size dispersity and bimodal distribution of the resulting particles. The holes and gaps within the shells result from grain growth (solid-state diffusion) during calcination, in which some Mn_3O_4 nanocrystals increase in size through Ostwald ripening. In essence, the thickness of the shells increases, but at the expense of surface coverage. TEM of the particles reveals that they are indeed hollow (Figure 5.9b). In fact, in some rare areas of the sample, hollow octahedra that have not completed the surface minimization process can be observed (Figure 5.9c).

5.3.6 Construction of Partial Phase Diagrams

A large number of compositions were produced and analyzed during the course of this investigation (see Figures 5.10–5.14). Categorizing the types of morphologies obtained for each synthesis and plotting the points vs. EG, CA, and M^{q+} molar ratios allows for the construction of ternary phase diagrams for the metal-oxides explored (Figure 5.15). As demonstrated above, the K_f of the metal determines the position of the "microsphere" phase along the M^{q+} axis; the Mn-based materials tend to form microspheres with lower concentrations of metal relative to CA, and the Fe-based materials tend to form microspheres at high concentrations of metal relative to CA. Slight deviations from compositions in the microsphere phase space tend to produce bicontinuous networks in all systems; this is particularly noticeable in Fe_2O_3 and Mn_3O_4, where the microsphere phase space is small and surrounded by bicontinuous network compositions. Additionally, with the exception of the mixed oxide, $Ce_{0.5}Mg_{0.5}O_{1.5}$, the bicontinuous network phase is generally located towards the center of the diagram. The

"hollow spheres" observed in the Mn system are observed only at high concentrations of EG, and only with the smaller (362 nm) templating spheres.

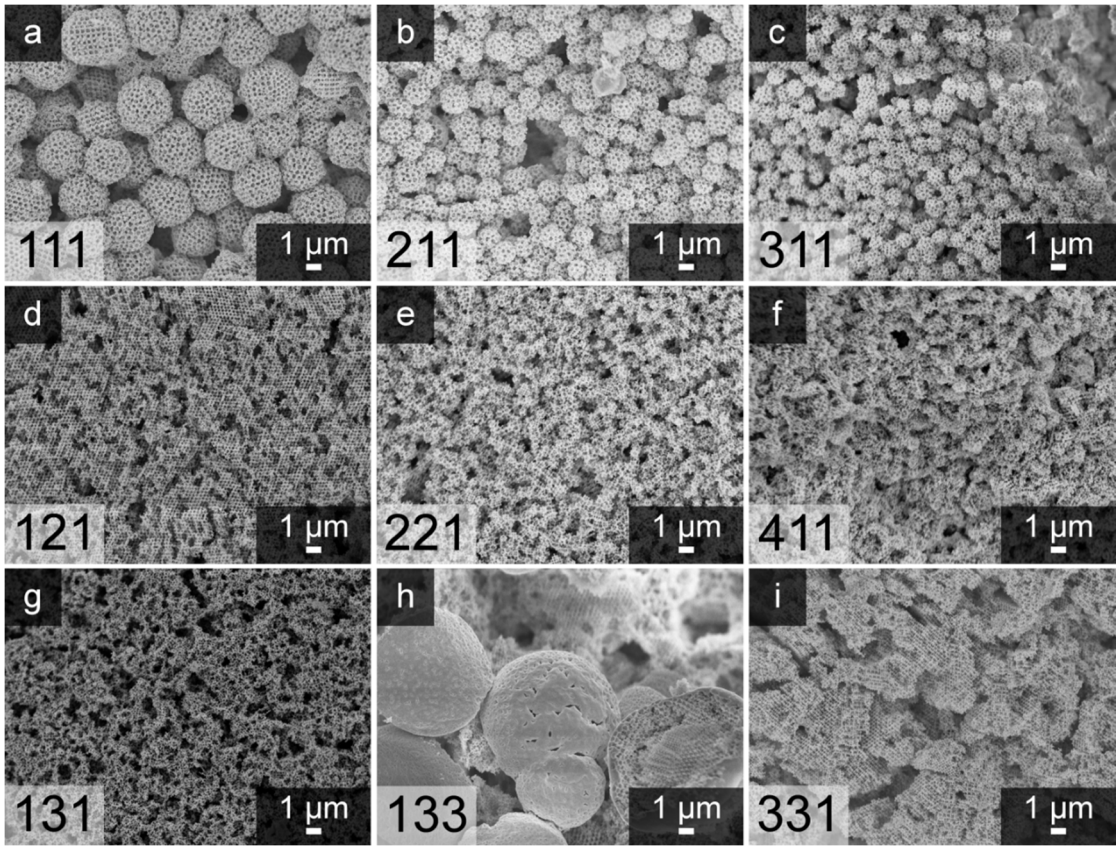

Figure 5.10. SEM images showing morphologies observable in $Ce_{0.5}Mg_{0.5}O_{1.5}$ via modification of EG:CA:TMI ratios. The three numbers listed in each image refer to the integral molar ratios of EG:CA:TMI. For example: 331 refers to 3 mol EG: 3 mol CA: 1 mol TMI. The same notation is used in the other figures.

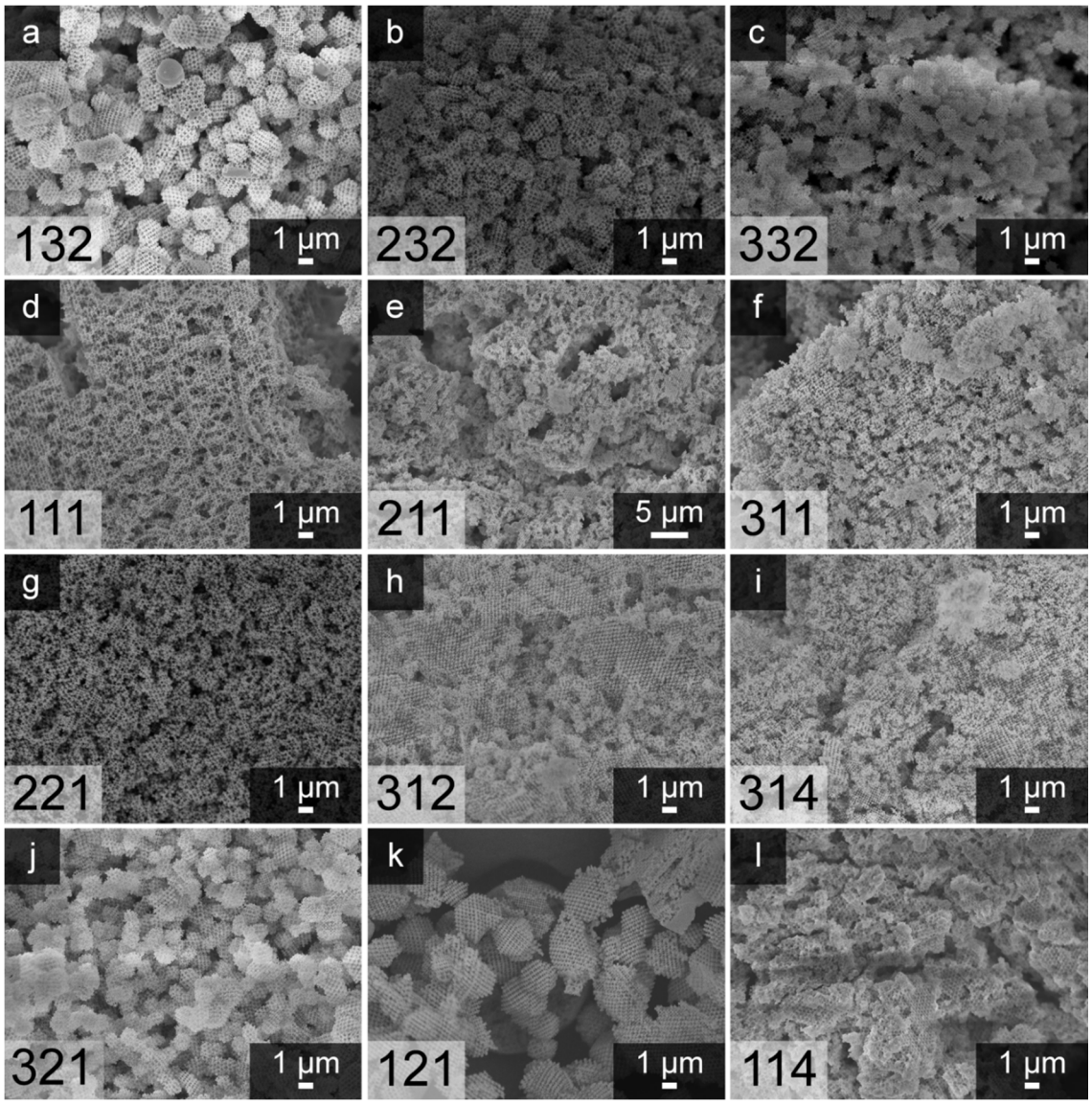

Figure 5.11. SEM images showing morphologies observable in CeO_2 via modification of EG:CA:TMI ratios.

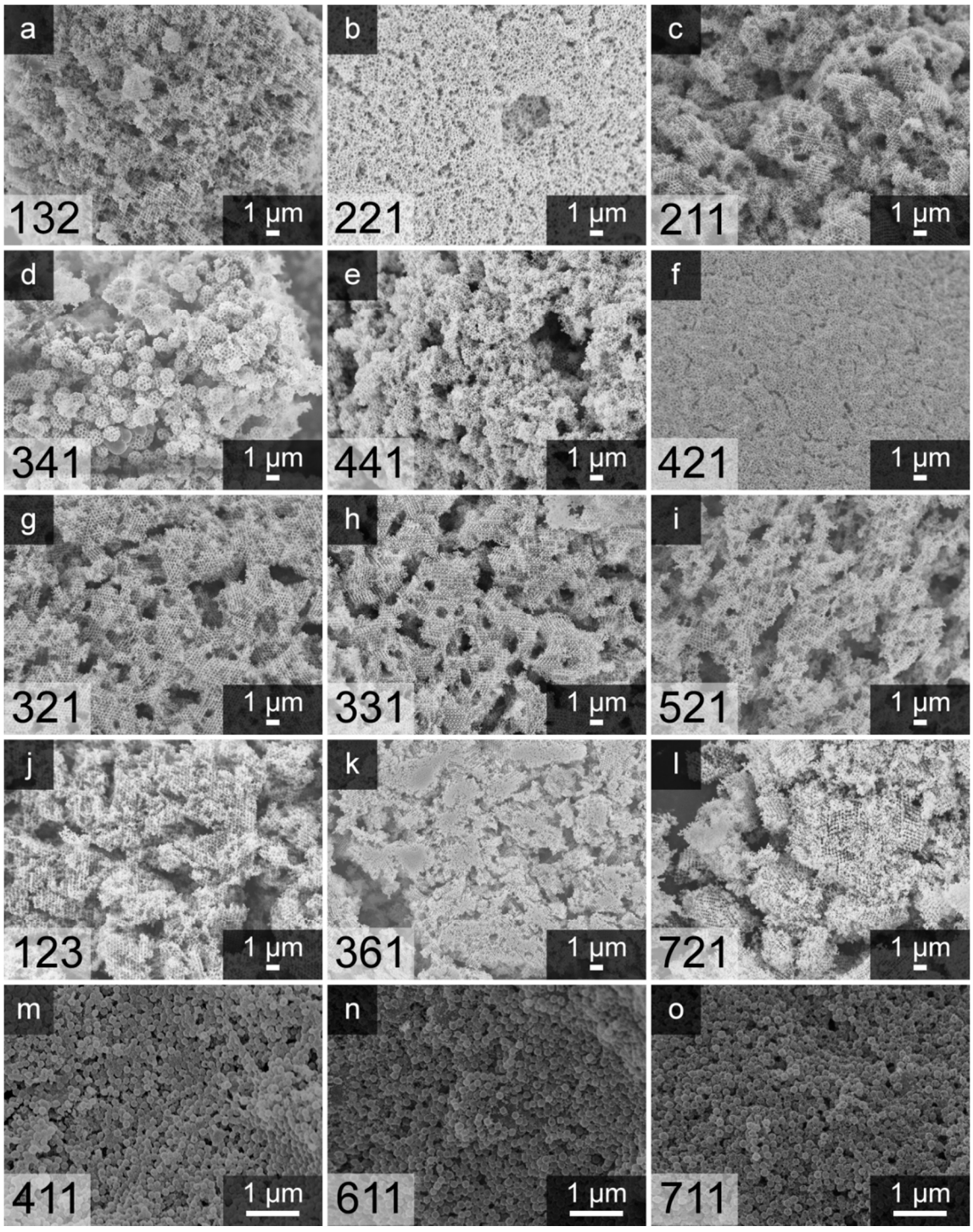

Figure 5.12. SEM images showing morphologies observable in Mn_3O_4 via modification of EG:CA:TMI ratios.

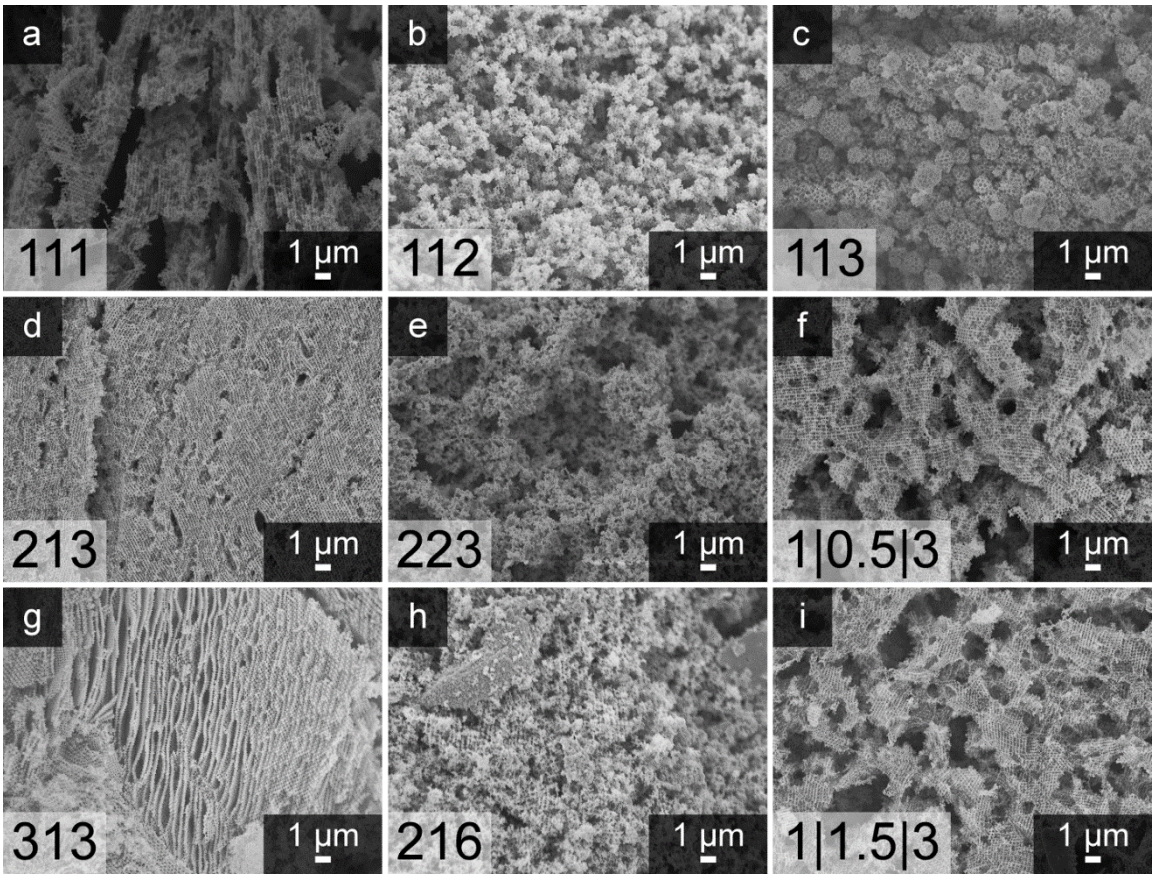

Figure 5.13. SEM images showing morphologies observable in Fe_2O_3 via modification of EG:CA:TMI ratios.

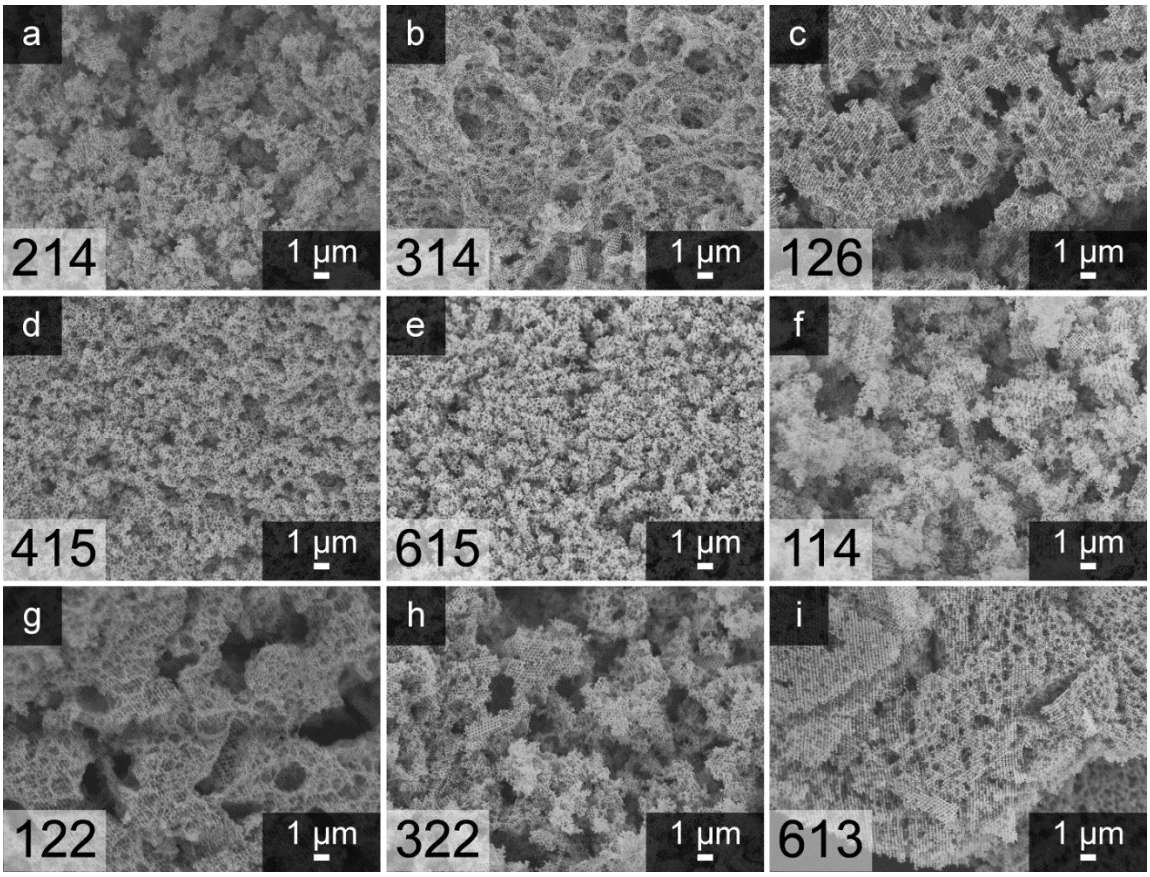

Figure 5.14. Additional SEM images showing morphologies observable in Fe_2O_3 via modification of EG:CA:TMI ratios.

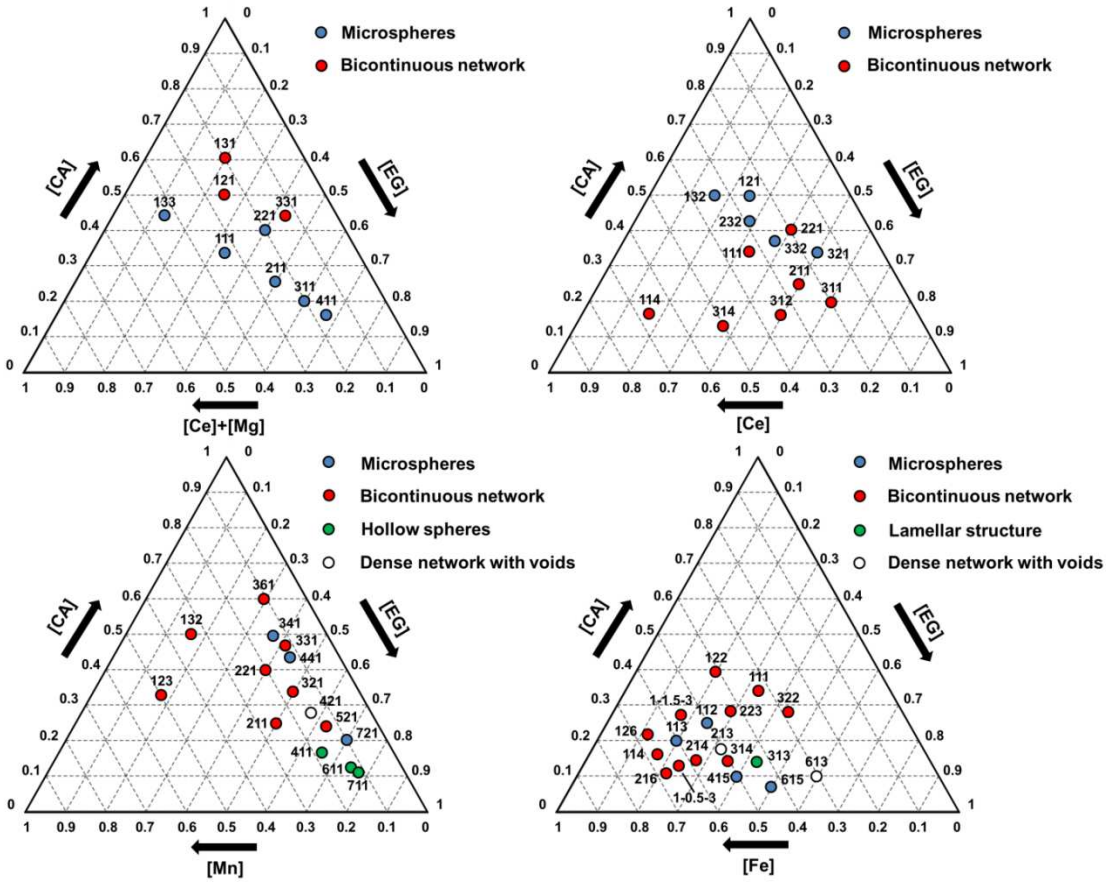

Figure 5.15. Phase diagrams generated from multiple precursor compostions and observations of morphology in those samples for several metal-oxides: $Ce_{0.5}Mg_{0.5}O_{1.5}$, CeO_2, Mn_3O_4, and Fe_2O_3.

Still, some questions remain. It is not apparent what controls the relative size of the phases for different metal ions; i.e., why is the range of EG:CA:M^{q+} ratios leading to microspheres for $Ce_{0.5}Mg_{0.5}O_{1.5}$ and CeO_2 different than for Fe_2O_3 and Mn_3O_4? The phase space corresponding to particular microstructures may not be continuous, as in the Fe_2O_3 diagram, where compositions like 112 and 113 are separated from 415 and 615 with bicontinuous network samples in between. The origin of microstructures like the Fe_2O_3 313 (Figure 5.13g) with partially separated lamellae (sheets) of 3DOM material are

not well-understood. Finally, the effect of the binding mode (i.e., how many citric acid molecules per cation are involved in chelation) and the molecular structure of the complex on molecular weight has not been investigated, and this relationship is not entirely clear. Further investigation of this method, particularly of the dynamics of gelation and the molecular weight of the metal-laced polyester under differing conditions, could yield still greater degrees of control over microstructure in templated systems.

5.4 Conclusions

The parameters that control the microstructural variation of CeO_2 and $Ce_{0.5}Mg_{0.5}O_{1.5}$ through polymerization-induced phase separation of precursors in templated Pechini-based syntheses were investigated. A variety of influencing factors were identified, including temperature, reagent concentration, number of functional groups in the complexing agent, counterion concentration, counterion identity, K_f of the CA-metal complex, and size of the templating polymer spheres. The common thread connecting these factors was that each of them affects the degree of polymerization during polyesterification, either through reaction kinetics, reagent imbalance, or confinement in the colloidal crystal template. On the basis of SEM analyses of samples prepared under different conditions, a "continuum" of morphologies was proposed, in which an increasing degree of polymerization results in morphological shifts, progressing along the following trend: full-volume 3DOM materials to 3DOM bicontinuous networks with high void fractions to 3DOM microspheres to 3DOM bicontinuous networks with high solid fractions and again to full-volume 3DOM materials. This proposed continuum was then applied to guide the synthesis of two model systems, Mn_3O_4 and Fe_2O_3, to test the

continuum model and to evaluate the ability to generalize this methodology. Many compositions were synthesized to construct ternary phase diagrams (EG vs. CA vs. TMI) for these systems, detailing the regions of particular microstructural regimes. Using the microsphere morphology as a test case, it was found that replacing the cation with Mn caused the phase space for microstructural variation to shift to high CA:M^{q+} ratios, whereas Fe shifted that phase space to low CA:M^{q+} ratios. Average diameters for 3DOM microspheres formed by this method ranged from 0.8 to 3.3 μm for $Ce_{0.5}Mg_{0.5}O_{1.5}$, 0.8–2.0 μm for CeO_2, 1.0–1.6 μm for Mn_3O_4, and 0.5–1.6 μm for Fe_2O_3 when 489-nm PMMA spheres were used in the colloidal crystal template. The observations and insights gained from this work indicate the feasibility of generalizing PIPS-based microstructural control to other water-soluble and acid-stable cations.

5.5 Acknowledgements

Synthesis of a large portion of the materials analyzed in this work was carried out by Denis Terzic, Sammy Shaker, and Réginald Le Maire. The author is indebted to their skillful labwork and thoughtful insight on this project.

Chapter 6: Controlling Self-Assembly of Collagen Fibrils Ex Vivo

6.1 Introduction

Disease and injury of the cornea has resulted in several million cases of blindness per annum worldwide.[136] Corneal transplant is the most common method of treating corneal insufficiency. However, due to cost, limited availability of donors, and tissue rejection, only tens of thousands of transplants are performed each year.[256] Plastic prosthetic corneas, or "keratoprostheses," have been clinically available for decades,[257] but they do not fully integrate with surrounding host tissue and have a high risk of complications requiring extensive follow-up after implantation.[140] A preferable solution would be a truly artificial cornea, generated synthetically from the same biological tissue as the cornea itself: collagen.

Collagen is the most ubiquitous protein in the human body. It is a structural protein responsible for producing and supporting mechanically flexible and generally robust anatomical structures, including connective tissue, skin and bone, among many others. Its chemical structure is relatively simple, consisting of a repeat unit of the form Gly-X-Y, where X and Y are most commonly occupied by proline and hydroxyproline, respectively.[258] These polypeptide chains assemble into a triple helical molecule.[259] The

triple helices self-assemble to form high aspect-ratio nanostructures known as fibrils.[260] These fibrils can further assemble into the microscale fibers typically observed in tissues.

Production of the cornea *in vivo* relies on a protein-directed aqueous self-assembly of collagen. During this process, the type I collagen of the cornea assembles into a series of fibrils, which then align themselves with the help of a class of structure-directing proteins known as proteoglycans.[261] The proteoglycans in the cornea serve a dual role during the assembly process. By binding to the surface of fibrils, they sterically prevent "bundling" of the fibrils into fibers and balance electrostatic forces such that the fibrils can retain a relatively consistent spacing and alignment.[262] The final structure resembles a lamellar polycrystalline film, with individual layers, or domains, consisting of aligned fibrils.[263, 264] Each domain has its own particular alignment, lending some degree of anisotropy to the structure, while still maintaining the alignment necessary for favorable scattering behavior.[265] These two factors—alignment of fibrils and structural anisotropy—are essential for giving the cornea its transparency and strength. However, if the entire structure were aligned in the same direction, substantial anisotropy would be observed in the mechanical strength of the material. The arrays of internally-ordered domains within the cornea provide mechanical robustness while maintaining the low-scattering behavior of the material.

Replication of this self-assembly behavior *in vitro* has proven difficult. Methods such as assembly on patterned substrates,[266] shear flow over thin layers,[267] and electrospinning[268] have demonstrated the ability to align fibrils, but these methods are frequently difficult to scale up and lack the ease of a one-pot synthesis. Recently, aligned

fibrils were produced by concentrating collagen solutions (prior to gelation) to concentrations greater than 175 mg/mL.[143] This work also demonstrated the ability to align fibrils throughout the thickness of a film. Full thickness alignment is necessary for eventually producing a collagen-based corneal prosthetic.

Here, we explore the possibility of using nanocrystalline cellulose (NCC) to achieve a similar alignment (Figure 1). Cellulose is the most abundant polymeric material on earth, as it is the major constituent of bacterial and plant cell walls. It is used in countless applications, from paper to adhesive tape, packaging films to clothing. With the growth of the field of polymer nanocomposites, interest in nanoscale cellulose particles and NCC films has increased due to their advantageous optical and mechanical properties.[269]

In this chapter, I present a method of generating cm-scale films of fully aligned collagen fibrils directly from aqueous solution of collagen and NCC, a biocompatible, non-toxic material (Figure 6.1). Fibril diameters and alignment are analyzed via electron microscopy and quantified. Cell compatibility studies are carried out on the composite samples. Finally, a mechanism for the alignment of collagen by NCC in aqueous solution is proposed.

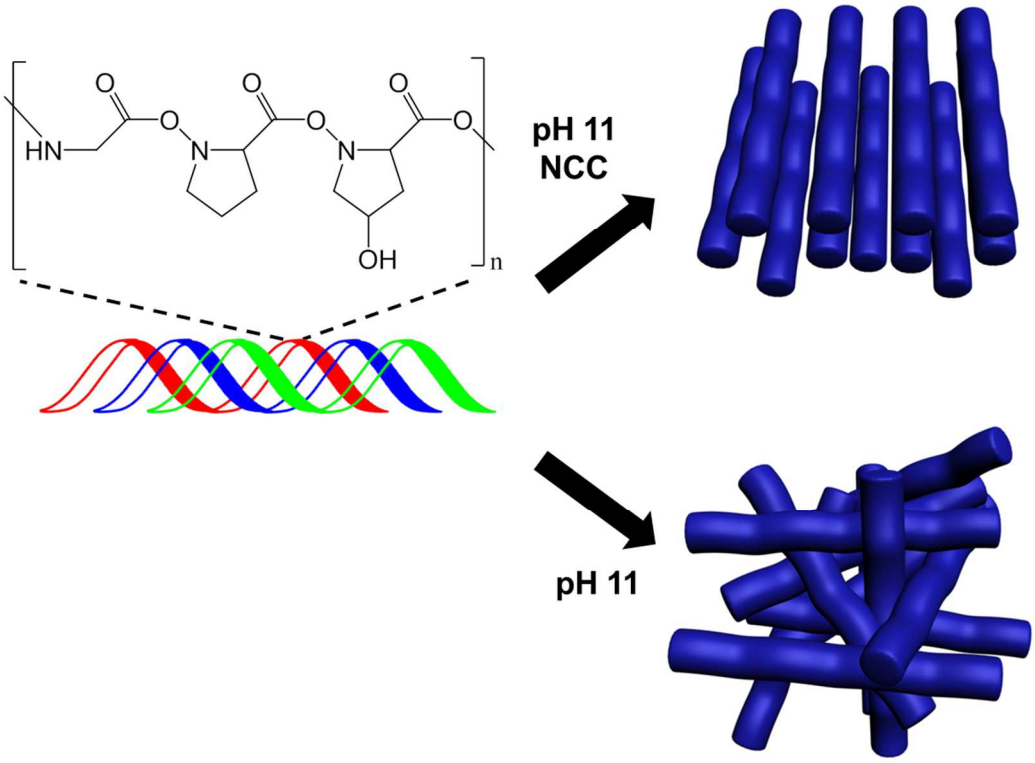

Figure 6.1. Schematic of the structures formed during collagen assembly and fibrillogenesis. Addition of NCC to a solution of soluble type I collagen at pH 3 and raising the pH to 11 yields a uniform alignment of fibrils. When NCC is excluded, fibrils form with random orientation.

6.2 Materials and Methods

6.2.1 Materials

A solution of type I rat-tail collagen was obtained from Olaf Pharmaceuticals (5 mg/mL, pH 3). Microcrystalline cellulose (ACS grade, powder, 20 μm), dialysis membranes (12 kDa), poly(ethylene glycol) (PEG, 99%, 35 kDa), methylcellulose powder (ACS grade), potassium bromide (FTIR grade, >99%), and ammonium hydroxide (30% wt/wt) were obtained from Sigma Aldrich, ethanol (200 proof) from Decon

Laboratories, propidium iodide (20 mg/L) from Fisher Scientific, trypsin (0.25% trypsin-EDTA in water) and Dubelcco's Modified Eagle medium (DMEM) from Gibco. Calcein AM (>95%) from BD Bioscience was diluted to 1 μM in de-ionized (DI) water. Phosphate buffered saline solution (PBS, 10X) from Gibco was diluted 10:1 in DI water. All chemicals were used as received, unless noted above. DI water (resistivity >18 MΩ·cm), filtered on-site, was used in all syntheses.

6.2.2 Concentrating the Collagen Solutions

Collagen was concentrated up to 150 mg/mL via dialysis with PEG. Dialysis fluid was prepared by mixing 10 g of PEG in 100 mL of DI water. A cellulose membrane was rinsed with DI water, and one end was pinched shut with a dialysis clip. The stock collagen solution was pipetted into the open end of the dialysis membrane followed by sealing the membrane with another dialysis clip. The collagen-filled membrane pouch was submerged in the dialysis fluid at 4 ˚C until the target concentration was reached.

6.2.3 Preparation of Collagen Composites

NCC was prepared by sonicating 20 g of microcrystalline cellulose in 500 mL of water with a Cole-Parmer 750 W ultrasonicator. The ultrasonicator was pulsed on for 2 s every 6 s for a total of 36 h (12 h total sonication time) at 38% amplitude. The resulting thick, milky-white suspension of nanocrystalline cellulose was added to the concentrated collagen in a petri dish, then manually stirred until visibly homogenous. The relative NCC loadings in weight percent reported for the samples refer to solid NCC to solid collagen, not considering the water content. The petri dish containing the composite was then placed in a sealed box with a concentrated solution of NH_4OH. This allowed for

vapor-phase transport of NH_3 to the sample, gradually raising its pH without diluting the collagen or NCC. Gelation was continued for 10 min, and then the sample was removed from the box. The sample solution achieved a final pH of 11.

Preparation of the methylcellulose composites followed the above methodology with one slight modification. Before sonication, 20 g of methylcellulose powder was dissolved in 500 mL water at 70 °C, and then cooled. This resulted in a viscous, slightly hazy suspension, which was then exposed to the sonication procedure detailed above. After sonication, the material was added to the appropriate amount of concentrated collagen and gelled following an identical procedure to the nanocrystalline cellulose composites.

6.2.4 Biocompatibility Studies

Human foreskin fibroblasts (HFFs; ATCC; Manassas, VA) were used to test the biocompatibility of the hybrid material. HFFs were detached from the bottom of the flask by adding 3 mL of trypsin and 5 mL of media. After 5 min of incubation, a cell pellet was formed by centrifuging (Marathon 6K, Fisher Scientific) in a 15 mL centrifuge tube for 10 min at 1000 rpm. The supernatant was removed and replaced with 3 mL of DMEM. Using a hemocytometer and Nikon TMS bright-field microscope, a cell count was performed, and the correct amount of DMEM was added to adjust the cell concentration to 10^5 cells/mL.

The collagen-NCC gel preparation procedure described above was used to prepare 2 mL of gel (5 mg/mL collagen, 2.0% NCC) that was neutralized in a six-well plate. The gels were rinsed with phosphate buffered saline solution (PBS), and 2 mL of the DMEM

cell solution was then pipetted onto the top surface. The well plate was covered and incubated for 1 h.

The viability of the cells was assessed at three different time points: 1, 24 and 72 h of incubation. Calcein AM diluted in PBS to a concentration of 2 mM was used to stain live cells. A propidium iodide solution made of 2 mL of 0.5 mg/mL propidium iodide stock solution and 47 mL of PBS was used to stain dead cells. For a given time point, the supernatant DMEM was removed, and 2 mL of calcein AM solution was added. The sample was incubated for 20 min. Images were then taken on a Zeiss Axioskop light microscope with a fluorescein isothiocyanate (FITC) filter (Zeiss 10, 450–490 nm excitation, 515–565 nm emission) attached. After the live cell images were taken, the calcein AM was removed and 2 mL of PI stain was pipetted into the well. The same microscope was used with a tetramethyl rhodamine isothiocyanate (TRITC) filter (Zeiss 20, 530–560 nm excitation, 590–650 nm emission) to image the dead cells.

6.2.5 Characterization

The morphology of the materials was examined using scanning electron microscopy (SEM). In order to preserve the sample morphology, collagen composites were soaked sequentially in a series of ethanol solutions (10, 25, 50, 75, 95, 100 vol%), 10 min in each solution. After this, the samples were dried in supercritical CO_2 with a Tousimis Samdri-780A critical point drier. Samples were mounted on stubs with double-sided carbon tape (Ted Pella). To obtain cross sections, the mounted films were cut with a razor blade perpendicular to the surface of the film to expose an internal region. Samples were subsequently coated with 50 Å of Pt and imaged with a JEOL 6700 electron microscope.

NCC particle morphology was examined via transmission electron microscopy (TEM). After sonication, a droplet from NCC suspension was placed onto a Formvar-coated copper grid (Ted Pella) and imaged in a Tecnai T12 microscope at 120 kV. Transmission UV-vis spectroscopy was performed with a Thermo Scientific Evolution 220 spectrometer in the spectral range from 300 to 800 nm. Fourier transform infrared spectroscopy (FTIR) was performed with a Nicolet Magna-IR 760 spectrometer from 4000 to 800 cm^{-1} with a resolution of 2 cm^{-1}. Samples were ground with KBr powder and pressed into pellets for FTIR analysis.

6.2.6 Statistics

SEM size measurements were performed using ImageJ software (NIH). Each reported feature size for NCC composites was averaged from 200 individual measurements each from three separate SEM images. Methylcellulose composites were averaged from 200 measurements. Size and angle distributions were plotted from these data sets. Data are presented as a mean ± 1 standard deviation. Histograms were produced by binning data sets from each image into 5 nm bins, averaging the counts for each bin, and then scatter plotting the averages. Bins are defined by the largest measurement accepted in that bin, e.g., the 20 nm bin contains all measurements that fall between 15 nm to 20 nm. Error bars for these histograms were calculated as standard error with n = 3.

6.3 Results

6.3.1 Collagen Gel Network Morphology

The neat collagen samples (NC0) consist of arrays of fibrils with largely random orientation and highly variable diameter (Figure 6.2a). A cross-sectional image of NC0 (Figure 6.2b) indicates the formation of some lamellar structure, but these lamellae are internally disordered and have many fibrils directed "out of plane." Whereas the fibril diameter and orientation *in vivo* would be controlled by proteoglycans binding to the fibrils, *in vitro* there are no such controls. However, when NCC is added to the collagen mixture (NC2 and NC16), the fibrils formed are more uniform in size, and are aligned relative to each other (Figure 6.2c–e). The NC2 cross-sectional image (Figure 6.2d) shows most fibrils running along the same direction throughout the thickness of the film. Additionally, NCC particles can be observed on the interior of the film. Higher magnification images (Figure 6.3) and images of wide areas of the sample (Figure 6.4) have also been included to more clearly depict the fibril alignment, as well as its extended continuity over the produced films. These changes are quantified via SEM image analysis (Figure 6.5), which shows that the fibrils formed in the presence of NCC have both a narrow size distribution and a uniform orientation relative to one another. Meanwhile, the neat collagen sample has fibrils that are randomly oriented, and no distinct peaks are observed in the histogram (Figure 6.5b). It is interesting to note that composites formed with 2 and 16 wt% NCC have essentially identical size and angle distributions; the values of full-width half-maximum for the NC2 and NC16 angle distributions are 18° and 16°, respectively.

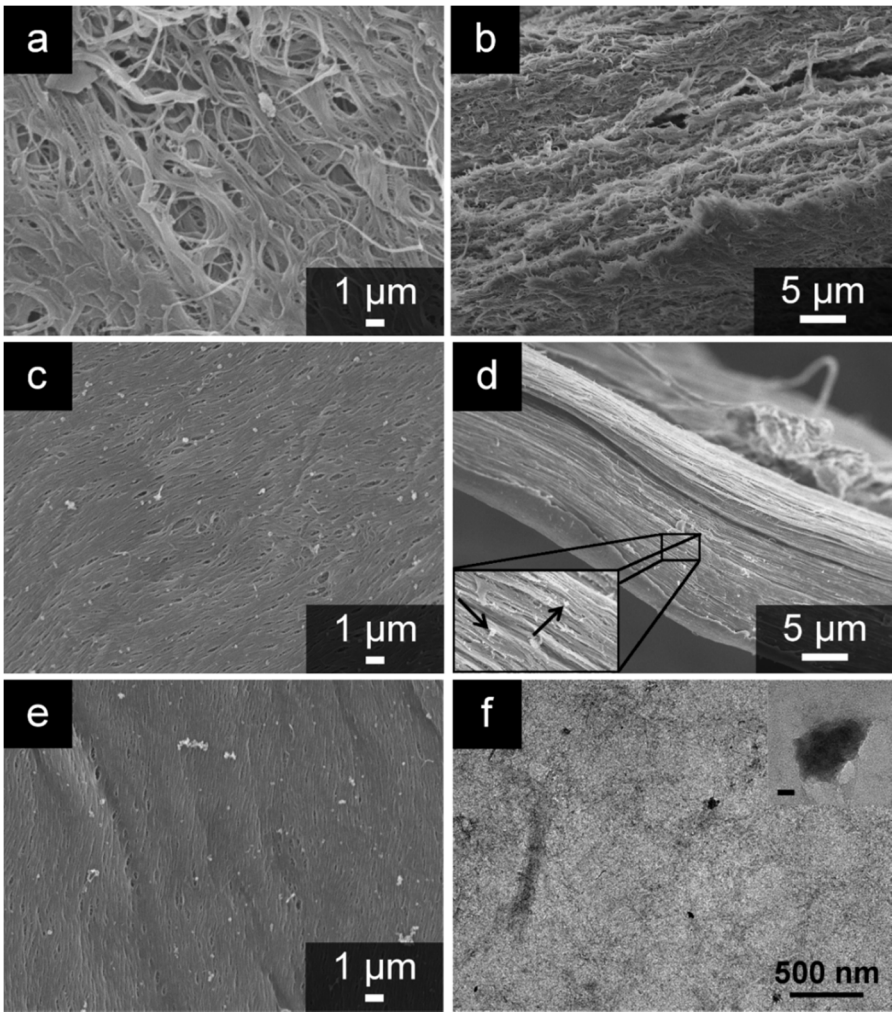

Figure 6.2. SEM images of collagen gelled and prepared via the method detailed above. (a) 150 mg/mL collagen (NC0). Note the large dispersity in fibril diameter and the lack of coherent direction. (b) Cross-sectional image of NC0. (c) 150 mg/mL collagen with 2 wt% NCC added before gelation (NC2). Fibrils are well-aligned and fall in a narrower distribution. (d) Cross-sectional image of NC2. Arrows in the inset point at NCC particles in the interior of the sectioned film. (e) 150 mg/mL collagen with 16 wt% NCC (NC16), similar alignment effects are observed as for NC2. NCC particles can be observed as the bright specks on the surface of the film. (f) NCC particles observed by TEM. The dark spots are the NCC particles on a Formvar film, most observed are smaller than 100 nm in diameter. Inset: a single NCC particle. Scale bar: 20 nm.

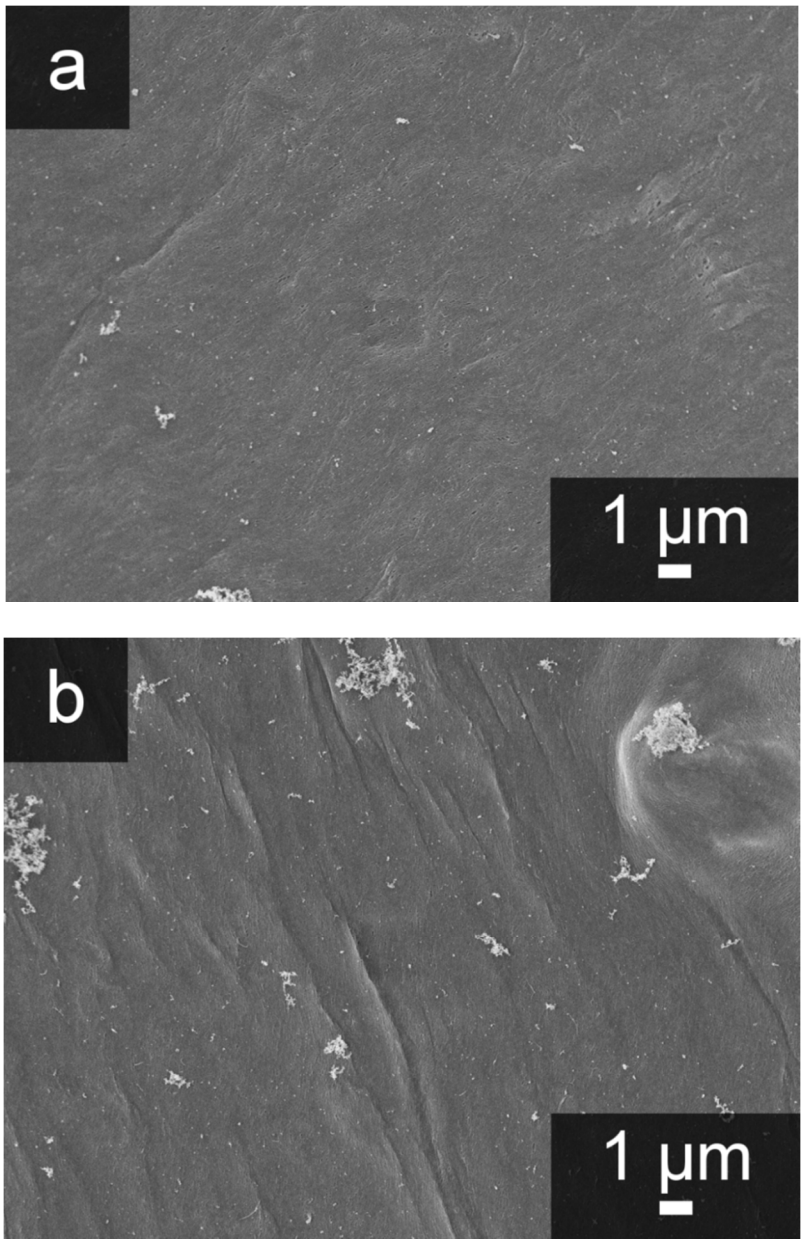

Figure 6.3. SEM images of (a) NC2 and (b) NC16 showing the alignment effect over extended areas. The images also show more large aggregates of NCC in NC16 compared to NC2, which is typical for most of these samples.

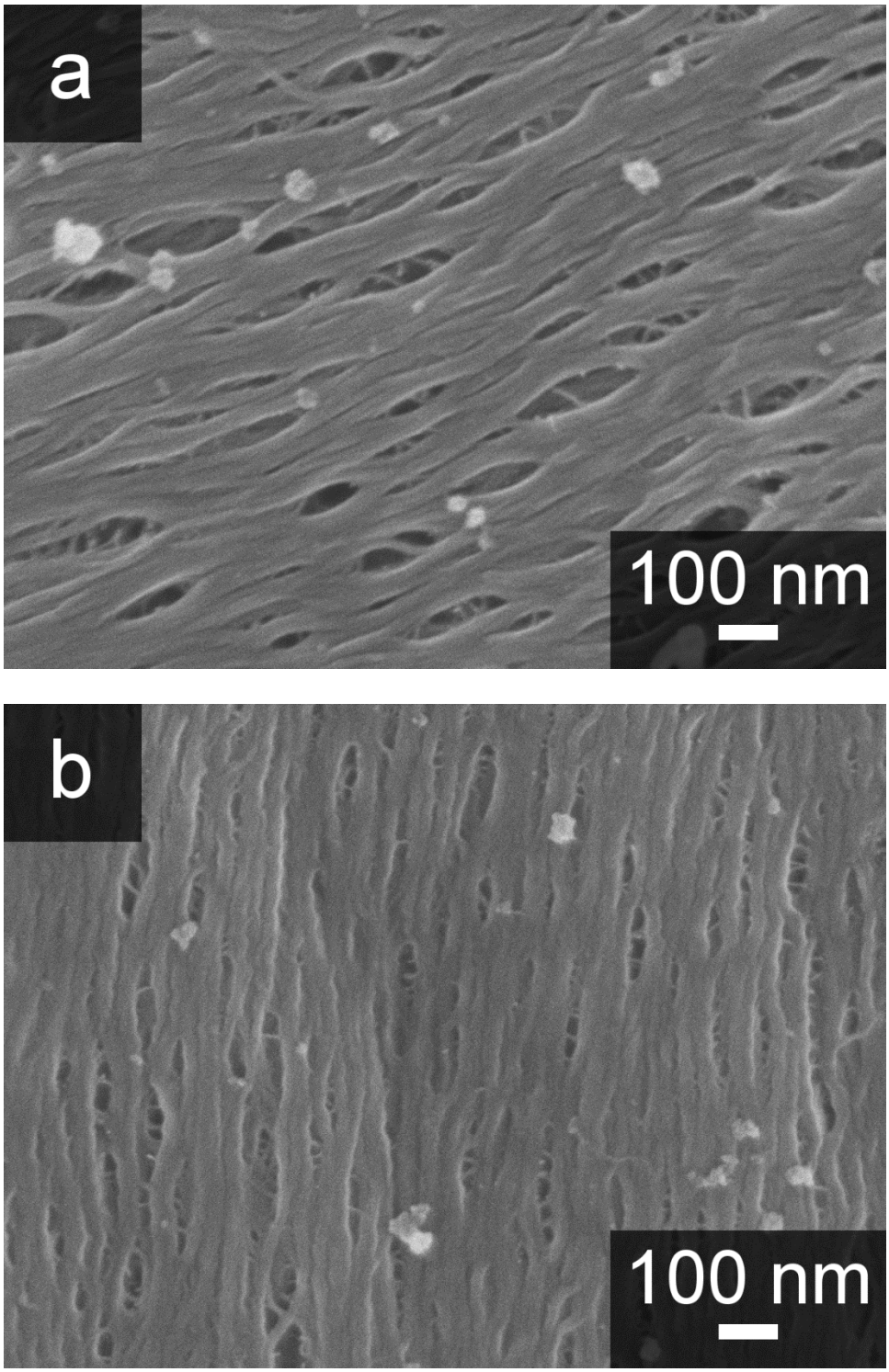

Figure 6.4. SEM images at higher magnification for (a) NC2 and (b) NC16.

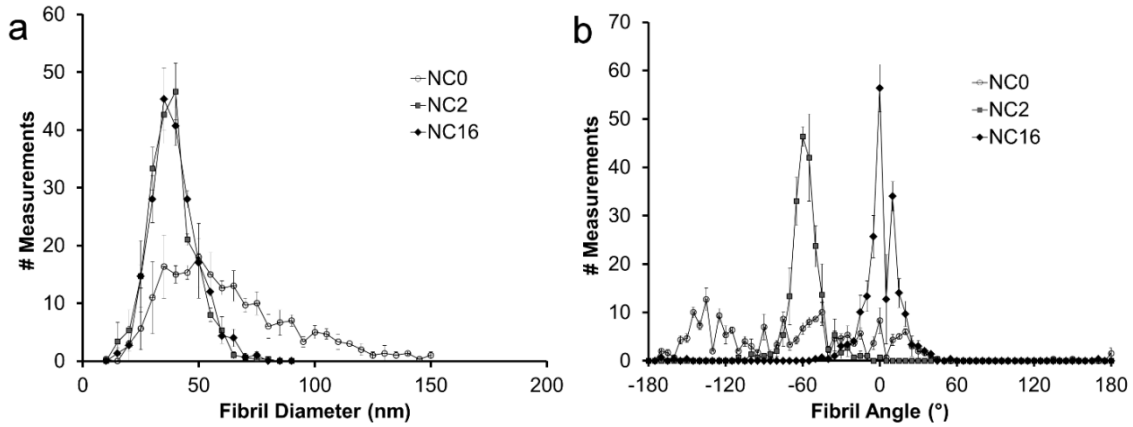

Figure 6.5. Histograms derived from measuring fibrils in SEM images. (a) Diameters of the fibrils. Addition of NCC is demonstrated to substantially narrow the distribution of fibril sizes. (b) Fibril angles relative to the absolute frame of the image. Addition of NCC produces orientation of fibrils along a narrow spread of angles.

The ultrasonicated NCC particles in suspension are under 100 nm in size and have been imaged via TEM (Figure 6.2f). They are also visible in the SEM images at the surface of the collagen film, though these particles are between 50 and 300 nm in size. There is evidence of NCC particle aggregation in the images which likely explains the size discrepancy. Additionally, due to the low mass fraction of NCC, most particles are likely below the surface (as evidenced by the cross-sectional image) and entangled with the fibrils themselves. Considerably greater aggregation of NCC particles is observed for the NC16 sample.

The fibril diameters for NC0, NC2, and NC16 are 64 ± 36 nm, 36 ± 10 nm, and 37 ± 10 nm respectively. This indicates that the amount of NCC loading has little effect on the

morphological characteristics of the resultant collagen fibrils, as long as some NCC is present. For comparison, fibrils in the cornea typically have diameters of 25–35 nm.[145, 263] It should be noted that the samples were critical-point dried (CPD) before imaging in order to preserve the microstructure; while this procedure successfully retains the structure, it does not avoid sample shrinkage entirely. CPD processing of biological tissues typically results in feature shrinkage of 20–30%.[270]

The transparency of the collagen and the NC2 is similar, >90% across the visible range (Figure 6.6). Within that range, the NC2 sample has marginally improved transparency, on the order of 3%. This is attributed to reduced scattering as a result of fibril alignment. The transparency of the NC16 sample is, however, diminished. Considering that the morphologies of the NC2 and NC16 samples are similar, the difference in optical behavior is likely due to the aggregate particles of NCC which form at the higher concentration (see also Figure 6.3), causing increased scattering (inset, Figure 6.6).

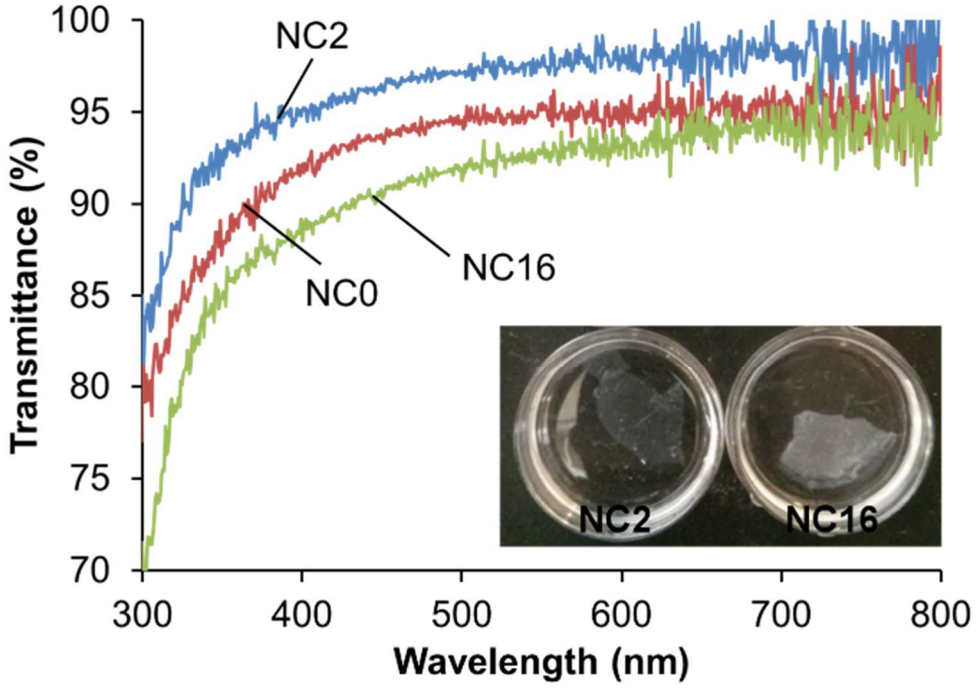

Figure 6.6. UV-vis spectra of collagen composites prepared with 0, 2, and 16 wt% NCC, and comparable thickness (~200 μm). Scattering behavior is wavelength-dependent, thus the decreased transmittance observed at lower wavelengths. Inset: the difference in transparency between NC2 and NC16 can be seen by eye.

6.3.2 Biocompatibility

The fluorescence images in Figure 6.7 show that HFF cells attach and begin to spread out on the composite gel surface after 1 h of incubation. Greater than 99% of the cells that have attached are viable based on staining. After 24 h, no dead cells are present, and the morphology of the cells becomes more typical of fibroblasts (elongated with pseudopodia extended over greater distances), indicating good attachment on the composite. By 72 h, the cells have proliferated and a more confluent layer of cells is formed on the gel surface with no indication of detachment or cell death.

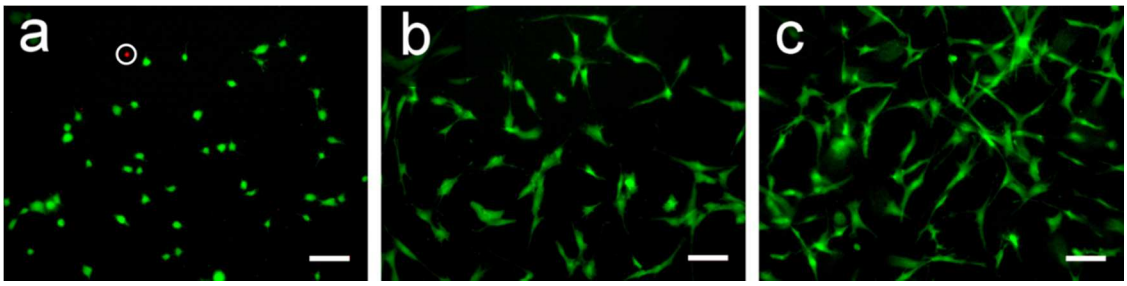

Figure 6.7. Fluorescent images of HFFs cultured on the surface of the NC2 composite gel obtained after (a) 1 h, (b) 24 h, and (c) 72 h of incubation. The calcein AM stain shows good cell viability and growth over 3 days (green = viable, red/circled = dead). The length of the scale bars is 10 μm.

6.3.3 Chemical Interactions

The interactions between collagen fibrils and NCC were examined using FTIR spectroscopy (Figure 6.8), focusing particularly on the behavior of the high frequency N–H and O–H stretching vibrations. The spectra for neat collagen (NC0) and NCC show distinct features in this region. The NCC has a broad plateau spanning from 3700 to 3100 cm^{-1} with a maximum at 3400 cm^{-1}, whereas NC0 has a narrower, sloped peak spanning from 3650 to 3150 cm^{-1} with a maximum at 3360 cm^{-1}. If there were no chemical interaction between the two phases in the composite, one would expect the NC16 peak to be the weighted sum of the NC0 and NCC –OH bands. Instead, the difference spectrum (NC16 – NC0, Figure 6.8b) yields a pattern that is dissimilar from the NCC spectrum. This indicates a change in the hydrogen bonding environment of the collagen due to the addition of NCC.

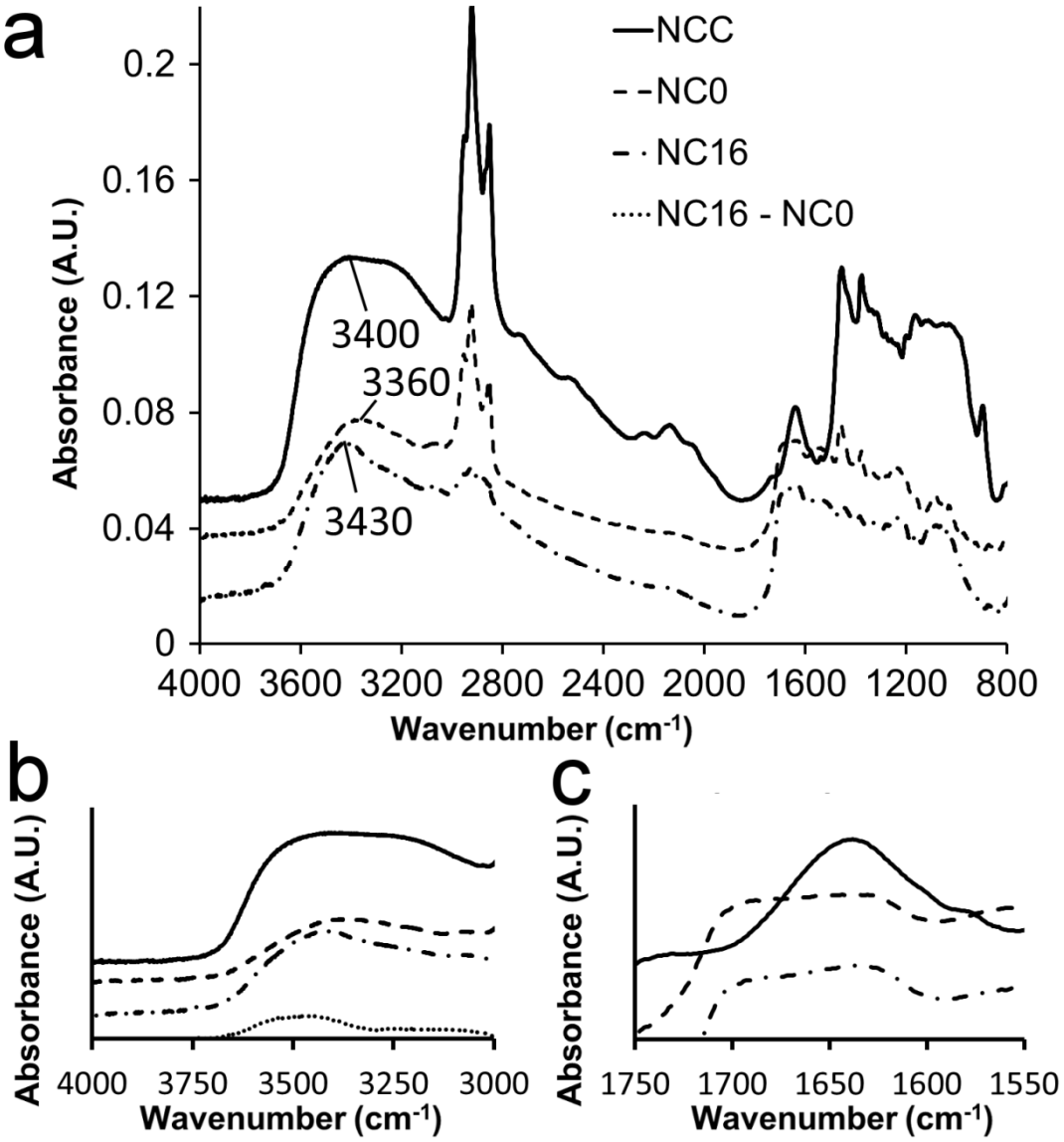

Figure 6.8. FT-IR spectra for NCC, collagen (NC0), and composite (NC16) samples. (a) Spectral region from 4000 to 800 cm-1. (b) Expanded region from 4000 to 3000 cm^{-1}, including a difference spectrum generated by subtracting the NC0 spectrum from the NC16 spectrum to show the peak shift induced by the addition of NCC. (c) Expanded region from 1750 to 1550 cm^{-1}, showing that the addition of NCC caused no change in the amide I region. Spectra have been offset for clarity.

The appearance of the broad peak from 3650 to 3150 cm^{-1} in the FTIR spectrum of collagen is due to an overlap of O–H stretching vibrations ("free": 3700–3500 cm^{-1} and hydrogen bonded: 3600–3200 cm^{-1}) and the so-called "amide A" vibrations (centered at 3300 cm^{-1}).[271] Examining changes in amide A vibrations are a good way to evaluate the hydrogen bonding behavior of the collagen backbone, as unlike the more-commonly studied amide I peaks (1600 to 1700 cm^{-1}), amide A is unaffected by the conformation of the backbone.[271] These vibrations are highly affected by the hydrogen bonding environment of the functional groups in question; hydrogen bonded groups tend to shift the absorption peaks to lower wavenumbers. The addition of NCC to collagen shifts the peak of the stretching vibrations up to ~3430 cm^{-1}, which is typically associated with "free" or non-hydrogen bonded amide stretching.[272] Meanwhile, the amide I peak remains unchanged between NC0 and NC16, indicating that the secondary structure of the collagen molecules has been largely unaltered (Figure 6.8c).

To examine the effect of surface polarity of the additive on the alignment and formation of collagen, NCC was substituted with methylcellulose. Methylcellulose is a common lubricant and food additive produced by reacting methyl halides with plant-derived cellulose, replacing the polar hydroxyl groups of cellulose with a non-polar methoxy group. This substitution results in a disordered collagen matrix (Figure 6.9). Unlike the NCC composites, the methylcellulose composites had no preferred orientation for fibrils. The orientation of fibrils in these images was random, much like the NC0 sample. However, the fibril sizes were significantly reduced, 25 ± 12 nm and 25 ± 8 nm

for 2% and 16% methylcellulose respectively, smaller even than for the NC2 and NC16 composites.

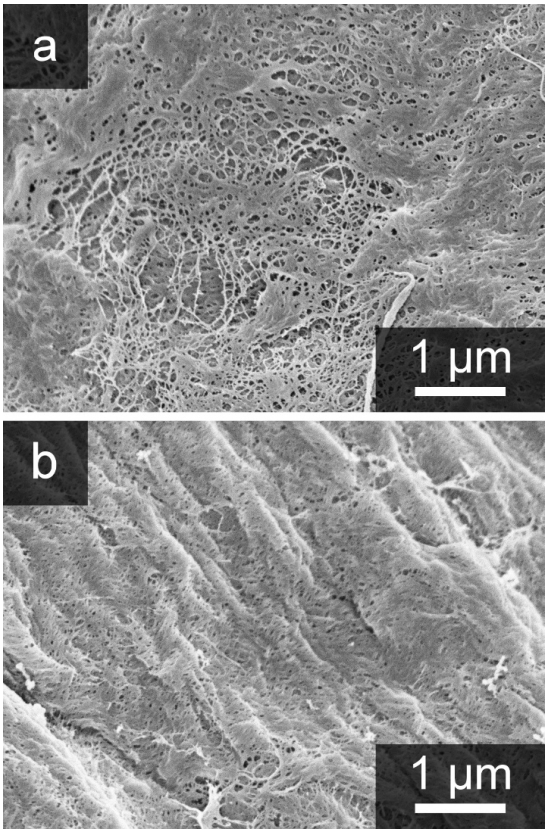

Figure 6.9. SEM images of gelled collagen networks with (a) 2 wt% methylcellulose and (b) 16 wt% methylcellulose.

6.4 Discussion

6.4.1 Formation of Collagen Gel Networks

Formation of collagen gels through pH-induced self-assembly is a well-established process in the literature.[273] Type I collagen is stable at pH 3, owing to the protonation and

increased polarity of the proline and hydroxyproline residues in collagen. When the pH is increased, individual collagen chains form a network of fibrils, causing the collagen in solution to form a gel. The mechanism of this process—called fibrillogenesis—is the subject of some disagreement in the literature, due to the complex reaction kinetics. Many researchers conclude that fibrillogenesis follows a nucleation and growth pathway,[274, 275] others contradict this and propose that the gel grows by accretion without nucleation sites.[276] Still others prefer to model it as diffusion-limited aggregation of the collagen molecules.[277] In any of these cases, increasing the pH to approximately 9 (the isoelectric point of collagen)[278, 279] causes the collagen molecules to collide and form superstructures in the form of networked fibrils, owing to the hydrogen bonding that occurs between collagen molecules.

The results in this study demonstrate that these collagen fibrils can be aligned through the addition of NCC. This alignment is observable throughout the thickness of the film, comprising multiple layers of aligned fibrils. The films produced with low NC2 have a slightly higher transparency in the visible spectrum, which may be explained by the enhanced alignment of the structure. Higher loading of NCC in the composites (16 wt%) was observed to increase aggregation and lead to larger NCC particles; this is correlated with a decrease in transparency below that of the neat collagen gels. Despite the alignment of the fibrils, the NCC aggregates scatter enough light to negatively impact the transparency of the film at the higher NCC loadings.

6.4.2 Mechanism of Collagen Alignment

Given that collagen gelled under the same conditions detailed above does not form aligned fibrils in the absence of NCC, the cause of the alignment in nanocomposites must be related to interactions of collagen with the surfaces of the NCC particles. Up to one third of the amino acid residues in collagen consists of hydroxyproline, which contains an uncoordinated hydroxyl group. It has been shown in the literature that collagen preferentially adheres to hydroxylated or carboxylated polymer surfaces;[280, 281] it is likely that the hydroxyproline hydroxyl group hydrogen bonds with these polar surfaces. So, when NCC particles are introduced to collagen suspensions, they create energetically-preferred sites for adhesion of collagen polypeptides, by virtue of their hydroxylated (and thus polar) surfaces. On these particles, the molecules may partially align prior to the pH-induced gelation.

Considering the proposal that NCC particles provide low-energy sites for adhesion of collagen, we can envision that the number of energetically-viable conformations for collagen self-assembly is effectively constrained. Considering that many researchers have characterized collagen fibrillogenesis as a nucleation-and-growth process, we suspect a similar process at work in the generation of ordered fibril domains: with NCC present, fibrils tend to form at the particle surfaces, limiting their degrees of rotational freedom and preventing entanglement during gelation. This yields large regions in which the fibrils share a preferred orientation (Figure 6.10) and then maintain that orientation during further growth, i.e., the inclusion of progressively more fibrils via collagen-to-collagen hydrogen bonding. Additionally, the size of the NCC particles in this study is

comparable to the fibril-to-fibril spacing in proteoglycan-mediated collagen gels,[282] and the NCC particles may act as spacers, much like proteoglycans in the native cornea.[262] The observed reduction in fibril diameter that occurs with the addition of NCC and especially with methylcellulose is likely related to this spacing effect, or "molecular crowding."[143]

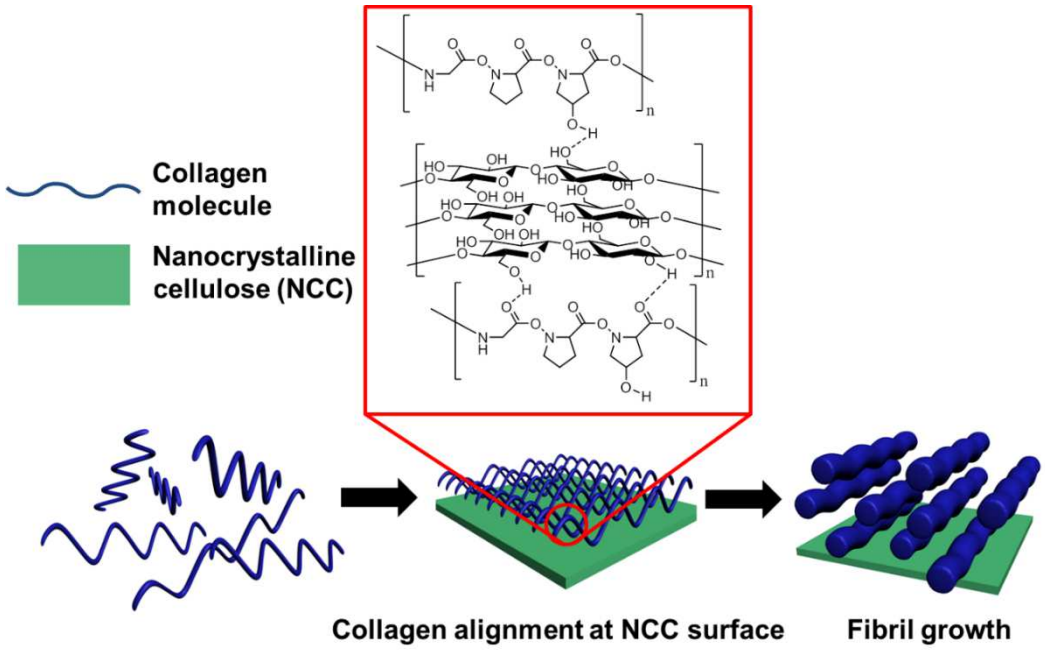

Figure 6.10. Proposed mechanism of fibril alignment. Free collagen molecules (blue) in solution preferentially adhere to NCC particles (green) due to hydrogen bonding between the collagen side chains and the NCC surface. The surface-stabilized collagen molecules form oriented fibrils, generating a preferred alignment in the final structure. Possible hydrogen bonding interactions between two collagen polypeptides and NCC are shown in the red box.

Evidence of this adhesion through hydrogen bonding interactions can be observed in the FTIR spectrum of the composite material (Figure 6.8), particularly in the peak position and shape of absorption bands. In general, N–H and O–H stretching absorption

bands are broad due to the tendency of these groups to participate in inter- and intramolecular hydrogen bonding in a variety of conformations and bonding environments. Increased hydrogen bonding of a group leads to a decrease in the wavenumber of the absorption. Hence, our observation of a peak shifting in the opposite direction—an increase in wavenumber—indicates a reduction in hydrogen bonding resulting from the addition of NCC; specifically a reduction in hydrogen bonding involving the amide linkages on the backbone of the collagen. The primary mode of intermolecular hydrogen bonding in peptides is N–H donating to C=O. Partial replacement of these interactions with NCC O–H to collagen C=O bonds (Figure 6.10, panel in red box) would result in an increase in free N–H groups on the collagen backbone, producing the observed peak shift. This model also explains the lack of change in the amide I region after addition of NCC, as any affected C=O groups remain hydrogen bonded to NCC O–H donor groups. Additionally, hydrogen bonding between side chains and the NCC surface could sterically inhibit interaction of the collagen backbone with other collagen molecules. This behavior would only affect the collagen molecules at the surfaces of fibrils, thus the subtlety of the change in peak shape.

These observations support the hypothesis that surface interactions between collagen and NCC are responsible for the alignment of collagen during gelation. Cellulose is highly ordered in three dimensions, as a result of hydrogen bonding between the linear chains of saccharides. Thus, despite the high affinity of water for the surface of cellulose, the particles resist swelling and remain tightly-packed solids, even when dispersed in aqueous suspension. If this hydrogen bonding is disrupted (e.g., through partial

methylation of the material), the cellulosic chains have less affinity for each other and can be more readily swollen by water. This produces a viscoelastic fluid, rather than a suspension of rigid particles. Greminger and Savage note that methylcellulose colloids remain similar in shape to the original cellulose.[283] Upon solvation, the structure expands to accommodate water, but the overall morphology of particles is retained, indicating that a change in the cellulose particle shape is not a factor in the ordering of collagen fibrils.

As the replacement of –OH groups in cellulose with $–CH_3$ substantially limits the intramolecular hydrogen bonding in the molecule, it stands to reason that intermolecular bonding would be affected as well. Considering that the ordered structures we observe with NCC composites are accompanied by changes in hydrogen bonding, disrupting the ability of the methylcellulose to form these bonds should result in morphologies similar to that of neat collagen, i.e., where hydrogen bonding occurs exclusively between collagen molecules. This is indeed observed, the only notable difference being a reduction in fibril size, which is likely caused by diffusion limitations introduced by adding a nonpolar phase to the collagen and by the crowding effects mentioned above.

6.5 Conclusions

Collagen fibrils can be aligned directly in aqueous solution with no further processing by adding a small weight percentage of NCC. The obtained fibrils are ~36 nm in diameter and possess reasonably low polydispersities (~20–25%, compared with over 50% for single-phase collagen gels). Alignment persists on the mm scale. The addition of 2 wt% NCC to the collagen gel increases the transparency of the gel slightly, however, at higher concentrations, the NCC additive leads to light scattering and reduced transparency. The

composites are biocompatible, as cells seeded on the composites attach and grow without issue. The mechanism for collagen alignment is elucidated in part, involving adhesion of collagen to NCC particles via hydrogen bonding between the structures. Future studies may further explore the causes of this phenomenon.

6.6 Acknowledgements

Michael DiVito constructed a device for concentration of collagen, and provided all the high-concentration collagen for this work. Additionally he provided the biocompatibility analysis shown in Figure 6.7 and discussed in section 6.3.2.

Chapter 7: Future Directions for Porous Materials Design

7.1 Chemical Energy Storage via Thermochemical Cycling

The work encompassed by this thesis has demonstrated the substantial kinetic advantages for conversion of CO_2 to CO that can be obtained through CeO_2 catalyst materials with templated porosity and increased surface area. In particular, this work has shown that by increasing the kinetics of the oxidation step, significant CO_2 to CO (or H_2O to H_2) conversion can be realized at temperatures nearly 250 °C lower than typically used in the literature.[208] At these temperatures, tenfold improvement in total gas release was observed for 3DOM CeO_2 over a sintered CeO_2 sample. Additionally, the 3DOM material's oxidation rate was at least 4 times faster than the sintered material, conclusively demonstrating the need for high-surface-area catalysts. Still, the total gas evolved was smaller than sintered materials, which can be used at higher temperatures.

In the broader context of the literature, even ultra-high-temperature processes (at or above 1500 °C) fail to realize meaningful solar-to-fuel efficiencies, with the highest reported values currently sitting just below 2%.[158] For comparison, polycrystalline silicon photovoltaic (PV) cells have a solar-to-electric efficiency of ~15%.[284] Even when paired with a water electrolyzer to generate H_2 operating at 50% efficiency (some processes can reach up to 90%),[285] this would lead to a solar-to-fuel efficiency of 7.5%. For the time being, direct thermochemical reduction of H_2O and CO_2 over CeO_2 still requires significant improvements before being competitive with PV-based technologies.

That said, CeO_2-based materials offer a considerable improvement over other two-step cycling materials, such as Fe_2O_3 and ZnO, in that they remain as a single solid crystalline phase throughout the process. When thermally reduced, CeO_2 only develops oxygen vacancies throughout the lattice, rather than undergoing melting, sublimation, or phase changes. However, the "depth" of reduction that can be obtained at commercially viable partial pressures of oxygen (i.e. $\sim 10^{-5}$ atm pO_2, the level typically observed in industrial grade N_2)[286] is insufficient to achieve competitive efficiencies in the bulk material unless the process temperature exceeds 1400 °C.[287]

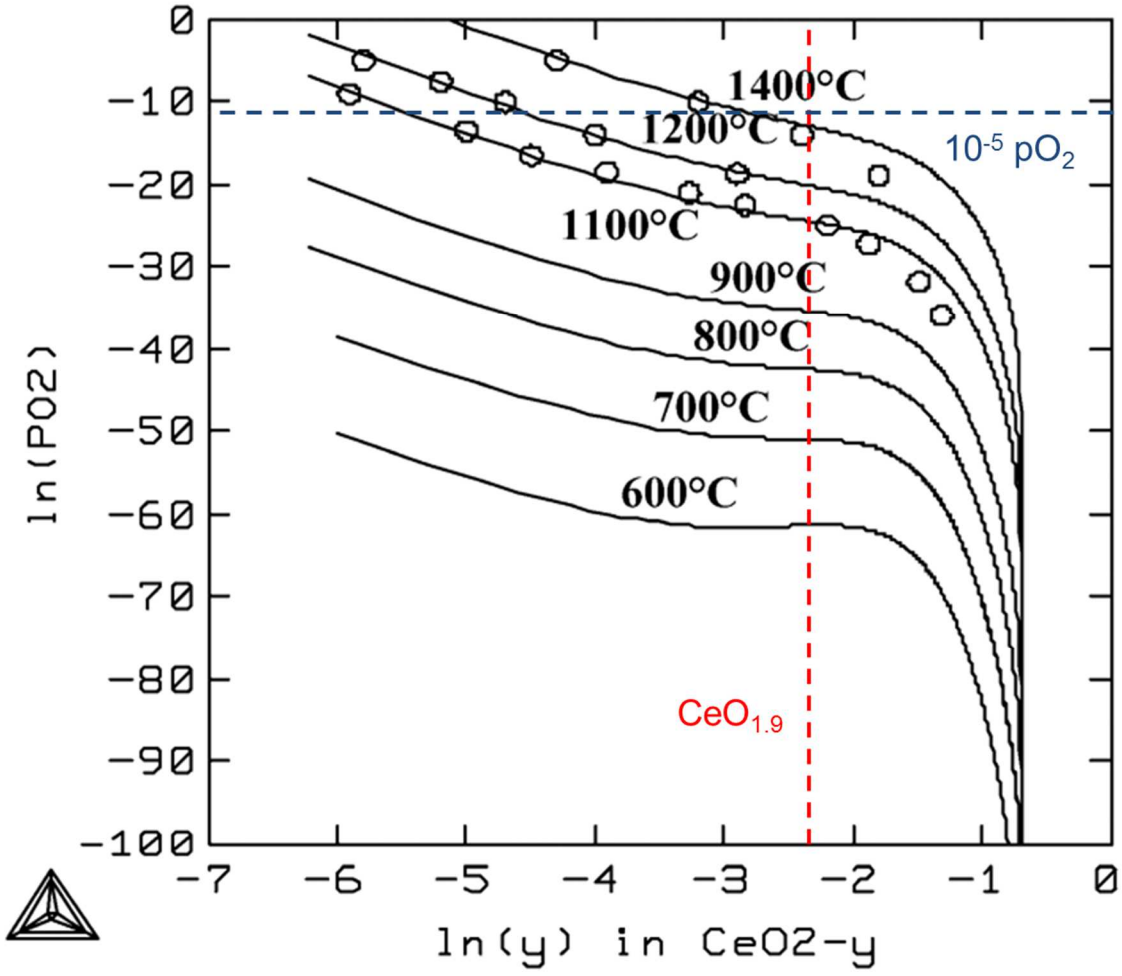

Figure 7.1. CeO_2 nonstoichiometry (represented here as "y") charted vs. partial pressure of oxygen (pO_2) charted at temperatures from 600 °C to 1400 °C. The lines are calculated values, while the circles are experimental data points. The dashed lines indicate appropriate conditions, a nonstoichiometry of 0.1 mol O/formula unit and 10^{-5} pO_2. Note that to achieve this nonstoichiometry at this pO_2, temperatures greater than 1400 °C are necessary. Image adapted from ref. 287 with permission.[†]

Chapter 2 demonstrated substantial benefits in the time-to-completion of the oxidation step when the catalyst material retains significant porosity and small feature

[†] Reproduced from Huang, S.; Li, L.; Van der Biest, O.; Vleugels, J., Influence of the oxygen partial pressure on the reduction of CeO_2 and CeO_2ZrO_2 ceramics. *Solid State Sci.* **2005,** 7, 539-544. Copyright © 2005 Elsevier Masson SAS. All rights reserved.

sizes. These approaches have seen limited application in the literature, as the desired operating temperatures for the reaction exceed 1400 °C. Indeed, the work presented in Chapter 3 has shown that maintaining the nanoscale structure of 3DOM CeO_2 materials in the 300–500 nm pore range at these high temperatures remains extremely difficult, if not practically impossible.

With these issues in mind, future basic research on solar thermochemical cycling should take a two-pronged approach: seek new oxygen-storage materials with even lower reduction temperatures than CeO_2 and, simultaneously, explore other high-surface-area structures that are less vulnerable to sintering. We have undertaken some initial investigations along these lines. Many perovskite-type structures can reversibly store and release oxygen, such as $YBaCo_4O_7$ (YBCO).[74, 288] This material is interesting as it accommodates a substantial oxygen nonstoichiometry, much like CeO_2, but at temperatures in the 400–1000 °C range. Our initial research supported this observation, but revealed that the YBCO material's kinetics were far too slow to be of use for rapid thermochemical cycling; 1 h of thermal treatment at 1100 °C was required to observe any O_2 production during the reduction step.

In an effort to produce microscale porosity in a framework that would similarly isolate walls from one another to reduce the deleterious effects of sintering on surface area, CeO_2 materials were produced using wood as a template.[192] These structures were able to retain significant surface area and reactivity even during thermochemical cycling at 1400 °C, producing up to 3 times the amount of CO as the 3DOM material in Chapter 2, with a similar oxidation time.

The bottleneck to discovering new materials capable of driving H_2O and/or CO_2 reduction thermochemically lies in the reactivity testing step. Either new reactor systems must be designed that could cycle in parallel, or, preferably, the capacity for generation of oxygen nonstoichiometry and/or kinetics thereof could be reduced to electrochemically measurable parameters. This would allow for truly rapid experimental screening of any new materials synthesized. Alternately, the energies of formation for oxygen vacancies for a number of lattices can be determined (with high accuracy) via computational methods. Barring an advance on experimental throughput, the screening process could be accomplished via modeling, providing a smaller range of promising test materials.

While solar thermochemical fuel production is unlikely to be a "silver bullet" for humanity's current and future energy challenges, it is similarly unlikely that any silver bullet exists. Transitioning our energy production infrastructure to 100% renewable resources will require a wide portfolio of many technologies. With a few key breakthroughs, as outlined above, this technology may have a place in that portfolio.

7.2 Sol-Gel Materials via Phase Separation

Prior to the research detailed in this thesis, microstructured ceramic materials generated through polymerization-induced phase separation (PIPS) could only be produced from a select few oxides, primarily SiO_2, TiO_2, and ZrO_2, as the tetrachlorides of the non-oxide atoms in question readily form alkoxides. Chapters 4 and 5 detail a method by which these structures can be generated from any metal cation that forms a water-soluble nitrate salt (aptly, Si, Ti, and Zr do not, as they are unstable with respect to the formation of oxygen anions in aqueous solution). Not only does this method allow for

production of μm-scale bicontinuous networks and microspheres, but it also produces hierarchical materials through the inclusion of a colloidal crystal host matrix for the PIPS process.

Chapter 5 poses some open questions regarding the methodology, all of which are worthy of continuing study and primarily focus on investigating the effects of cation properties on the mechanism of phase separation. A broader study on a variety of cations would yield greater insight into the mechanism while concurrently expanding the efficacy of the method across the periodic table. What is still lacking in this research, both in the Nakanishi studies and the research presented in Chapters 4 and 5, is scope and resolution on the microstructure quasi-phase diagrams.

The most effective experiments to include in this hypothetical study would be obtaining real molecular weight distributions for a variety of precursor composition, via techniques such as size-exclusion chromatography (SEC) or matrix-assisted laser desorption/ionization (MALDI). Interpretation of SEC in the context of branched polymers can be somewhat difficult, insofar as the selection of appropriate standards is concerned.[289] MALDI functions on time-of-flight mass spectrometry, so as long as the polymer chains can be ablated intact, there should be no issues with interpretation.[290]

Once molecular weights are obtained, the proposed dependence on molecular weight in Chapters 4 and 5 could be directly verified, and expansion into new metals would likely become trivial. As long as the appropriate average molecular weight can be produced in a precursor gel containing that metal, the gel should generate the desired

microstructure. Once these relationships are more quantitatively understood, this technology can be considered mature.

7.3 Formation of Ordered Collagen Fibrils

The final section of this thesis describes a method for producing films of aligned collagen fibrils. Fibril alignment is accomplished through the incorporation of NCC into the structure, and a mechanism for this alignment behavior is proposed based on the hydrogen bonding interactions between the collagen and the NCC. At present, several strategies exist to align fibrils, but many are poorly scalable, such as electrospinning[268] or shear flow.[267] NCC is an inexpensive, bio-derived, and biocompatible material, and the synthesis procedure detailed here requires only reconcentration of the collagen, direct mixing with NCC, and a pH change to induce gelation.

However, the synthesized films have a distinctly different collagen structure from the cornea. For the production of a truly synthetic cornea with full mimicry of the tissue's ultrastructure, the materials produced during the work described in Chapter 6 actually order too well. The domain size of these aligned fibrils (that is, the area in which the fibrils all share a single orientation), is on the order of millimeters. The cornea, meanwhile, consists of a series of "patches," each with its own fibril orientation.[145] This is how the cornea possesses such uniform tensile strength. If the NCC hybrids produced in this thesis were subjected to tensile testing, we suspect that anisotropic results would be obtained, as pulling in line with the film's fibril orientation would yield a high strength, while pulling perpendicular to that orientation would result in rapid failure. Unfortunately, this suspicion is non-trivial to confirm; characterization techniques that

allow probing of the fibrils orientation (such as electron microscopy) tend to be destructive, as they require fixation and coating. It was thus difficult to ascertain the orientation of a fibril film prior to testing, and constraints on reagent availability precluded the generation of a large and statistically significant data set to probe this effect.

Thus, future research on this project specifically should focus on ways to reduce the domain size generated by NCC addition. In all probability, this involves perturbing the ordering process during gelation of the collagen, perhaps through slight weakening of the hydrogen bonding interactions between collagen and NCC. One way to accomplish this could be to add varying concentrations of a competing hydrogen bond donor/acceptor along with the NCC, such as poly(acrylic acid).

7.4 A Self-Assembled Conclusion

These somewhat disparate studies all have a common thread that ties them together: the design and/or influence of material micro- and nanostructure guided by basic principles of bonding, intermolecular interactions, and diffusion. While so-called "top-down" methods for the production of designed porosity and structure (such as lithography) can answer many academic and commercial applications, these processes remain difficult to scale. There is a great need to bring morphology control out of the vacuum system and in to the wet lab, and this thesis constitutes a focused effort to do just that. The research detailed here is wholly focused on creating and exploring flexible, yet remarkably facile approaches to producing designed structures.

The dream of solution-phase materials design, and indeed, of nanotechnologists everywhere, is atom-by-atom control over extended domains of solid-state structures. We may never get there, but the work in this thesis indicates that there are plenty of ways to influence and bend molecules' natural tendencies to our purposes. Perhaps the way forward is to think less as players or micromanagers, and more as conductors of a molecular orchestra. Nature and physics have provided us the score, but it is up to us to determine the performance.

Bibliography

1. Perego, C.; Millini, R., Porous materials in catalysis: challenges for mesoporous materials. *Chem. Soc. Rev.* **2013,** 42, 3956-3976.
2. Parlett, C. M. A.; Wilson, K.; Lee, A. F., Hierarchical porous materials: catalytic applications. *Chem. Soc. Rev.* **2013,** 42, 3876-3893.
3. Bae, Y.-S.; Snurr, R. Q., Development and Evaluation of Porous Materials for Carbon Dioxide Separation and Capture. *Angew. Chem. Int. Ed.* **2011,** 50, 11586-11596.
4. Li, J.-R.; Kuppler, R. J.; Zhou, H.-C., Selective gas adsorption and separation in metal-organic frameworks. *Chem. Soc. Rev.* **2009,** 38, 1477-1504.
5. Wang, G.; Zhang, L.; Zhang, J., A review of electrode materials for electrochemical supercapacitors. *Chem. Soc. Rev.* **2012,** 41, 797-828.
6. Ji, L.; Lin, Z.; Alcoutlabi, M.; Zhang, X., Recent developments in nanostructured anode materials for rechargeable lithium-ion batteries. *Energ. Environ. Sci.* **2011,** 4, 2682-2699.
7. Mumpton, F. A., La roca magica: Uses of natural zeolites in agriculture and industry. *P. Natl. Acad. Sci. USA* **1999,** 96, 3463-3470.
8. Armor, J. N., A history of industrial catalysis. *Catal. Today* **2011,** 163, 3-9.
9. Stöber, W.; Fink, A.; Bohn, E., Controlled growth of monodisperse silica spheres in the micron size range. *J. Colloid Interf. Sci.* **1968,** 26, 62-69.

10. Holland, B. T.; Blanford, C. F.; Stein, A., Synthesis of Macroporous Minerals with Highly Ordered Three-Dimensional Arrays of Spheroidal Voids. *Science* **1998,** 281, 538-540.

11. Fan, J.; Weng, D.; Wu, X. D.; Wu, X. D.; Ran, R., Modification of CeO_2–ZrO_2 Mixed Oxides by Coprecipitated/Impregnated Sr: Effect on the Microstructure and Oxygen Storage Capacity. *J. Catal.* **2008,** 258, 177–186.

12. Yan, H.; Blanford, C. F.; Holland, B. T.; Smyrl, W. H.; Stein, A., General synthesis of periodic macroporous solids by templated salt precipitation and chemical conversion. *Chem. Mater.* **2000,** 12, 1134-1141.

13. Reese, C. E.; Asher, S. A., Emulsifier-free emulsion polymerization produces highly charged, monodisperse particles for near infrared photonic crystals. *J. Colloid Interf. Sci.* **2002,** 248, 41-6.

14. Nagpal, P.; Josephson, D. P.; Denny, N. R.; DeWilde, J.; Norris, D. J.; Stein, A., Fabrication of carbon/refractory metal nanocomposites as thermally stable metallic photonic crystals. *J. Mater. Chem.* **2011,** 21, 10836-10843.

15. Sadakane, M.; Kato, R.; Murayama, T.; Ueda, W., Preparation and formation mechanism of three-dimensionally ordered macroporous (3DOM) MgO, $MgSO_4$, $CaCO_3$, and $SrCO_3$, and photonic stop band properties of 3DOM $CaCO_3$. *J. Solid State Chem.* **2011,** 184, 2299-2305.

16. Lee, K. T.; Lytle, J. C.; Ergang, N. S.; Oh, S. M.; Stein, A., Synthesis and rate performance of monolithic macroporous carbon electrodes for lithium-ion secondary batteries. *Adv. Funct. Mater.* **2005,** 15, 547-556.

17. Park, S. H.; Xia, Y., Macroporous membranes with highly ordered and three-dimensionally interconnected spherical pores. *Adv. Mater.* **1998,** 10, 1044-1047.

18. Fan, W.; Snyder, M. A.; Kumar, S.; Lee, P.-S.; Yoo, W. C.; McCormick, A. V.; Lee Penn, R.; Stein, A.; Tsapatsis, M., Hierarchical nanofabrication of microporous crystals with ordered mesoporosity. *Nat. Mater.* **2008,** 7, 984-991.

19. Denny, N. R.; Han, S. E.; Norris, D. J.; Stein, A., Effects of Thermal Processes on the Structure of Monolithic Tungsten and Tungsten Alloy Photonic Crystals. *Chem. Mater.* **2007,** 19, 4563-4569.

20. Ozin, G. A., Panoscopic materials: synthesis over 'all' length scales. *Chem. Comm.* **2000**, 419-432.

21. Zhang, H.; Yu, X.; Braun, P. V., Three-dimensional bicontinuous ultrafast-charge and -discharge bulk battery electrodes. *Nat. Nano.* **2011,** 6, 277-281.

22. Ergang, N. S.; Fierke, M. A.; Wang, Z.; Smyrl, W. H.; Stein, A., Fabrication of a Fully Infiltrated Three-Dimensional Solid-State Interpenetrating Electrochemical Cell. *J. Electrochem. Soc.* **2007,** 154, A1135-A1139.

23. Ergang, N. S.; Lytle, J. C.; Lee, K. T.; Oh, S. M.; Smyrl, W. H.; Stein, A., Photonic Crystal Structures as a Basis for a Three-Dimensionally Interpenetrating Electrochemical-Cell System. *Adv. Mater.* **2006,** 18, 1750-1753.

24. Aboav, D. A., The stability of grains in a polycrystal. *Metallography* **1971,** 4, 425-441.

25. Olevsky, E. A.; Tikare, V.; Garino, T., Multi-Scale Study of Sintering: A Review. *J. Am. Ceram. Soc.* **2006,** 89, 1914-1922.

26. Tang, X.; Li, Y.; Huang, X.; Xu, Y.; Zhu, H.; Wang, J.; Shen, W., MnO_x–CeO_2 Mixed Oxide Catalysts for Complete Oxidation of Formaldehyde: Effect of Preparation Method and Calcination Temperature. *Appl. Catal., B* **2006,** 62, 265–273.

27. Liau, L. C.-K.; Wu, R.-K., Optimal Control of the Sintering Strain Rate of Yttria-Stabilized Zirconia Electrolytes for Solid Oxide Fuel Cells Using a Thermal−Mechanical Analyzer during the Sintering Process. *Ind. Eng. Chem. Res.* **2009,** 48, 7567-7573.

28. Palmer, M. A.; Glicksman, M. E.; Rajan, K., Grain growth of thin films conforming to a curved surface. *Philos. Mag. A* **1999,** 79, 763-774.

29. Lange, F., Densification of powder compacts: An unfinished story. *J. Eur. Ceram. Soc.* **2008,** 28, 1509-1516.

30. Sokolov, S.; Bell, D.; Stein, A., Preparation and Characterization of Macroporous α-Alumina. *J. Am. Ceram. Soc.* **2003,** 86, 1481-1486.

31. Whittemore Jr, O. J.; Sipe, J. J., Pore growth during the initial stages of sintering ceramics. *Powder Technol.* **1974,** 9, 159-164.

32. Olah, G. A., Beyond oil and gas: the methanol economy. *Angew. Chem. Int. Ed.* **2005,** 44, 2636-9.

33. Solomon, S.; Qin, D.; Manning, M.; Chen, Z.; Marquis, M.; Averyt, K. B.; Tignor, M.; Miller, H. L. *Climate change 2007: the physical science basis*; Geneva, Switzerland, 2007; pp 93-93.

34. Zimov, S. A.; Schuur, E. A. G.; Chapin, F. S., III, Permafrost and the global carbon budget. *Science* **2006,** 312, 1612-1613.

35. Rignot, E.; Thomas, R. H., Mass balance of polar ice sheets. *Science* **2002,** 297, 1502-6.

36. Züttel, A.; Remhof, A.; Borgschulte, A.; Friedrichs, O., Hydrogen: the future energy carrier. *Phil. Trans. R. Soc. A* **2010,** 368, 3329-42.

37. Lyons, D. M.; Ryan, K. M.; Morris, M. A., Preparation of ordered mesoporous ceria with enhanced thermal stability. *J. Mater. Chem.* **2002,** 12, 1207-12.

38. Brabec, C.; Waidhas, M., Advanced energy materials needed. *Adv. Mater.* **2010,** 22, 4-5.

39. Kang, K.-S.; Kim, C.-H.; Park, C.-S.; Kim, J.-W., Hydrogen Reduction and Subsequent Water Splitting of Zr-Added CeO_2. *J. Ind. Eng. Chem.* **2007,** 13, 657-663.

40. Abanades, S.; Flamant, G., Thermochemical Hydrogen Production From a Two-Step Solar-Driven Water-Splitting Cycle Based on Cerium Oxides. *Sol. Energy* **2006,** 80, 1611-1623.

41. Abanades, S.; Le Gal, A.; Cordier, A.; Peraudeau, G.; Flamant, G.; Julbe, A., Investigation of Reactive Cerium-Based Oxides for H_2 Production by Thermochemical Two-Step Water-Splitting. *J. Mater. Sci.* **2010,** 45, 4163-4173.

42. Nakanishi, K.; Tanaka, N., Sol–Gel with Phase Separation. Hierarchically Porous Materials Optimized for High-Performance Liquid Chromatography Separations. *Acc. Chem. Res.* **2007,** 40, 863-873.

43. Bedrane, S., Investigation of the oxygen storage process on ceria- and ceria–zirconia-supported catalysts. *Catal. Today* **2002,** 75, 401-405.

44. Mamontov, E.; Egami, T.; Brezny, R.; Koranne, M.; Tyagi, S., Lattice Defects and Oxygen Storage Capacity of Nanocrystalline Ceria and Ceria-Zirconia. *J. Phys. Chem. B* **2000,** 104, 11110-11116.

45. Kašpar, J.; Fornasiero, P.; Graziani, M., Use of CeO_2-Based Oxides in the Three-Way Catalysis. *Catal. Today* **1999,** 50, 285–298.

46. Yang, H. G.; Zeng, H. C., Preparation of Hollow Anatase TiO_2 Nanospheres via Ostwald Ripening. *J. Phys. Chem. B* **2004,** 108, 3492-3495.

47. Kraum, M.; Baerns, M., Fischer-Tropsch Synthesis: The Influence of Various Cobalt Compounds Applied in the Preparation of Supported Cobalt Catalysts on Their Performance. *Appl. Catal. A* **1999,** 186, 189–200.

48. Spadaro, L.; Arena, F.; Granados, M. L.; Ojeda, M.; Fierro, J. L. G.; Frusten, F., Metal–Support Interactions and Reactivity of Co/CeO_2 Catalysts in the Fischer-Tropsch Synthesis Reaction. *J. Catal.* **2005,** 234, 451–462.

49. Chueh, W. C.; Haile, S. M., A Thermochemical Study of Ceria: Exploiting an Old Material for New Modes of Energy Conversion and CO_2 Mitigation. *Phil. Trans. R. Soc. A* **2010,** 368, 3269-3294.

50. Waterhouse, G. I. N.; Metson, J. B.; Idriss, H.; Sun-Waterhouse, D., Physical and optical properties of inverse opal CeO_2 photonic crystals. *Chem. Mater.* **2008,** 20, 1183-1190.

51. Funk, J. E., Thermochemical Hydrogen Production: Past and Present. *Int. J. Hydrogen Energ.* **2001,** 26, 185-190.

52. Pfeffer, R. A.; Macon, W. A., Nuclear Power: An Option for the Army's Future. *Army Logis.* **2001,** 33, 4-8.

53. Funk, J. E.; Reinstrom, R. M., Energy requirements in the production of hydrogen from water. *Ind. Eng. Chem. Process Des. Dev.* **1966,** 5, 336-342.

54. Abanades, S.; Charvin, P.; Flamant, G.; Neveu, P., Screening of Water-Splitting Thermochemical Cycles Potentially Attractive for Hydrogen Production by Concentrated Solar Energy. *Energy* **2006,** 31, 2805-2822.

55. Kodama, T.; Gokon, N., Thermochemical Cycles for High-Temperature Solar Hydrogen Production. *Chem. Rev.* **2007,** 107, 4048-4077.

56. Penner, S. S., Steps toward the hydrogen economy. *Energy* **2006,** 31, 33-43.

57. Müller, R.; Steinfeld, A., H2O-splitting thermochemical cycle based on ZnO/Zn-redox: Quenching the effluents from the ZnO dissociation. *Chem. Eng. Sci.* **2008,** 63, 217-227.

58. Loutzenhiser, P. G.; Elena Gálvez, M.; Hischier, I.; Graf, A.; Steinfeld, A., CO_2 splitting in an aerosol flow reactor via the two-step Zn/ZnO solar thermochemical cycle. *Chem. Eng. Sci.* **2010,** 65, 1855-1864.

59. Dholabhai, P. P.; Adams, J. B.; Crozier, P.; Sharma, R., Oxygen Vacancy Migration in Ceria and Pr-Doped Ceria: A DFT + *U* Study. *J. Chem. Phys.* **2010,** 132, 094104.

60. Giordano, F.; Trovarelli, A.; de Leitenburg, C.; Dolcetti, G.; Giona, M., Some Insight into the Effects of Oxygen Diffusion in the Reduction Kinetics of Ceria. *Ind. Eng. Chem. Res.* **2001,** 40, 4828-4835.

61. Bruce, L., Surface area control during the synthesis and reduction of high area ceria catalyst supports. *Appl. Catal. A-Gen.* **1996,** 134, 351-362.

62. Qu, X.; Song, H.; Pan, G.; Bai, X.; Dong, B.; Zhao, H.; Dai, Q.; Zhang, H.; Qin, R.; Lu, S., Three-dimensionally ordered macroporous ZrO2: Eu3+: photonic band effect and local environments. *J. Phys. Chem. C* **2009,** 113, 5906-5911.

63. Narendar, Y.; Messing, G. L., Mechanisms of phase separation in gel-based synthesis of multicomponent metal oxides. *Catal. Today* **1997,** 35, 247-268.

64. Nakanishi, K.; Kobayashi, Y.; Amatani, T.; Hirao, K.; Kodaira, T., Spontaneous Formation of Hierarchical Macro−Mesoporous Ethane−Silica Monolith. *Chem. Mater.* **2004,** 16, 3652-3658.

65. Kaneko, H.; Ishihara, T.; Taku, S.; Naganuma, Y.; Hasegawa, N.; Tamaura, Y., Cerium Ion Redox System in CeO_2–xFe_2O_3 Solid Solution at High Temperatures (1,273–1,673 K) in the Two-Step Water-Splitting Reaction for Solar H_2 Generation. *J. Mater. Sci.* **2008,** 43, 3153–3161.

66. Charvin, P.; Abanades, S.; Flamant, G.; Lemont, F., Two-Step Water Splitting Thermochemical Cycle Based on Iron Oxide Redox Pair for Solar Hydrogen Production. *Energy* **2007,** 32, 1124-1133.

67. Abanades, S.; Charvin, P.; Lemont, F.; Flamant, G., Novel Two-Step SnO_2/SnO Water-Splitting Cycle for Solar Thermochemical Production of Hydrogen. *Int. J. Hydrogen Energy* **2008,** 33, 6021-6030.

68. Miller, J. E.; Allendorf, M. D.; Diver, R. B.; Evans, L. R.; Siegel, N. P.; Stuecker, J. N., Metal Oxide Composites and Structures for Ultra-High Temperature Solar Thermochemical Cycles. *J. Mater. Sci.* **2008,** 43, 4714-4728.

69. Chueh, W. C.; Haile, S. M., Ceria as a Thermochemical Reaction Medium for Selectively Generating Syngas or Methane from H_2O and CO_2. *ChemSusChem* **2009,** 2, 735–739.

70. Gálvez, M. E.; Loutzenhiser, P. G.; Hischier, I.; Steinfeld, A., CO_2 splitting via two-step solar thermochemical cycles with Zn/ZnO and FeO/Fe_3O_4 redox reactions: Thermodynamic analysis. *Energ. Fuels* **2008,** 22, 3544-3550.

71. Loutzenhiser, P. G.; Gálvez, M. E.; Hischier, I.; Stamatiou, A.; Frei, A.; Steinfeld, A., CO_2 splitting via two-step solar thermochemical cycles with Zn/ZnO and FeO/Fe_3O_4 redox reactions II: Kinetic analysis. *Energ. Fuels* **2009,** 23, 2832-2839.

72. Price, R. J.; Morse, D. A.; Hardy, S. L.; Fletcher, T. H.; Hill, S. C.; Jensen, R. J., Modeling the direct solar conversion of CO_2 to CO and O_2. *Ind. Eng. Chem. Res.* **2004,** 43, 2446-2453.

73. Lerot, L.; Legrand, F.; De Bruycker, P., Chemical control in precipitation of spherical zirconia particles. *J. Mater. Sci.* **1991,** 26, 2353-2358.

74. Hao, H.; Cui, J.; Chen, C.; Pan, L.; Hu, J.; Hu, X., Oxygen adsorption properties of $YBaCo_4O_7$-type compounds. *Solid State Ionics* **2006,** 177, 631-637.

75. Vioux, a., Nonhydrolytic sol−gel routes to oxides. *Chem. Mater.* **1997,** 9, 2292-2299.

76. Ebelmen, J., Sur les combinaisons des acides borique et silicique avec les ethers. *Ann. Chim. Phys.* **1846,** 16, 129-166.

77. Lee, G. R.; Crayston, J. A., Sol-gel processing of transition-metal alkoxides for electronics. *Adv. Mater.* **1993,** 5, 434-442.

78. Rezgui, S.; Gates, B. C., Genesis of a Metal Oxide Gel by the Sol-Gel Process: Evidence from Scanning Electron Microscopy. *Chem. Mater.* **1994,** 6, 339-342.

79. Brinker, C. J.; Scherer, G. W., *Sol-gel science: the physics and chemistry of sol-gel processing*. Gulf Professional Publishing: 1990.

80. Rubešová, K.; Jakeš, V.; Hlásek, T.; Vašek, P.; Matějka, P., Gel stabilization in chelate sol–gel preparation of Bi-2223 superconductors. *J. Phys. Chem. Solids* **2012,** 73, 448-453.

81. Hsu, K.-F.; Tsay, S.-Y.; Hwang, B.-J., Synthesis and characterization of nano-sized $LiFePO_4$ cathode materials prepared by a citric acid-based sol-gel route. *J. Mater. Chem.* **2004,** 14, 2690-2695.

82. Sun, Y.-K.; Oh, I.-H.; Hong, S.-A., Synthesis of ultrafine $LiCoO_2$ powders by the sol-gel method. *J. Mater. Sci.* **1996,** 31, 3617-3621.

83. Wang, X.; Chen, X.; Gao, L.; Zheng, H.; Ji, M.; Shen, T.; Zhang, Z., Citric acid-assisted sol–gel synthesis of nanocrystalline $LiMn_2O_4$ spinel as cathode material. *J. Cryst. Growth* **2003,** 256, 123-127.

84. Yue, Z.; Li, L.; Zhou, J.; Zhang, H.; Gui, Z., Preparation and characterization of NiCuZn ferrite nanocrystalline powders by auto-combustion of nitrate–citrate gels. *Mater. Sci. Eng. B* **1999,** 64, 68-72.

85. Roy, S.; Sharma, D. A.; Roy, S. N.; Maiti, H. S., Synthesis of $YBa_2Cu_3O_{7-x}$ powder by autoignition of citrate-nitrate gel. *J. Mater. Res.* **1993,** 8, 2761-2766.

86. Marinšek, M.; Zupan, K.; Maèek, J., Ni–YSZ cermet anodes prepared by citrate/nitrate combustion synthesis. *J. Power Sources* **2002,** 106, 178-188.

87. Martell, A. E.; Smith, R. M., *Critical Stability Constants: Inorganic Complexes*. Plenum Press: New York, NY, 1989; Vol. 4.

88. Pechini, M. P. A method of preparing lead and alkaline earth titanates and niobates and coating method using the same to form a capacitor. U.S. Patent 3,330,697, July 11, 1967.

89. Petkovich, N. D.; Rudisill, S. G.; Venstrom, L. J.; Boman, D. B.; Davidson, J. H.; Stein, A., Control of Heterogeneity in Nanostructured $Ce_{1-x}Zr_xO_2$ Binary Oxides for Enhanced Thermal Stability and Water Splitting Activity. *J. Phys. Chem. C* **2011,** 115, 21022–21033.

90. Alifanti, M.; Baps, B.; Blangenois, N.; Naud, J.; Grange, P.; Delmon, B., Characterization of CeO_2−ZrO_2 Mixed Oxides. Comparison of the Citrate and Sol−Gel Preparation Methods. *Chem. Mater.* **2002,** 15, 395-403.

91. Nakanishi, K.; Soga, N., Phase Separation in Gelling Silica–Organic Polymer Solution: Systems Containing Poly(sodium styrenesulfonate). *J. Am. Ceram. Soc.* **1991,** 74, 2518-2530.

92. Nakanishi, K.; Komura, H.; Takahashi, R.; Soga, N., Phase Separation in Silica Sol-Gel System Containing Poly(ethylene oxide). I. Phase Relation and Gel Morphology. *Bull. Chem. Soc. Jpn.* **1994,** 67, 1327-1335.

93. Nakanishi, K.; Soga, N., Phase Separation in Silica Sol-Gel System Containing Poly(ethylene oxide) II. Effects of Molecular Weight and Temperature. *Bull. Chem. Soc. Jpn.* **1997,** 70, 587-592.

94. Nakanishi, K.; Soga, N., Phase separation in silica sol-gel system containing polyacrylic acid II. Effects of molecular weight and temperature. *J. Non-Cryst. Solids* **1992,** 139, 14-24.

95. Nakanishi, K.; Soga, N., Phase separation in silica sol-gel system containing polyacrylic acid I. Gel formaation behavior and effect of solvent composition. *J. Non-Cryst. Solids* **1992,** 139, 1-13.

96. Nakanishi, K., Pore Structure Control of Silica Gels Based on Phase Separation. *J. Porous Mat.* **1997,** 4, 67-112.

97. Cahn, J. W., On spinodal decomposition. *Acta Metall. Mater.* **1961,** 9, 795-801.

98. Cahn, J. W., Phase Separation by Spinodal Decomposition in Isotropic Systems. *J. Chem. Phys.* **1965,** 42, 93-99.

99. Cahn, J. W.; Hilliard, J. E., Free Energy of a Nonuniform System. I. Interfacial Free Energy. *J. Chem. Phys.* **1958,** 28, 258-267.

100. Schwartz, L. H.; Mahajan, S.; Plewes, J. T., Spinodal decomposition in a Cu-9 wt% Ni-6 wt% Sn alloy. *Acta Metall. Mater.* **1974,** 22, 601-609.

101. Cornie, J. A.; Datta, A.; Soffa, W. A., An electron microscopy study of precipitation in Cu-Ti sideband alloys. *Metall. Trans.* **1973,** 4, 727-733.

102. Ditchek, B.; Schwartz, L. H., Applications of Spinodal Alloys. *Ann. Rev. Mater. Sci.* **1979,** 9, 219-253.

103. Choo, W. K.; Kim, J. H.; Yoon, J. C., Microstructural change in austenitic Fe-30.0wt%Mn-7.8wt%Al-1.3wt%C initiated by spinodal decomposition and its influence on mechanical properties. *Acta Mater.* **1997,** 45, 4877-4885.

104. Moore, K. T.; Johnson, W. C.; Howe, J. M.; Aaronson, H. I.; Veblen, D. R., On the interaction between Ag-depleted zones surrounding γ plates and spinodal decomposition in an Al-22 at.% Ag alloy. *Acta Mater.* **2002,** 50, 943-956.

105. Hwang, J.; Jo, C.; Hur, K.; Lim, J.; Kim, S.; Lee, J., Direct Access to Hierarchically Porous Inorganic Oxide Materials with Three-Dimensionally Interconnected Networks. *J. Am. Chem. Soc.* **2014,** 136, 16066-16072.

106. Takahashi, R.; Sato, S.; Sodesawa, T.; Suzuki, K.; Tafu, M.; Nakanishi, K.; Soga, N., Phase Separation in Sol–Gel Process of Alkoxide-Derived Silica-Zirconia in the Presence of Polyethylene Oxide. *J. Am. Ceram. Soc.* **2001,** 84, 1968-1976.

107. Konishi, J.; Fujita, K.; Nakanishi, K.; Hirao, K., Monolithic TiO_2 with Controlled Multiscale Porosity via a Template-Free Sol−Gel Process Accompanied by Phase Separation. *Chem. Mater.* **2006,** 18, 6069-6074.

108. Baekeland, L. H. Method of making insoluble products of phenol and formaldehyde. US Patent #942609,. 1909.

109. Carothers, W. H., Polymerization. *Chem. Rev.* **1931,** 8, 353-426.

110. Carothers, W. H.; Hill, J. W., Studies of polymerization and ring formation. XII. Linear superpolyesters. *J. Am. Chem. Soc.* **1932,** 54, 1559-1566.

111. Carothers, W. H., Studies on polymerization and ring formation. I. An introduction to the general theory of condensation polymers. *J. Am. Chem. Soc.* **1929,** 51, 2548-2559.

112. Carothers, W. H.; Arvin, J. A., Studies on polymerization and ring formation. II. Poly-esters. *J. Am. Chem. Soc.* **1929,** 51, 2560-2570.

113. Carothers, W. H.; Hill, J. W., Studies of polymerization and ring-formation. XIII. Polyamides and mixed polyester-polyamides. *J. Am. Chem. Soc.* **1932,** 54, 1566-1569.

114. Flory, P. J., Fundamental Principles of Condensation Polymerization. *Chem. Rev.* **1946,** 39, 137-197.

115. Flory, P. J., The Mechanism of Vinyl Polymerizations. *J. Am. Chem. Soc.* **1937,** 59, 241-253.

116. Hiemenz, P. C.; Lodge, T. P., In *Polymer Chemistry*, 2nd ed.; CRC Press: Boca Raton, FL, 2007; p 54.

117. Carothers, W. H., Polymers and polyfunctionality. *Trans. Faraday Soc.* **1936,** 32, 39-49.

118. Flory, P. J., Kinetics of Polyesterification: A Study of the Effects of Molecular Weight and Viscosity on Reaction Rate. *J. Am. Chem. Soc.* **1939,** 61, 3334-3340.

119. Liu, K.; Nie, Z.; Zhao, N.; Li, W.; Rubinstein, M.; Kumacheva, E., Step-Growth Polymerization of Inorganic Nanoparticles. *Science* **2010,** 329, 197-200.

120. Nudelman, F.; Sommerdijk, N. A. J. M., Biomineralization as an Inspiration for Materials Chemistry. *Angew. Chem. Int. Ed.* **2012,** 51, 6582-6596.

121. Kim, S.; Park, C. B., Bio-Inspired Synthesis of Minerals for Energy, Environment, and Medicinal Applications. *Adv. Funct. Mater.* **2013,** 23, 10-25.

122. Chung, K.; Yu, S.; Heo, C.-J.; Shim, J. W.; Yang, S.-M.; Han, M. G.; Lee, H.-S.; Jin, Y.; Lee, S. Y.; Park, N.; Shin, J. H., Flexible, Angle-Independent, Structural Color Reflectors Inspired by Morpho Butterfly Wings. *Adv. Mater.* **2012,** 24, 2375-2379.

123. Peng, W.; Zhu, S.; Wang, W.; Zhang, W.; Gu, J.; Hu, X.; Zhang, D.; Chen, Z., 3D Network Magnetophotonic Crystals Fabricated on Morpho Butterfly Wing Templates. *Adv. Funct. Mater.* **2012,** 22, 2072-2080.

124. Kang, S. M.; Ryou, M.-H.; Choi, J. W.; Lee, H., Mussel- and Diatom-Inspired Silica Coating on Separators Yields Improved Power and Safety in Li-Ion Batteries. *Chem. Mater.* **2012,** 24, 3481-3485.

125. Liu, J.; Antonietti, M., Bio-inspired NADH regeneration by carbon nitride photocatalysis using diatom templates. *Energ. Environ. Sci.* **2013,** 6, 1486-1493.

126. Munch, E.; Launey, M. E.; Alsem, D. H.; Saiz, E.; Tomsia, A. P.; Ritchie, R. O., Tough, Bio-Inspired Hybrid Materials. *Science* **2008,** 322, 1516-1520.

127. Jin, X.; Shi, B.; Zheng, L.; Pei, X.; Zhang, X.; Sun, Z.; Du, Y.; Kim, J. H.; Wang, X.; Dou, S.; Liu, K.; Jiang, L., Bio-Inspired Multifunctional Metallic Foams Through the Fusion of Different Biological Solutions. *Adv. Funct. Mater.* **2014,** 24, 2721-2726.

128. Duailibi, M. T.; Duailibi, S. E.; Young, C. S.; Bartlett, J. D.; Vacanti, J. P.; Yelick, P. C., Bioengineered Teeth from Cultured Rat Tooth Bud Cells. *J. Dent. Res.* **2004,** 83, 523-528.

129. Kikuchi, M.; Itoh, S.; Ichinose, S.; Shinomiya, K.; Tanaka, J., Self-organization mechanism in a bone-like hydroxyapatite/collagen nanocomposite synthesized in vitro and its biological reaction in vivo. *Biomaterials* **2001,** 22, 1705-1711.

130. Stupp, S. I.; Ciegler, G. W., Organoapatites: Materials for artificial bone. I. Synthesis and microstructure. *J. Biomed. Mater. Res.* **1992,** 26, 169-183.

131. Stupp, S. I.; Hanson, J. A.; Eurell, J. A.; Ciegler, G. W.; Johnson, A., Organoapatites: Materials for artificial bone. III. Biological testing. *J. Biomed. Mater. Res.* **1993,** 27, 301-311.

132. Stupp, S. I.; Mejicano, G. C.; Hanson, J. A., Organoapatites: Materials for artificial bone. II. Hardening reactions and properties. *J. Biomed. Mater. Res.* **1993,** 27, 289-299.

133. Zakaria, S. M.; Sharif Zein, S. H.; Othman, M. R.; Yang, F.; Jansen, J. A., Nanophase Hydroxyapatite as a Biomaterial in Advanced Hard Tissue Engineering: A Review. *Tissue Eng. B* **2013,** 19, 431-441.

134. Olsen, T., On the calculation of power from curvature of the cornea. *Br. J. Ophthalmol.* **1986,** 70, 152-154.

135. Lodish, H.; Berk, A.; Zipursky, S. L., Collagen: The Fibrous Proteins of the Matrix. In *Molecular Cell Biology*, 4 ed.; W. H. Freeman: New York, 2000.

136. Whitcher, J. P.; Srinivasan, M.; Upadhyay, M. P., Corneal blindness: a global perspective. *B. World Health Organ.* **2001,** 79, 214-221.

137. Moffatt, S. L.; Cartwright, V. A.; Stumpf, T. H., Centennial review of corneal transplantation. *Clin. Exp. Ophthalmol.* **2005,** 33, 642-657.

138. Le Discorde, M.; Moreau, P.; Sabatier, P.; Legeais, J.-M.; Carosella, E. D., Expression of HLA-G in human cornea, an immune-privileged tissue. *Hum. Immunol.* **2003,** 64, 1039-1044.

139. Ament, J. D.; Spurr-Michaud, S. J.; Dohlman, C. H.; Gipson, I. K., The Boston Keratoprosthesis: Comparing Corneal Epithelial Cell Compatibility with Titanium and PMMA. *Cornea* **2009,** 28, 808-811.

140. Lam, F. C.; Liu, C., The future of keratoprostheses (artificial corneae). *Br. J. Ophthalmol.* **2011,** 95, 304-305.

141. Zucker, B. B., HYdration and transparency of corneal stroma. *Arch. Ophthalmol-Chic.* **1966,** 75, 228-231.

142. Kadler, K. E.; Hill, A.; Canty-Laird, E. G., Collagen fibrillogenesis: fibronectin, integrins, and minor collagens as organizers and nucleators. *Curr. Opin. Cell Biol.* **2008,** 20, 495-501.

143. Saeidi, N.; Karmelek, K. P.; Paten, J. A.; Zareian, R.; DiMasi, E.; Ruberti, J. W., Molecular crowding of collagen: A pathway to produce highly-organized collagenous structures. *Biomaterials* **2012,** 33, 7366-7374.

144. Ushiki, T., Collagen Fibers, Reticular Fibers and Elastic Fibers. A Comprehensive Understanding from a Morphological Viewpoint. *Arch. Histol. Cyol.* **2002,** 65, 109-126.

145. Holmes, D. F.; Gilpin, C. J.; Baldock, C.; Ziese, U.; Koster, A. J.; Kadler, K. E., Corneal collagen fibril structure in three dimensions: Structural insights into fibril assembly, mechanical properties, and tissue organization. *P. Natl. Acad. Sci. USA* **2001,** 98, 7307-7312.

146. Venstrom, L. J.; Petkovich, N.; Rudisill, S.; Stein, A.; Davidson, J. H., The Effects of Morphology on the Oxidation of Ceria by Water and Carbon Dioxide. *J. Sol. Energy Eng.* **2012,** 134, 011005.

147. Hillert, M., Solute drag in grain boundary migration and phase transformations. *Acta Mater.* **2004,** 52, 5289-5293.

148. Kang, S. L., *Sintering: Densification, Grain Growth, and Microstructure*. Butterworth-Heinemann: Oxford, UK, 2005; p 280.

149. Lewis, N. S.; Nocera, D. G., Powering the Planet: Chemical Challenges in Solar Energy Utilization. *Proc. Natl. Acad. Sci. U. S. A.* **2006,** 103, 15729-15735.

150. Scott, S. A.; Davey, M. P.; Dennis, J. S.; Horst, I.; Howe, C. J.; Lea-Smith, D. J.; Smith, A. G., Biodiesel from Algae: Challenges and Prospects. *Curr. Opin. Chem. Biol.* **2010,** 21, 277-286.

151. Melis, A., Photosynthesis-to-Fuels: From Sunlight to Hydrogen, Isoprene, and Botryococcene Production. *Energy Environ. Sci.* **2012,** 5, 5531-5539.

152. Gibson, T. L.; Kelly, N. A., Optimization of Solar Powered Hydrogen Production Using Photovoltaic Electrolysis Devices. *Int. J. Hydrogen Energy* **2008,** 33, 5931-5940.

153. Chen, X.; Shen, S.; Guo, L.; Mao, S. S., Semiconductor-based Photocatalytic Hydrogen Generation. *Chem. Rev.* **2010,** 110, 6503-6570.

154. Alonso, D. M.; Bond, J. Q.; Dumesic, J. A., Catalytic Conversion of Biomass to Biofuels. *Green Chem.* **2010,** 12, 1493-1513.

155. Roy, S. C.; Varghese, O. K.; Paulose, M.; Grimes, C. A., Toward Solar Fuels: Photocatalytic Conversion of Carbon Dioxide to Hydrocarbons. *ACS Nano* **2010,** 4, 1259-1278.

156. Licht, S., Efficient Solar-Driven Synthesis, Carbon Capture, and Desalinization, STEP: Solar Thermal Electrochemical Production of Fuels, Metals, Bleach. *Adv. Mater.* **2011,** 47, 5592-5612.

157. Teets, T. S.; Nocera, D. G., Photocatalytic Hydrogen Production. *Chem. Commun.* **2011,** 47, 9268-9274.

158. Chueh, W. C.; Falter, C.; Abbott, M.; Scipio, D.; Furler, P.; Haile, S. M.; Steinfeld, A., High-Flux Solar-Driven Thermochemical Dissociation of CO_2 and H_2O Using Nonstoichiometric Ceria. *Science* **2010,** 330, 1797-1801.

159. Roeb, M.; Sack, J. P.; Rietbrock, P.; Prahl, C.; Schreiber, H.; Neises, M.; de Oliveira, L.; Graf, D.; Ebert, M.; Reinalter, W.; Meyer-Grunefeldt, M.; Sattler, C.;

Lopez, A.; Vidal, A.; Elsberg, A.; Stobbe, P.; Jones, D.; Steele, A.; Lorentzou, S.; Pagkoura, C.; Zygogianni, A.; Agrafiotis, C.; Konstandopoulos, A. G., Test Operation of a 100 kW Pilot Plant for Solar Hydrogen Production from Water on a Solar Tower. *Sol. Energy* **2011,** 85, 634-644.

160. Loutzenhiser, P. G.; Meier, A.; Steinfeld, A., Review of the Two-Step H_2O/CO_2-Splitting Solar Thermochemical Cycle Based on Zn/ZnO Redox Reactions. *Materials* **2010,** 3, 4922-4938.

161. Furler, P.; Scheffe, J. R.; Steinfeld, A., Syngas Production by Simultaneous Splitting of H_2O and CO_2 *via* Ceria Redox Reactions in a High-Temperature Solar Reactor. *Energy Environ. Sci.* **2012,** 5, 6068-6103.

162. Kaneko, H.; Miura, T.; Ishihara, H.; Taku, S.; Yokoyama, T.; Nakajima, H.; Tamaura, Y., Reactive Ceramics of CeO_2-MO_x (M=Mn, Fe, Ni, Cu) for H_2 Generation by Two-Step Water Splitting Using Concentrated Solar Thermal Energy. *Energy* **2007,** 32, 656-663.

163. Le Gal, A.; Abanades, S.; Flamant, G., CO_2 and H_2O Splitting for Thermochemical Production of Solar Fuels Using Nonstoichiometric Ceria and Ceria/Zirconia Solid Solutions. *Energy Fuels* **2011,** 25, 4836–4845.

164. Meng, Q.-L.; Lee, C.; Ishihara, T.; Kaneko, H.; Tamaura, Y., Reactivity of CeO_2-Based Ceramics for Solar Hydrogen Production via a Two-Step Water-Splitting Cycle with Concentrated Solar Energy. *Int. J. Hydrogen Energy* **2011,** 36, 13435–13441.

165. Körner, R.; Ricken, M.; Nölting, J.; Riess, I., Phase Transformation in Reduced Ceria: Determination by Thermal Expansion Measurements. *J. Sol. State Chem.* **1989,** 78, 136-147.

166. Kodama, T.; Kondoh, Y.; Yamamoto, R.; Andou, H.; Satou, N., Thermochemical Hydrogen Production by a Redox System of ZrO_2-Supported Co(II)-Ferrite. *Sol. Energy* **2005,** 78, 623-631.

167. Steinfeld, A., Solar Hydrogen Production via a Two-Step Water-Splitting Thermochemical Cycle Based on Zn/ZnO Redox Reactions. *Int. J. Hydrogen Energy* **2002,** 27, 611-619.

168. Lapp, J.; Davidson, J. H.; Lipiński, W., Efficiency of two-step solar thermochemical non-stoichiometric redox cycles with heat recovery. *Energy* **2012,** 37, 591-600.

169. Wang, S.-F.; Xiang, X.; Sun, G.; Gao, X.-L.; Chen, B.; Ding, Q.-P.; Li, Z.-J.; Zhang, C.; Zu, X.-T., Role of pH, Organic Additive, and Chelating Agent in Gel Synthesis and Fluorescent Properties of Porous Monolithic Alumina. *J. Phys. Chem. C* **2013,** 117, 5067-5074.

170. Lee, C.; Meng, Q.-L.; Kaneko, H.; Tamaura, Y., Reactive ceramics of $Ce_xSc_{1-x}O_{2-\delta}$ for solar hydrogen production by two-step water splitting. *ASME Conf. Proc. 2011*, 1681-1687.

171. Meredig, B.; Wolverton, C., First-Principles Thermodynamic Framework for the Evaluation of Thermochemical H_2O- or CO_2-Splitting Materials. *Phys. Rev. B* **2009,** 80, 245119.

172. Ruiz-Morales, J. C.; Canales-Vázquez, J.; Peña-Martínez, J.; Marrero-López, D.; Irvine, J. T. S.; Núñez, P., Microstructural Optimization of Materials for SOFC Applications Using PMMA Microspheres. *J. Mater. Chem.* **2006,** 16, 540-542.

173. Stein, A.; Li, F.; Wang, Z., Synthesis of shaped particles and particle arrays by disassembly methods. *J. Mater. Chem.* **2009,** 19, 2102-2106.

174. Schroden, R. C.; Al-Daous, M.; Sokolov, S.; Melde, B. J.; Lytle, J. C.; Stein, A.; Carbajo, M. C.; Fernández, J. T.; Rodríguez, E. E., Hybrid Macroporous Materials for Heavy Metal Ion Adsorption. *J. Mater. Chem.* **2002,** 12, 3261-3267.

175. Touloukian, Y. S., In *Thermophysical Properties of High Temperature Solid Materials*, Macmillan: New York, NY, 1968; Vol. 4, p 119.

176. Whitaker, S. B., Forced convection heat transfer correlation for flow in pipes past flat plates, single cylinders, single spheres, and for flow in packed beds and tube bundles. *AICHEJ* **1972,** 18, 361-371.

177. Panlener, R. J.; Blumenthal, R. N.; Garnier, J. E., A thermodynamic study of nonstoichiometric cerium dioxide. *J. Phys. Chem. Solids* **1975,** 36, 1213-1222.

178. Mayo, M. J., Processing of nanocrystalline ceramics from ultrafine particles. *Int. Mater. Rev.* **1996,** 41, 85-115.

179. Chen, D.; Mayo, M. J., Rapid rate sintering of nanocrystalline ZrO_2-3 mol% Y_2O_3. *J. Am. Ceram. Soc.* **1996,** 79, 906-912.

180. Tiwari, G. P., Solid State Diffusion and Bulk Properties. In *Diffusion Processes in Advanced Technological Materials*, Gupta, D., Ed. William Andrew: Norwich, NY, U.S.A., 2005; pp 71-75.

181. Shane, M.; Mecartney, M. L., Sol-gel synthesis of zirconia barrier coatings. *J. Mater. Sci.* **1990,** 25, 1537-1544.

182. Benamira, A.; Deloume, J. P.; Durand, B., Molten salt synthesis and characterization of non-doped hafnia. *J. Mater. Chem.* **1999,** 9, 2659-2662.

183. Mann, M.; Kolis, J., Hydrothermal crystal growth of yttrium and rare earth stabilized hafnia. *J. Cryst. Growth* **2010,** 312, 461-465.

184. Rhodes, W. H., Agglomerate and Particle Size Effects on Sintering Yttria-Stabilized Zirconia. *J. Am. Ceram. Soc.* **1981,** 64, 19-22.

185. Moure, A.; Tartaj, J.; Moure, C., Synthesis, sintering and electrical properties of yttria–calcia-doped ceria. *J. Eur. Ceram. Soc.* **2009,** 29, 2559-2565.

186. Budnikov, P. P.; Matveev, M. A.; Yanovskii, V. K., Sintering high purity, magnesia with additions of hafnium dioxide. *Refract. Ind. Ceram.* **1965,** 6, 190-195.

187. Rahaman, M. N.; Zhou, Y. C., Effect of solid solution additives on the sintering of ultra-fine CeO2 powders. *J. Eur. Ceram. Soc.* **1995,** 15, 939-950.

188. Bernal, S.; Blanco, G.; Cauqui, M. A.; Cifredo, G. A.; Pintado, J. M.; Rodriguez-Izquierdo, J. M., Influence of Reduction Treatment on the Structural and Redox Behavior of Ceria, La/Ce and Y/Ce Mixed Oxides. *Catal. Lett.* **1998,** 53, 51–57.

189. Kim, G.; Vohs, J. M.; Gorte, R. J., Enhanced Reducibility of Ceria–YSZ Composites in Solid Oxide Electrodes. *J. Mater. Chem.* **2008,** 18, 2386–2390.

190. Kharton, V. V.; Figueiredo, F. M.; Navarro, L.; Naumovich, E. N.; Kovalevsky, A. V.; Yaremchenko, A. A.; Viskup, A. P.; Carneiro, A.; Marques, F. M. B.;

Frade, J. R., Ceria-based materials for solid oxide fuel cells. *J. Mater. Sci.* **2001,** 36, 1105-1117.

191. Liotta, L. F.; Macaluso, A.; Longo, A.; Pantaleo, G.; Martorana, A.; Deganello, G., Effects of Redox Treatments on the Structural Composition of a Ceria-Zirconia Oxide for Application in the Three-Way Catalysis. *Appl. Catal. A* **2003,** 240, 295-307.

192. Malonzo, C. D.; De Smith, R. M.; Rudisill, S. G.; Petkovich, N. D.; Davidson, J. H.; Stein, A., Wood-Templated CeO_2 as Active Material for Thermochemical CO Production. *J. Phys. Chem. C* **2014,** 118, 26172-26181.

193. Zhang, L.; Mao, Z.; Thomason, J. D.; Wang, S.; Huang, K., Synthesis of a Homogeneously Porous Solid Oxide Matrix with Tunable Porosity and Pore Size. *J. Am. Ceram. Soc.* **2012,** 95, 1832-1837.

194. Wang, R.; Crozier, P. A.; Sharma, R., Nanoscale Compositional and Structural Evolution in Ceria Zirconia During Cyclic Redox Treatments. *J. Mater. Chem.* **2010,** 20, 7497-7505.

195. Klein, S. M.; Manoharan, V. N.; Pine, D. J.; Lange, F. F., Synthesis of Spherical Polymer and Titania Photonic Crystallites. *Langmuir* **2005,** 21, 6669-6674.

196. Gunawan, P.; Mei, L.; Teo, J.; Ma, J.; Highfield, J.; Li, Q.; Zhong, Z., Ultrahigh Sensitivity of Au/1D α-Fe_2O_3 to Acetone and the Sensing Mechanism. *Langmuir* **2012,** 28, 14090-14099.

197. Ballato, J.; James, A., A Ceramic Photonic Crystal Temperature Sensor. *J. Am. Ceram. Soc.* **1999,** 82, 2273-2275.

198. Ruzimuradov, O.; Hasegawa, G.; Kanamori, K.; Nakanishi, K., Preparation of Hierarchically Porous Nanocrystalline $CaTiO_3$, $SrTiO_3$ and $BaTiO_3$ Perovskite Monoliths. *J. Am. Ceram. Soc.* **2011,** 94, 3335-3339.

199. Li, F.; Wang, Z.; Ergang, N. S.; Fyfe, C. A.; Stein, A., Controlling the Shape and Alignment of Mesopores by Confinement in Colloidal Crystals: Designer Pathways to Silica Monoliths with Hierarchical Porosity. *Langmuir* **2007,** 23, 3996-4004.

200. Kamperman, M.; Burns, A.; Weissgraeber, R.; van Vegten, N.; Warren, S. C.; Gruner, S. M.; Baiker, A.; Wiesner, U., Integrating Structure Control over Multiple Length Scales in Porous High Temperature Ceramics with Functional Platinum Nanoparticles. *Nano Lett.* **2009,** 9, 2756-2762.

201. Su, B.-L.; Sanchez, C.; Yang, X.-Y., *Hierarchically Structured Porous Materials: From Nanoscience to Catalysis, Separation, Optics, Energy, and Life Science*. 1st ed.; Wiley-VCH Verlag & Co. KGaA: Weinheim, Germany, 2011; p 651.

202. Wang, S.; Lu, Z.; Wang, D.; Li, C.; Chen, C.; Yin, Y., Porous monodisperse V_2O_5 microspheres as cathode materials for lithium-ion batteries. *J. Mater. Chem.* **2011,** 21, 6365-6369.

203. Stein, A.; Wilson, B. E.; Rudisill, S. G., Design and functionality of colloidal-crystal-templated materials-chemical applications of inverse opals. *Chem. Soc. Rev.* **2013,** 42, 3721-3739.

204. Deng, Y.; Liu, C.; Yu, T.; Liu, F.; Zhang, F.; Wan, Y.; Zhang, L.; Wang, C.; Tu, B.; Webley, P. A.; Wang, H.; Zhao, D., Facile Synthesis of Hierarchically Porous

Carbons from Dual Colloidal Crystal/Block Copolymer Template Approach. *Chem. Mater.* **2007,** 19, 3271-3277.

205. Kamegawa, T.; Suzuki, N.; Che, M.; Yamashita, H., Synthesis and Unique Catalytic Performance of Single-Site Ti-Containing Hierarchical Macroporous Silica with Mesoporous Frameworks. *Langmuir* **2011,** 27, 2873-2879.

206. DiVito, M. D.; Rudisill, S. G.; Stein, A.; Patel, S. V.; McLaren, J. W.; Hubel, A., Silica Hybrid for Corneal Replacement: Optical, Biomechanical, and Ex Vivo Biocompatibility Studies. *Invest. Ophth. Vis. Sci.* **2012,** 53, 8192-8199.

207. Nakanishi, K., Macroporous Morphology Control by Phase Separation. In *Handbook of Sol-Gel Science and Technology*, Sakka, S., Ed. Springer Science+Business Media Inc.: New York, NY, 2005; pp 529-538.

208. Rudisill, S. G.; Venstrom, L. J.; Petkovich, N. D.; Quan, T.; Hein, N.; Boman, D. B.; Davidson, J. H.; Stein, A., Enhanced Oxidation Kinetics in Thermochemical Cycling of CeO_2 through Templated Porosity. *J. Phys. Chem. C* **2012,** 117, 1692–1700.

209. Rudisill, S. G.; Hein, N. M.; Terzic, D.; Stein, A., Controlling Microstructural Evolution in Pechini Gels through the Interplay between Precursor Complexation, Step-Growth Polymerization, and Template Confinement. *Chem. Mater.* **2013,** 25, 745-753.

210. Kaji, H.; Nakanishi, K.; Soga, N., Polymerization-induced phase separation in silica sol-gel systems containing formamide. *J. Sol-Gel Sci. Technol.* **1993,** 1, 35-46.

211. Nakanishi, K.; Soga, N., Phase separation in silica sol-gel system containing polyacrylic acid I. Gel formation behavior and effect of solvent composition. *J. Non-Cryst. Solids* **1992,** 139, 1-13.

212. Rudisill, S. G.; Wang, Z.; Stein, A., Maintaining the Structure of Templated Porous Materials for Reactive and High-Temperature Applications. *Langmuir* **2012,** 28, 7310-7324.

213. Liu, X.; Luo, Y.; Lin, J., Synthesis and characterization of spherical Sr_2CeO_4 phosphors by spray pyrolysis for field emission displays. *J. Cryst. Growth* **2006,** 290, 266-271.

214. Messing, G. L.; Zhang, S.-C.; Jayanthi, G. V., Ceramic Powder Synthesis by Spray Pyrolysis. *J. Am. Ceram. Soc.* **1993,** 76, 2707-2726.

215. Titirici, M.-M.; Antonietti, M.; Thomas, A., A Generalized Synthesis of Metal Oxide Hollow Spheres Using a Hydrothermal Approach. *Chem. Mater.* **2006,** 18, 3808-3812.

216. Yu, H.; Yu, J.; Liu, S.; Mann, S., Template-free Hydrothermal Synthesis of CuO/Cu_2O Composite Hollow Microspheres. *Chem. Mater.* **2007,** 19, 4327-4334.

217. Zhu, Y. F.; Fan, D. H.; Shen, W. Z., Template-Free Synthesis of Zinc Oxide Hollow Microspheres in Aqueous Solution at Low Temperature. *J. Phys. Chem. C* **2007,** 111, 18629-18635.

218. Wang, Y.; Xu, H.; Wang, X.; Zhang, X.; Jia, H.; Zhang, L.; Qiu, J., A General Approach to Porous Crystalline TiO_2, $SrTiO_3$, and $BaTiO_3$ Spheres. *J. Phys. Chem. B* **2006,** 110, 13835-13840.

219. Kakihana, M.; Borjesson, L.; Eriksson, S.; Svedlindh, P., Fabrication and characterization of highly pure and homogeneous $YBa_2Cu_3O_7$ superconductors from sol-gel derived powders. *J. Appl. Phys.* **1991,** 69, 867-873.

220. Aneggi, E.; de Leitenburg, C.; Dolcetti, G.; Trovarelli, A., Promotional Effect of Rare Earths and Transition Metals in the Combustion of Diesel Soot over CeO_2 and CeO_2-ZrO_2. *Catal. Today* **2006,** 114, 40-47.

221. Umeda, G. A.; Chueh, W. C.; Noailles, L.; Haile, S. M.; Dunn, B. S., Inverse Opal Ceria–Zirconia: Architectural Engineering for Heterogeneous Catalysis. *Energy Environ. Sci.* **2008,** 1, 484–486.

222. Mogensen, M.; Lindegaard, T.; Hansen, U. R.; Mogensen, G., Physical Properties of Mixed Conductor Solid Oxide Fuel Cell Anodes of Doped CeO_2. *J. Electrochem. Soc.* **1994,** 141, 2122-2128.

223. Fu, M.; Zhou, J.; Huang, X.; He, D.; Wang, Y., The electrodeposition of zinc oxide two-dimensional nanomesh and three-dimensional inverse opal complex connected structures. *J. Nanosci. Nanotechno.* **2010,** 10, 1928-1933.

224. Nakanishi, K., Porous Gels Made by Phase Separation: Recent Progress and Future Directions. *J. Sol-Gel Sci. Technol.* **2000,** 19, 65-70.

225. Hetherington, N. B. J.; Kulak, A. N.; Kim, Y.-Y.; Noel, E. H.; Snoswell, D.; Butler, M.; Meldrum, F. C., Porous Single Crystals of Calcite from Colloidal Crystal Templates: ACC Is Not Required for Nanoscale Templating. *Adv. Funct. Mater.* **2011,** 21, 948-954.

226. Feng, S.; Zheng, M.; Li, N.; Ji, G.; Cao, J., Synthesis of Ordered Macroporous Co_3O_4 Microspheres via an Easy Melt Infiltration Route. *Chem. Lett.* **2009,** 38, 1050-1051.

227. Wang, S.; An, C.; Zhang, Y.; Zhang, Z.; Qian, Y., Ethanothermal reduction to MoO_2 microspheres via modified Pechini method. *J. Cryst. Growth* **2006,** 293, 209-215.

228. Schroden, R. C.; Al-Daous, M.; Blanford, C. F.; Stein, A., Optical Properties of Inverse Opal Photonic Crystals. *Chem. Mater.* **2002,** 14, 3305-3315.

229. Krishna, K.; Bueno-López, A.; Makkee, M.; Moulijn, J. A., Potential Rare-Earth Modified CeO_2 Catalysts for Soot Oxidation: Part III. Effect of Dopant Loading and Calcination Temperature on Catalytic Activity with O_2 and $NO+O_2$. *Appl. Catal., B* **2007,** 75, 210–220.

230. Pusey, P. N.; van Megen, W.; Bartlett, P.; Ackerson, B. J.; Rarity, J. G.; Underwood, S. M., Structure of crystals of hard colloidal spheres. *Phys. Rev. Lett.* **1989,** 63, 2753-2756.

231. Li, X.; Agarwal, V.; Liu, M.; William S. Rees, J., Investigation of the mechanism of sol-gel formation in the $Sr(NO_3)_2$/citric acid/ethylene glycol system by solution state ^{87}Sr nuclear magnetic resonance spectroscopy. *J. Mater. Res.* **2000,** 15, 2393-2399.

232. Twigg, M. V.; Richardson, J. T., Fundamentals and Applications of Structured Ceramic Foam Catalysts. *Ind. Eng. Chem. Res.* **2007,** 46, 4166-4177.

233. Sun, Z.; Sun, B.; Qiao, M.; Wei, J.; Yue, Q.; Wang, C.; Deng, Y.; Kaliaguine, S.; Zhao, D., A General Chelate-Assisted Co-Assembly to Metallic Nanoparticles-Incorporated Ordered Mesoporous Carbon Catalysts for Fischer–Tropsch Synthesis. *J. Am. Ceram. Soc.* **2012,** 134, 17653-17660.

234. Shao, Y.; Liu, J.; Wang, Y.; Lin, Y., Novel catalyst support materials for PEM fuel cells: current status and future prospects. *J. Mater. Chem.* **2009,** 19, 46-59.

235. Brandon, N. P.; Brett, D. J., Engineering porous materials for fuel cell applications. *Philos. T. R. Soc. A* **2006,** 364, 147-159.

236. Jacobson, A. J., Materials for Solid Oxide Fuel Cells. *Chem. Mater.* **2010,** 22, 660–674.

237. Leofanti, G.; Padovan, M.; Tozzola, G.; Venturelli, B., Surface area and pore texture of catalysts. *Catal. Today* **1998,** 41, 207-219.

238. Kakihana, M., Invited Review "Sol-Gel" Preparation of High Temperature Superconducting Oxides. *J. Sol-Gel Sci. Technol.* **1996,** 6, 7-55.

239. Cividanes, L. S.; Campos, T. M.; Rodrigues, L. A.; Brunelli, D. D.; Thim, G. P., Review of mullite synthesis routes by sol–gel method. *J. Sol-Gel Sci. Technol.* **2010,** 55, 111-125.

240. Wan, Y.; Zhao, D., On the controllable soft-templating approach to mesoporous silicates. *Chem. Rev.* **2007,** 107, 2821-2860.

241. Petkovich, N. D.; Stein, A., Colloidal Crystal Templating Approaches to Materials with Hierarchical Porosity. In *Hierarchically Structured Porous Materials: From Nanoscience to Catalysis, Separation, Optics, Energy, and Life*

Science, Su, B.-L.; Sanchez, C.; Yang, X.-Y., Eds. Wiley-VCH Verlag GmbH & Co. KGaA: Weinheim, Germany, 2012; Vol. 1, pp 55-129.

242. Rauda, I. E.; Buonsanti, R.; Saldarriaga-Lopez, L. C.; Benjauthrit, K.; Schelhas, L. T.; Stefik, M.; Augustyn, V.; Ko, J.; Dunn, B.; Wiesner, U.; Milliron, D. J.; Tolbert, S. H., General Method for the Synthesis of Hierarchical Nanocrystal-Based Mesoporous Materials. *ACS Nano* **2012,** 6, 6386-6399.

243. Fu, M.; Zhao, A.; He, D.; Wang, Y., Colloidal Crystal Templates Direct the Morphologies of Fabricated Porous Cuprous Oxide Particles. *Chem. Mater.* **2014,** 26, 3084-3088.

244. Fu, M.; Cui, J.; Yang, M.; Jiang, R.; He, D.; Wang, Y., Template effects on the morphology of ZnO via colloidal crystals with different functional groups. *Cryst. Res. Technol.* **2012,** 47, 1249-1254.

245. Li, C.; Qi, L., Bioinspired Fabrication of 3D Ordered Macroporous Single Crystals of Calcite from a Transient Amorphous Phase. *Angew. Chem. Int. Ed.* **2008,** 47, 2388-2393.

246. Nakanishi, K.; Soga, N., Phase-separation in gelling silica organic polymer-solution - systems containing poly(sodium styrenesulfonate). *J. Am. Ceram. Soc.* **1991,** 74, 2518-2530.

247. Nakanishi, K., Pore Structure Control of Silica Gels Based on Phase Separation. *J. Porous Mater.* **1997,** 4, 67-112.

248. Nakanishi, K.; Soga, N., Phase separation in silica sol-gel system containing polyacrylic acid I. Gel formation behavior and effect of solvent composition. *J. Non-Cryst. Solids* **1992,** 139, 1-13.

249. Odian, G., In *Principles of Polymerization*, 3rd ed.; John Wiley & Sons, Inc.: Hoboken, NJ, 1991; pp 110-115.

250. Getsova, M.; Todorovsky, D.; Enchev, V.; Wawer, I., Cerium(III/IV) and Cerium(IV)–Titanium(IV) Citric Complexes Prepared in Ethylene Glycol Medium. *Monatsh. Chem.* **2007,** 138, 389-401.

251. Zakhidov, A. A.; Baughman, R. H.; Iqbal, Z.; Cui, C.; Khayrullin, I.; Dantas, S. O.; Marti, J.; Ralchenko, V. G., Carbon Structures with Three-Dimensional Periodicity at Optical Wavelengths. *Science* **1998,** 282, 897-901.

252. Stein, A.; Rudisill, S. G.; Petkovich, N. D., Perspective on the Influence of Interactions Between Hard and Soft Templates and Precursors on Morphology of Hierarchically Structured Porous Materials. *Chem. Mater.* **2013,** 26, 259-276.

253. Dong, W.; Bongard, H. J.; Marlow, F., New Type of Inverse Opals: Titania With Skeleton Structure. *Chem. Mater.* **2003,** 15, 568-574.

254. Dong, W.; Marlow, F., Tuning of ordered porous skeleton structures. *Micropor. Mesopor. Mater.* **2007,** 99, 236-243.

255. Li, F.; Wang, Z.; Stein, A., Shaping Mesoporous Silica Nanoparticles by Disassembly of Hierarchically Porous Structures. *Angew. Chem. Int. Ed.* **2007,** 46, 1885-1888.

256. Mannis, M. J.; Holland, E. J.; Gal, R. L.; Dontchev, M.; Kollman, C.; Raghinaru, D.; Dunn, S. P.; Schultze, R. L.; Verdier, D. D.; Lass, J. H.; Raber, I. M.; Sugar, J.; Gorovoy, M. S.; Sugar, A.; Stulting, R. D.; Montoya, M. M.; Penta, J. G.; Benetz, B. A.; Beck, R. W., The Effect of Donor Age on Penetrating Keratoplasty for Endothelial Disease: Graft Survival after 10 Years in the Cornea Donor Study. *Ophthalmology* **2013,** 120, 2419-2427.

257. Barnham, J. J.; Roper-Hall, M. J., Keratoprosthesis: a long-term review. *Br. J. Ophthalmol.* **1983,** 67, 468-474.

258. Beck, K.; Brodsky, B., Supercoiled Protein Motifs: The Collagen Triple-Helix and the α-Helical Coiled Coil. *J. Struct. Biol.* **1998,** 122, 17-29.

259. Orgel, J. P. R. O.; Irving, T. C.; Miller, A.; Wess, T. J., Microfibrillar structure of type I collagen in situ. *P. Natl. Acad. Sci. USA* **2006,** 103, 9001-9005.

260. Sweeney, S. M.; Orgel, J. P.; Fertala, A.; McAuliffe, J. D.; Turner, K. R.; Di Lullo, G. A.; Chen, S.; Antipova, O.; Perumal, S.; Ala-Kokko, L.; Forlino, A.; Cabral, W. A.; Barnes, A. M.; Marini, J. C.; Antonio, J. D. S., Candidate Cell and Matrix Interaction Domains on the Collagen Fibril, the Predominant Protein of Vertebrates. *J. Biol. Chem.* **2008,** 283, 21187-21197.

261. Rada, J. A.; Cornuet, P. K.; Hassell, J. R., Regulation of Corneal Collagen Fibrillogenesis In Vitro by Corneal Proteoglycan (Lumican and Decorin) Core Proteins. *Exp. Eye Res.* **1993,** 56, 635-648.

262. Lewis, P. N.; Pinali, C.; Young, R. D.; Meek, K. M.; Quantock, A. J.; Knupp, C., Structural Interactions between Collagen and Proteoglycans Are Elucidated by

Three-Dimensional Electron Tomography of Bovine Cornea. *Structure* **2010,** 18, 239-245.

263. Komai, Y.; Ushiki, T., The three-dimensional organization of collagen fibrils in the human cornea and sclera. *Invest. Ophth. Vis. Sci.* **1991,** 32, 2244-2258.

264. Meek, K., Corneal collagen—its role in maintaining corneal shape and transparency. *Biophys. Rev.* **2009,** 1, 83-93.

265. Knupp, C.; Pinali, C.; Lewis, P. N.; Parfitt, G. J.; Young, R. D.; Meek, K. M.; Quantock, A. J., The Architecture of the Cornea and Structural Basis of Its Transparency. In *Advances in Protein Chemistry and Structural Biology*, Alexander, M., Ed. Academic Press: New York, 2009; Vol. Volume 78, pp 25-49.

266. Denis, F. A.; Pallandre, A.; Nysten, B.; Jonas, A. M.; Dupont-Gillain, C. C., Alignment and Assembly of Adsorbed Collagen Molecules Induced by Anisotropic Chemical Nanopatterns. *Small* **2005,** 1, 984-991.

267. Lanfer, B.; Freudenberg, U.; Zimmermann, R.; Stamov, D.; Körber, V.; Werner, C., Aligned fibrillar collagen matrices obtained by shear flow deposition. *Biomaterials* **2008,** 29, 3888-3895.

268. Buttafoco, L.; Kolkman, N. G.; Engbers-Buijtenhuijs, P.; Poot, A. A.; Dijkstra, P. J.; Vermes, I.; Feijen, J., Electrospinning of collagen and elastin for tissue engineering applications. *Biomaterials* **2006,** 27, 724-734.

269. Habibi, Y.; Lucia, L. A.; Rojas, O. J., Cellulose Nanocrystals: Chemistry, Self-Assembly, and Applications. *Chem. Rev.* **2010,** 110, 3479-3500.

270. Gusnard, D.; Kirschner, R. H., Cell and organelle shrinkage during preparation for scanning electron microscopy: effects of fixation, dehydration and critical point drying. *J. Microsc.* **1977,** 110, 51-57.

271. Barth, A.; Zscherp, C., What vibrations tell about proteins. *Quarterly Reviews of Biophysics* **2002,** 35, 369-430.

272. Metzler, D. E.; Metzler, C. M., Light and Life. In *Biochemistry: The Chemical Reactions of Living Cells*, 2nd ed.; Academic Press 2001: San Diego, CA, USA, 2001; p 1277.

273. Wallace, D. G.; Rosenblatt, J., Collagen gel systems for sustained delivery and tissue engineering. *Adv. Drug Deliv. Rev.* **2003,** 55, 1631-1649.

274. Comper, W. D.; Veis, A., The mechanism of nucleation for in vitro collagen fibril formation. *Biopolymers* **1977,** 16, 2113-2131.

275. Na, G. C.; Butz, L. J.; Carroll, R. J., Mechanism of in vitro collagen fibril assembly. Kinetic and morphological studies. *J. Biol. Chem.* **1986,** 261, 12290-12299.

276. Williams, B. R.; Gelman, R. A.; Poppke, D. C.; Piez, K. A., Collagen fibril formation. Optimal in vitro conditions and preliminary kinetic results. *J. Biol. Chem.* **1978,** 253, 6578-6585.

277. Parkinson, J.; Kadler, K. E.; Brass, A., Simple physical model of collagen fibrillogenesis based on diffusion limited aggregation. *J. Mol. Biol.* **1995,** 247, 823-831.

278. Tanaka, S.; Hata, R.-I.; Nagai, Y., Two-dimensional Electrophoresis of the α-Chains of Collagens and Its Application to the Determination of their Isoelectric Points. *Coll. Rel. Res.* **1981,** 1, 237-246.

279. Usha, R.; Ramasami, T., Effect of pH on dimensional stability of rat tail tendon collagen fiber. *J. Appl. Polym. Sci.* **2000,** 75, 1577-1584.

280. Bisson, I.; Kosinski, M.; Ruault, S.; Gupta, B.; Hilborn, J.; Wurm, F.; Frey, P., Acrylic acid grafting and collagen immobilization on poly(ethylene terephthalate) surfaces for adherence and growth of human bladder smooth muscle cells. *Biomaterials* **2002,** 23, 3149-3158.

281. Matsumura, K.; Hyon, S.-H.; Nakajima, N.; Peng, C.; Tsutsumi, S., Surface modification of poly(ethylene-co-vinyl alcohol) (EVA). Part I. Introduction of carboxyl groups and immobilization of collagen. *J. Biomed. Mater. Res.* **2000,** 50, 512-517.

282. Stamov, D. R.; Müller, A.; Wegrowski, Y.; Brezillon, S.; Franz, C. M., Quantitative analysis of type I collagen fibril regulation by lumican and decorin using AFM. *J. Struct. Biol.* **2013,** 183, 394-403.

283. Greminger, G. K.; Savage, A. B., Methylcellulose and Its Derivatives. In *Industrial Gums: Polysaccharides and Their Derivatives*, Whistler, R. L.; BeMiller, J. N., Eds. Academic Press Inc.: New York, NY, 1959; p 580.

284. Parida, B.; Iniyan, S.; Goic, R., A review of solar photovoltaic technologies. *Renew. Sust. Energ. Rev.* **2011,** 15, 1625-1636.

285. Barbir, F., PEM electrolysis for production of hydrogen from renewable energy sources. *Sol. Energy* **2005,** 78, 661-669.

286. Praxair, *http://www.praxairdirect.com/Product2_10152_10051_14568_-1_11532___* **2015,** Accessed 2/26/2015.

287. Huang, S.; Li, L.; Van der Biest, O.; Vleugels, J., Influence of the oxygen partial pressure on the reduction of CeO_2 and CeO_2ZrO_2 ceramics. *Solid State Sci.* **2005,** 7, 539-544.

288. Wang, S.; Hao, H.; Zhu, B.; Jia, J.; Hu, X., Modifying the oxygen adsorption properties of $YBaCo_4O_7$ by Ca, Al, and Fe doping. *J. Mater. Sci.* **2008,** 43, 5385-5389.

289. Gaborieau, M.; Castignolles, P., Size-exclusion chromatography (SEC) of branched polymers and polysaccharides. *Anal. Bioanal. Chem.* **2011,** 399, 1413-1423.

290. Nielen, M. W. F., Maldi time-of-flight mass spectrometry of synthetic polymers. *Mass Spectrom. Rev.* **1999,** 18, 309-344.